



Towards understanding the role of 'silicon' in life

Aneeqa Fayyaz

A thesis submitted in partial fulfilment of the requirements of
Nottingham Trent University for the degree of Doctor of
Philosophy

October 2020

This work is the intellectual property of the author. You may copy up to 5% of this work for private study, or personal, non-commercial research. Any re-use of the information contained within this document should be fully referenced, quoting the author, title, university, degree level and pagination. Queries or requests for any other use, or if a more substantial copy is required, should be directed in the owner(s) of the Intellectual Property Rights.

Abstract

Silicon is an essential trace element that is required for physiological bone growth and health. Though silicon has been shown to have an essential effect on mineralised tissues, current research is still lacking understanding of many aspects of the mechanism involved and further knowledge enhancement is needed to fulfil this research gap. Another area of silica science where understanding is relatively more developed is the study of living organisms such as bacteria and plants that deposit silica during a process called biosilicification though even here the chemistry of the silica phase is incompletely understood. The main aims of this PhD research were to focus on understanding the role of silicon in different organisms.

An Optically Sectioned Planar Format Indicator Displacement Assay (O-IDA) was developed to study silica-biomolecule interactions. An analytical tool to map surface charge properties of silica in silicifying organisms (both non-living and living samples) was implemented. And, a study to understand the role of silicon in animals through a transcriptome evaluation method, RNA sequencing with evaluation of differential gene expression, was performed. A fluorophore, PDMPO (2-(4-pyridyl)-5-((4-(2-dimethylaminoethylaminocarbonyl)methoxy)phenyl)oxazole), was utilised to develop O-IDA and to implement the analytical tool to map surface charge. The binding affinities of a number of small molecules with different functionalities (amino acids, a drug, a polyamine) and large biomolecules (7-mer peptides) were studied through O-IDA where ΔG_{ads} values ranging from -12.82 to -7.82 kcal mol⁻¹ were obtained where Ibuprofen was best and peptide L7 (LDHSLHS) was the worst silica binder. Hence, O-IDA has potential to be used to screen silica binders. The implementation of the surface charge mapping tool allowed a proxy measure of silica chemistry/acidity through zeta potential estimation. On application to various silicifying organisms, an exemplary sample of the basal stem of *Equisetum arvense* cell wall showed a range of -25 to -33 mV zeta potential values which led to an estimation of varying silica particle sizes to up to 100 nm.

An RNA transcriptome using an animal bone tissue enhanced the understanding of the mechanisms involved in utilising silicate from diet for bone health. The detected

biological pathways demonstrated the role of silicon as anti-inflammatory (affected pathways; osteoclast differentiation, T cell differentiation, phagosome and cytokine-cytokine receptor interaction) and anti-oxidative (affected pathways; glutathione metabolism and ribosome) on bone tissue which promote osteogenesis through possible non-genetic routes.

Acknowledgements

First and foremost, I would like to start by sincerely thanking my supervisor, Prof. Carole C. Perry, for her continuous support, invaluable guidance and encouragement throughout the PhD studies (both with research and thesis writing). Also, a sincere thanks to my co-supervisor Dr. Quentin Hanley for his suggestions and advice throughout the PhD. I am grateful to my supervisors for providing me with this PhD opportunity and the Vice Chancellor's scholarship from Nottingham Trent University (NTU) for the funding which made this PhD possible.

I would like to thank and acknowledge the support and discussions that I have had with Dr. David Belton, Dr. Graham Hickman, Dr. Victor Volkov, Dr. Monika Michaelis, Dr. Igor Efimov and Dr. Mithun Parambath which have somehow contributed to this thesis. I would like to extend my thanks to my independent assessor, Dr. Elisabetta Verderio Edwards, for valuable discussions and encouragement during the PhD studies. A special thanks to Dr. Emily Burton and her team at Brackenhurst Campus who organised the animal trial and made suitable arrangements for the tissue sampling. I also acknowledge all fellow colleagues of the Biomolecular and Materials Interface Group during my time at NTU which made my time at NTU a memorable experience; Dr. Veeranjanyulu Thota, Dr. Zayd Westcott, Sumaira Kousar, Sajida Farheen, Daniel Oliver, Kathryn Kroon, Rajeharish Rajendran, Anuradha Bandaranayake, Jason Sanderson, Vladimir Astachov, Anna Sola Rabada, Robyn Plowright and Samiat Adeitan. I would also like to thank everyone outside my research group with whom I have spent memorable times.

Last but not least, I would also like to express my gratitude to my parents, Mr. Fayyaz Asghar and Mrs. Kalsoom Fayyaz, for their countless sacrifices, support, unconditional love and prayers which have led me to where I am today. A huge thanks to my brothers, Asad and Ahad, for their countless support and encouragement whenever I needed it. I would also like to sincerely thank my husband, Raheel, for being supportive and understanding towards my commitment for PhD studies over the last few years. This PhD studies would not have been possible without the love and support of my whole family. I would also like to thank my dear friend, Lubna, who has always been available for me during the ups and downs of my life over the last 10 years.

Table of Contents

Abstract.....	ii
Acknowledgements.....	iv
Chapter 1. Introduction	1
1.1. Role of amorphous silica in living organisms (excluding animals – see section 1.8)	1
1.2. Chemistry of silica and silica polymerisation	3
1.3. Silica-biomolecule interest and scope.....	5
1.4. Silica materials.....	5
1.5. Implications of silica materials in research industry	7
1.6. Previous techniques employed to study silica size/chemistry and biosilicification	9
1.7. Fluorescence dye, PDMPO and confocal scanning laser microscopy	10
1.8. Role of silicon in animals	12
1.9. Bone related diseases such as osteoporosis and their impact on healthcare	13
1.10. Current proposed mechanisms of role of silicon in bone homeostasis.....	14
1.11. Thesis outline: Towards understanding the role of ‘silicon’ in life	15
Chapter 2. Methodology.....	17
2.1. Introduction.....	17
2.2. Solid Phase Peptide Synthesis	18
2.3. High Performance Liquid Chromatography.....	21
2.4. Matrix-Assisted Laser Desorption Ionization Time-of-Flight Mass Spectrometry.....	24
2.5. Contact angle measurements	27
2.6. Confocal Scanning Laser Microscopy	28
2.6.1. Background to fluorescence	30
2.7. Zeta Potential and Dynamic light scattering	32
2.8. Scanning Electron Microscopy	34
2.9. Inductively Coupled Plasma Optical Emission Spectrometry.....	36
2.10. RNA sequencing.....	38
2.11. Bioanalyzer	42
Chapter 3. Development of a novel Displacement Assay for screening abiotic/biotic interactions	44

3.1.	Introduction.....	44
3.2.	Materials.....	46
3.3.	Methodology	46
3.3.1.	Silica surface preparation.....	46
3.3.2.	CSLM and experimental parameters	48
3.3.3.	Background and importance of the assay system and its design	48
3.3.4.	Preliminary experimentation	49
3.3.5.	Setting up of O-IDA technique	53
3.3.6.	Data fitting - Origin.....	53
3.4.	Theory behind O-IDA	55
3.4.1.	Binding affinity of the Indicator – O-IDA.....	55
3.4.2.	Indicator Displacement Assay - O-IDA	57
3.4.3.	Fitting procedure used for the extraction of surface bound contribution, B (Intensity).....	62
3.5.	Discussion (data analysis and key findings).....	67
3.5.1.	Amino acids - Histidine, Aspartic acid and Alanine.....	73
3.5.2.	Polyamine - Spermine	75
3.5.3.	Drug - Ibuprofen.....	75
3.5.4.	Peptides.....	76
3.6.	Conclusion	80
Chapter 4.	Implementation of a fluorescence-based surface charge mapping method to study silica chemistry in biological tissues	82
4.1.	Introduction.....	82
4.1.1.	Biologically relevant tissues	84
4.2.	Development of the surface charge mapping method	85
4.2.1.	Silica nanoparticle synthesis and characterisation	85
4.2.2.	Production of the calibration plot for surface charge mapping method development.....	86
4.2.3.	Calibration plot and related equations	89
4.3.	Chemicals and Materials	91
4.4.	Experimental methodology	91
4.4.1.	Scanning Electron Microscopy	91
4.4.2.	CSLM and experimental parameters	91

4.4.3.	Processing the fluorescence emission intensity data collected using CSLM	92
4.5.	Background fluorescence	94
4.6.	Exemplary samples for surface charge mapping	94
4.6.1.	<i>Equisetum arvense</i>	95
4.6.2.	Diatoms	98
4.7.	Results and Discussion	99
4.7.1.	Background fluorescence.....	99
4.7.2.	<i>Equisetum arvense</i>	101
4.7.3.	Diatoms	116
4.8.	Conclusion	130
Chapter 5.	Towards understanding the biological mechanisms involved in the role of silicon (as silicate) uptaken from dietary intake through transcriptome analysis using RNA sequencing	132
5.1.	Introduction.....	132
5.1.1.	Techniques available for transcriptome analysis.....	133
5.1.2.	Background to bone homeostasis.....	134
5.1.3.	Bone metabolism or repair	137
5.2.	Materials and Methods	137
5.2.1.	Experimental design for animal trial.....	137
5.2.2.	Sample collection and preparation	138
5.2.2.1.	Blood plasma silicon content analysis	138
5.2.2.2.	Disrupting bone (hard tissue) samples using liquid nitrogen	140
5.2.2.3.	RNA extraction and purification.....	141
5.2.2.4.	DNA removal using Invitrogen DNA free kit	147
5.2.2.5.	Zymo RNA clean up and concentrator	147
5.2.2.6.	Quality control	149
5.2.3.	RNA sequencing (transcriptome) and bioinformatics	152
5.2.3.1.	Quality control by BGI	152
5.2.3.2.	Comparisons studied.....	155
5.3.	Results and Discussion	155
5.3.1.	Parameters studied	155
5.3.2.	Principle component analysis	159

5.3.3.	Venn diagrams	162
5.3.4.	Differentially Expressed Genes	164
5.3.4.1.	DEG plots.....	165
5.3.4.2.	Heatmaps	165
5.3.4.3.	KEGG pathways and related findings.....	171
5.4.	Conclusion	197
5.5.	Appendix.....	199
Chapter 6.	Conclusion and Future works.....	213
6.1.	Development of a novel Displacement Assay for screening abiotic/biotic interactions.....	213
6.1.1.	Conclusion	213
6.1.2.	Future work.....	214
6.2.	Implementation of a fluorescence-based surface charge mapping method to study silica chemistry in biological tissues	215
6.2.1.	Conclusion	215
6.2.2.	Future work.....	216
6.3.	Towards understanding the biological mechanisms involved in the role of silicon (as silicate) uptaken from dietary intake through transcriptome analysis using RNA sequencing.....	217
6.3.1.	Conclusion	217
6.3.2.	Future work.....	218
References.....		220
Publication.....		252

Table of Figures

Figure 1.1 – Silica polymerisation process for different environmental conditions.....	4
Figure 2.1 – Illustration of SPPS and the steps involved.....	20
Figure 2.2 – Basic setup of the HPLC instrumentation.	22
Figure 2.3 – Basic setup of MALDI-TOF mass spectrometer and illustration of MS process.	26
Figure 2.4 – Contact angles (θ) of different surfaces, A. Hydrophilic and B. Hydrophobic	27
Figure 2.5 – Principle mechanism of the laser pathway in CSLM.	29
Figure 2.6 – Representation of electronic and vibrational transitions giving rise to fluorescence emission.....	31
Figure 2.7 – Electrical double layer around a negatively charged particle surface.	33
Figure 2.8 – Basic components of SEM instrumentation.....	35
Figure 2.9 – Schematic of electron – sample interactions.....	35
Figure 2.10 – Major components of the ICP-OES instrument.	37
Figure 2.11 – Process of library construction in RNA sequencing.	40
Figure 2.12 – Bio-informatics analysis pipeline	41
Figure 3.1 – Interaction of water droplet with the silica surface over time.....	47
Figure 3.2 – Characteristics of fluorescent dye, PDMPO, to silica under CSLM	52
Figure 3.3 – An overview of the binding assay of the selected indicator, PDMPO, and the optically sectioned planar format IDA for silica.....	54
Figure 3.4 – An overview of O-IDA using silica surface – two-step process explained in detail.....	58
Figure 3.5 – An overview of the Silica/PDMPO interaction in an optically sectioned planar format indicator displacement assay.....	65
Figure 3.6 – Comparison between the two fitting methods for the extraction of surface bound contribution, B, using dose response curves.....	66
Figure 3.7 – Dose response curves obtained through O-IDA to silica	70
Figure 3.8 – Structures of Histidine, Aspartic acid, Alanine, Spermine and Ibuprofen ..	71
Figure 3.9 – Dose response curves obtained through O-IDA to silica	72
Figure 4.1 – Electrical double layer around a negatively charged particle surface.	88

Figure 4.2 – Left: Calibration plot - zeta potential (ζ) against log of PDMPO emission ratio ((PDMPOH ₂) ²⁺ /PDMPOH ⁺), Right: Zeta potential (ζ) against the size (as diameter) of SNP	89
Figure 4.3 – Diatoms collected or used for the surface charge determination method.	98
Figure 4.4 – Functional images showing the background fluorescence intensity under different circumstances within the confocal scanning laser microscope used.	100
Figure 4.5 – A graph displaying the normalised fluorescence intensity in form of fluorescence emission spectrum for chlorophyll.....	101
Figure 4.6 – Functional images illustrating the time dependent behaviour of PDMPO uptake into the stomata and star shaped rosette like structures within Equisetum arvense.....	103
Figure 4.7 – Functional imaging of charge on stomata and ridges of Equisetum arvense	104
Figure 4.8 – Functional imaging of charge on stomata of Equisetum arvense	105
Figure 4.9 – Functional imaging of charge on stomata and ridges of Equisetum arvense	106
Figure 4.10 – Functional imaging of charge on stomata, star shaped rosettes like structures, and a random array of pilulae covering the nodal plane of the cell wall of Equisetum arvense.....	107
Figure 4.11 – Functional imaging of charge on stomata, star shaped rosettes like structures, and a random array of pilulae covering the nodal plane of the cell wall of Equisetum arvense.....	108
Figure 4.12 – SEM images of spores of Equisetum arvense	109
Figure 4.13 – Functional imaging of charge on a spore with elaters of Equisetum arvense	110
Figure 4.14 – Functional imaging of charge on multiple wrapped spores of Equisetum arvense	111
Figure 4.15 – Functional imaging of charge on spherical silica structures disassociated from the surface of the spores of Equisetum arvense	112
Figure 4.16 – Functional imaging of charge on diatom, Coscinodiscus Wailesii (valve view).....	118

Figure 4.17 – Functional imaging of charge on diatom, <i>Coscinodiscus Wailesii</i> (valve view).....	119
Figure 4.18 – Functional imaging of charge on diatom, <i>Coscinodiscus Wailesii</i> (girdle view).....	120
Figure 4.19 – Functional imaging of charge on diatom, <i>Coscinodiscus Wailesii</i> (girdle view).....	121
Figure 4.20 – Functional imaging of charge on diatom, <i>Cylindrotheca Closterium</i>	122
Figure 4.21 – Functional imaging of charge on diatom, <i>Diatoma mesodon</i>	123
Figure 4.22 – Functional imaging of charge on diatom, <i>Diatoma mesodon</i>	124
Figure 4.23 – Functional imaging of charge on diatom, <i>Diatoma vulgare</i> bory (separating diatoms)	126
Figure 4.24 – Functional imaging of charge on diatom, <i>Diatoma vulgare</i> bory (joined)	127
Figure 4.25 – Functional imaging of charge on diatom, <i>Diatoma vulgare</i> bory (joined)	128
Figure 4.26 – Functional imaging of charge on diatom, <i>Diatoma vulgare</i> bory (joined)	129
Figure 5.1 – Calibration curve for ICP-OES analysis	139
Figure 5.2 – Bone sampling of right tibia. (a) Whole bone with all the muscle, tendon and articular cartilage removed. (b) An example of growth plates and middle of bone.	140
Figure 5.3 – An overview of RNA extraction process.....	143
Figure 5.4 – RNA nanochip preparation.....	151
Figure 5.5 – Bone characteristics - a) height b) width c) weight and Bird characteristics - d) weight e) Blood plasma SiO ₂ level	157
Figure 5.6 – PCA analysis for all sample groups studied in both the control and silicon treated diets (a) PC2 vs PC1 (b) PC4 vs PC3	161
Figure 5.7 – Venn diagram of gene expression between the different comparisons studied.....	163
Figure 5.8 – Summary of statistics of DEGs for all the different comparisons studied.	164
Figure 5.9 – Scatter plot of DEGs (a) Day 7 GP C vs Day 14 GP C (b) Day 7 M C vs Day 14 M C (c) Day 7 GP Si vs Day 14 GP Si.....	166

Figure 5.10 – Scatter plot of DEGs (a) Day 7 M Si vs Day 14 M Si (b) Day 7 GP Si vs Day 7 GP C (c) Day 7 M Si vs Day 7 M C	167
Figure 5.11 – Scatter plot of DEGs (a) Day 14 GP Si vs Day 14 GP C (b) Day 14 M Si vs Day 14 M C	168
Figure 5.12 – Heatmap of DEGs (a) Day 7 GP C vs Day 14 GP C (b) Day 7 M C vs Day 14 M C (c) Day 7 GP Si vs Day 14 GP Si (d) Day 7 M Si vs Day 14 M Si	169
Figure 5.13 – Heatmap of DEGs (a) Day 7 GP Si vs Day 7 GP C (b) Day 7 M Si vs Day 7 M C (c) Day 14 GP Si vs Day 14 GP C (d) Day 14 M Si vs Day 14 M C	170
Figure 5.14 – Osteoclast differentiation pathway	175
Figure 5.15 – Gene expression level of the DEGs identified under osteoblast differentiation pathway (a) CSF1 (b) IL1R1 (c) TEC (d) SOS3 (e) SYNGR3	183
Figure 5.16 – Gene expression level of the DEGs identified under osteoblast differentiation pathway (a) LOC107050017 (b) SPI1 (c) LOC100857409 (d) LOC107050774 (e) LOC107049125	184
Figure 5.17 – Gene expression level of the DEGs identified under osteoblast differentiation pathway (a) LOC107050283 (b) LOC112529962 (c) CHIR-AB1 (d) LOC107055386 (e) LOC112531100	185
Figure 5.18 – Gene expression level of the DEGs identified under osteoblast differentiation pathway (a) LOC107049514 (b) CSF1R (c) MAPK11 (d) CTSK (e) ACP5	186
Figure 5.19 – Gene expression level of the DEGs identified under osteoblast differentiation pathway (a) CHIR-AB-600 (b) LOC100857375 (c) LOC101747711 (d) MAPK9 (e) PPARG	187
Figure 5.20 – Th17 cell differentiation pathway	190
Figure 5.21 – Glutathione metabolism pathway	195
Figure 6.1 – Orientation of PDMPO dye on silica surface.....	215

Table of Tables

Table 3.1 – Binding affinities of selected biomolecules to silica surfaces	69
Table 3.2 – Binding affinities of selected peptides to silica surfaces.....	71
Table 3.3 – Binding affinities of chosen peptides to silica surfaces in literature compared to the ones calculated through this study	80
Table 5.1 – A comparison of the RNA extraction methods and the effects of the number of elution on RNA yield.	142
Table 5.2 – The birds’ allocation to the groups for transcriptome analysis for the control pen.....	154
Table 5.3 – The bird’s allocation to the groups for transcriptome analysis for the silicate treated pen.....	154
Table 5.4 – Comparisons studied for the transcriptome analysis	155
Table 5.5 – Bone’s parameters, bird’s weight and blood plasma content on day 7 control and silicate treatment pen and day 14 control and silicate treatment pen.....	156
Table 5.6 – Bone’s parameters and blood plasma content normalised to bird weight on day 7 control and silicate treatment pen. p-value < 0.05 was considered significant.	158
Table 5.7 – Bone’s parameters and blood plasma content normalised to bird weight on day 14 control and silicate treatment pen. p-value < 0.05 was considered significant.	158
Table 5.8 – Significantly enriched KEGG pathways involved for Day 14 M Si vs Day 7 M Si	174
Table 5.9 – Significantly enriched KEGG pathways involved for Day 14 GP Si vs Day 7 GP Si	193

Chapter 1. Introduction

Silicon, Si, is the second most abundant element in the earth's crust. Due to its chemical nature, it is rarely found in its elemental form in nature (WHO report 532, 1973). Most commonly, silicon is present in nature in the form of oxides (silica) and silicates (WHO report 532, 1973). Silica, SiO₂, is largely found in nature and forms the second most common biogenic mineral after carbonates (Lowenstam, 1989). In nature, silica exists in two forms: amorphous (non-crystalline - doesn't exhibit any order) or crystalline (ordered). Crystalline silica which is commonly found as α -quartz forms a basic compound of soil, sands and rocks (Iler, 1979). On the other hand, amorphous silica is what different living organisms deposit in order to provide them with structural and mechanical support which plays an important role in their lives (Perry, 2003).

1.1. Role of amorphous silica in living organisms (excluding animals – see section 1.8)

The living organisms capable of depositing silica are called silicifying organisms. Examples of such living organisms include higher land plants (i.e., mare's tail/horsetail), single cellular organisms (i.e., diatoms) and multicellular organisms (i.e., sponges) (Sola-Rabada et al., 2016; Sola-Rabada et al., 2018; Hildebrand, 2003; Müller et al., 2003). The understanding of this area of silica science involving such silicifying organisms is more developed and still growing as compared to the role of silicon in living organisms such as animals which will be discussed later.

With silica being slightly soluble in water, silica is present as soluble species in small quantities in natural water which forms a supply for these living organisms. The biomineralization process that forms biogenic or naturally hydrated silica (SiO₂·nH₂O) in living organisms from these soluble species is known as biosilicification. A range of inorganic polymerization reactions are involved in the process of biosilicification where the presence of organic species such as proteins, polyamines or proteoglycans are considered to regulate the biosilicification process in different organisms (Perry and Keeling-Tucker, 2000; Perry and Keeling-Tucker, 2003; Belton et al., 2008). Hence,

biosilicification process by living organisms to form highly ordered functional silica structures is a best example of silica-biomolecule interactions leading to mineral (silica) formation which led to a great interest in studying silica binding peptides to understand biosilicification.

Characterisation of the biomolecules entrapped within the isolated amorphous silica of the frustule revealed the role of long-chain polyamines and cationic polypeptides (silaffins) in diatom's biosilicification (Kröger et al., 2000; Kröger et al., 1999). Although both of these silica associated biomolecules have shown to accelerate silica formation from silicic acid *in vitro*, the mechanism behind this is still not well understood (Kröger et al., 2000; Kröger et al., 1999). Later studies suggested that it's the composition of the polyamines and amino acids in polypeptides that affect the silica condensation where it has been proposed that the cationic and hydroxyl groups of amino acids (such as serine and tyrosine) interact with anionic silica and neutral silanol groups respectively that induce or catalyse the precipitation of silica (Belton et al., 2008; Sumper and Kröger, 2004; Bernecker et al., 2010; Wieneke et al., 2011; Wenzl et al., 2008).

For most of the silicifying organisms, the silica structures produced serve as their skeleton and account for majority of their body mass (Sumper and Kröger, 2004). Silicifying organisms such as diatoms and horsetail biologically deposit complex patterned silica within their cell wall as they have the ability to uptake, store and process soluble silicon (Hildebrand, 2003). In diatoms, silicic acid transported by silicic acid transporters into the diatom cell wall gets concentrated in silica deposition vesicles (SDV) where polymerization takes place to form hydrated amorphous silica ranging from nano- to micro-meter in size (Kröger et al., 2000). The patterned silica cell wall with pores is termed as frustules where the patterning of the silica structures in the cell wall is species-specific and only seen replicated in diatom progeny (Sumper and Kröger, 2004).

Natural production of biogenic silica by silicifying organisms is carried out under mild conditions as compared to the harsh conditions required for the industrial process of silica production (Belton et al., 2012). Through improving the knowledge of biosilicification process and its mechanism involved, a more environmentally friendly

conditions could be adapted for *in vitro* synthesis of silica with reduced pollution as the current requirement of high energy could be tackled (Perry, 2003; Patwardhan et al., 2005). Hence, there is a great interest in biomimetic studies to effectively produce silicon-based materials.

1.2. Chemistry of silica and silica polymerisation

Upon silica polymerisation, soluble species such as silicic acid are usually condensed such that the number of siloxane bonds (Si-O-Si) are maximised in forming cyclic species which form a large proportion of silica with exposed silanol groups (Si-OH) on the surface (or as ionic siloxide group (SiO⁻) under aqueous conditions when water molecules are adsorbed on to the surface) (Belton et al., 2012). The silica polymerisation process can be explained in the following steps. At circumneutral pH, monosilicic acid in aqueous solution at levels above 100 ppm would condense spontaneously to form dimers followed by its growth to trimers and oligomers before forming stable silica particles of different sizes with kinetically distinct properties amongst each other (Belton et al., 2010). Presence of silanol groups on silica particles can lead to their aggregation with the adjacent nanoparticles through hydrogen bonding which either leads to formation of interconnected chains or branched network (gel) or as separated agglomerates/precipitate (sol or powder) depending on the environmental conditions such as pH or presence of salts/other ions (Iler, 1979). The silica polymerisation process is also shown in Figure 1.1 which also includes the effects of environmental conditions on their synthesis.

Generally due to the chemistry of silica surface, silica is usually hydrophilic due to the presence of silanol groups (Si-OH); however, the presence of a few hydrophobic sites as siloxanes (Si-O-Si) on the surface also provides possibilities of hydrophobic interactions with biomolecules etc. Moreover, the extent and proportion of these groups determine the character/chemistry of silica surface which can be tailored further through functionalising the silanol group. pK_a of exposed silanol groups of silica particles (1 nm size in diameter) is usually 6.8; hence, they carry a negative surface charge. In biological settings, these silica particles interact with the biochemical environment in which the silica is deposited which can shift its pK_a.

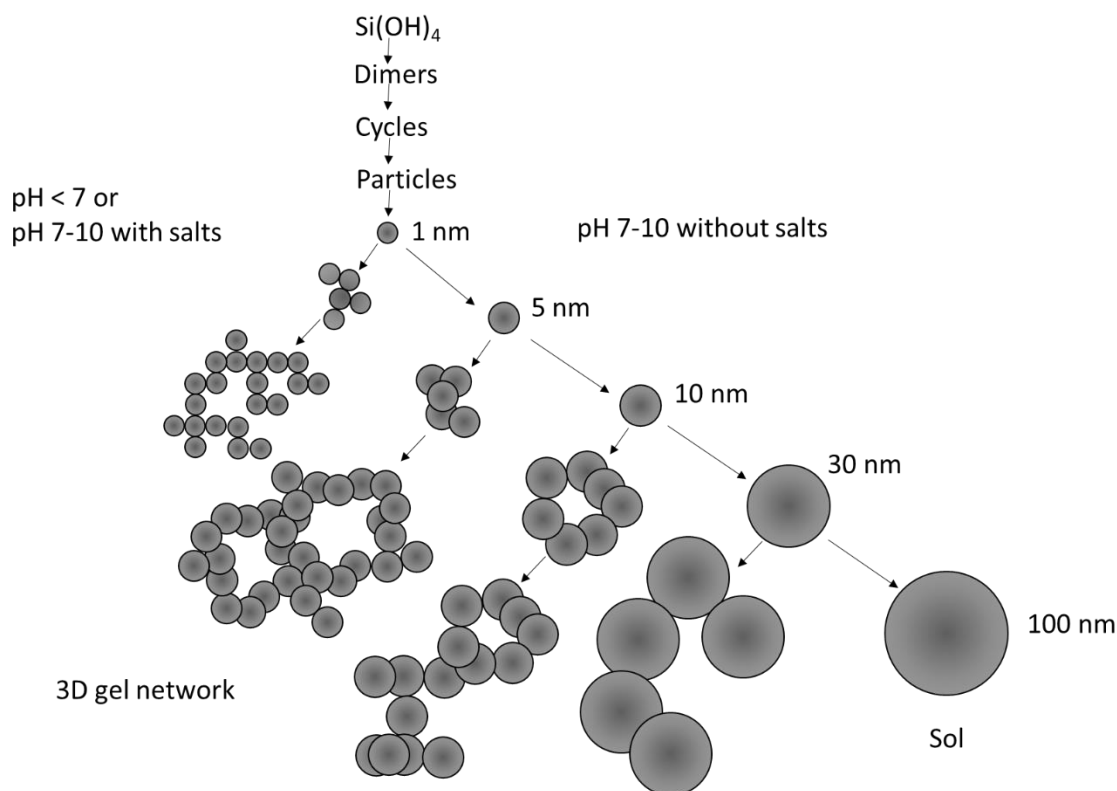


Figure 1.1 – Silica polymerisation process for different environmental conditions.

Adapted and modified from Iler, 1979.

The surface charge of silica surface depends on the number of the silanol groups present which affects the interactions of silica with biomolecules. Since an increase in size of silica particle mean an increase in the number of silanol groups, this increases the surface ionisation (charge density) leading to a higher surface activity (Patwardhan et al., 2012). Surface charge estimation is vital in biosilicification; therefore, an ability to accurately measure the local surface charge would be an exceptional advancement towards examining the mechanisms of silica nanostructures formation *in vivo*. Zeta potential measurement (Stern, 1924) is a proxy of the surface charge potential and a commonly used measurement for surface charge estimations.

The Guy-Chapman-Stern model explains the interface between silica and water using an electrical double layer comprised of two regions (Brown et al., 2015). The first inner layer from the silica surface (Stern layer) comprises of hydrogen ions adsorbed onto the surface due to chemical interactions. The stern layer is followed by a second double layer (also known as Diffuse layer) which is composed of freely moving cations and anions weakly attracted to the surface.

1.3. Silica-biomolecule interest and scope

The surface chemistry affects the biomolecule's affinity through the relative covalent bonding, electrostatic interactions and hydrogen bonding (Puddu and Perry, 2014; Sola-Rabada et al., 2018). In addition to the effects of surface chemistry of silica, surface water that adsorbs to silica through hydrogen bonding also plays a key role in biomolecule adsorption and interaction (Rimola et al., 2013). The affinity of a biomolecule also depends on its chemical properties as biomolecules with more polar groups as opposed to neutral groups will adsorb better through hydrogen bonding with the silanol groups (Patwardhan et al., 2012). In addition, since the biomolecules isolated from the silicifying organisms are large and complicated, smaller regions of macromolecules which have been identified as important usually form the basis for the model studies.

The research interest in interaction studies of the mineral (amorphous silica) with water and/or biomolecules at interfaces and/or the effect of biomolecules on regulating mineral (silica) formation is rising to understand the biogenic silica formation through the biosilicification process and to contribute towards the widespread applications of amorphous silica in material science (to develop biologically relevant materials inspired by nature) respectively (Sanchez et al., 2005).

1.4. Silica materials

The research interests mentioned above have also led to the fabrication of complex silica structured materials to fulfil these needs and form the basis of model studies. Amorphous silica can be synthesised in different forms where the silica nanoparticles (non-porous and porous) and silica fabricated films (surfaces) are commonly used. Both forms pose silanol groups that can be functionalised to tailor the surface chemistry depending on the needs of the research of interest.

Silica nanoparticles are commonly produced by a sol-gel method which consists of the hydrolysis of silica precursor to form silicon hydroxide $\text{Si}(\text{OH})_4$ followed by their

condensation into oligomers leading to silica nanoparticle formation (Brinker and Scherer, 1990). The size of silica particle is dependent on the rate of nucleation (hydrolysis) and growth (condensation) (Van Blaaderen et al., 1992). The rate of hydrolysis is affected by the presence of the acids or bases which lead to an increase in either the hydronium or hydroxide ions (Iler, 1979). The condensation process of silica is affected by a range of variables such as the concentration of starting unit (i.e., faster rate if it is over the solubility limit of amorphous silica which is concentration of 100 - 200 ppm equivalent of SiO₂), pH, temperature, pressure, and presence of other ions (Iler, 1979). The pH conditions utilised for the silica nanoparticles production affects their physical properties. Generally, acid-based methods produce particles with low porosity and higher density; whereas, the alkaline conditions produce mesoporous (with pores) spherical particles.

Stöber process is the most effective and commonly used route for the synthesis of silica nanoparticles which utilises basic conditions and changing the concentrations of reactants can produce a variety of particle sizes ranging from 10 nm to 2 µm (Stöber et al., 1968). Other methods of silica nanoparticles production include microemulsion method (basic conditions for hydrolysis) (Osseo-Asare and Arriagada, 1990), acid-based hydrolysis methods (Karmakar et al., 2000; Izutsu et al., 1997; Kawaguchi and Ono, 1990), microwave-assisted acid catalysed method (Lovingood et al., 2013) and chemical vapour condensation method (Vansant et al., 1995) which is commercially used and involves metal-organic precursors' decomposition, such as SiCl₄, under high temperature flame.

Different silica functionalised tissue culture polystyrene surfaces, hydrophobic and hydrophilic, can also be effectively produced by the sol-gel method (Hickman et al., 2012; Nicklin et al., 2014; Hickman et al., 2014; Hickman et al., 2016). This utilises the hydrophobic tissue culture polystyrene surfaces which is initially functionalised with polyaniline (PANI) through the polymerisation of aniline using ammonium peroxodisulfate as an oxidising agent such that the green PANI film adheres to the polystyrene surface through hydrophobic interactions. The PANI film is then treated with glutaric dialdehyde which allows protein immobilisation through covalent interactions where lysozyme is the protein of choice due to its previous use in generating

uniform silica films (Rai and Perry, 2009). Lysozyme adsorbs uniformly onto the areas of the surface with either PANI or glutaric dialdehyde and play an important role in silica film formation through precipitating the condensed silica precursor (tetramethyl orthosilicate) particles. The electrostatic interaction of the positively charged lysozyme molecules and the negatively charged silica particles is what most likely promotes the precipitation of silica around the lysozyme leading to the silica film formation with exposed silanol groups (Rai and Perry, 2009; Xu et al., 2003). The silanol groups can be functionalised to produce different surfaces with varying hydrophilicity or hydrophobicity. Other examples of methods to produce silica film include hybrid sol-gel film method that uses polylysine (Zolkov et al., 2004) and silica fabricated gel bioactive glass discs (Dieudonné et al., 2002).

1.5. Implications of silica materials in research industry

Silica is one of the most important inorganic material with direct implications in biomedicine and bio-nanotechnology (De Jong and Borm, 2008; Korzeniowska et al., 2013). Silica has lots of other technological uses, some of which are briefly discussed below.

Silica nanoparticles form ideal candidates for biomedical applications due to their biocompatibility and bioresorbable nature. The cytotoxicity studies of silica nanoparticles on cells show that they exhibit low toxicity where their toxicity depends on the amount of material used, time of exposure and size of nanoparticles (i.e., smaller sizes (< 20 nm) show higher toxicity) (Kim et al., 2015; Napierska et al., 2009). Mesoporous silica nanoparticles are commonly used as drug delivery systems where the use of silica nanoparticles was attracted due to the relatively large surface area, tuneable size, large pore volume (leading to incorporation of drugs, peptides etc.), easy surface modification, low toxicity, robustness and great stability in physiological fluids (Vallet-Regí et al., 2007; Fernandez-Fernandez et al., 2011; Baeza et al., 2014; Argyo et al., 2013).

Silica is usually non-fluorescent; however, the ease of functionalisation of silica nanoparticles has led to their labelling with extrinsic probes. Fluorescent composite

materials of silica nanoparticles over conventional fluorophores have been advantageous in various technological applications such as biomedical detections (Zhao et al., 2003), intracellular delivery (Fuller et al., 2008), sensors (Hornig et al., 2008; Latterini and Amelia, 2009) etc. Moreover, mesoporous silica particles (< 50 nm pore diameter size) have also attracted attention for enzyme immobilization such that expensive biological catalysts can be hosted within the pores which would allow them to be repeatedly utilised for as long as they remain active (Girelli and Mattei, 2005; Zucca and Sanjust, 2014). Other uses of bioinspired silica materials include optical biosensing (Monton et al., 2011), cell imaging (Korzeniowska et al., 2013) and tissue engineering (Wang et al., 2012) etc.

Silica has also been used to determine silica specific polypeptides through the phage display technique for silica-biomolecule studies (Patwardhan et al., 2012; Naik et al., 2002). Phage display technique relies on generic sequences (from combinatorial libraries) to identify polypeptides expressed on surface of phage against a target site (material of interest such as silica) through allowing their binding to the target sites (Smith, 1985; McCafferty et al., 1990). Larger silica particles, as both non-porous and porous (< 2 nm pore diameter size), have also been widely used in chromatography columns as stationary phase for isolation of various compounds in a solution (Kirkland et al., 2000).

Different silica functionalised tissue culture polystyrene surfaces, hydrophobic and hydrophilic, have been studied for biomedical applications such as in proliferation of cells and cancer metastasis research to improve the understanding of the disease and find possible cures without the requirement for animal studies (Hickman et al., 2012; Nicklin et al., 2014; Hickman et al., 2014; Hickman et al., 2016). Other uses of slightly different silica films include tissue derived cell growth (Zolkov et al., 2004) and osteoblast differentiation in cultures of bone marrow stromal cells (Dieudonné et al., 2002).

1.6. Previous techniques employed to study silica size/chemistry and biosilicification

The size or chemistry of silica microstructures and their interconnections within living organisms have been previously studied through various methods. Scanning electron microscopy has been used to study silica distribution in horsetails, *Equisetum arvense* (Anderson et al., 1990). Energy dispersive X-ray analysis combined with scanning or transmission electron microscopy has been used to identify co-localised inorganic mineral species including silicon within *Piper*, Piperaceae (Silva et al., 2014). Small and wide-angle X-ray diffraction methods along with transmission electron microscopy have been used for determining silica particle sizes in horsetail, *Equisetum arvense* (Holzhuter et al., 2003). Species specific differences in structural and fractal properties of biosilica from diatoms have also been studied using ultra small, small and wide-angle X-ray diffraction methods (Vrieling et al., 2004). Small and wide-angle X-ray diffraction has also been utilised to study the nanoscale uniformity of porous architecture in diatomaceous silica (Vrieling, et al. 2000). Using Infrared and Raman spectroscopy, colloidal and solid-state properties of silica have also been studied (Roach et al., 2006; Rai and Perry, 2012).

The silica condensation (*in vitro*) and biosilicification within living organisms (*in vivo*) have also been previously studied through various methods. UV-Vis absorbance spectroscopy has been utilised for solution-based studies to follow silica precipitation and the kinetics involved through studying scattering effects (Iler, 1979, Belton et al., 2012). Molybdenum blue colorimetric assay is another popular method which is commonly utilised for the measurement of monomeric silicic acid and has been used to study the stages of silica condensation from silica precursor, silicic acid (Perry and Lu, 1992).

Fluorescence-based assays have also been utilised to understand the biosilicification process. Previously, attempts have been made to label silica fluorescently in nature using a commonly available fluorophore, Rhodamine 123 (Li et al., 1989). It was shown that dye readily entered diatom's cell and became entrapped into the silica deposition

vesicle where it was co-deposited into the newly formed silica as the subsequently formed valves and girdle bands rich in silica displayed fluorescence. However, this dye exhibited low accumulation efficiency when compared to the bright auto fluorescence of the diatom cells (Li et al., 1989). Another dye, Bis(cytopentadienyl)titanium dichloride, has been used as a surface hydroxyl staining agent for biological silica (Perry et al., 1990). However, the insolubility of this dye in aqueous solution hindered its applicability in living specimens. Another dye, fluorescein, has been used as a staining agent which was covalently linked to isolated purified silica through the aid of a silane coupling agent, 3-aminopropyl triethoxysilane (Hodson, et al. 1994). However, this covalently linked dye method was solely feasible for the post-staining of silica exposed on a surface *in vitro* and is not applicable to living specimen. Another method combined scanning electron microscopy with confocal scanning laser microscopy to construct three-dimensional models of diatom frustules using a dye, luoresceinthioisocyanat-(3-aminopropyl) trimethoxysilane (Friedrichs et al., 2012). However, this technique was applied for staining of silica *in vitro* only.

A fluorescent dye, PDMPO (2-(4-pyridyl)-5-((4-(2-dimethylaminoethylaminocarbamoyl) methyl)phenyl)oxazole) has also been used to study silica biosilicification *in vivo* and it has been shown to exhibit a high accumulation efficiency (Leblanc and Hutchins, 2005; Shimizu et al., 2001). PDMPO has been used as a medical probe where it has been proven to be an effective tracer for silica contributing to the understanding of the biosilicification process (Shimizu et al., 2001). A study measured silica deposition in diatom using PDMPO which was incorporated into the silicified structures of diatom over time as silica was deposited (McNair et al, 2015). The fluorescence emissions of PDMPO from diatoms is what was used to estimate the amount of silica deposited (McNair et al, 2015).

1.7. Fluorescence dye, PDMPO and confocal scanning laser microscopy

Fluorophores are generally aromatic molecules which differ in their chemistry. Many fluorophores exhibit two excited states where their proportion depends on the environmental conditions. Both excited states may show fluorescence with different quantum yields or emission spectrums (Lakowicz, 2010). When exposed to a material,

an equilibrium exists between the bound and unbound states under aqueous conditions. The fluorescence of a fluorophore may only be observed in the presence of a material etc. as opposed to showing fluorescence all the time either when it is in bound or unbound form.

Fluorescence based analytical methods using fluorescence microscopy form powerful tools in research with a range of fluorophores or fluorescent labelled materials available for different purposes (Cambi and Lidke 2011). Fluorometric techniques are relatively more sensitive compared to other absorbance-based methods due to development of highly sensitive detectors where a small amount of fluorophore would usually be required (Demertzis, 2004; Lakowicz, 2010).

Fluorescent dye, PDMPO is a weakly basic oxazole dye that selectively accumulates within compartments with low pH (acidic environment) containing silica (Diwu et al., 1999). Thus, PDMPO or similar dyes are potential targets for researchers wishing to understand the chemical and structural properties of silica microstructures within silicifying organisms. The silicophilic (silica specific) behaviour of PDMPO has been further demonstrated in a detailed study that explore the silica-PDMPO interactions under different solvent and pH environments probed through fluorescence spectroscopy and UV-vis with supported computational data, dynamic light scattering and zeta potential measurements (Parambath et al., 2016). PDMPO exhibits both dual excitation and dual emission spectral peaks whose proportion is affected by pH particularly in the presence of silica and it was also suggested that pH modified the mode of attachment of PDMPO to silica where both a single-point (low anisotropy) or multipoint (high anisotropy) mode of interaction is possible (Parambath et al., 2016). Hence, both excited/charged emission states exhibit fluorescence with different quantum yields or emissions spectrum which are observed both when bound to silica or unbound under aqueous conditions.

PDMPO has unique non-covalent interactions with silica and a history of applications as a probe (Shimizu et al., 2001). PDMPO's preferred location of interaction is within the stern layer (Parambath et al., 2016) which is explained by the Guy-Chapman-Stern model (Brown et al., 2015). The knowledge of the interactions of PDMPO with silica can

be further explored to understand silica chemistry, biosilicification process and the interactions of different biomolecules with silica. In addition, the diverse chemistry of PDMPO makes it a suitable candidate for a wide range of applications through fluorometric techniques. During the PhD, PDMPO combined with confocal scanning laser microscopy (CSLM), a specialised fluorescence microscopy technique, has been utilised for a quantitative assay to study silica-biomolecule interactions and a tool for labelling and localisation of silica microstructures as well as study their surface charge properties.

CSLM (Minsky, 1961; Minsky, 1988) allows detection of fluorescence of a slice through the thickness of specimen making it a useful and non-invasive technique. CSLM formed an ideal instrument to explore the interaction of PDMPO with silica which aided the development of a quantitative assay to study silica-biomolecule interactions. CSLM also formed a useful technique to study molecules in a defined region such as silica microstructures in silicifying organisms as they exhibit an improved spatial resolution compared to conventional fluorescence microscopy. However, the spatial resolution of CSLM is still limited when compared to scanning or transmission electron spectroscopy. Hence, the aims with CSLM were to explore the silica chemistry using spectral imaging and not to study the nanoscale structures in detail.

1.8. Role of silicon in animals

Silicon is thought to be an essential trace element (WHO report 532, 1973) responsible for many biological functions of several living organisms but its role as an essential mineral is still uncertain (Farooq and Dietz, 2015). The silicon is found to be present in almost all organs and tissues with the connective tissue and bone having the highest concentration (Jugdaohsingh, 2007). It has been shown that silicon plays a role in the physiological bone growth and development (Wang et al., 2014; Carlisle, 1986); however, its mode of action is not yet fully understood. Numerous nutritional intakes of silicon in epidemiological studies have shown the beneficial health effects of silicon on bone (bone mineral density) and connective tissue.

Animal studies (Carlisle, 1986; Schwarz and Milne, 1972; Carlisle, 1972) have shown that silicon deficiency in the diet produces defects in connective and skeletal tissues. There is a strong positive association between silicon dietary intake and bone mineral density (Jugdaohsingh, 2007). Silicon has also shown to have a potential role in the formation and health of mineralised tissues independent of calcium and vitamin D (Carlisle, 1981). However, diet used during these animal studies were either amino acids or peptides based. Such a diet is ethically inappropriate and is not practiced anymore with a balanced diet been required for any animal experimentation. The extreme nutritional design of the prior animal experiments from 70's/80's also raises questions on the validity of the research outcomes. The role of silicon in animals is not well understood and is an area of interest for many researchers but poses many challenges as silicon is a difficult element to tackle in biological tissues including bone.

A positive association between the bone mineral density and dietary silicon has been documented in a few studies including men and/or postmenopausal women (Jugdaohsingh et al., 2003; Macdonald et al., 2012). Furthermore, a few studies also provide an evidence of the positive benefits of silicon through use of silica supplementation. An increase in the bone mineral density was associated to silica supplementation of 28mg/day given over 12 weeks to women with low bone mass (Jugdaohsingh, 2007). Other studies utilising silicon supplementation as choline stabilised orthosilicic acid at 6-12mg/day increased the bone forming marker (serum procollagen type 1 N-terminal propeptide), improved photodamaged skin surface as well as its mechanical properties and decreased hair or nail brittleness (Spector et al., 2008; Barel et al., 2005).

1.9. Bone related diseases such as osteoporosis and their impact on healthcare

Osteoporosis is a systemic disease that leads to increased bone fragility and susceptibility to fractures due to reduced bone mass which may contribute to considerable disability and even death in extreme cases (World Health Organ report, 2003). Many factors such as age, gender, ethnicity, diet, lifestyle, some medications and

other medical conditions may contribute to this condition. According to an estimate, more than nine million cases of fragility bone fractures are reported every year around the world (Johnell and Kanis, 2006) including 300,000 cases of within the UK (British Orthopaedic Association, 2007). Such a huge number of cases had costed the UK healthcare economy around £1.8 billion in 2000 and has been estimated to increase to up to £2.2 billion by 2025 (Burge et al., 2001). With UK having a 17.7% of total population (percentage estimated to increase to around 20% over the 10 years) comprising elderly population aged 65 years or over (Ons.gov.uk, 2018), the magnitude of this problem is significant.

As a current treatment of osteoporosis, calcium and vitamin D supplements are recommended and regularly prescribed (SIGN guideline 142, 2015). Though silicon is shown to have an essential effect on mineralised tissues, the current research is still lacking many aspects of the mechanism involved and further knowledge enhancement is needed to come up with novel approaches to tackle the rising bone health problem. Despite studies being present showing a link between the silicon and bone and skeletal muscle health, not enough information is present to be able to establish recommended daily intake (RDI). Silicon supplements as silica are available commercially for the general public as supplements extracted from Horsetail (*Equisetum arvense*) or Bamboo but with varying recommended dosages with no established RDI. The available animal and human data were judged by Institute of Medicine (IOM, 2001) to set RDI for silicon; however, the data used was too limited such that it was difficult to define the RDI. Since evidence exists that silicon has beneficial effects to several biological processes and can prevent abnormalities, an intake of 10-25mg/day is recommended to be sufficient (Nielsen, 2014).

1.10. Current proposed mechanisms of role of silicon in bone homeostasis

At present, the mechanism of action of silicon in the body is not entirely understood (Currie and Perry, 2007). Silicon bound to glycosaminoglycan has been suggested to be involved in the formation of cross-linking between collagen and proteoglycans (Carlisle, 1981; Schwarz, 1973). An *in vitro* study reported that such biological interactions of

silicon stimulate the synthesis of organic matrix (e.g., collagen type 1) and osteoblast differentiation (Reffitt, et al., 2003). In addition, silicon is thought to increase the level of calcium in the bone matrix though its location is unknown (Carlisle, 1981). Silicon is found to form anions with hydroxylated molecules in the bone growth regions which attract calcium ions leading to the apatite formation; however, silicon is lost after the calcification process which is why it is found in highest amounts in unmineralized bone tissue and lowest amounts in the fully mineralised bone tissue (Carlisle, 1997, Jugdaohsingh et al., 2015). Silicon has also been shown to affect the immune or inflammatory response and oxidative stress in murine macrophages (Kim et al., 2013). The production of inflammatory cytokines and its mediators was suppressed due to reduced radical scavenger activity and down-regulation of gene expression of inflammatory mediators studied through Reverse Transcription Polymerase Chain Reaction (RT-PCR) (Kim et al., 2013).

No gene expression analysis has ever been performed using animal tissue sample to determine the genes or pathways that may be involved in the mechanisms of silicon in bone growth and development. Hence, it is desired that efforts are made to understand the role of silicon using bone tissues from an animal trial with a balanced diet through transcriptome analysis.

1.11. Thesis outline: Towards understanding the role of 'silicon' in life

The thesis comprises of 6 chapters where chapters 3 - 5 comprise individual research studies with each including its own introduction, materials and methods section, results, discussion and a brief conclusion.

Chapter 1: This current chapter introduces the PhD project and the importance of the work carried out in chapters 3 - 5 which will contribute towards enhancing the current understanding of 'silicon' in life (different living organisms) where efforts are made to fill some of the gaps addressed. Each of the aims and objectives of this PhD study has been discussed below in their corresponding chapters (chapters 3 - 5).

Chapter 2: This chapter will include the instrumentation and discusses the background to the instruments and experimental methods used for the studies.

Chapter 3: The knowledge and understanding of a silicophilic fluorescent dye, PDMPO, and its interactions with silica are explored to develop a novel indicator displacement assay to study silica biomolecule interactions *in vitro* using confocal scanning laser microscopy. This will benefit a few areas of research such as drug delivery involving silica-based delivery systems, materials for biomedical use and biosilicification. Different amino acids, a polyamine and a drug were studied through this assay which aided its development. The displacement assay was then extended and applied to different 7-mer peptides to see the limitations of the assay and how the analysis may differ for larger biomolecules.

Chapter 4: The silicophilic fluorescence of PDMPO and its knowledge of interactions with silica were further explored to develop an imaging method to understand the surface charge properties of silica microstructures. Surface charge estimation will contribute towards an understanding of deposited biosilica and would play an essential role in understanding biosilicification process. The method development is based on spectral imaging through confocal scanning laser microscopy and it has been applied to different silicifying organisms.

Chapter 5: It is known that the silicon is an essential trace element and an important element for healthy bone growth. However, the biological pathways involved that induce the bone growth and the mechanism of its role in bone formation (osteogenesis) is not well understood. This chapter involves an RNA transcriptome analysis study with an aim to understand the different pathways involved in the mechanism of action of silicon in bone health.

Chapter 6: This chapter involves a discussion of the findings and their impact on the current research being carried out with the scope for possible future works and their benefits.

Chapter 2. Methodology

2.1. Introduction

This chapter will briefly introduce the principles of different characterisation techniques and methods employed during the PhD research. The theory behind the technique or method will be explained followed by a brief summary of its usage in the PhD research. Basic information on the instrument's company used and conditions of operation is included where appropriate for the research carried out and further details on its application can be found in the corresponding chapters.

Peptide sequences selected for the biomolecule and silica surface interaction study using the developed indicator displacement assay were synthesized using solid phase peptide synthesis (SPPS) protocol and their purity and molecular weight were determined using high performance liquid chromatography (HPLC) and matrix assisted laser desorption ionization time-of-flight (MALDI-TOF) mass spectrometry respectively. Contact angle measurements were carried out for the confirmation of the hydrophilicity of the synthesised silica surface used within the indicator displacement assay prior to its use. Confocal Scanning Laser Microscopy (CSLM) had been used for both the indicator displacement assay and the surface charge determination method for different living organisms. Zeta potential and dynamic light scattering measurements were carried as part of the development of the surface charge mapping tool. The morphology of the spore heads and spores of *Equisetum arvense* was studied using scanning electron microscopy (SEM) which aided the analysis of spore's surface charge determinations. Inductively coupled plasma - optical emission spectroscopy (ICP-OES) was used to quantify the silicon element in blood plasma (obtained from the birds used for the transcriptome analysis). RNA-sequencing was used for the transcriptome analysis to study the role of silicon (as sodium metasilicate) in bone health and growth where Bioanalyzer was utilised for the quality control checks of the total RNA samples used for RNA sequencing.

2.2. Solid Phase Peptide Synthesis

In solid Phase Peptide Synthesis (SPPS), the creation of a peptide chain is carried out in solution and initiated on an amino acid covalently connected to an insoluble polymeric support known as resin which forms the starting point for peptide synthesis. A series of deprotection and coupling steps take place for the consequent incorporation of desired amino acid and this process is replicated until the desired peptide chain length is achieved (Merrifield, 1963). In a final step known as cleavage towards the end of the peptide synthesis procedure, the solid resin support and protecting groups (generally present to prevent side reactions) within the side chains are removed to produce the desired final peptide.

The conventional peptide chemistry involved for its synthesis is a time-consuming process where purification and characterisation steps are needed after every amino acid addition which lead to a reduced yield for the final peptide. SPSS has immensely transformed the conventional peptide chemistry (and its associated disadvantages) due to the peptide remaining attached to the resin support throughout the whole synthesis process as it is carried out in the same reaction vessel leading to a minimal physical loss of peptide. Usually with SPSS, an excess quantity of reagents is utilised in order to ensure successful formation of the peptide where the non-reacted reagents can be easily washed out. The operations of synthesising peptide using SPSS is carried out in an automated manner which saves time as opposed to the conventional method (Merrifield, 1963). Even in SPPS, there is a possibility of side reactions or in-complete peptide synthesis to occur which could make peptide purification difficult in those cases (Cudic and Fields, 2008). The peptide synthesis using SPPS is dependent upon number of factors such as the nature of the resin and its linkage, type of protecting groups and coupling chemistries (single coupling is common but certain amino acids such as arginine require double coupling).

Figure 2.1 shows an illustration of the SPPS procedure. The peptide synthesis in SPPS starts at the C-terminal amino acid which is attached to the resin through a carboxyl group with the help of a linker which is later cleaved under acidic conditions. Further synthesis advances from C to N direction. The functional groups of the amino acid side

chains (R-groups) are usually protected in order to ensure the synthesis of the amino acid chain is directed from C to N direction and avoid any side chain reactions. These semi-permanent protecting groups (denoted as Y in Figure 2.1) are unaffected by the synthesis conditions of the peptide synthesis process using SPPS. The commonly used semi-permanent protecting groups are 2,2,4,6,7-pentamethyl-dihydrobenzofuran-5-sulfonyl (Pbf), trityl (Trt) and tertiary-butyl (tBu) (Pedersen et al., 2012).

During the initial loading, temporary protection group (denoted as X in Figure 2.1) is present on the N^α-amino group of the resin linked amino acid which becomes deprotected selectively using a deprotecting agent such as piperazine followed by a washing step for the removal of this temporary protecting group. This prepares for the addition of the second amino acid in excess with an activated carboxylic group (denoted as A in Figure 2.1) to be able to form an amide bond in a process called coupling which is carried out under basic conditions. The commonly used temporary protecting groups are 9-fluorenylmethyl carbamate (Fmoc) and tert-butoxycarbonyl (Boc) (Pedersen et al., 2012). Coupling is followed by a washing step that eliminates the excess of the reagents and prepares for the addition of the next amino acid. This process of deprotection of the temporary protection group of the amino acid followed by a washing step and coupling with the next amino acid followed by a washing step is carried out repeatedly until the desired peptide length is achieved (Albericio and Kates, 2000). After the last amino acid has been attached, the washing step deprotects the N-terminal amino acid through the removal of the associated temporary protecting group.

The synthesised peptide undergoes a final cleavage step which uses an acidic cleavage mixture, ensuring that this minimally affects the peptide, to detach and recover the peptide from the resin. The cleavage mixture contains an acid such as 90-95% trifluoroacetic acid, TFA, and a nucleophilic reagent (as scavenger) such as water, thioanisole, phenol, etc. The same cleavage mixture also leads to the deprotection of semi-permanent protecting groups in the side chain residues of the synthesised peptide. Scavengers are essential to prevent the undesirable reactions during the cleavage process as highly reactive cationic species are generated from the protecting groups, resin linkers and the amino acids of peptides containing electron rich functional groups. After the cleavage stage, the peptide is re-precipitated in chilled diethyl ether with

subsequent washes with diethyl ether to remove any impurities. The solvent is evaporated prior to lyophilisation of the synthesised peptide (Albericio and Kates, 2000).

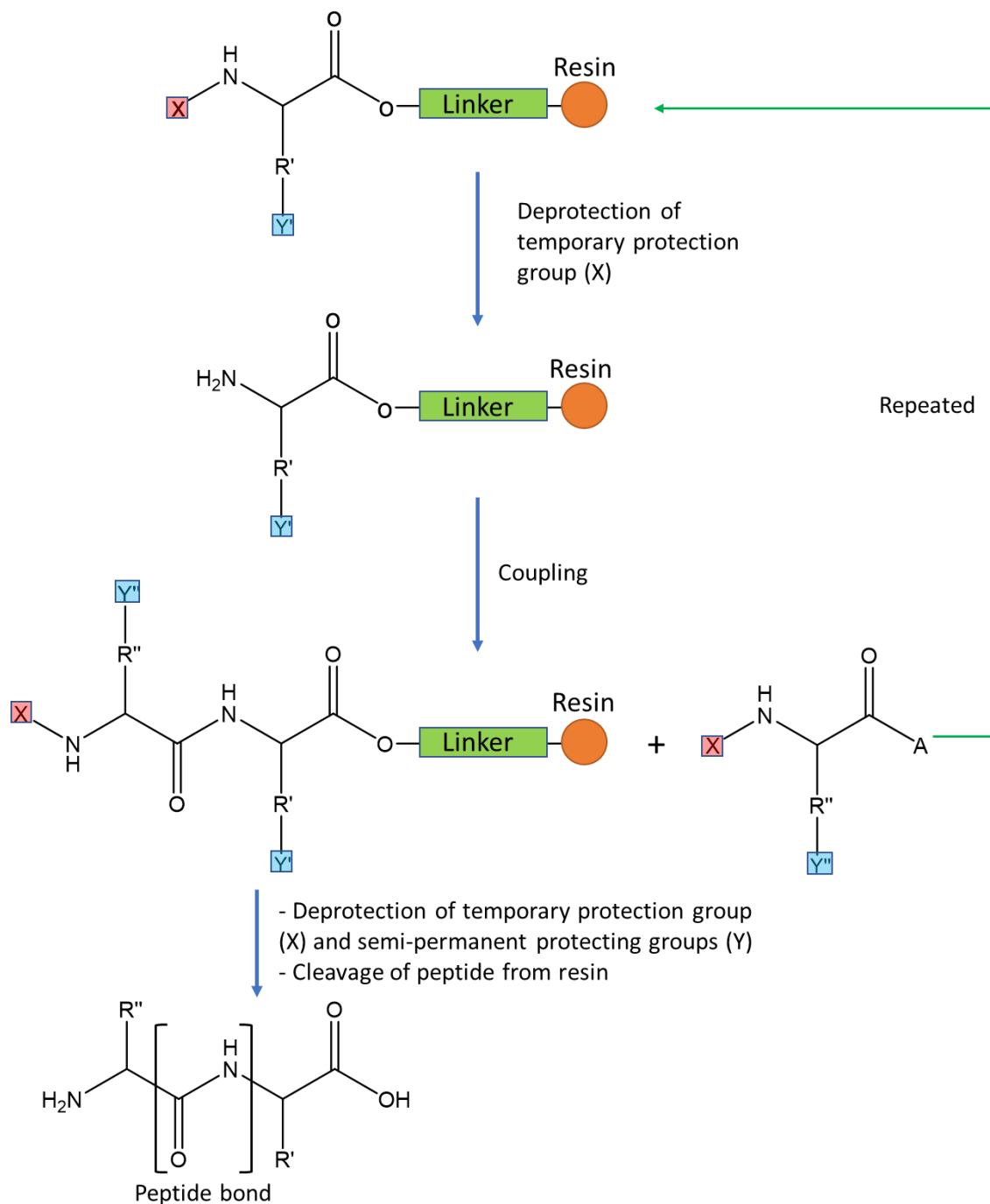


Figure 2.1 – Illustration of SPPS and the steps involved.

Adapted and modified from Cudic and Fields, 2008.

Here, X is the temporary protecting group, Y is the semi-permanent protecting group and A represents the activated carboxylic group of the amino acid being added.

The solid phase peptide synthesizers use microwave heating for the coupling process which has the following advantages: increases the speed of the reaction that saves time, reduces interactions within and between the peptide molecule(s) during the synthesis process and improves the purity and yield of the peptide sequences. Microwave assisted solid phase peptide synthesizer has allowed a synthesis of peptide sequences of up to over 100 amino acids (Pedersen et al., 2012).

During the PhD research, a Liberty Blue™ Automated Microwave Peptide Synthesizer (CEM Corporation) was used for the SPPS which allowed the preparation of the peptides utilised. The solid support used was a TGT resin preloaded with protected Fmoc. Several different side chain (of amino acid) and temporary (for N^α-amino group) protecting groups were utilised. The activator and activator base used for the coupling were O-Benzotriazole-N,N,N',N'-tetramethyl-uronium-hexafluorophosphate (HBTU) in N,N-dimethylformamide (DMF) and N,N'-Diisopropylethylamine (DIPEA) in N-methyl-2-pyrrolidinone (NMP) respectively. Single coupling chemistry was used. Before each coupling, Piperazine in DMF was used for N-terminal deprotection. Cleavage mixture containing TFA, thioanisole, 3,6-Dioxa-1,8-octanedithiol (DODT) and type I water was used to cleave and release the peptide from resin and to deprotect the side chains all in one step. Finally, reprecipitation of the cleaved peptides in chilled diethyl ether was carried out followed by several washing steps using chilled diethyl ether through centrifugations and discarding of the supernatant every time. The solvent was evaporated, and a few millilitres of water added to the peptide to allow lyophilisation at -70 °C using a freeze-dryer.

2.3. High Performance Liquid Chromatography

High Performance Liquid Chromatography (HPLC) is an analytical technique which separates compounds according to the differences in their structure and/or composition and can provide useful information about the purity and/or content of the different compounds present in a sample quantitatively (Kupiec, 2004). HPLC is popular for its ease, sensitivity, reproducibility and possibility of recovering the sample which can be reused for other purposes (Kupiec, 2004; Hennessy et al., 2003). HPLC requires the samples to be as liquid mixtures. Solid samples would either need to be dissolved or

extracted into a suitable solvent. Figure 2.2 shows a basic setup of the HPLC instrumentation which consists of a high-pressure pump, mobile phase reservoir, sample injector, solid stationary phase column, detector and data acquirer (data processor and display system).

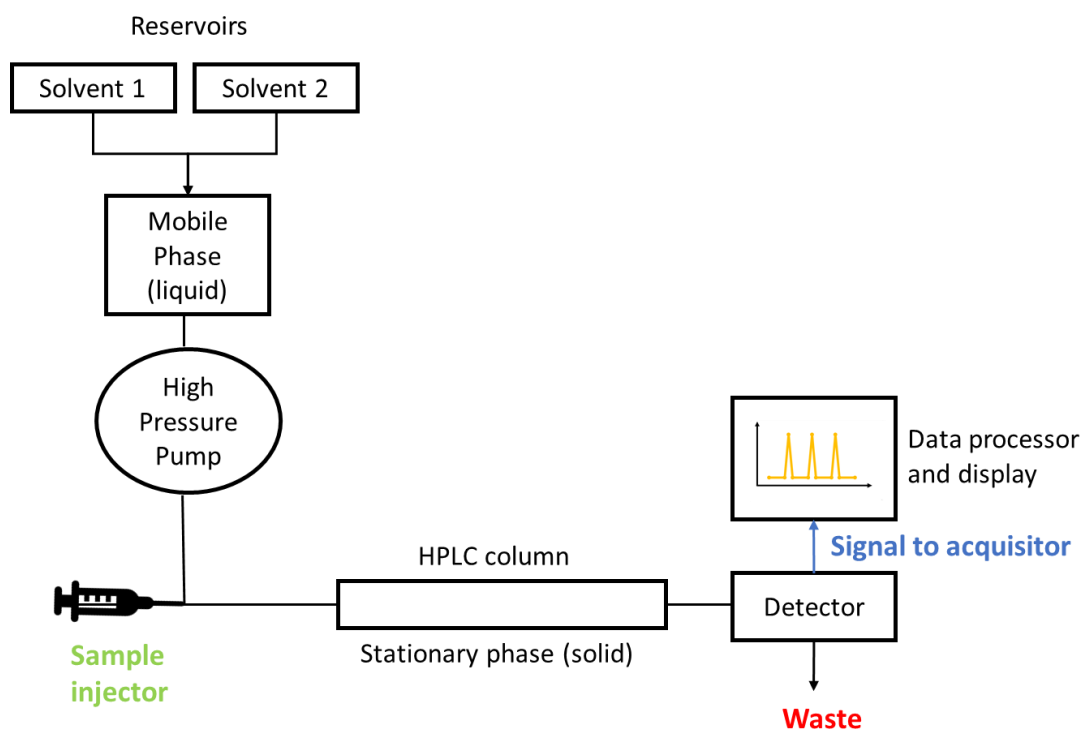


Figure 2.2 – Basic setup of the HPLC instrumentation.

Adapted and modified from Solà Rabadà, A., 2016.

A sample in form of a liquid is injected into the HPLC system through sample injector which can be a single injection or an automated injection system with multiple sampling positions making it easy to operate. A pressurised liquid known as mobile phase continuously pumps the sample through a column containing a solid adsorbent material known as stationary phase through the presence of a high-pressure pump. The pump speeds the separation process compared to the conventional gravitational column chromatography. The stationary phase is composed of porous particles which maximises the surface area for interactions of the compound molecules in the sample. The commonly used stationary phases are immobilized silica or alumina. Hence, the choice of the stationary phase as well as the mobile phase hugely depend on the types of compounds in the sample of interest to obtain the best separation or elution results.

Over time, the components of the sample separate depending on their chemical properties and affinity to the nature and composition of stationary and mobile phase respectively. A mixture of polar and non-polar liquid components commonly makes the mobile phase where their proportions can be altered depending on the types of compounds in the sample of interest to obtain the best separation or elution results. Different compounds travel with different velocities through the column which determines their corresponding retention time (the time when a compound is eluted from the column). Retention time is usually a characteristic of compounds under defined circumstances. The presence of an acquisition system such as a computer leads to the signal analysis of the data collected by the detector. For the chromatographic separation, the response of each detected component is presented in form of a chromatogram which is a plot of intensity of signal (y-axis) against retention time (x-axis).

There are two types of HPLC methods which are based on the type of the stationary and mobile phases: normal-phase (NP) or reverse-phase (RP). The separation is considered normal phase (NP-HPLC) when the stationary phase is more polar than mobile phase; whereas, the separation is considered reverse phase (RP-HPLC) when the stationary phase is less polar than mobile phase. RP-HPLC is the commonly used method for the separation of compounds based on their hydrophobic properties and is a powerful and useful method for the analysis of peptides (Kupiec, 2004).

During this PhD research, the purity of the synthesized peptides was found through a Dionex HPLC with a UV detector and a Jupiter 4u Proteo 90A C12 Reverse Phase column (Phenomenex). Chromeleon® software was used for the data processing. The chromatograph was used to quantify all the components in the sample through determining the area under the peaks and the purity determined through separating contaminant's contribution. The solid stationary phase used was tightly packed silica particles in a column. The mobile phase used was a mixture of two components: the polar component consisted of 95 % HPLC grade water and 5% HPLC grade acetonitrile and the lesser polar component consisted of 5 % HPLC grade water with 95% HPLC grade acetonitrile and 0.1% formic acid. A blank sample as HPLC grade water was run before and after each sample analysis to flush the system and minimise contamination.

2.4. Matrix-Assisted Laser Desorption Ionization Time-of-Flight Mass Spectrometry

Mass Spectrometry (MS) is an analytical method that allows for an accurate determination of molecular weight (Da) of a compound by measuring the mass to charge ratio (m/z) of its ionised species. MS can be used to analyse and identify a variety of different compounds (and their structures) ranging from smaller chemicals to larger biological molecules such as peptides, proteins etc. Principally, the basic process of Mass Spectrometer has three major components: an ion source for sample ionisation (depending on the method utilised – e.g., laser beam), separation of ions according to the m/z ratio through a mass analyser, and a detector for detection of the charged ions. The output of the collected ions by the detector is displayed in a form of a plot of intensity (ion abundance) against m/z ratio.

MS is capable of providing structural information on the analytes of interest which is often essential when analysing a sample as samples can be complex or often contain a small though usually acceptable amounts of impurities. Spectrometers would have inadequate mass accuracy which lead to difficulties in determining the identity of a species based on its singly charged and non-fragmented parent ion mass alone. Hence, two mass analysers are usually present in spectrometers named as MS/MS to eradicate this limitation. Presence of another mass analyser leads to another MS of the fragmented parent ion which increases the ability of spectrometers to analyse compounds. Besides the problem of identification, quantification is also a considerable problem with MS as ionisation of the sample is not usually uniform and ion suppression may prevent the detected ion intensity from reflecting the actual abundance within the sample. Hence, quantification of analytes if needed can be carried out by other analytical methods.

There are different variations and combinations of MS available (Hoffmann and Stroobant, 2007). The development of Matrix-Assisted Laser Desorption Ionization Time-of-Flight (MALDI-TOF) MS has massively led to the advancement of MS's usage from just chemical sciences to also biological sciences. The modern instruments such as

MALDI-TOF MS have increased capability to analyse and process data of various compounds with improved quality. MALDI-TOF MS technique has the following advantages: improved accuracy and sensitivity, a requirement for a very small amount of sample for analysis, a mass range between 500 to 300,000 Da can be analysed, exhibits a relatively higher tolerance to buffers and salts and an automated set up allows for hundreds of samples to be analysed daily (Marvin et al., 2003; Hou, Chiang-Ni and Teng, 2019).

The basic setup of MALDI-TOF mass spectrometer and illustration of MS process are shown in Figure 2.3. For sample analysis by MALDI-TOF MS, the sample (analyte) is mixed or coated with a UV-adsorbent organic matrix on a conductive sample support/probe which is introduced into the instrument's vacuum system for analysis. The use of organic matrix instead of direct irradiation of an analyte prevents the significant fragmentation of samples which could reduce the ion yields. However, this is what limits the analysis of samples with low molecular weight of below 500 Da due to the degree of noise that is usually seen at m/z ratio because of the matrix used. The matrix and analyte are co-crystallized by drying where the analyte gets entrapped within the matrix.

The UV laser beam desorbs and photo-volatizes the analyte within the matrix producing gas-phase protonated ions due to desolvation and ionisation of the analyte through proton transfer within the matrix (see Figure 2.3 - enlarged overview of sample ionisation). The protonated ions are extracted by the electric field (electrode) and accelerated at a fixed potential towards the TOF mass analyser (Ellis et al., 2013; Singhal et al, 2015). The exact mechanism behind the extraction of ions with electric field is unknown (Marvin et al., 2003). The ions drift and separate from each other based on their m/z ratio which is measured by determining the time required for the ions to travel the length of the flight tube known as time-of-flight (TOF) prior to their detection by the detector (see Figure 2.3 – drift through mass analyser). TOF is longer for larger ion masses and shorter for shorter ion masses as long as their given initial energies are identical (Jurinke et al., 2004). The mass spectrum produced from the ions collected by the detector is also shown in Figure 2.3.

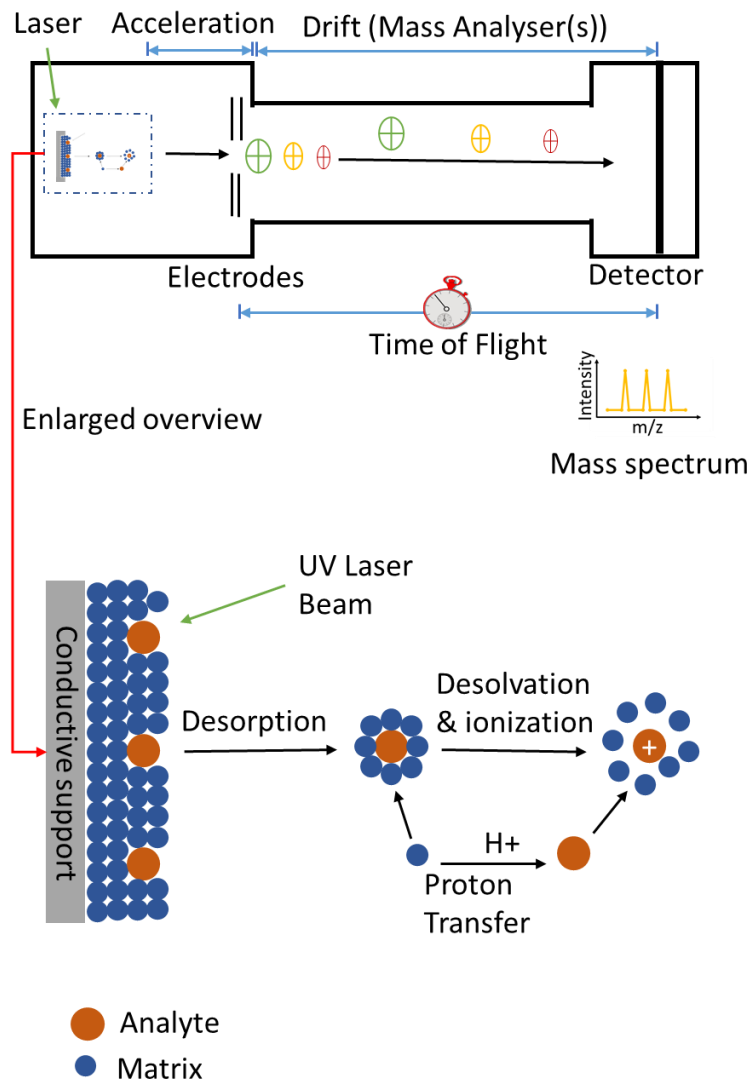


Figure 2.3 – Basic setup of MALDI-TOF mass spectrometer and illustration of MS process.

Adapted and modified from Pusch et al., 2003 and Kicman et al., 2007.

During this PhD research, a MALDI-TOF Mass Spectrometer (Applied Biosystems®, USA) instrument was employed to confirm the mass of the peptides used for the interaction studies of peptides with silica surface through the indicator displacement assay. The sample runs for MS analysis were kindly performed by the help of Dr. Graham Hickman from the research group.

2.5. Contact angle measurements

Contact angle measurements of surfaces are utilised to evaluate and determine the wetting properties of the material of interest (Yuan and Lee, 2013). It can also provide an insight into the surface energy of the materials. A droplet of liquid, usually HPLC grade water, on the surface of the material is used for the contact angle determination. Contact angle is the angle where the liquid-vapour interface meets the solid surface and leads to the quantification of wettability. Wettability is a measure of the capability of a liquid to maintain contact with a solid surface through intermolecular interactions at the solid-liquid interface.

The contact angle (θ) can be determined through the application of Young's equation which denotes the relationship between surface tension at the solid-liquid (SL), solid-vapour (SV) and liquid-vapour (LV) interfaces of the drop (See Equation 2.1 and Figure 2.4) (Kwok et al., 2000). If the contact angle is $<90^\circ$ or $>90^\circ$, the surface is known as hydrophilic (high wettability) or hydrophobic (low wettability) respectively; whereas, the contact angles of $<5^\circ$ and $>120^\circ$ additionally characterises the surface to super hydrophilic and super hydrophobic respectively (Kubo & Tatsuma, 2005). See Figure 2.4 for examples of the different surfaces, hydrophilic and hydrophobic, and their expected contact angles.

$$\gamma_{sv} = \gamma_{sl} + \gamma_{lv} \cos(\theta) \quad (2.1)$$

Here, γ_{sv} is interfacial tension at the solid-vapour, γ_{sl} is interfacial tension at the solid-liquid, γ_{lv} is interfacial tension at the liquid-vapour and θ is the contact angle.

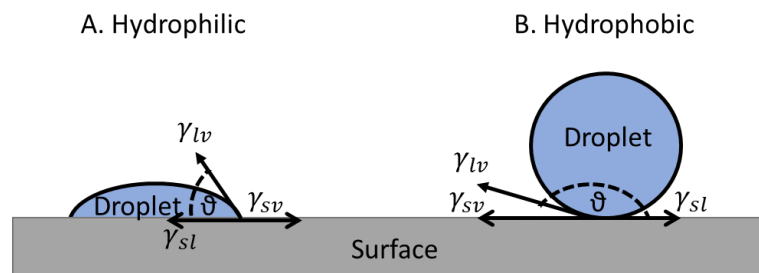


Figure 2.4 – Contact angles (θ) of different surfaces, A. Hydrophilic and B. Hydrophobic

During the PhD research, contact angle measurements were carried out using an Attension Theta Lite Tensiometer and its software for data analysis, OneAttension, to study the wetting property of the silica surface utilised for the indicator displacement assay.

2.6. Confocal Scanning Laser Microscopy

Confocal Scanning Laser Microscopy (CSLM) is an advanced fluorescence microscopy technique which differs from the conventional widefield optical microscopy and offers several advantages which enables access to high quality images (Swedlow et al., 2002; Murray et al., 2007). The principle of a conventional widefield optical microscope is that the volume of the specimen under focus is evenly and simultaneously illuminated. The fluorescence emissions collected would display an out of focus blur (secondary fluorescence) from the non-focused surroundings of the specimen which adversely affects the contrast and resolution of the images obtained (Amos and White, 2003). On the other hand, CSLM is capable of mechanically adjusting laser through the help of a pinhole (small aperture), controlling depth of field and collecting different optical sections within the entire specimen thickness (Paddock, 2000; Amos and White, 2003).

Figure 2.5 shows the principle mechanism of the laser pathway in CSLM and its different features. CSLM uses a laser excitation source for the excitation of the specimen of interest. The presence of the illumination (light source) and detection pinhole apertures lead to adjustment of laser illuminating only a narrow section of the specimen (desired focal plane) which spatially filters and eliminates majority of the out of focus light enabling image formation by the detector of the area in focus with minimal interferences from outside of the desired focal plane. The detection pinhole also prevents the detection of the emissions originating from outside of the focal plane through preventing them from reaching the photomultiplier tube (detector). Being able to remove out of focus light significantly enhances the sharpness and quality of the image attained. A much greater optical resolution in the z plane is provided by CSLM compared to a conventional widefield optical microscope. A resolution of <200 nm in x and y and 500 nm in z can be attained using a conventional CSLM if optimal conditions are present (Schermelleh et al., 2010). In contrast, opening the pinhole aperture

enhances transmission of light which can aid in the detection of weaker fluorescing areas, but this will also allow more out of focus light to reach the detector which reduces the z resolution.

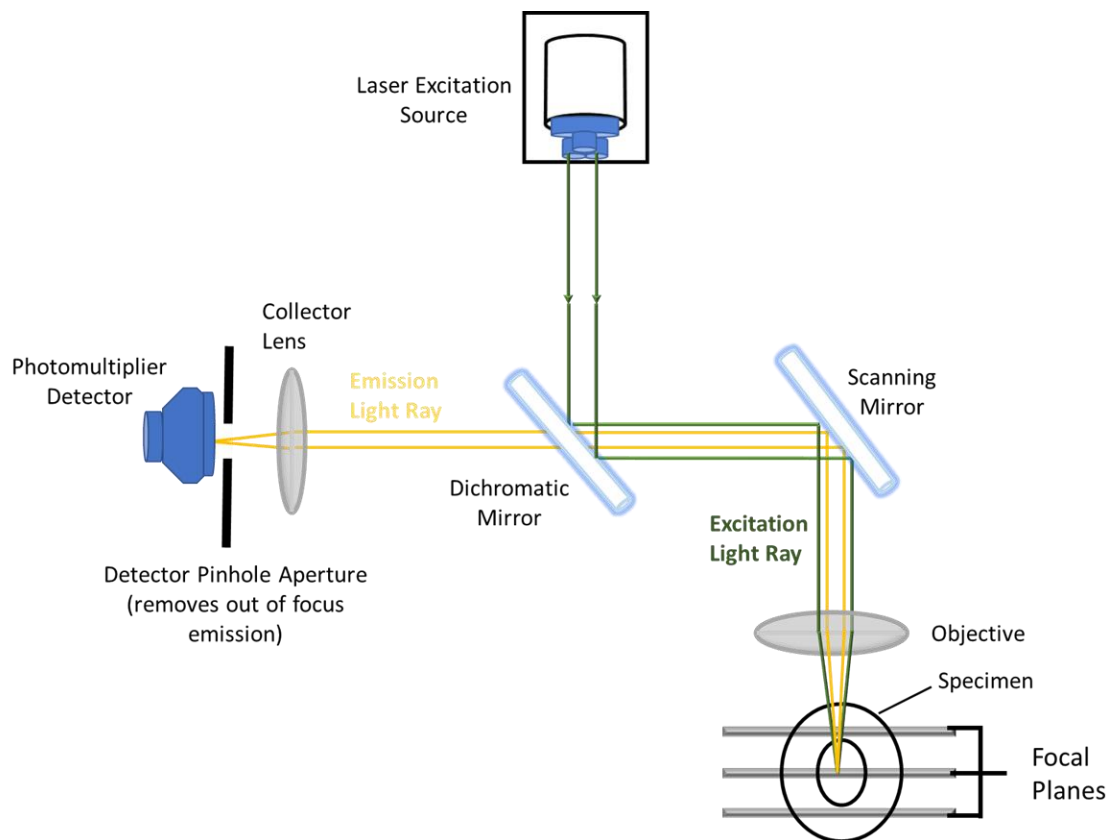


Figure 2.5 – Principle mechanism of the laser pathway in CSLM.

Adapted and modified from Gell et al, 2006; Pottle, 2021 and Paddock, 2020.

CSLM also requires a stringent control of excitation and emission bands for the respective fluorophores to effectively utilise them for different purposes. CSLM is also known as an optical sectioning technique that allows three-dimensional imaging through acquiring physical sections with high axial resolution within a specimen (Zemanová et al., 2003). Another major parameter which affects the resolution of CSLM is the numerical apertures (NA). NA affects the axial resolution which is along the optical axis and controls the depth of the field of the laser. Thus, a higher NA improves the resolution of the three-dimensional image through reducing the size of the focal plane or slice of the specimen under observation (Amos and White, 2003; Földes-Papp, Demel and Tilz, 2003). Three-dimensional images are obtained through capturing fluorescence of selected focal planes within the entire specimen thickness. Moving the focal plane

along the z axis of the fixed specimen through the help of a moving stage can also provide further useful insight into the changes in fluorescence through the layers of the specimen. However, movement of the specimen can occasionally lead to a loss of resolution in the image which would need to be resolved prior to capturing image of the desired z position.

In addition, CSLM is also capable of spectral imaging which is a combination of the principles of microscopy and spectroscopy which, in turn, enables determination of both the optical intensity and spectral properties of a specimen for individual pixels within an image (Strasser et al., 2019). In a traditional imaging, only the optical intensity of the individual pixel is yielded. Spectral imaging is majorly different to the traditional imaging such that the fluorescence emission wavelength as well as the fluorescence intensity for the individual pixels are provided. On top of all the advantages of CSLM, it is a non-invasive technique which allows for all these measurements for a living specimen as well as the non-living specimen making it a very useful approach in biomedical research applications.

2.6.1. Background to fluorescence

The fluorescence nature of a fluorophore is best explained by the diagram in Figure 2.6 (Lakowicz, 2010). Fluorophores exhibit many electronic states where S_0 , S_1 and S_2 represent the ground, first and second electronic states etc. Each of the electronic states have several vibrational energy levels. At resting state, the electrons of a fluorophores usually occupy the lowest vibrational level of the ground electronic state. When exposed to a beam of light (usually UV), fluorophores absorb light and results in transition of electrons between the electronic states. This also leads to the excitation of nuclear motion to a higher vibrational level known as excited vibrational state. This is followed by the relaxation of the nuclear motion to the lowest vibration level of a lower electronic state (for example: $S_2 \rightarrow S_1$ or $S_1 \rightarrow S_0$) dissipating part of the absorbed energy without photoemission in a process called internal conversion (represented as IC in Figure 2.6) prior to emission of the remaining adsorbed energy in the form of a photon/fluorescence which is when the electron travels back to the ground electronic state.

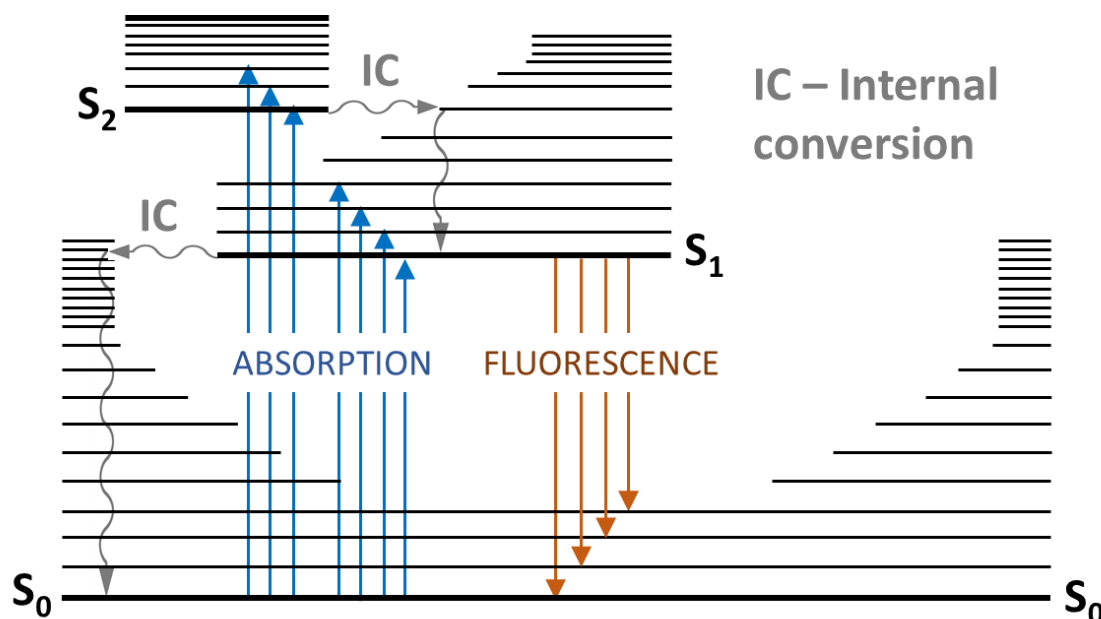


Figure 2.6 – Representation of electronic and vibrational transitions giving rise to fluorescence emission.

Adapted and modified from Valeur, 2002.

The amount of energy released depends on the vibrational state populated within the ground electronic state. The separation between S_1 and S_0 is of significance and determines the distinct emission wavelength unique to the fluorophore (hence the ‘colour’ of fluorescence). Fluorophores are generally aromatic molecules and their structure determines their unique excitation and emission wavelengths. Since the energy of emission is lower than the absorbed energy as some energy is lost during vibrational relaxation, the emission wavelength would be higher than excitation wavelength. This phenomenon of population of lower vibrational levels leading to fluorescence is described as Stoke’s shift (Stokes, 1852). The ratio of the number of photons emitted over absorbed determines the quantum yield which indicates the efficacy of a fluorophore.

During the PhD research, Confocal Scanning Laser Microscope from Leica TCS SP5, Leica microsystems (Germany) was used. Two different methods were studied using a fluorophore through the utilisation of CSLM. One was to study the abiotic-biotic interactions at interface through an indicator displacement assay and the other was to study the surface charge properties of silicifying organisms through the visualisation,

localisation and quantification of the fluorescent probe uptake in their cellular compartments. The software from the Leica microsystems for CSLM and ImageJ v1.50c were used for the image processing as required for the analysis.

2.7. Zeta Potential and Dynamic light scattering

In solution, surface of electrically charged species affects the distribution of the surrounding ions at interfacial region. The Guy-Chapman-Stern model explains the interface between a charged surface and solvent using an electrical double layer comprised of two regions (Brown et al., 2015). The first inner layer close to the surface (Stern layer) comprises of tightly adsorbed counter ions (opposite charge to particle) that are chemically attracted to surface. The stern layer is followed by an outer second layer (Diffuse layer) which is composed of freely moving cations and anions weakly attracted/bound to the surface. See Figure 2.7 for an illustration of electrical double layer. These ions within the electrical double layer are a stable entity that surround the particle which migrate with the moving particle (due to gravity); whereas, the other ions beyond the boundary of slipping plane are unaffected.

With moving away from surface, an exponential decay in electric potential is observed (see graph in Figure 2.7). The potential that exists at the surface and slipping plane are known as surface potential and zeta potential respectively (see Figure 2.7). In research, zeta potential is a commonly used proxy measurement of surface charge due to its ease of accessibility in a research environment. Particles that have a large positive or negative zeta potential of above +30 mV and below -30 mV respectively repel each other and form stable suspensions (Malvern Instruments, 2004). However, the particles with zeta potential between -30 mV to +30 mV tend to flocculate (Malvern Instruments, 2004). The zeta potential of particles is largely affected by the pH of the solution they are dispersed in with it being more positive with reducing pH and *vice versa*. The pH at which the zeta potential is zero (no charge) is known as the isoelectric point which is when a system is most unstable (Malvern Instruments, 2004).

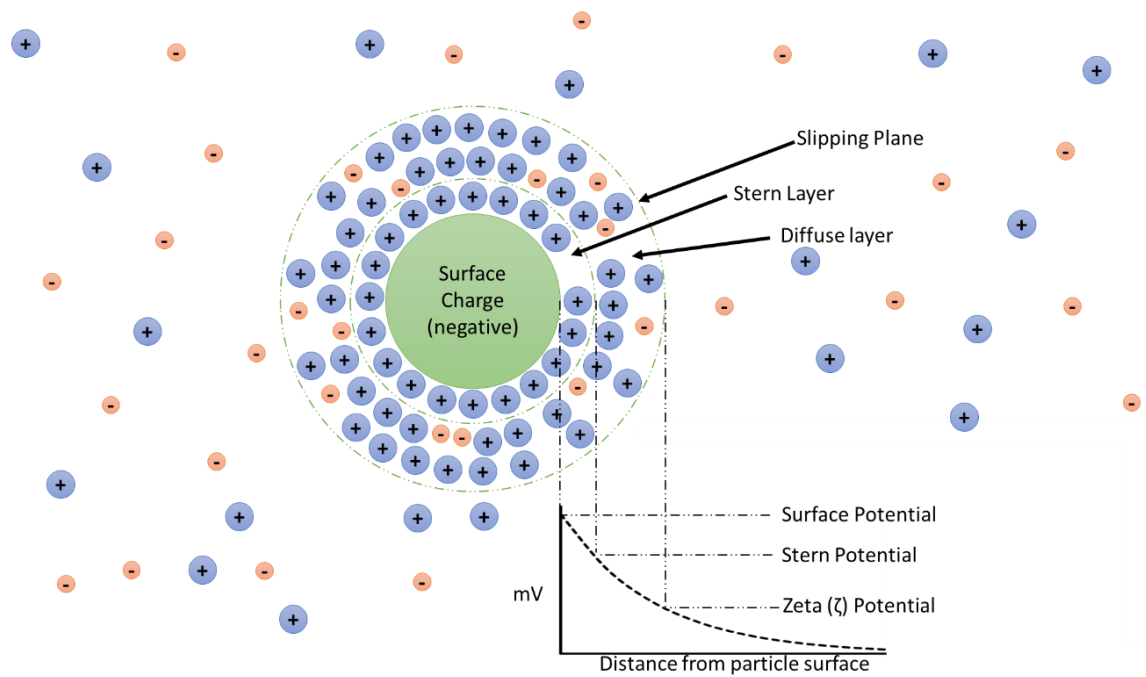


Figure 2.7 – Electrical double layer around a negatively charged particle surface.

Adapted and modified from Williams, 2016.

Dynamic light scattering (DLS) is a technique used to measure size (hydrodynamic radius) of particles in a solution. Particles in solution undergo Brownian motion (random movements) due to continuous collisions from the molecules of the surrounding medium. In solution, smaller particles tend to move faster than larger particles. In DLS, a suspension is illuminated with a laser where some of the light gets scattered due to the presence of the particles in solution. A speckle pattern of light (due to scattering) and dark patches is captured by the photomultiplier detector which continuously changes over time as the dispersed particles in solution are continuously moving. This change in rate of the intensity fluctuations of the scattered light over time is analysed to mathematically estimate the size of particles which is delivered as a size range distribution (Malvern Instruments, 2004). Stokes-Einstein equation (Equation 2.2) combines the relationship of the particle size to its diffusion rate through which the hydrodynamic radius of particle can be determined (Malvern Instruments, 2004).

$$D = \frac{k_B T}{6\pi\eta r} \quad (2.2)$$

Here, D is the diffusion constant, k_B is the Boltzmann's constant ($1.38 \times 10^{-23} \text{ J K}^{-1}$), T is the room temperature in Kelvin (K), π is the constant pi (3.1415), η is the dynamic viscosity and r is the hydrodynamic radius of the particle.

During this PhD research, a Zeta Sizer Nano Series (Malvern, UK) was used to determine the particle size and zeta potential measurements of silica nanoparticles in solution.

2.8. Scanning Electron Microscopy

Scanning Electron Microscopy (SEM) is a powerful magnification tool which is widely utilised in research to study the morphological and topographical features of materials within the scale ranging from nanometres (nm) to micrometres (μm) (Akhtar et al., 2018). A three-dimensional image captured by SEM can provide useful and detailed information on the size, shape, texture, micro-structures and composition of the surface of the sample being analysed (Goldstein et al., 2003).

Since the prepared samples are placed on a sample stage under vacuum pressure, SEM is limited to solid based samples which can withstand this high pressure. When the samples are prepared, it is also important to be considerate of the type of material being analysed. For example, non-conductive samples would need to be coated with a material that is conductive (such as gold or carbon) which is to avoid build-up of static electric charge on the sample when the sample is exposed to electrons (the use of coating doesn't affect the image quality) (Goldstein et al., 2003). Figure 2.8 shows the basic components of SEM instrumentation. The SEM instrument has an electron source which consists of a heated filament (cathode) covered with a Wehnelt cap that generates a stream of electrons which is directed by the positive electrical potential of the anode to an electromagnetic condenser lens which confines and focuses it into a fine monochromatic electron beam. The scan coil then deflects the beam in X and Y axes which then is confined and focused into a fine monochromatic electron beam again due to the presence of objective lens such that the selected surface of the sample gets scanned in a raster fashion (McMahon, 2007). The users can adjust magnification and beam to scan the desired region of the sample.

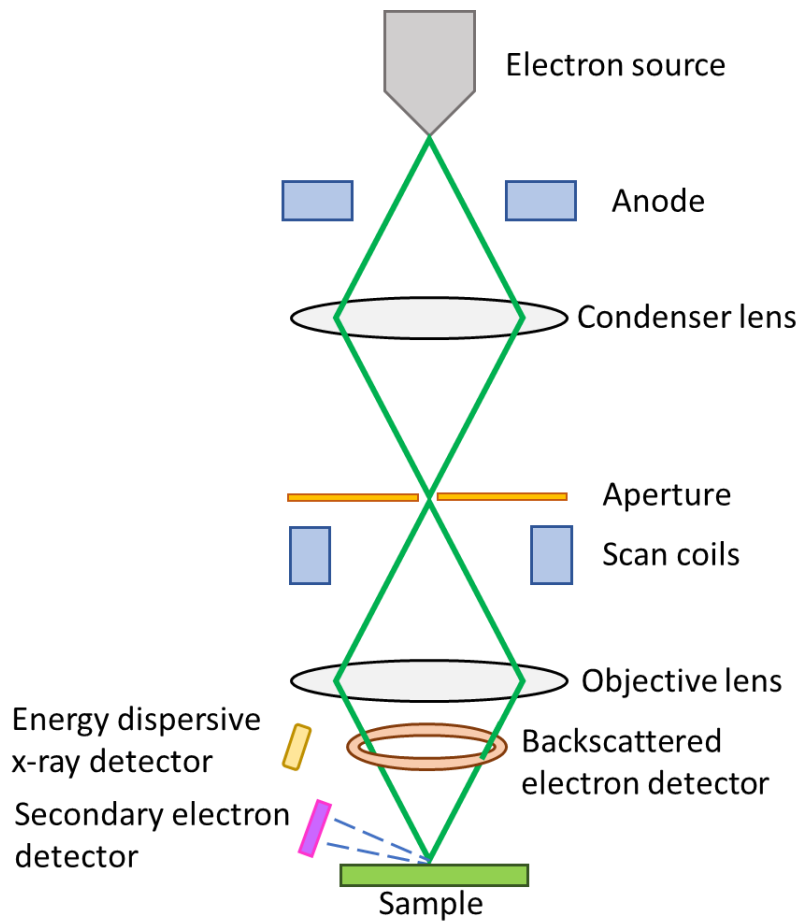


Figure 2.8 – Basic components of SEM instrumentation.
Adapted and modified from Shah et al., 2019.

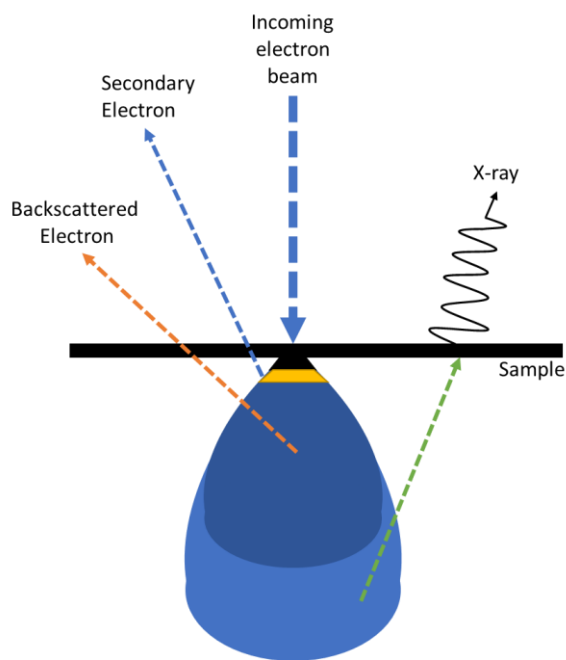


Figure 2.9 – Schematic of electron – sample interactions.
Adapted and modified from Akhtar et al., 2018.

The monochromatic electron beam irradiates the sample and leads to various interactions with the atoms of the sample which are affected by the acceleration rate of the incident beam. A higher acceleration rate would mean interactions deeper into the sample. As a result of irradiation, various signals such as released secondary electrons, x-rays and backscattered electrons are detected by the appropriate detectors as shown in Figure 2.8. The irradiation leads to the electrons of the atoms to become excited which may escape the atom as low energy secondary electrons which is what yields the information on the topography of the sample. In cases where the lost electron of the atom creates an electron vacancy and gets replaced by a higher shell electron over time, the excess energy is released as x-rays etc. X-ray can provide useful information about the elemental composition of the sample. The backscattered electrons are the reflected high energy electrons from the incident beam and depend on the atomic number of the sample. The electron – sample interactions at the site of the incident electron beam are shown in Figure 2.9 with a few examples of the types of signals generated.

During the PhD research, A JEOL 7100FEG SEM was used to study the morphology of the spore heads and spores of *Equisetum arvense*.

2.9. Inductively Coupled Plasma Optical Emission Spectrometry

Inductively Coupled Plasma Optical Emission Spectrometry (ICP-OES) is an optical emission spectrometric method which is a widely used powerful technique in inorganic analysis for the detection of trace elements, mainly metals. ICP-OES is often compared to Atomic Absorbance Spectrophotometer (AAS) and is found to be more efficient. AAS uses air-acetylene flame which provides an excitation temperature between 2000 to 3000 K whereas the ICP-OES uses an inert gas (argon, Ar) which provides an excitation temperature of 5000 to 7000 K. Since ICP-OES uses argon and exhibits a higher excitation temperature, ICP-OES can excite many elements and lesser oxides or nitrides are generated which are what contribute to more efficient elemental analysis. Utilising ICP-OES can detect the presence of different elements qualitatively which can also be quantitatively identified. Hence, both the elemental composition and the respective concentrations can be determined.

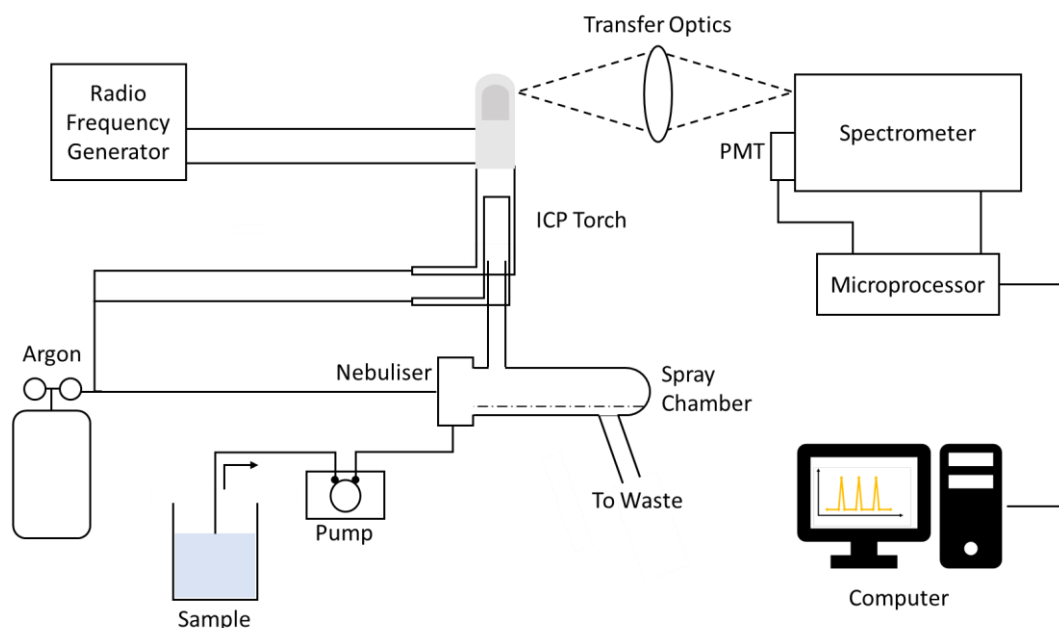


Figure 2.10 – Major components of the ICP-OES instrument.

Adapted and modified from Boss and Fredeen, 2004.

ICP-OES requires the samples to be in liquid form. Solid samples would either need to be dissolved or extracted into a suitable solvent. Figure 2.10 shows the major components of the ICP-OES instrument. Liquid samples are introduced into the nebuliser by a peristaltic pump and gets vaporised and dissociated into atoms in gaseous state when exposed to the high temperature Ar gas generated by ICP torch produced by high power radio frequency signal. As the compound gets decomposed into atoms which become excited by the Ar plasma, the movement of electrons occur from high to low energy states which results in emission of different characteristic wavelengths of light (atomic spectral lines) by atoms of different elements in the sample giving the qualitative information of the elements (Cazes and Ewing, 2005). The emission is measured as the amount of electromagnetic radiations (intensity) emitted by the atoms of the different elements in the sample detected by the transfer optics giving the quantitative information of the elements. The measured intensity is directly proportional to the concentration of the atoms of the element of interest. Monitoring of these emissions is achieved by a monochromator and detector (Photomultiplier tube - PMT) within the spectrometer which identify and determine the abundance of specific elements respectively through the generation of a calibration curve for an element of

interest using its known standards. Presence of the microprocessor transfers the optical signal to display the data on a computer.

It is not possible to study Ar and atmospheric elements (such as H, N, O and C) through ICP-OES due to their presence in the generation of plasma and the solvent used for the sample preparation. Over 70 elements can be identified using ICP-OES even at trace levels within a range of concentration below 1 µg/L (ppb) (Hou and Jones, 2000). Although a vast majority of elements can be identified, the elements such as halogens and short-lived radioactive elements that necessitate high energy for excitation can also be challenging to analyse (Boss and Fredeen, 1997; Hou and Jones, 2000). The actual sensitivity of ICP-OEs to detect elements alters from element to element and with the matrix type used to dissolve the sample before excitation in the plasma.

During the PhD research, an Optima™ 2100 DV ICP-OES (model PQ Excell VG Elemental Perkin Elmer®, USA) was employed for the detection and quantification of elemental Si (at 251.611 nm) in biological samples (blood plasma) to assess the bioavailability of the silicon supplement used for the animal trial. A stock solution of 1000 ppm Si as SiO₂ obtained from BDH Laboratory Supplies was used for the preparation of the standard solutions of interest which were used to produce calibration standard curves. The calibration standard curve was obtained as a plot of detected intensity signal against the concentrations (ppm) of the standards used where the accepted correlation co-efficient (R²) was at least 0.999.

2.10. RNA sequencing

RNA-sequencing is a technique which is used for transcriptome analysis to determine the quantity and sequences of RNA in a sample compared to a control. The aim of RNA sequencing was to understand the different pathways that may be involved in the mechanism of action of silicon in bone health. Hence, the extracted RNA samples were subject to a quality check for this study prior to the library construction and bioinformatics analysis. The workflow of the library construction and bioinformatics for total RNA sequencing using RNA transcriptome analysis is briefly explained below and was carried out by BGI Genomics. The report provided by BGI was used for this purpose.

The process of RNA sequencing is shown in Figure 2.11. The first step involved mRNA enrichment through using the poly-T oligo attached magnetic beads to purify the poly-A containing mRNA molecules from the total RNA. After purification, divalent cations were used under elevated temperature to fragment the mRNA into small pieces. Using reverse transcriptase and random N6 primers, the cleaved RNA fragments were copied into first strand cDNA. Following transcription, second strand cDNA synthesis using DNA Polymerase I and RNase H was carried out. The cDNA fragments underwent ER/A-tailing such that a single 'A' base was added to the 3' end with subsequent ligation of a bubble adapter (capable of producing a fluorescing signal). The products were then purified and enriched through PCR amplification. The PCR yield was then quantified. The amplified double stranded cDNA was heat separated and converted to single strand DNA circle (ssDNA circle) held together with a splint oligo. The samples were pooled together which gave the final library. DNA nanoballs (DNBs) were generated through replicating the ssDNA circle by rolling circle replication (RCR) to increase the fluorescent signals enabling the sequencing process.

The DNBs were loaded into the patterned nanoarrays and pair-end reads of 100 bp (PE 100) were read through BGISEQ-500 platform for the transcriptome analysis study. In BGISEQ-500 platform, DNBs based nanoarrays was combined with a stepwise sequencing through utilising Combinational Probe Anchor Synthesis Sequencing Method for a high throughput and quality.

The RNA sequencing data (detected reads) were filtered to get clean reads through removal of the low-quality reads, reads with adaptors and reads with unknown bases. The clean reads were mapped onto the reference genome (*Gallus gallus*, GRCg6a for chicken) which led to the detection of novel genes and spliced genes. Differentially Expressed Genes (DEGs) between the different groups in the comparisons studied were detected and PCA analysis carried out. Using the DEGs, KEGG pathway analysis was carried out providing functional annotations. The bio-informatics analysis pipeline which was carried out is shown in Figure 2.12.

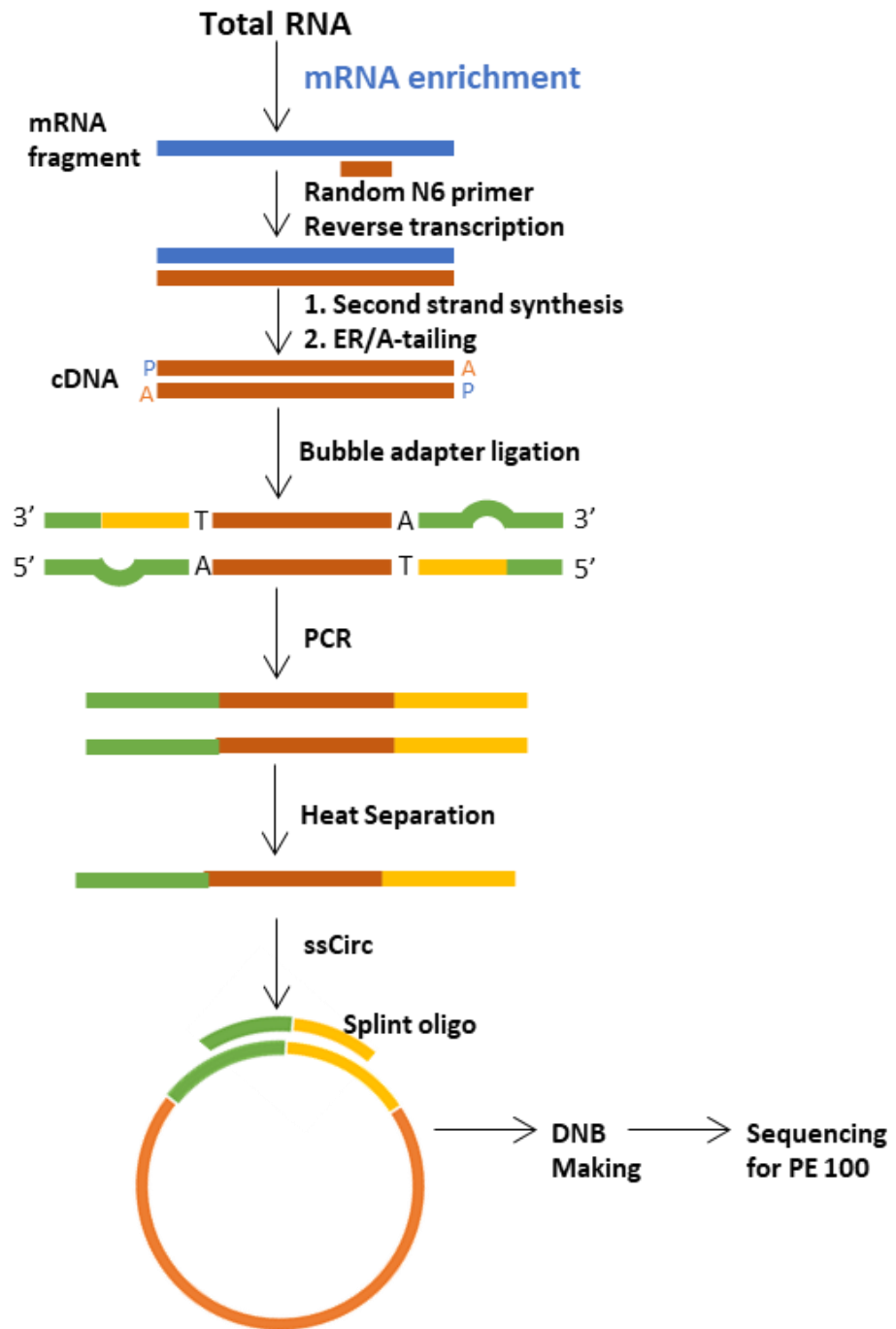


Figure 2.11 – Process of library construction in RNA sequencing.
 Reproduced from the schematic provided by BGI.

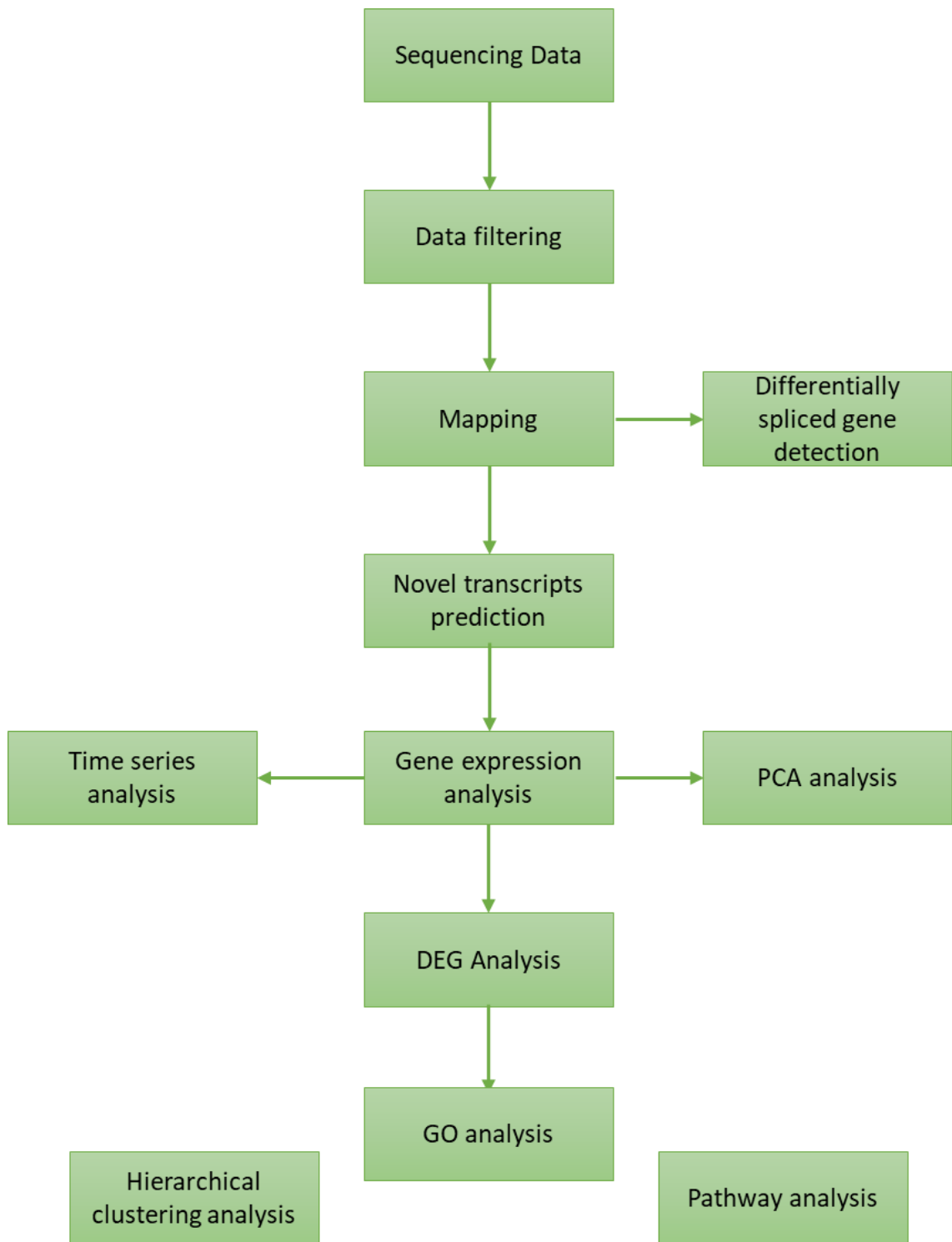


Figure 2.12 – Bio-informatics analysis pipeline

Prior to utilising the total RNA samples for the transcriptome analysis through RNA sequencing, quality checks were carried out using Bioanalyzer which is explained below.

2.11. Bioanalyzer

It is essential to perform adequate quality checks on the RNA samples before executing total RNA sequencing analysis using RNA transcriptome. During this PhD research, the RNA integrity (which is a measure of RNA quality and provides information about its degradation) was determined using an Agilent 2100 Bioanalyzer (Santa Clara, CA) using Agilent RNA 6000 nano kit protocol (see chapter 5 section 5.2.2.6). Through this technique, the RNA integrity can be assessed through the detection of ribosomal RNA (rRNA) which accounts for approximately 80% of total RNA as opposed to messenger RNA (mRNA) which accounts for only 1-3% of total RNA (as it can reduce detection and affect overall sensitivity).

rRNA primarily comprises of 18S and 28S rRNA species which can be detected using a micro fabricated chip with Agilent 2100 Bioanalyzer. The chip utilises the concept of capillary electrophoresis which separates these RNA species by mass-to-charge ratio. These can be detected and quantified by the help of a fluorescent dye which can help translate this data into an image with bands at different weights and present as electropherograms. This technique assumes that the RNA quality is measured through rRNA quality which is also a true reflection of the mRNA population and total RNA.

A high integrity of RNA would generally be denoted by two clean bands of 28S and 18S rRNA on agarose gel such that the rRNA ratio as 28S/18S equals 2.0 (Sambrook et al.,1989). A ratio of 2:1 for 28S and 18S respectively would be an indicator of intact RNA whereas the degraded RNA will typically show peaks before 18S indicating a relatively reduced RNA quality. However, obtaining a value of 2.0 is not possible as would be anticipated in ideal cases. It does not necessary mean that a lower rRNA ratio indicates poor quality. This is usually not true for the majority of total RNA samples. An algorithm is built in within the Agilent 2100 Bioanalyzer software which calculates and delivers an RNA Integrity number (RIN) value based on the electrophoresis data. The RIN value ranges from 1-10. 10 stands for completely intact RNA whereas 1 would mean a

completely degraded RNA. A RIN value of 7 and above is usually considered adequate quality for the RNA based analysis.

Hence, rRNA ratio and RIN value are indicators of the quality and integrity of RNA. Agilent 2100 Bioanalyzer also provided quantitative information about the RNA concentration.

Chapter 3. Development of a novel Displacement Assay for screening abiotic/biotic interactions

This chapter partially includes the development of assay work already published in the paper below. Peptides formed a natural extension of the assay which has not yet been published.

Michaelis, M.‡, Fayyaz, A‡., Parambath, M.‡, Koeppen, S., Ciacchi, L., Hanley, Q. and Perry, C., 2019. Platform for Screening Abiotic/Biotic Interactions Using Indicator Displacement Assays. *Langmuir*, 35(44), pp.14230-14237.

3.1. Introduction

Studying interactions at the abiotic-biotic interfaces have always been of fundamental interest as this knowledge could benefit wide range of applications. Knowledge of silica binding interactions are of importance to further understand the drug delivery process that utilises silica-based drug delivery systems (Barbé et al., 2004; Delle Piane et al., 2018), synthesis of new materials for biomedical use (Sola-Rabada et al., 2018) and processes such as biosilicification or bio-mineralisation (Townson et al., 2014; Kaehr et al., 2012) in mineralising organisms (Kröger et al., 1999; Kroger et al., 2000; Hildebrand, 2008). The advancements in this area of research will have direct implications for important applications in material science, biomedicine and bio-nanotechnology.

Quartz crystal microbalance (QCM) (O'Sullivan and Guilbault, 1999), surface plasmon resonance (SPR) (Homola, Yee and Gauglitz, 1999) or single molecule force spectroscopy (Dudko et al., 2003) are the commonly used methods for the experimental quantification of the interactions at the material's surfaces. However, these techniques take an indirect approach to measure these interactions and heavily rely on the models that are applied during data analysis. The experimental procedure and the associated analysis to these techniques can be very time-consuming. Another available method, isothermal titration calorimetry (ITC) (Freire et al., 1990), allows a direct measurement of binding enthalpies but is limited to systems involving stable suspensions.

Indicator displacement assay (IDA) (Hennig, Bakirci and Nau, 2007; Nguyen, Wiskur and Anslyn, 2004; Nguyen and Anslyn, 2006) is another frequently used method in drug discovery and high throughput screening for measurements of interactions which is based on the direct observation of competitive binding between a reference compound and the analyte of interest towards a given interaction site. IDA has not previously been applied to screening molecules that bind to abiotic material surfaces. An important advancement in the field of abiotic/biotic interaction measurements would be to adapt this approach which could enable comprehensive screening of interactions at the analyte/material interface. Screenable displacement assays in an optical sectioning planar format assay (OSPFA) have been previously employed for immunoassays (Ghafari et al., 2009) and receptor ligand interactions (Ghafari, Parambath, and Hanley, 2012). This approach can indeed be adapted to measure molecular interactions with abiotic/biotic surfaces as it will be shown in this chapter.

This novel approach was established using a representative functional oxide, silicon oxide or silica (SiO). For this SiO system, representative amino acids (histidine, aspartic acid and alanine), a small polyamine (spermine) (Pegg, 2016), and a drug, ibuprofen, that is often used in model studies (Salonen et al., 2005; Andersson et al., 2004; Delle Piane et al., 2014) were selected. Following the development of the method, the assay was extended to larger biomolecules, peptides (7-mers), to test for any limitations with the type of molecules that can be studied through this approach (as peptides exhibits multiple binding sites due to its large size). The technique introduced here is also applied to another functional oxide, ZnO (Michaelis et al., 2019) which is not included in this chapter. Hence, the approach explained in this chapter are general and could be applied to a wide range of material surfaces.

This chapter will describe an approach, Optically Sectioned Planar Format Indicator Displacement Assay (O-IDA), to measure abiotic/biotic interactions which is a novel fluorescent-based technique that involves the combination of OSPFA using confocal scanning laser microscopy (CSLM) and an IDA for screening of compounds binding to abiotic surfaces. The use of OSPFA in O-IDA allows for a more direct access to study interactions through visualisation of how the intensity of the indicator changes in presence and absence of the analyte investigated.

3.2. Materials

PDMPPO (LysoSensor™ yellow/blue DND-160, 1 mM in dimethyl sulfoxide) was obtained from Life Technologies. All the other reagents used, aniline hydrochloride, ammonium persulfate, glutaric dialdehyde (50% v/v), amino acids (alanine, histidine and aspartic acid), lysozyme, tetramethyl orthosilicate (TMOS), polyamine (spermine), hydrochloric acid, sodium hydroxide, ibuprofen, monobasic potassium phosphate monohydrate, and dibasic potassium phosphate were obtained from Sigma-Aldrich.

96 microwell glass bottom black plates (Nunc 164588) were obtained from Nunc. The bottom of the plate was coated with a polystyrene layer.

Peptides were synthesised using a Liberty Blue™ Automated Microwave Peptide Synthesizer (CEM Corporation) which allowed preparation of peptides using SPPS method as explained in Chapter 2 section 2.2. The molecular weights of K7, A7 and L7 (743.4 g/mol, 717.8 g/mol and 807.4 g/mol respectively) were confirmed using mass spectrometry through m/z ratio of 744.4 m/z, 718.4 m/z and 808.1 m/z respectively. A MALDI-TOF Mass Spectrometer (Applied Biosystems®, USA) was used. Dionex HPLC with a UV detector and a Jupiter 4u Proteo 90A C12 Reverse Phase column (Phenomenex) was used to test the purity (peptides of above 85% purity were utilised).

3.3. Methodology

3.3.1. Silica surface preparation

Previously described protocol (Rai and Perry, 2010; Hickman et al., 2012; Nicklin et al., 2014) was followed to produce hydrophilic silica surface and this silica surface formation procedure was adapted to wells of a 96 microwell plate. First step was to coat the wells with a polyaniline film through reacting 1:1 molar ratio of 0.25 M aniline hydrochloride in 1 M HCl with 0.08 M ammonium persulfate in distilled water. Plates were incubated at room temperature for 15 minutes followed by several washes with excess distilled water and air-dried. Wells were then treated with 2% (v/v) glutaric dialdehyde to

maintain the same coating volumes of the surface to ensure uniformity. Plates were incubated at 57 °C for 2 hours followed by several washes with excess distilled water and air-dried. Wells were then treated with 1 mg/mL of lysozyme in 0.1 M phosphate buffer (made with monobasic potassium phosphate monohydrate and dibasic potassium phosphate), pH 7.2. Plates were incubated at room temperature for 2 hours followed by several washes with excess distilled water and air-dried. Lastly to prepare the silica surface, 0.5 M tetramethyl orthosilicate (TMOS) was pre-hydrolysed in 1 mM hydrochloric acid for 15 minutes. The pH of this solution was raised to 4 by adding 0.1 M sodium hydroxide in a drop-wise manner prior to surface application. Wells were treated with the pH adjusted pre-hydrolysed TMOS solution for 2 hours at room temperature to allow for silica film formation followed by several washes with excess distilled water. Plates were then air-dried overnight before use.

For accessibility of the contact angle for the silica surface, Attension Theta Lite Tensiometer was used. It allowed the measurement of wettability of the silica surface. A 5 μ L drop of ddH₂O was used for this purpose and three replicates were taken for the surfaces. Figure 3.1 shows the interaction of a water droplet with the silica surface over time. It can be seen that the droplet lies flat on the surface hence indicating the hydrophilicity of the surface.

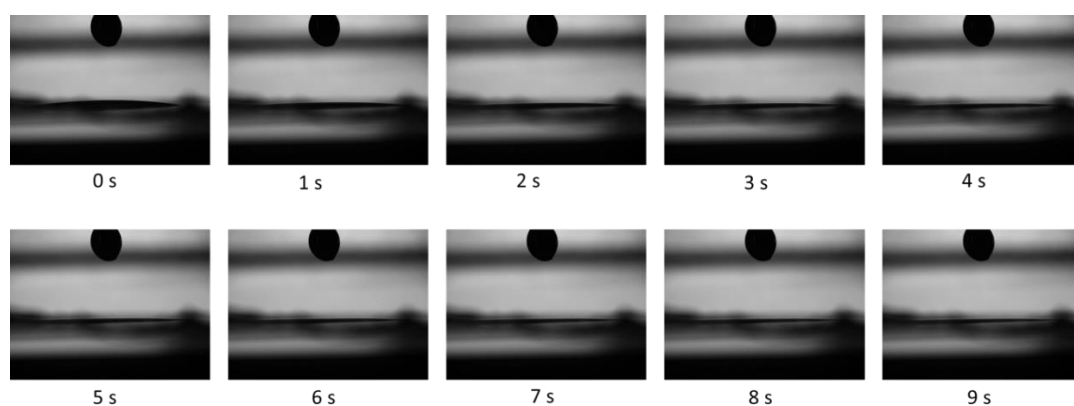


Figure 3.1 – Interaction of water droplet with the silica surface over time.

3.3.2. CSLM and experimental parameters

The CSLM used was from Leica microsystems (Leica TCS SP5, Leica microsystems). CSLM experiments were conducted using 96 microwell glass bottom black plates (Nunc 164588). After the wells had been treated, they were subjected to CSLM. A 405 nm laser diode line was used for excitation of PDMPO dye. The instrumental parameters that were kept the same throughout the experiments were as follows: the numerical aperture (0.5 NA), objective (Leica HCX PL Fluotar 20×), pinhole size (84 μm) and an average of 250 steps of 0.5 μm step size, photomultiplier tube (PMT) gain (1107 V), offset (2.7 %), 512 x 512 pixels and a laser intensity (77 %). An emission wavelength range of 480 nm to 600 nm was used to detect the emitted fluorescence data along the z-axis at room temperature.

3.3.3. Background and importance of the assay system and its design

CSLM (Minsky, 1961; Minsky, 1988), a fluorescence microscope, allows the detection of fluorescence of a slice through the thickness of specimen which is useful to study the changes at the abiotic/biotic interface and reduces the undesirable effects due to the irregularity in the surface of interest or the background interferences. Hence, designing O-IDA using CSLM could fulfil the goal of using this technique for high throughput screening of molecule libraries to identify compounds with relative material binding affinity to abiotic surfaces.

The fabricated silica film chosen for O-IDA is a hydrophilic surface with many silanol (hydroxyl) groups along with some hydrophobic siloxane (-Si-O-Si-) groups. The hydroxyl groups mainly comprise the binding sites for the PDMPO dye under aqueous conditions. The contact angle measurements were carried out to confirm the hydrophilicity of the silica surface. On average, a contact angle of $3.1 \pm 0.5^\circ$ was obtained for the silica surface which corresponds to a super hydrophilic surface in agreement with Hickman et al., 2012.

Choosing an indicator with high affinity and specificity toward the surface of interest under the desired solvent conditions is the key to this assay. PDMPO, (2-(4-pyridyl)-5-

((4-(2dimethylaminoethylaminocarbamoyl)methoxy)phenyl)oxazole), was the fluorescent dye chosen for this silica system due to its silicaphilic nature and its unique non-covalent interactions with silica (Parambath et al., 2016) as these properties make it an ideal indicator for this assay. PDMPO was also the choice to use for this technique due to its history of applications as a probe (Shimizu et al., 2001). To be able to use the indicator, PDMPO dye, in O-IDA, it was characterised prior to carrying out O-IDA. The chemical structure of PDMPO is shown in Figure 3.2 (a).

In accordance with the previous binding studies (Sola-Rabada et al., 2018) and conditions used for both studies of biomineralization and drug delivery, an aqueous medium was chosen for this silica system in this study. As the competitive molecules studied for binding to silica may be affected by pH and the fluorescent dye, PDMPO, also exhibits a pH dependent behaviour (Parambath et al., 2016), a buffered aqueous environment was selected such that the fluorescence measurements taken are not affected by the addition of the competitive molecules studied. PDMPO is also known to be relatively insensitive to the presence of different ions and ionic strength in aqueous medium (Diwu et al., 1999) which concludes that the presence of other ions has no dominant interference with this assay for the dye used. This assay is not restricted to a specific type of a solvent system and can be applied to systems where the materials are insoluble in an aqueous environment. Applicability of this assay to different solvent systems showcases the versatility of the approach.

3.3.4. Preliminary experimentation

Developing the methodology for this assay was based on the assumption of an equilibrium state being attained between the PDMPO dye and the silica surface. Several supporting experiments were conducted to validate this assumption. These initial experiments contributed to deciding the assay style as their results provided an estimate of the time required for PDMPO or an interested biomolecule to be exposed to the surface for equilibrium to be reached and the ideal acquisition time needed to collect the data by CSLM.

a. Excitation and emission spectra for PDMPO

Excitation and emission spectra were determined for PDMPO using TECAN M200 PRO plate reader and CSLM respectively and was utilised in setting up the O-IDA. The excitation spectrum was measured with an emission wavelength of 600 nm using a collection wavelength range from 400 nm to 515 nm. For the emission spectra, a 405 nm laser diode line was used as the excitation wavelength using a collection wavelength range of 480 nm to 600 nm. See Figure 3.2 (b) for the normalised excitation and emission spectra.

b. Time dependent adsorption of PDMPO to silica surface

To study the time dependent adsorption behaviour of PDMPO on a fabricated silica surface, 200 μ l of 1 μ M PDMPO in 0.1 M phosphate buffer at pH 7.2 was added to a well with fabricated silica film. CSLM measurements were started as soon as possible at a selected z-position with further readings every 30 mins over a period of 3 hrs. The thin layer intensities at each time point were normalised to maximal thin layer intensity (B/B_{max}). B/B_{max} versus time (min) was plotted – see Figure 3.2 (d). The outcome of this shows that the equilibrium reached after an hour and features the maximum time (2-hours selected) for incubation for the time dependent measurements when the PDMPO is applied to the silica surface.

c. Time dependent desorption of PDMPO from silica surface

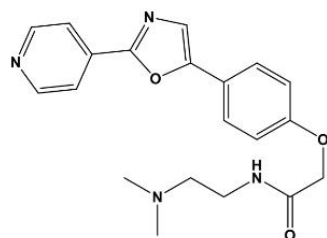
To study the desorption behaviour of PDMPO from a fabricated silica surface, 200 μ l of 1 μ M PDMPO in 0.1 M phosphate buffer at pH 7.2 was added to a well with fabricated silica film. After 2 hrs of incubation, the PDMPO over layer was removed and replaced with 200 μ l of 0.1 M phosphate buffer at pH 7.2 ONLY. CSLM measurements were started as soon as possible at a selected z-position with further readings taken every 30 mins over a period of 2.5 hrs. The thin layer intensities at each time point were normalised to maximal thin layer intensity (B/B_{max}). B/B_{max} versus time (min) was plotted – see Figure 3.2 (f). The outcome of this shows that the equilibrium reached in less than an hour and features the maximum time (2-hours selected) for incubation for the time

dependent measurements when the compound of interest is applied to the silica surface.

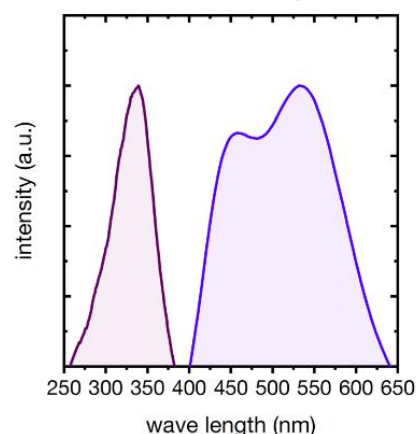
d. Bleaching effect of the laser on PDMPO

To study the bleaching effect of the 405 nm laser (77% intensity) in CSLM on PDMPO dye's stability, a xy plane within the well (without silica surface) filled with 200 μl of 1 μM PDMPO in 0.1 M phosphate buffer at pH 7.2 was selected and CSLM measurements taken continuously over a period of around 5 hours to see how the fluorescence decreased with time. The PDMPO intensity that remains at the selected xy plane with respect to the maximal intensity as B/B_{max} was plotted versus time (min), see Figure 3.2 (c).

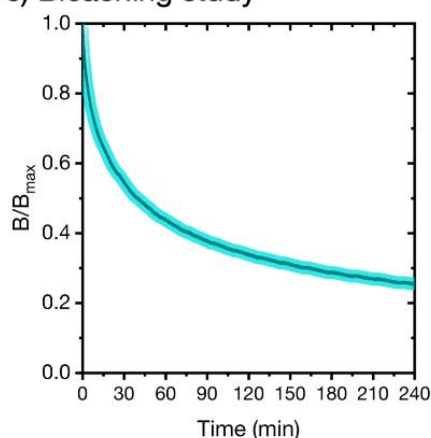
a) Chemical structure



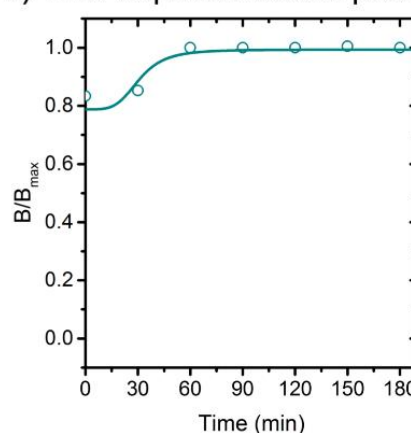
b) Excitation/emission spectra



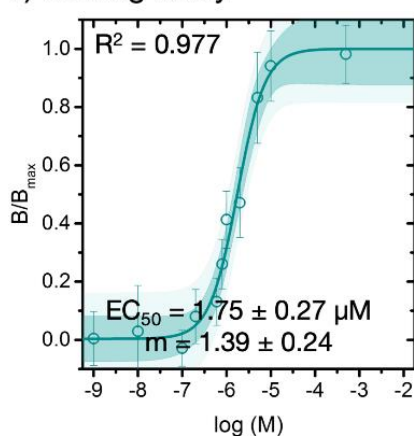
c) Bleaching study



d) Time-dependent adsorption



e) Binding study



f) Time-dependent desorption

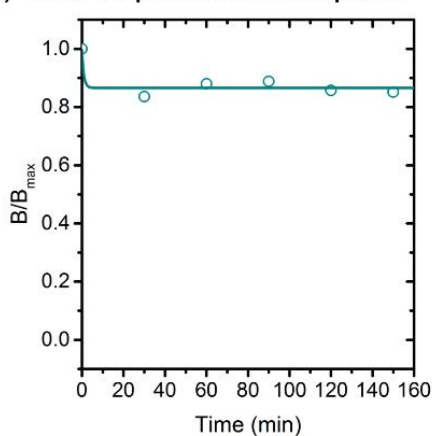


Figure 3.2 – Characteristics of fluorescent dye, PDMPO, to silica under CSLM

(a) Chemical structure of PDMPO. (b) Excitation/Emission spectra of PDMPO. (c) Time dependent bleaching effect of the laser diode used in CSLM. (d) Time dependent adsorption of PDMPO to the fabricated silica film. (e) PDMPO dose response curve – concentration dependent adsorption behaviour of PDMPO to fabricated silica film with determination of EC_{50} and hill slope m of PDMPO for silica leading to binding affinity calculations. (f) Time dependent desorption of PDMPO from the fabricated silica film.

3.3.5. Setting up of O-IDA technique

a. Determination of binding constant (K_d) of PDMPO to silica surface

To determine the binding constant of the PDMPO dye to the fabricated silica surfaces, the concentration-dependent adsorption behaviour and the time-dependent increase of the fluorescence intensity upon interaction with the indicator, PDMPO, were measured. 200 μ l of varying concentrations of PDMPO in 0.1 M phosphate buffer at pH 7.2 was exposed to the fabricated silica surface. After 2 hours of exposure at room temperature, CSLM measurements were done. A minimum of three replicates were used where the thin layer intensities were averaged for each PDMPO concentration and normalized to the maximal thin layer intensity.

b. Studying the binding affinity for the compounds of interest

To measure the binding of the compounds of interest to the fabricated silica surface, the following protocol was adopted. The concentration of the fluorescent dye used is kept constant for all O-IDA experiments. 200 μ l of 1 μ M PDMPO in 0.1 M phosphate buffer at pH 7.2 was applied to the fabricated silica surface and incubated (2 hrs at room temperature). The supernatant was then removed and replaced with test compounds with varying concentrations followed by incubation (2 hrs at room temperature) prior to carrying out CSLM measurements. A minimum of two to three replicates were used where the thin layer intensities were averaged for each inhibitor molecule concentration and normalized to the maximal thin layer intensity.

3.3.6. Data fitting - Origin

The assay results were fitted using a modification of the generalized logistic function using commercially available software (Origin; OriginLab 2015) using a Levenberg–Marquardt algorithm with a tolerance of 10^{-9} and a maximum number of 400 iterations. The resulting curve is plotted along with 95% confidence intervals and 95% prediction intervals.

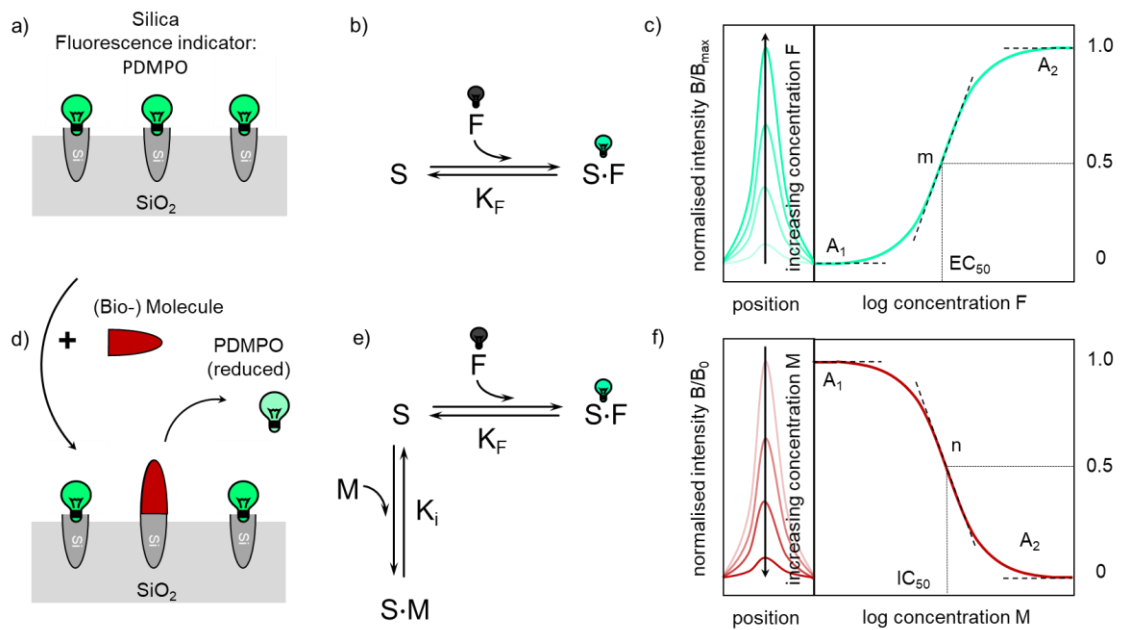


Figure 3.3 – An overview of the binding assay of the selected indicator, PDMPO, and the optically sectioned planar format IDA for silica.

Michaelis et al., 2019

(a,d) Schematic representation of the interaction at the silica interface (“reduced” indicates a reduction in signal intensity). (b,e) Model reaction schemes and their equilibrium constants during the binding assay and the displacement assay, respectively. S corresponds to the number of binding sites on the surface, F denotes the fluorescent dye, and M denotes the biomolecule of interest. (c) Concentration-dependent increase of the normalized fluorescent thin layer intensity B/B_{\max} , fitted by a modification of the generalized logistic function, leading to four fitting parameters including two asymptotes (A_1 , A_2), the slope m , and the concentration producing 50% of the maximal response (EC_{50}). (f) Concentration-dependent decrease of the normalized fluorescent thin layer intensity B/B_0 fitted by a modification of the generalized logistic function, leading to four fitting parameters including the two asymptotes (A_1 , A_2), the slope n , and the concentration producing a 50% reduction in the response (IC_{50}).

3.4. Theory behind O-IDA

O-IDA is a surface-bound assay based on a two-step process: (i) the indicator is brought into contact with the surface where it binds reversibly (Figure 3.3 (a), 3.3 (c)) and (ii) a competitive molecule is added at an increasing concentration to test its ability to displace the indicator (Figure 3.3(d), 3.3(f)). Depending on the capability of the test biomolecule to cause the indicator to move from the surface into solution, this response can be detected through studying the reduction in fluorescence due to indicator's displacement from the surface of interest (Figure 3.3 (f)). This phenomenon is what is exploited in IDA (Nguyen, Wiskur and Anslyn, 2004; Nguyen and Anslyn, 2006).

Figure 3.3 shows the reaction schemes involved at each of the two steps:

- Binding assay (Figure 3.3 (b)): F (fluorescent dye) interacting with S (number of binding sites on the surface) to form S.F complex.
- Displacement assay (Figure 3.3 (e)): M (biomolecule of interest) interacts with S.F complex and displaces F from S to form S.M complex.

3.4.1. Binding affinity of the Indicator – O-IDA

Before elucidating the interaction of the inhibitor molecules, the interaction of the indicator (fluorescent dye), PDMPO with the substrate (surface of interest), silica must be calculated based on a binding assay. This binding assay describes the formation of the fluorescent dye layer (thin layer) on the substrate. Upon maximum coverage of the substrate with the indicator, saturation of the maximum fluorescence intensity is observed, and further addition of indicator molecules does not contribute to a rise in the measured thin layer intensity, meaning it does not alter the binding equilibrium.

a. Calculation of EC₅₀

EC₅₀ here refers to half maximal effective concentration which is the concentration required to reach half saturation of the surface with the indicator. The value of EC₅₀ is obtained by fitting the indicator/dye concentrations and their associated intensities to a logistic dose–response Equation 3.1. A semi-logarithmic approach was chosen due to

its symmetric distribution properties leading to a better comparison of binding affinities (Motulsky and Christopoulos, 2004).

$$\frac{B}{B_{max}} = A_1 + \frac{A_2 - A_1}{1 + 10^{(x - \log x_0)m}} \quad (3.1)$$

Plotting the fluorescence intensity, B, against the logarithm of the molar concentration, x, results in a sigmoidal shape where the m is the value of the slope of the dose–response curve which will vary depending on the nature of the interactions of indicator to the surface. A₁ and A₂ describe the asymptotes and x₀ corresponds to x at the sigmoid midpoint (point of inflection), which gives the EC₅₀ value as 10^{x₀}. If the fluorescence intensities are normalized to maximal fluorescence intensity, B_{max}, A₂ = 1 and in the case where there is no residual background, A₁ simplifies to 0. The surface specific binding constant, K_F of the fluorescence dye depends on the slope, m, of the curve and can be derived via Equation 3.2. See Figure 3.2 (e) for the dose response curve for PDMPO to the silica surface as B/B_{max} against logarithm of molar concentration, x.

b. Calculation of K_F

A quantity analogous to dissociation constant, K_F, can be defined for the fluorescent dye from the surface. K_F is an indicator of the binding affinity of the fluorescent dye to the surface. In cases where m = 1, EC₅₀ would be equivalent to the dissociation constant, K_F.

$$K_F = EC_{50}^m \quad (3.2)$$

c. Calculation of the Free Energy of fluorescent dye binding, ΔG_F

The availability of an equilibrium dissociation constant for the binding of the fluorescent dye, K_F, allows for the calculation of its binding affinity through the calculation of free energy using Equation 3.3 where \bar{v}_s is the partial molar volume of the solvent used which in this case is $\bar{v}_s = 0.018 \text{ l mol}^{-1}$ for the aqueous environment (Alsteens et al., 2015).

$$\Delta G_F = -RT \ln(\bar{v}_s \cdot K_F) \quad (3.3)$$

3.4.2. Indicator Displacement Assay - O-IDA

To perform the O-IDA, a fixed concentration of the indicator, PDMPO, is firstly applied to the fabricated silica surface and the supernatant including the nonbonded indicator molecules is removed to access the fluorescence intensity after an incubation period. This fluorescence signal is the initial state for the following displacement assay and provides the reference intensity (B_0). For the displacement assay, the compound of interest (inhibitor) is added in solution at different concentrations and the fluorescence signal is measured after an equilibration period and compared to the initial state. After full replacement of the dye, additional binding would not be detected, for instance, for the formation of multilayers. Figure 3.4 shows an overview of the O-IDA technique where the two-step process is explained in more detail schematically. The specimen marked as the asterisk (*) is what is observed under CSLM to study the extent of fluorescent dye displacement through detecting the varying optical signal.

Figure 3.3 (f) also shows a schematic for concentration dependent decrease in the optical signal due to the presence of the competitive compound of interest inducing the displacement of the PDMPO dye. Since the indicator, PDMPO, fluoresces when found both bound to the silica surface and in bulk solution, the contributions from both must be isolated from the observed spectral response from CSLM. The approach to separate out the value of interest is described in section 3.4.3. The surface-bound contribution (as explained in section 3.4.3) is the quantity of interest for subsequent EC_{50} and IC_{50} determinations.

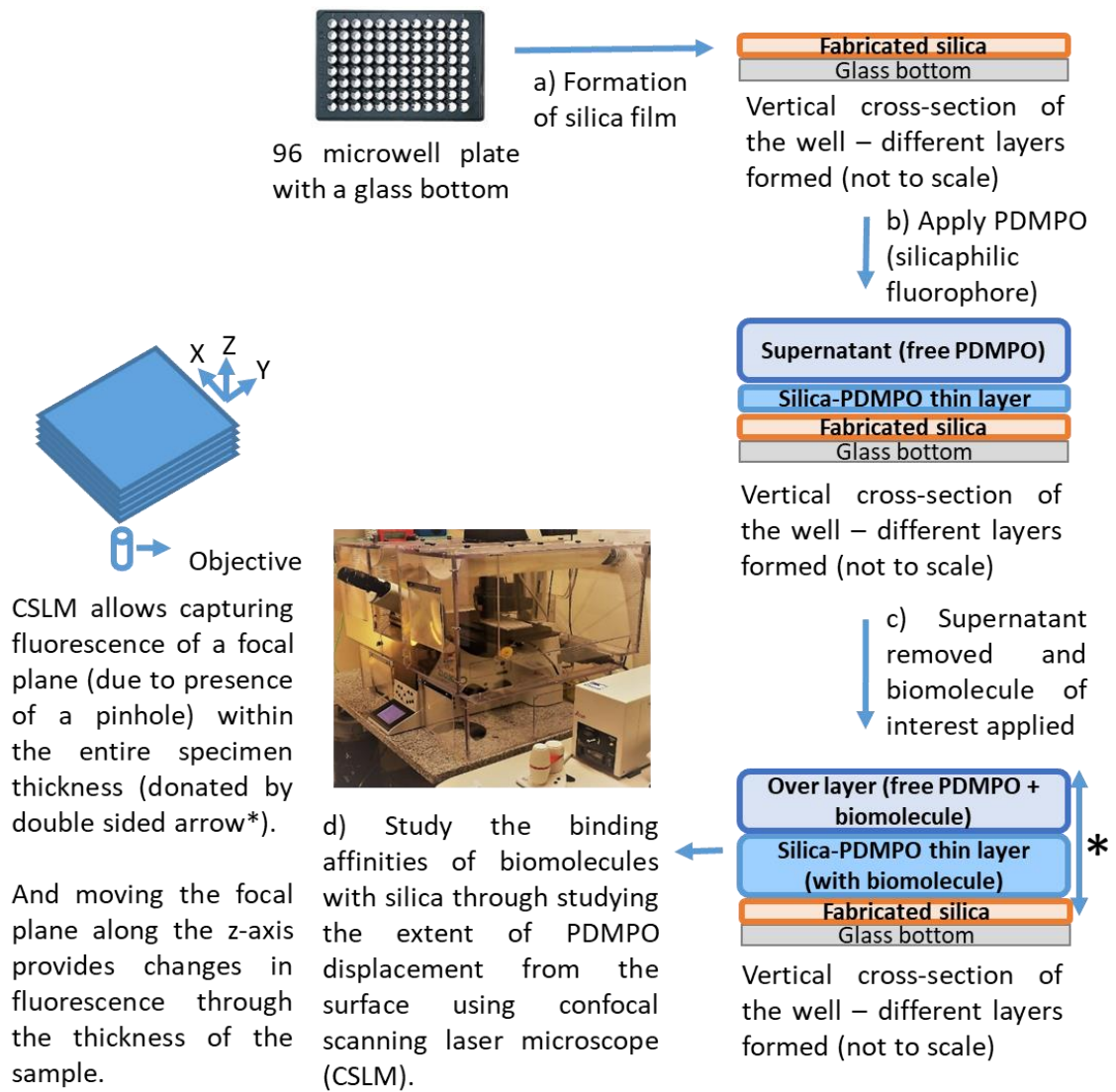


Figure 3.4 – An overview of O-IDA using silica surface – two-step process explained in detail.

(a) Formation of fabricated silica film. (b) Fluorescent dye, PDMPO, is applied to the fabricated silica film – thin layer formation. (c) Supernatant (free unbound PDMPO) is removed and replaced with the biomolecule of interest – biomolecule displaces the PDMPO on the fabricated silica. (d) CSLM used to study binding affinities of biomolecules to the silica through studying the extent of the PDMPO displacement.

The background and assumptions to the calculations of IC_{50} , K_i and ΔG_{ads} are discussed below.

a. Calculation of IC_{50}

O-IDA allows access to IC_{50} value which is the half maximal inhibitory concentration. Here in O-IDA, IC_{50} is defined as the concentration of the inhibitor (compound of interest) required to displace 50% of the bound indicator molecules in the thin layer from the initial state. IC_{50} is determined through studying the effect of the concentration-dependent analyte of interest on the fluorescence of the indicator on the surface (see Figures 3.7 and 3.9 for all the compounds studied) from the initial state. Hence, IC_{50} describes the potency of an assayed test compound. Modifying the generalized logistic function in Equation 3.1 to account for a displacement by changing the sign of the exponent yields Equation 3.4 where the parameters are the same as in Equation 3.1.

$$\frac{B}{B_0} = A_2 + \frac{A_1 - A_2}{1 + 10^{-(x - \log x_0)n}} \quad (3.4)$$

For amino acids, a polyamine and a drug, the fits were simplified by applying a one-site competition curve, which is a dose–response curve with a Hill slope n equal to 1. For peptides, the fits were expected to be more complex and a dose–response curve with a Hill slope n different to 1 was applied. IC_{50} is then obtained from 10^{x_0} . Here, A_1 and A_2 can be used to account for residual fluorescence not treated already and to account for irreversible binding of the indicator dye.

With regards to the interactions of amino acids, a polyamine and a drug to the silica surface and their geometric considerations, the hill slope n was 1 as it was assumed that one fluorescent dye molecule was replaced by one molecule of analyte of interest. However, the behaviour of the interactions of peptides to the silica surface is more complex as their comparably large size would mean that peptides could replace more than one fluorescent dye molecule. Hence, it may also be assumed that the hill slope n

indicates the number of replaced fluorescent dye molecules. In addition, cooperative and entropic contributions may rise due to the rearrangement of the fluorescent dye.

b. Calculation of K_i (Michaelis, 2018)

A quantity analogous to the inhibitory binding constant (Yung-Chi and Prusoff, 1973), K_i , can be defined for this assay. K_i is the dissociation constant for the equilibrium attained for the inhibitor's (compound of interest) interaction to the surface to form the inhibitor-surface complex and it can be obtained from the IC_{50} . The approach from Yung-Chi and Prusoff, 1973 is commonly applied for the calculation of K_i and it is a simple proportionality relationship between the K_i and IC_{50} and is known as Cheng-Prusoff equation (see Equation 3.5).

$$K_i = \frac{IC_{50}}{1 + \frac{[F]}{K_F}} \quad (3.5)$$

Here, $[F]$ corresponds to the agonist' (fluorescent dye in this study) concentration used for the assay and K_F is the dissociation constant of the agonist to the surface.

However, this approach has associated limitations and drawbacks which have been reported by several researchers (Leff and Dougall, 1993; Craig, 1993; Lazareno and Birdsall, 1993; Cheng, 2001; Cheng, 2004). The main concern was that it is only valid for antagonist's (analyte of interest in this study) dose response curves with a hill slope of $n = 1$ (Lazareno and Birdsall, 1993; Cheng, 2001). Hence, this showcased a need for an extension of this approach for a more generalised version which will also be valid for the cases with non-hyperbolic binding having a hill slope n different than 1 (Leff and Dougall, 1993)³⁵. Lazareno and Birdsall, 1993 also documented that using this approach to calculate K_i for dose response curves will give an overestimation in cases with a hill slope of $n < 1$ and an underestimation for $n > 1$. It was also reported that the concentration of the agonist and the hill slope m from its dose response curve were also important for the determination of K_i in displacement assays (Lazareno and Birdsall, 1993; Cheng, 2004).

A generalised form of this approach was introduced by Leff and Dougall, 1993 which was further improved by Lazareno and Birdsall, 1993 which comprised the hill slopes n and m from the dose response curves of the agonist and antagonist respectively. See Equation 3.6 below.

$$K_i = \frac{IC_{50}^n}{\left(2 + \left(\frac{[F]}{EC_{50}}\right)^m\right)^{\frac{1}{m}} + 1} \quad (3.6)$$

Here, each of the parameters have been explained earlier in this section.

Later, Cheng (Cheng, 2001; Cheng, 2004) also noted the importance of the hill slope functions m and n . An extension to the approach of Cheng and Prusoff equation (Equation 3.5) was introduced and is stated below (Equation 3.7).

$$K_i = \frac{IC_{50}^n}{1 + \left(\frac{[F]}{EC_{50}}\right)^m} = \frac{IC_{50}^n}{1 + \frac{[F]^m}{K_F}} \quad (3.7)$$

Here, each of the parameters have been explained earlier in this section. As noted above for amino acids, a polyamine and a drug, it was assumed that $n = 1$. On contrary, the hill slope n is different than 1 for peptides. Hence for any cases with hill slopes m and n equalling 1, Equation 3.7 will be simplified to the Cheng-Prusoff equation (Equation 3.5).

From the range of approaches considered (Yung-Chi and Prusoff, 1973; Leff and Dougall, 1993; Lazareno and Birdsall, 1993; Cheng, 2001; Cheng, 2004), the approach from Cheng (Cheng, 2001; Cheng, 2004), who highlighted the importance of the slope function, appears to be the most suitable for the treatment because it is obtained directly from the law of mass (Cheng, 2001; Cheng, 2004). On contrary, the Lazareno and Birdsall, 1993 approach utilises a mathematical model based on the assumptions that the competitive inhibitor follows a logistic function for the binding sites with the agonist. The comparison showing the different strategies is shown in Tables 3.1 and 3.2 but the binding affinity comparisons are done using Cheng approach in this chapter (Cheng, 2001; Cheng, 2004) as it is not based on any mathematical assumptions.

c. Calculation of the Free Energy of adsorption ΔG_{ads}

Similarly as above, the availability of an inhibitory binding constant for the interactions of the inhibitory molecules of interest, K_i , allows for the calculation of its binding affinity through the calculation of free energy of adsorption, ΔG_{ads} , using Equation 3.8. Free energy of adsorption, ΔG_{ads} , is an indicator of the strength of interactions present between two molecules. The potency of the compounds of interest in this study was studied through K_i . When comparing the ΔG_{ads} with the different interaction energies obtained, it is essential to consider that the binding affinity calculations are dependent on the assay conditions and uses K_i in this study.

$$\Delta G_{ads} = -RT \ln(\bar{v}_s \cdot K_i) \quad (3.8)$$

Here, v_s and K_i are as described above, R is the gas constant ($8.3144 \text{ J K}^{-1} \text{ mol}^{-1}$) and T is the room temperature in Kelvin, K .

3.4.3. Fitting procedure used for the extraction of surface bound contribution, B (Intensity)

When a silica surface is exposed to aqueous PDMPO, PDMPO – silica interactions at the interface leads to the formation of a thin fluorescent PDMPO layer and an overlayer fluorescent unbound PDMPO layer due to unbound or free PDMPO in solution. Due to diffraction limits of CSLM, the thickness of the thin layer cannot be measured but the position of these layers along the axial response and the fluorescence emission from these layers can be measured.

In the CSLM, the measured response of a system comprised of a thin layer (due to surface bound PDMPO molecules) and an over layer (due to PDMPO molecules in bulk solution) which includes contributions from the object function of molecules in the two distinct locations and effects of the point spread function. Further, there may be contributions from any further system components that fluoresce. Hence for this silica-PDMPO system, the measured optical response can be normalised and fitted to the Cauchy-Lorentz function and the cumulative Cauchy-Lorentz function (Ghafari et al.,

2009; Ghafari, Parambath and Hanley, 2012), Equation 3.9, which can be approximated as:

$$M(z) = C_1 \frac{1}{\pi\gamma \left[1 + \left(\frac{(z - z_0)^2}{\gamma} \right) \right]} + C_2 \left(\frac{\frac{1}{\pi} \arctan\left(\frac{(z - z_0)}{\gamma}\right)}{\gamma} + \frac{1}{2} \right) + O \quad (3.9)$$

In this representation, $M(z)$ is the measured CSLM axial response, z_0 is the position (centre) of a thin PDMPO layer attached to the surface, γ is the width at half maximum of the response, $C_1(z)$ and $C_2(z)$ represent the fluorescence intensity from the surface bound PDMPO and PDMPO in the bulk solution, respectively, and O corrects for background fluorescence in the plate materials e.g. polystyrene, electronic offsets, and the photomultiplier tube background in the CSLM. Figure 3.5 (b) - (d) gives an annotated example and shows the individual components along with the fitted curve which fits well with the outcome from CSLM (Figure 3.5 (d)).

The area of the peak described by $C_1(z)$ is the quantity of interest (the intensity) for subsequent EC_{50} and IC_{50} determinations. It is important to note that due to the overlapping signals described in Equation 3.9, considering the raw optical response under such circumstances is insufficient and misleading. In the text, 'B' refers to 'intensity' which can either be measured as the area under the peak described by $C_1(z)$, the integrated intensity or the amplitude of the optical response. As the data can be normalized to reference intensities or maximal response, all approaches are valid. For this PDMPO-silica system, it is necessary to first perform the described fitting procedure above to isolate the thin layer component as the integrated peak area (intensity).

The output from CSLM also revealed fluorescence from the polystyrene bottom of the plate (see Figure 3.5 (b)). Further, it should also be noted that moving forward, experiments would benefit from the use of different plates that do not have a polystyrene bottom. However, this approach also allows for a consideration of the background fluorescence via the lower asymptote in the fitting procedures.

Initially, it was also considered to study the peak from the polystyrene bottom and hence applied a fitting with an additional parameter surrounding this peak. See Equation 3.10 which is same as Equation 3.9 with $C_0(z)$ for the polystyrene bottom peak.

$$M(z) = C_0 \frac{1}{\pi\gamma \left[1 + \left(\frac{(z - z_0)^2}{\gamma} \right) \right]} + C_1 \frac{1}{\pi\gamma \left[1 + \left(\frac{(z - z_1)^2}{\gamma} \right) \right]} + C_2 \left(\frac{1}{\pi} \arctan \frac{(z - z_1)}{\gamma} + \frac{1}{2} \right) + O. \quad (3.10)$$

Here, all the parameters are as described before and $C_0(z)$ represents the fluorescence intensity from the polystyrene bottom and z_0 and z_1 are the centre of the polystyrene film and the position (centre) of a thin PDMPO layer attached to the surface respectively.

Figure 3.6 shows a comparison between the two models with Alanine and Spermine's dose response curves as examples using the respective surface bound contributions, B , from each model. Two peak fitting model in Equation 3.10 led to a two to three-fold increase in the error for IC_{50} values, bigger confidence and prediction intervals and smaller correlation co-efficient (R^2) values revealing a relatively poor fit as opposed to the one peak fitting model in Equation 3.9 which only analyses the peak for the interaction of PDMPO to silica. Hence, the one peak fitting model (see Figure 3.5 (b) - (d)) using Equation 3.9 was used for this assay. Hence, the two peak fitting model in Equation 3.10 was rejected.

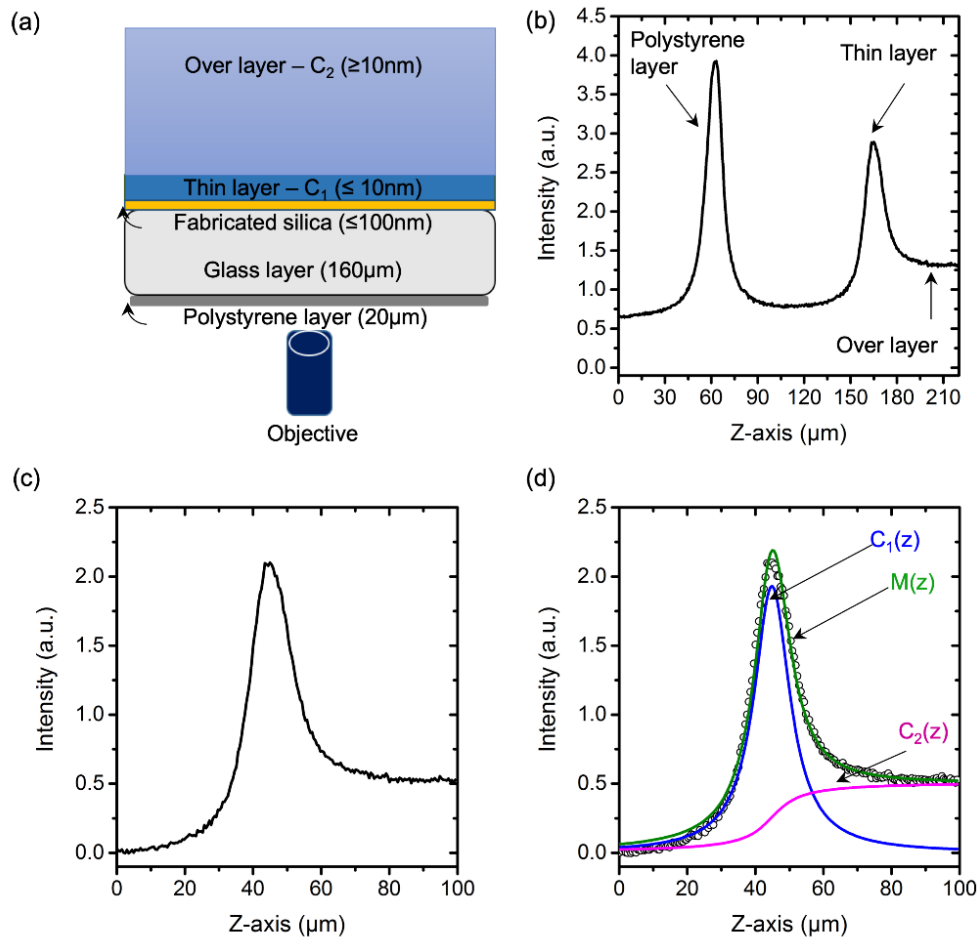
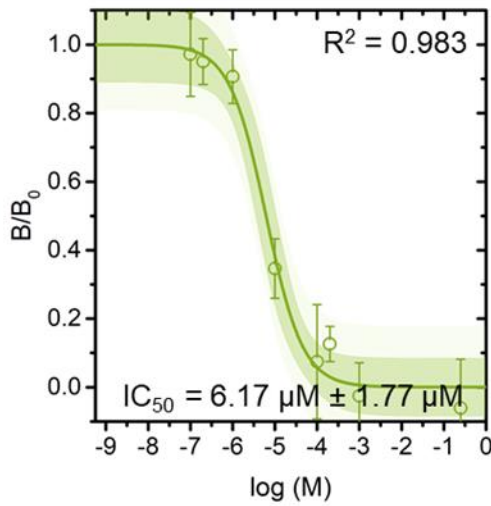


Figure 3.5 – An overview of the Silica/PDMPO interaction in an optically sectioned planar format indicator displacement assay.

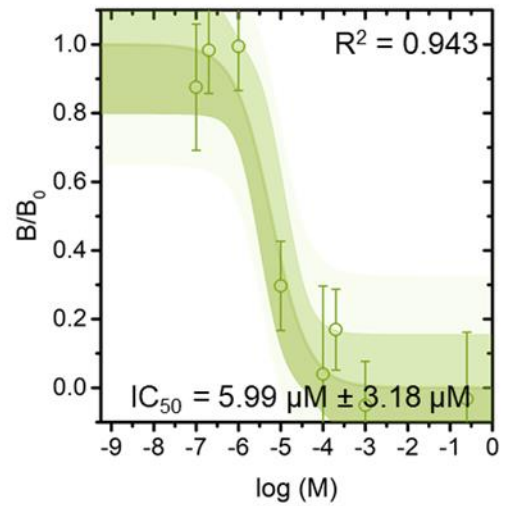
Michaelis et al., 2019

(a) Schematic representation (not drawn to scale) of the experimental setup using silica/PDMPO interactions in a 96 microwell glass bottom plate. (b) The axial response obtained through CSLM shows three distinctive features. (c) The axial response of interest including the thin layer and over layer (normalized). (d) The Cauchy-Lorentz function and the cumulative Cauchy-Lorentz function (Equation 3.9) used for the fitting to isolate the spectral contributions with annotations showing the components: thin layer ($C_1(z)$ in blue), over layer ($C_2(z)$ in pink) and fitted combination ($M(z)$ in green).

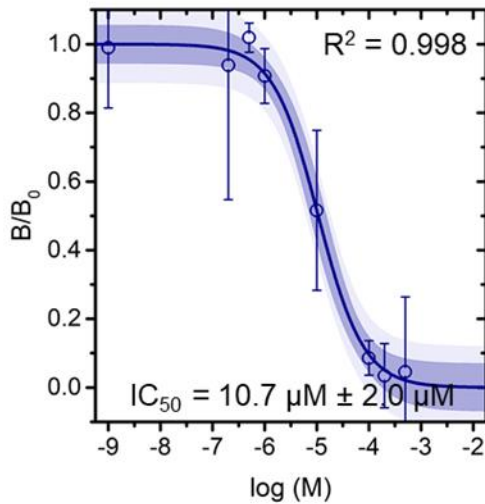
a) Alanine using selected model



b) Alanine using rejected model



c) Spermine using selected model



d) Spermine using rejected model

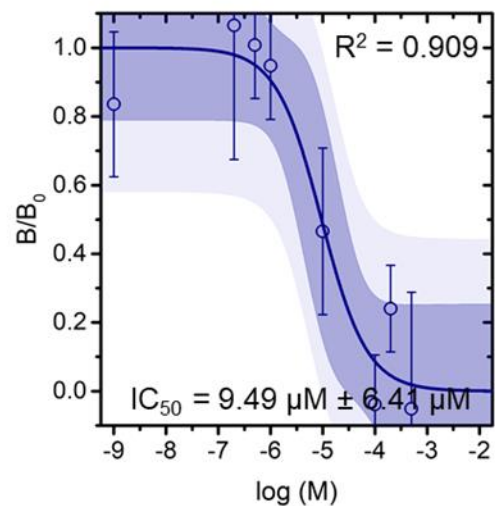


Figure 3.6 – Comparison between the two fitting methods for the extraction of surface bound contribution, B , using dose response curves

(a) and (c) are the dose response curves with the surface bound contribution, B , using the fitting model in Equation 3.9. (b) and (d) are the dose response curves with the surface bound contribution, B , using the fitting model in Equation 3.10. (a) and (b) for Alanine and (c) and (d) for Spermine allow the comparison between the two fitting models (one peak using Equation 3.9 and two peaks using Equation 3.10).

3.5. Discussion (data analysis and key findings)

An increasing silica-PDMPO thin layer intensity is observed with an increasing PDMPO concentration (see Figure 3.3 (c)). The measurement of the binding affinity of the fluorescent dye, PDMPO, in phosphate buffer to silica (Figure 3.2 (e)) yielded an EC_{50} value of $1.75 \pm 0.27 \mu\text{M}$, $m = 1.39 \pm 0.24$, $K_F = 0.01 \pm 0.02 \mu\text{M}$, and a binding energy $\Delta G_F = -13.28 \pm 0.12 \text{ kcal mol}^{-1}$.

As stated above, the assay system was challenged with the molecules of interests. Amino acids (alanine, histidine and aspartic acid), a polyamine (spermine), and a drug (ibuprofen) were chosen for the purpose of developing the method. For the extension of the method to larger biomolecules to test for any limitations with the type of molecules that can be studied through this approach, three 7-mer silica binding peptides were used. These specific amino acids were chosen as they are commonly found in peptides that bind to silica (Belton et al., 2004). A polyamine was selected as it has been found to be part of the posttranslational modifications of proteins isolated from silicifying organisms such as some diatoms (Mathé et al., 2013; Otzen, 2012). It has also been shown to moderate silica formation *in vitro* (Belton, Patwardhan and Perry, 2005; Belton et al., 2008). Ibuprofen was selected as an example of a commonly used hydrophobic drug which could serve as a test case for silica-based drug-delivery systems that can control the release of drugs and deliver them to specific targets. The 7-mer silica binding peptides (K7 (KLPGWSG) - positively charged (cationic), A7 (AFILPTG) - neutral and L7 (LDHSLHS) - negatively charged (anionic)) identified through phage display were selected for this study as they were known good binders of silica (Patwardhan et al., 2012; Puddu and Perry, 2012).

The dose–response behaviour of the selected biomolecules is presented in Figures 3.7 and 3.9 for all systems. The competitive fitting suggests a non-cooperative binding of the compounds of interest studied towards the silica surface as the binding affinity of the compounds of interest is not affected by the presence of the indicator, PDMPO dye. A decreasing silica-PDMPO thin layer intensity is observed with an increasing compound of interest's concentration (see Figure 3.3 (f)). The calculated IC_{50} , K_i (all three approaches) and ΔG_{ads} values are presented in Tables 3.1 and 3.2. The ΔG_{ads} calculated

through the three approaches of K_i showed the same trend for the binding affinities of the compounds studied with $n = 1$. The binding affinities obtained from the traditional Cheng and Prusoff equation showed a slightly higher affinity compared to the Lazareno and Birdsall, 1993 approach for compounds with $n = 1$. The differences seen are due to the hill slope m of the PDMPO dye where the hill slope $n = 1$ for the compounds of interest studied. No trend was observed for the binding affinities obtained from the traditional Cheng and Prusoff equation for peptides exhibiting n different to 1. However, similar trends were observed using the Cheng (Cheng, 2001; Cheng, 2004) and Lazareno and Birdsall, 1993 approach which showcases the importance of hill slopes m and n in obtaining binding affinities for all compounds. On the other hand, the Cheng (Cheng, 2001; Cheng, 2004) approach showed the relatively highest binding affinities for all compounds when compared to Lazareno and Birdsall, 1993 approach. As stated earlier, the binding affinity comparisons are done using Cheng (Cheng, 2001; Cheng, 2004) approach in this study.

To check the reproducibility and robustness of the assay, some of the selected compounds of interest were repeated and very similar binding affinity values were observed. The competitive fitting procedure for the O-IDA was also challenged with different number of data points to identify the optimal number for the effective determination of the binding affinities. Around 5-8 data points were understood to be the optimal as the binding affinity values calculated did not show large changes which agree with the research available in this area for the optimum number of measurements needed for the data points used (Iversen et al., 2012).

Of the compounds that were tested using this method, ibuprofen had the strongest affinity for the silica surface and spermine had the weakest affinity. The binding energies covered the range from -12.82 to -9.39 kcal mol⁻¹ using the Cheng (Cheng, 2001; Cheng, 2004) approach. Of the peptides that were tested using this method, K7 had the strongest affinity for the silica surface and L7 had the weakest affinity. The binding energies covered the range from -8.84 to -7.82 kcal mol⁻¹ using the Cheng (Cheng, 2001; Cheng, 2004) approach.

Table 3.1 – Binding affinities of selected biomolecules to silica surfaces

Name of compound	IC ₅₀	K _i ¹	K _i ²	K _i ³	ΔG _{ads} ¹	ΔG _{ads} ²	ΔG _{ads} ³	
	(μM)	(μM)			(kcal mol ⁻¹)			
Amino acids	Alanine	6.17	3.93	4.23	6.76	-9.76	-9.71	-9.43
		±	±	±	±	±	±	±
		1.77	1.13	1.30	2.70	0.17	0.18	0.24
	Histidine	0.54	0.35	0.37	0.60	-11.19	-11.15	-10.87
		±	±	±	±	±	±	±
		0.11	0.07	0.08	0.20	0.11	0.12	0.20
	Aspartic acid	3.43	2.19	2.35	3.76	-10.10	-10.06	-9.78
		±	±	±	±	±	±	±
		0.71	0.45	0.52	1.30	0.12	0.13	0.20
Polyamine	Spermine	10.69	6.81	7.33	11.72	-9.43	-9.39	-9.11
		±	±	±	±	±	±	±
		1.94	1.24	1.45	3.88	0.11	0.12	0.20
Drug	Ibuprofen	0.032	0.021	0.022	0.035	-12.87	-12.82	-12.55
		±	±	±	±	±	±	±
		0.003	0.002	0.003	0.010	0.06	0.08	0.18

The standard error of the fitting for the IC₅₀ values are propagated during the calculations.

The K_i and its corresponding ΔG_{ads} have been calculated using all the three approaches explained in section 3.4.2 for K_i which have been numbered as subscripts. ¹ corresponds to Cheng and Prusoff approach (Equation 3.5), ² corresponds to the Cheng approach (Equation 3.7) and ³ corresponds to the Lazareno and Birdsall approach (Equation 3.6).

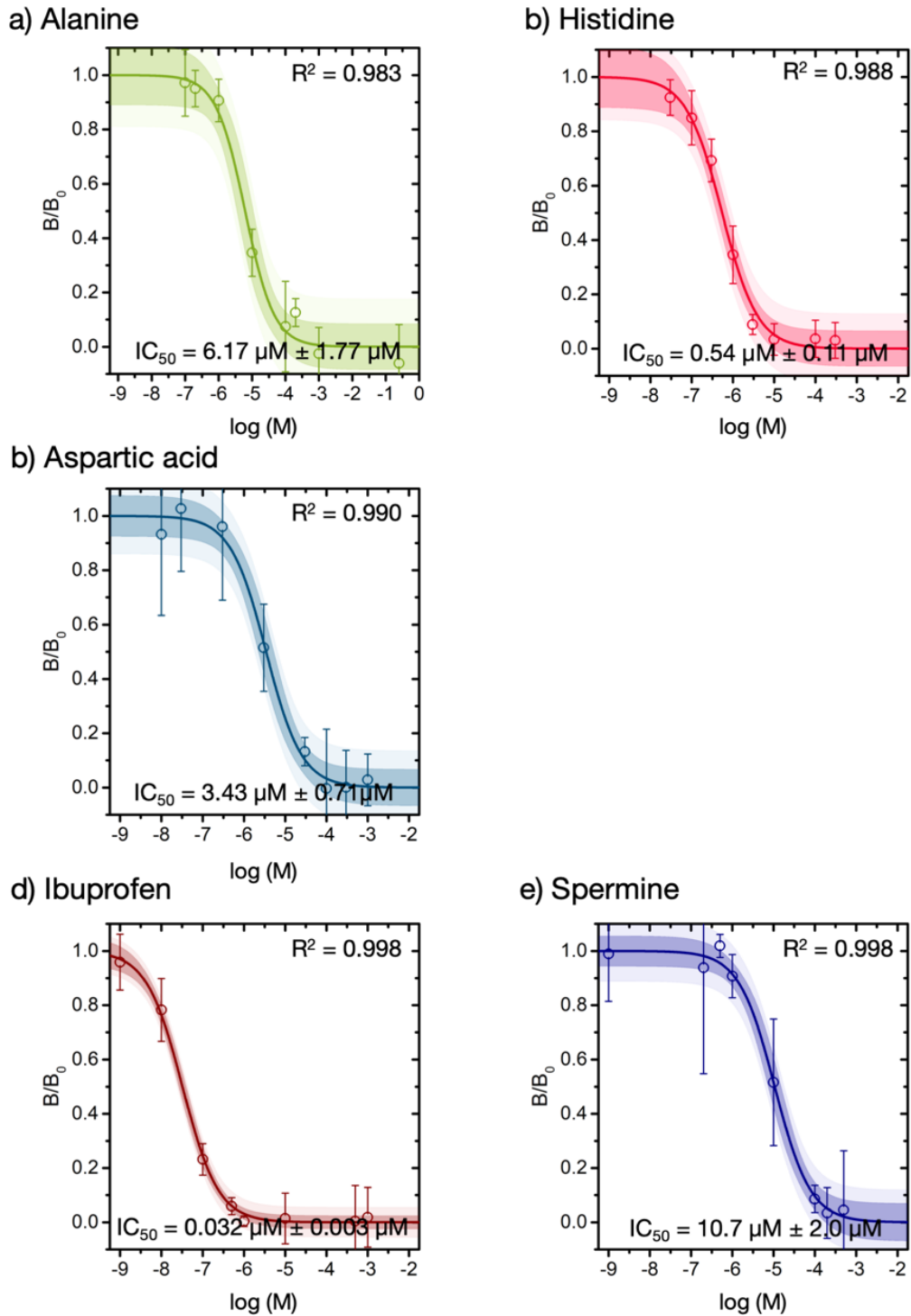


Figure 3.7 – Dose response curves obtained through O-IDA to silica

Selected amino acids, a polyamine and a drug - (a) Alanine (b) Histidine (c) Aspartic acid (d) Ibuprofen (e) Spermine. The fitting is performed using a one-site competition curve with a Hill slope n equal to 1 along with the 95% confidence intervals as well as the 95% of prediction intervals.

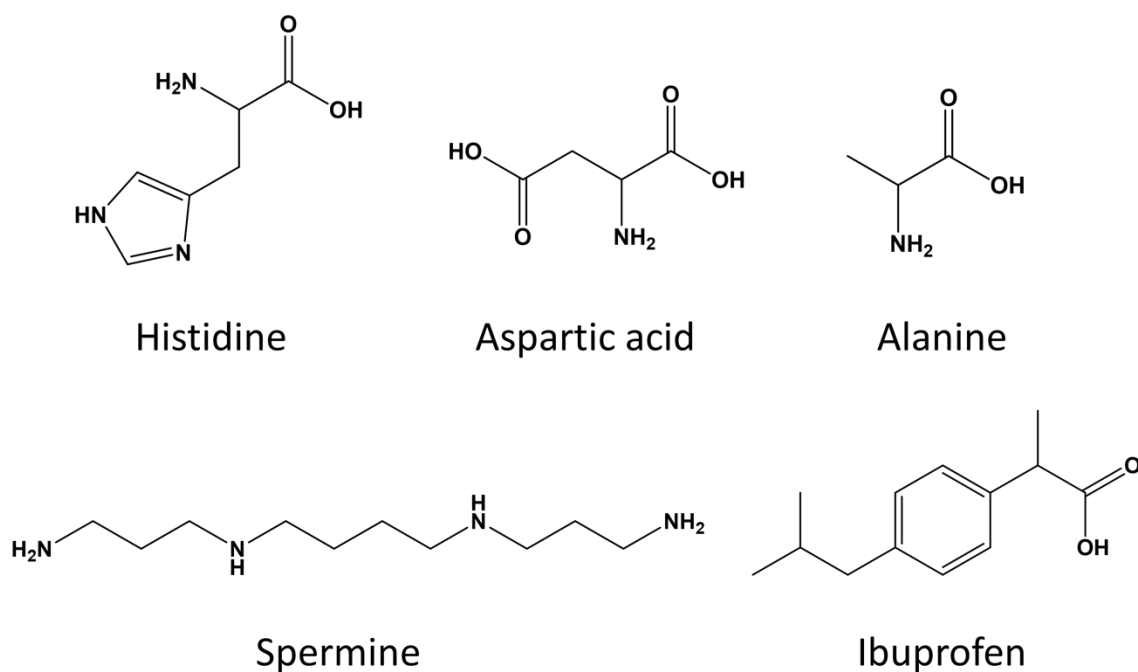


Figure 3.8 – Structures of Histidine, Aspartic acid, Alanine, Spermine and Ibuprofen

Table 3.2 – Binding affinities of selected peptides to silica surfaces

Name of peptide	IC ₅₀ (μM)	n (slope)	K _i ¹	K _i ²	K _i ³	ΔG _{ads} ¹	ΔG _{ads} ²	ΔG _{ads} ³
			(μM)			(kcal mol ⁻¹)		
K7 (KLPGWSG)	31.03	1.01	19.76	18.38	29.39	-8.80	-8.84	-8.56
	±	±	±	±	±	±	±	±
	3.36	0.13	2.14	2.49	8.75	0.06	0.08	0.18
A7 (AFILPTG)	698.16	1.27	444.64	66.07	105.65	-6.95	-8.08	-7.80
	±	±	±	±	±	±	±	±
	25.10	0.06	15.99	6.03	29.64	0.02	0.05	0.17
L7 (LDHSLHS)	0.014	0.49	0.009	103.00	164.69	-13.37	-7.82	-7.54
	±	±	±	±	±	±	±	±
	0.006	0.10	0.004	23.76	57.90	0.26	0.14	0.21

The standard error of the fitting for the IC₅₀ values are propagated during the calculations.

The K_i and its corresponding ΔG_{ads} have been calculated using all the three approaches explained in section 3.4.2 for K_i which have been numbered as subscripts. ¹ corresponds to Cheng and Prusoff approach (Equation 3.5), ² corresponds to the Cheng approach (Equation 3.7) and ³ corresponds to the Lazareno and Birdsall approach (Equation 3.6).

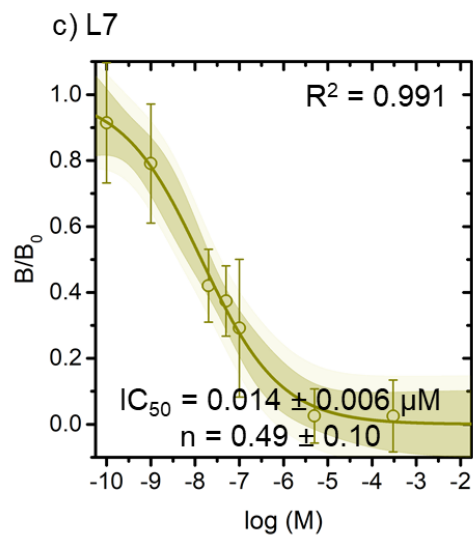
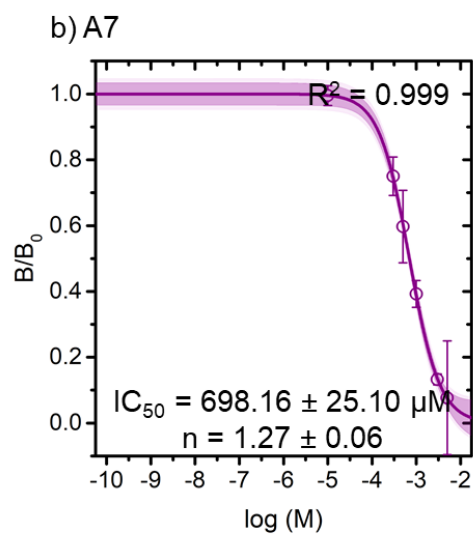
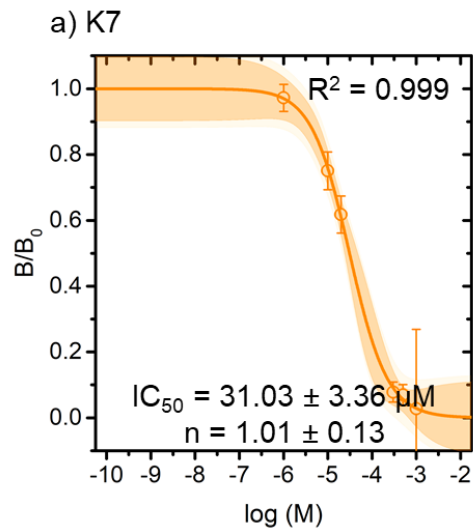


Figure 3.9 – Dose response curves obtained through O-IDA to silica Selected peptides - (a) K7 (b) A7 (c) L7. The fitting is performed using a dose response curve with a Hill slope n different to 1 along with the 95% confidence intervals as well as the 95% of prediction intervals.

3.5.1. Amino acids - Histidine, Aspartic acid and Alanine

Understanding polypeptide's interactions at interfaces are complex; hence, amino acids are often chosen as model building blocks of polypeptides to gain an insight into the possible interactions at interfaces in different environments. All amino acids are characterised by their functional groups (carboxyl (COOH) and amine (NH₂)) with the other properties being determined by their side chains (such as polar/non-polar, acidic/basic etc.). Either the functional groups or side chain functionalities may contribute towards the interactions with surfaces. With hydroxylated silica surface being weakly acidic, the most likely interactions will be with the amine group of all amino acids and others with the side chain functionalities under aqueous environment.

The available studies were used to understand the observed binding affinities through elucidating the possible interactions and their comparable mechanisms which are responsible for biosilicification procedure. Of the amino acids studied with O-IDA, the binding affinity of amino acids toward hydroxylated silica were in the following order: histidine > aspartic acid > alanine, and this trend aligns with a computational study that studied the binding affinities of several amino acids to an amorphous hydroxylated silica surface with relatively different hydrophilicity performed under gas conditions (Rimola, Sodupe and Ugliengo, 2009). The adsorption process in this computational study were dictated by the hydrogen-bond interactions between both the COOH moiety and the side-chain functionalities of the amino acids with the terminal silanol groups of the surface. The final adsorption energies took into consideration the dispersive forces as they also play a fundamental role on the interactions that drive adsorption of amino acids to the silica surface. The findings show the following affinity of amino acids towards the hydroxylated silica: nonpolar/polar (neutral) < polar (amidic) / polar (acidic) < polar (basic). It can be concluded that the interactions become more favourable as the number of polar groups in the amino acid side chain increase as the formation of hydrogen bonds with the silica surface will increase. The final adsorption energy, ΔG_{ads} , for the wide range of amino acids studied ranged from -1.8 to -9.8 kcal mol⁻¹.

Upon research in literature, it was noted that computational studies of isolated amino acids' binding studies to silica have only been performed on different surfaces of fully

hydroxylated quartz in vacuum or for amino acid analogues on fully hydroxylated quartz in an aqueous environment. Quartz is a crystalline form of silica which is structurally different from the hydroxylated silica film in this study which is amorphous silica (Hickman et al., 2012). Thus, there is no directly comparable computational or experimental data available for the adsorption of amino acids on hydroxylated silica surface in aqueous environment that will enable setting up a quantitative affinity scale that is reliable for comparison of similar studies. This is because there are differences either in the type of surface utilised (different structure or distribution and density of the surface groups) or with the conditions the computational study was carried out. Of the data that is available, computed adsorption enthalpies (ΔE_{ads}) for alanine and aspartic acid on the (10–10) surface of quartz range from ca. -17 to -20 kcal mol⁻¹ (Han and Sholl, 2009; Han and Sholl, 2010). For studies of “models of amino acids” (e.g., methane for alanine; methanol for serine; butylamine for lysine; and acetic acid for glutamic acid), the values are all around the -1 to -2 kcal mol⁻¹ range (Wright and Walsh, 2012).

Histidine’s highest binding affinity to silica most likely includes interactions of the imidazole side chain interacting with silanol/siloxide groups on the silica surface as has been reported for peptides containing histidine (Rimola, Sodupe and Ugliengo, 2009; Patwardhan et al., 2012). It is proposed that protonated N atoms of the imidazole ring may form direct hydrogen bonds with the deprotonated silanol terminal group of the silica surface that would be present at the pH of the experiment. Another contribution to binding will arise when the imidazole ring inserts flat into locally hydrophobic pockets while still forming hydrogen bonds with terminal OH groups. Both behaviours have been observed for peptide silica binding interactions (Rimola, Sodupe and Ugliengo, 2009; Patwardhan et al., 2012). For the other two investigated amino acids, similar values were obtained for their binding affinity toward silica. The side chain of aspartic acid has a carboxylic acid and alanine has a non-polar (hydrophobic) group (see Figure 3.8 for the chemical structures for the amino acids used). With respect to the very different side chain functionalities, a common binding configuration via the amine and carboxyl groups are expected which is known from molecular dynamics simulations on silica (Rimola, Sodupe and Ugliengo, 2009; Emami et al., 2014).

3.5.2. Polyamine - Spermine

For the investigated polyamine (Menzel et al., 2003), the interaction with silica will most probably be mediated by the amine groups, leading to a comparable binding affinity. See Figure 3.8 for spermine's chemical structure showing the amine groups. Though with increasing number of amine groups, the binding affinity would be expected to increase. This was not seen in this study because the steric effects may be prominent due to the size of Spermine. Similarly, there are no computational data available for comparison.

3.5.3. Drug - Ibuprofen

In our experimental study, ibuprofen (see Figure 3.8 for its chemical structure) was found to exhibit the highest binding affinity for silica amongst all studied binding partners, with $\Delta G_{\text{ads}} = -12.82 \pm 0.08 \text{ kcal mol}^{-1}$. In recent density functional theory simulations (Delle Piane et al., 2014; Delle Piane et al., 2014b), interactions of ibuprofen with a hydroxylated silica surface were indeed shown to be exothermic and exergonic. Weak hydrogen bonding between the carboxylic functionality of ibuprofen and OH surface groups of the silica surface and dispersive attractions between the nonpolar portion of ibuprofen and the surface were both found to be important, particularly in the presence of added water molecules (Delle Piane et al., 2014b).

Ibuprofen is known to form a dimer through sharing a hydrogen bond between two ibuprofen monomers. A computational study (Delle Piane, Corno and Ugliengo, 2016) showed little differences in the computed energy derived through interacting monomer or dimer of Ibuprofen with mesoporous silica. This confirmed that dimer formation does not have any effects on the high binding affinity observed for ibuprofen in this study.

3.5.4. Peptides

Of the peptides studied with O-IDA, the binding affinity of peptides toward hydroxylated silica were in the following order: K7 (KLPGWSG) > A7 (AFILPTG) > L7 (LDHSLHS), and this trend aligns with prior research studies that studied the binding affinities of these peptides to amorphous silica surfaces of particles from 28-200nm in diameter (Sola-Rabada et al., 2018; Oliver et al., 2019). See Table 3.3 for a comparison.

With silica surfaces being anionic, positively charged (cationic) peptides would be generally strongly attracted to them where the polar groups of the peptides interact with the silanol or siloxide (SiO^-) groups of the silica surface by hydrogen bonding, ion-dipole, dipole-dipole and van-der-Waals interactions (Patwardhan et al., 2012). The strong attraction of positively charged peptide (K7) to anionic silica surfaces is also explained by the electrostatic interactions such as ion pairing of protonated N-termini and basic Lysine side chain with negatively charged siloxide groups (Puddu and Perry, 2012).

In a research study, the effect of differently charged peptides (K7, A7 and L7) at neutral pH (using phosphate buffered saline) have been studied against an aqueous silica particle interface where electrostatic/hydrophobic interactions and hydrogen bonding were found to be prominent at the interface (Patwardhan et al., 2012; Puddu and Perry, 2012). The binding affinities of the peptides studied towards the silica surface showed the greatest affinity for the positively charged peptide (K7) followed by a relatively lower affinity for A7 and L7 (exhibited the lowest affinity). The peptides without cationic groups would interact with or adsorb to silica through non-electrostatic interactions only confirming their importance where a relatively higher concentration of peptide would be commonly required for adsorption (Patwardhan et al., 2012).

As A7 is mainly constituted of non-polar amino acids leading to its hydrophobic properties, non-electrostatic interactions would most likely exist between the hydrophobic domains of A7 and the siloxane bridges of silica surface (Patwardhan et al., 2012). With L7 being anionic at the pH of the study due to the presence of the aspartic acid's carboxylic acid side chain, the negative electrostatic interactions would prevent

its binding to the silica surface (also discussed later). Hence, the hydrophobic interactions and hydrogen bonding overcome these electrostatic repulsions existing between the peptide and silica which is probably responsible for the observed binding affinity (Patwardhan et al., 2012).

It was seen that the pH of the system in which the binding studies are carried out also affects the adsorption of biomolecules to silica (Patwardhan et al., 2012; Puddu and Perry, 2012; Meng et al., 2004). In addition, an increase in the silica particle size also influenced the amount of peptide that adsorbed onto the silica surface which can be explained due to the larger silica surface ionization (Patwardhan et al., 2012; Emami et al., 2014b). Though usually for many of peptides identified through the phage display approach that bind to silica, the information provided on the material type is usually not adequate for comparisons with experimental studies. These quantitative findings on the mechanisms of peptide-silica interactions as a function of pH and particle size (surface chemistry) have been experimentally compared where a good agreement between simulation and experimentation is observed as the surface used for both were comparable and well documented (Patwardhan et al., 2012; Emami et al., 2014b).

Small changes in the silica surface chemistry with regards to the degree of different functional groups also significantly affect the binding interactions of peptides and their mechanism at the silica-peptide interface (Patwardhan and Clarkson, 2005; Patwardhan et al., 2012; Puddu and Perry, 2014; Puddu and Perry, 2012; Sola-Rabada et al., 2018). In addition, other factors such as binding/kinetic energies and/or orientation/conformation of peptides also significantly affect the binding of peptides to a silica surface (Sola-Rabada et al., 2018; Roach et al., 2005; Gray, 2004; Rabe et al., 2011).

Fluorescence based assays that use fluorophores and dyes have been previously used to study the peptide binding interactions with silica through measuring the remaining peptide concentrations in solution to allow a quantification of the amount of peptide adsorbed on amorphous silica nanoparticles (Patwardhan et al., 2012; Puddu and Perry, 2014; Puddu and Perry, 2012). Through this, different sizes and/or functionalities under varying environmental pH can be considered to study the different binding mechanisms.

With the degree of amine functionalized silica, a switch in peptide adsorption behaviour was also observed (Sola-Rabada et al., 2018).

It has been previously demonstrated that a competition between peptide-peptide interactions and peptide-surface interactions is observed especially at low concentrations of peptide where the peptide self-assembly becomes more favoured than silica-peptide interaction (Patwardhan et al., 2012; Puddu and Perry, 2012). Hence, it is important to consider this behaviour of peptides within the solvent used when interpreting the results as the binding configuration of the self-assembled peptide molecules would be different to the single peptide molecules. This also explains the lower thin layer intensities (B) observed with some of the lower peptide concentrations used in the current study. Upon careful interpretation of the data collected, these did not form part of the dose response curve analysis.

In a computational study which used molecular dynamics simulations with the CHARMM-INTERFACE force field, it was shown that pH affected the adsorption of charged peptides (K7 and L7) with no significant difference observed for neutral peptides (A7) (Emami et al., 2014a, Emami et al., 2014b). Again, both hydrogen bonds and hydrophobic interactions were observed to be important for their adsorption where they were relatively weaker for the neutral peptide (Emami et al., 2014a, Emami et al., 2014b).

In a more recent computational study which used molecular dynamics simulations with the CHARMM-INTERFACE force field, the peptide L7 was reported as not a good binder of silica as was previously known (Oliver et al., 2019). For an aqueous silica system with sodium ions chemically adsorbed to it, it was shown that the negative C-terminus of the peptide orients itself in a way such that the number of Na⁺ ions around the polypeptide and the interface to silica surface would decrease. Such a charge imbalance at that point of contact leads to unfavourable electrostatic interactions between the peptide and the silica surface. This stimulates peptide's dissociation from the surface; hence, a fluctuating engage-disengage character of the peptide in association with the surface is observed leading to a similar floating behaviour of the peptide due to slow diffusion of

sodium ions contributing towards the unfavourable electrostatic charges which repels the peptide away from the point of contact making it a poor binder of silica.

An odd IC_{50} is observed for L7, much smaller than the peptides K7 and A7 which is not what would be expected. With L7 being a large biomolecule, a multiple displacement of PDMPO dye would be expected. However, L7 also presented an odd n value of 0.49 ± 0.10 . Initially, it was thought that this technique may not be applicable to larger negatively charged compounds due to what was observed with L7. Having found that L7 is not a good silica binder (Oliver et al., 2019) explains the results obtained for L7. A probable slow displacement of PDMPO is what is led to the n value of 0.49 ± 0.10 . Hence, it can be concluded that a combined knowledge of IC_{50} and the slope, n , which gives valuable information about the types of interactions observed with the silica surface can still provide an estimation of the binding affinity of such poor binders of silica. If the results were to be interpreted using the Cheng and Prusoff approach (Equation 3.5), an overestimation of the binding affinity is seen ($\Delta G_{ads} = -13.37 \pm 0.26$). Hence, the importance of the slope n and its interpretation become important for such biomolecules of interest. Hence, a careful exploration of the results is needed to be able to interpret as much information as possible.

A couple of studies (Sola-Rabada et al., 2018; Oliver et al., 2019) utilise Isothermal Titration Calorimetry (ITC) for determining the binding affinity, ΔG , from the association constant, K_a , for the chosen peptides (K7 and L7) in this study against differently sized silica nanoparticles. Table 3.3 shows the ΔG values calculated using the Cheng approach (Equation 3.7) through the K_a provided in both studies. On the other hand, it is essential to also note that the binding affinity calculations (ΔG_{ads}) in the current study are dependent on the assay conditions and uses K_i in this study. Although the calculated ΔG values from literature could have been utilised as a comparison of binding affinities and to estimate the trend of the chosen peptides (K7, A7 and L7) against silica surfaces, this is not ideal as the silica nanoparticle sizes are different within these studies. Hence, no studies are again available which would allow a direct comparison of the binding affinities obtained through O-IDA as the surfaces used within the studies available in literature may differ in properties. However, the binding affinity trend found from the literature still aligns with that found in the current study.

Table 3.3 – Binding affinities of chosen peptides to silica surfaces in literature compared to the ones calculated through this study

Name of peptide	Net charge at pH 7.4	ΔG (literature) (kcal mol⁻¹)	Silica nanoparticle size as diameter (nm)	ΔG_{ads}^2 (current) (kcal mol⁻¹)
K7 (KLPGWSG)	+1	-5.81 ± 0.07	28 nm (Sola-Rabada et al., 2018)	-8.84 ± 0.08
A7 (AFILPTG)	0	N/A	N/A	-8.08 ± 0.05
L7 (LDHSLHS)	-1	-5.05 ± 0.05	200 nm (Oliver et al., 2019)	-7.82 ± 0.14

The standard error of the fitting for the IC₅₀ values are propagated during the calculations.

The ΔG (literature) and ΔG_{ads} (current) for this study have been calculated using the Cheng approach (Equation 3.7).

3.6. Conclusion

This study reports the first quantitative measurements of small and large molecule interactions with silica surfaces using O-IDA. They can be performed in any solvent and with any material (as long as it is stable and homogeneous), provided a suitable fluorescent dye is available and the system overall does not produce interfering fluorescence. The applicability of this approach to other systems could give great insights into interactions at interfaces. Additionally, investigation of interaction kinetics may be possible, provided that the interactions investigated happen on a timescale slower than the time of image acquisition in the CSLM.

The transfer of traditional IDAs to study the abiotic/biotic interface also requires one to keep in mind the underlying receptor occupancy theory together with its assumptions (Hill, 1910; Clark, 1933; Ruffolo, 1982; Colquhoun, 2006). For a direct comparison, the number of accessible binding sites on the surface of interest are not known because of surface protonation and system dynamics. In the framework of abiotic/biotic interactions, the maximum number of binding sites corresponds to the number that can be occupied by a known concentration of the fluorescent dye. However, it is important

to note that steric hindrance might prevent full occupancy. Further, during the displacement assay, non-indicator-occupied binding sites might be accessible, and additionally, not all analytes interact at the same binding site as the fluorescent dye due to the different chemistry that may be involved. For instance, the dye binds to the silica surface species, while some of the investigated amino acids will probably interact with the molecule adsorbed and/or dissociated water molecules present on the surface; in this case, the dye would be displaced because of “steric” considerations.

There are a few considerations to consider when designing O-IDA but not always present. These include problems with solubility of the compounds of interest in the selected solvent environment at higher concentrations and the observation of the prozone effect (Butch, 2000) at high concentrations which is a false increase of fluorescence intensity at higher concentrations which could mislead results.

The O-IDA approach introduced here could be used similarly to fluorescence-based IDAs in pharmacological screening because the method used is convenient, robust, sensitive and scalable to high-throughput formats. In this form, O-IDAs could be of interest for assessing the binding of medicinally relevant peptides or analytes for different applications. This technique has advantages over QCM and SPR approaches by avoiding the issues associated with isolating the behaviour of molecules versus solvent/ions (QCM) and the need for a conductive surface (SPR). The only main limitation of the O-IDA technique is the requirement for a fluorescent dye which has a specific interaction toward the abiotic surface of interest. A major advantage in comparison to the alternative approaches is the direct visualization of the adsorption events, which allows for quality control judgements regarding the homogeneity and spatial distributions of the response.

Chapter 4. Implementation of a fluorescence-based surface charge mapping method to study silica chemistry in biological tissues

4.1. Introduction

Surface charge estimation on silica surfaces plays a pivotal role in various applications and technologies such as monitoring DNA hybridization (Azam and Gibbs-Davis, 2013), protein transport (Wu et al., 2012), measurement of surface topography (Ozcelik and Barisik, 2019), drug delivery (Kotcherlakota et al., 2016), cellular uptake (Kotcherlakota et al., 2016), and microchip biosensors (Song et al., 2013) etc. Surface charge estimation is vital in biosilicification; therefore, an ability to accurately measure the local surface charge would be an exceptional advancement towards examining the mechanisms of silica nanostructures' formation *in vivo*. The maintenance of surface charge is fundamentally important in silica deposition (Ikuma et al., 2014), silica condensation (Cho et al., 2014), adsorption of solutes (Roach et al., 2006; Kroutil et al., 2015) and adaptive response to environmental pH variation (Kroutil et al., 2015).

The quantification of surface charge density on silica *in vivo* or even *in vitro* is not an easy task. The quantification of surface charge density on silica can be extremely useful in comprehending biosilicification and nanoscale processes at the silica-water interface. The surface charge density is affected by temperature (Al Mahrouqi et al., 2016), surface area (Barisik et al., 2014), pH (Ovanesyan et al., 2016), ionic strength or conductivity (Salis et al., 2016) and the presence of counter ions (Brown et al., 2015). Hence, all these factors should be considered for surface charge density determinations to be consistent ensuring desirable levels of reliability and reproducibility.

For measurement of surface charge at the solid-liquid interfaces, techniques such as Kelvin Probe Force Microscopy (Guo et al., 2012), Atomic Force Microscopy (AFM) (Gan and Franks, 2006) and zeta potential (ζ) measurements (Stern, 1924) are commonly used. Zeta (ζ) potential is a proxy of the surface charge potential and a commonly used measurement for surface charge estimations. To the best of our knowledge, there is no

optical technique available that can measure surface charge density on silica structures. The utilisation of such a technique would be advantageous in the study of biological silicification where many structural particulate arrangements at nanoscale exist within a single microscopic sample (Perry and Fraser, 1991; Kröger and Poulsen, 2008). In this chapter, an optical based imaging surface charge mapping technique that uses confocal scanning laser microscopy (CSLM) spectral imaging below the diffraction limit and a fluorophore, PDMPO dye (2-(4-pyridyl)-5((4-(2dimethylaminoethylaminocarbamoyl) methoxy)phenyl)oxazole) will be discussed.

The fluorescent dye, PDMPO, exhibits unique silicophilic fluorescence properties which lead to its use as a probe to trace silica to study biological silicification (Shimizu et al., 2001). Hence, PDMPO was chosen in this study due to its unique non-covalent interactions with silica and its history of applications as a probe as it accumulates in compartments of cells containing silica. It has been shown that PDMPO's preferred residing location of interaction is within the Stern layer when bound to silica under aqueous conditions which affects its excited state dynamics and chromaticity (Parambath et al., 2016). When PDMPO is excited, two excited/protonation states of PDMPO, $(\text{PDMPOH}_2)^{2+}$ and PDMPOH^+ , are observed which are hugely dependent on the surrounding pH and silica particle size (Parambath et al., 2016).

CSLM (Minsky, 1961; Minsky, 1988), a fluorescence microscope, allows the detection of fluorescence of a slice through the thickness of specimen making it a useful and non-invasive technique. CSLM is also capable of spectral imaging. Along with capturing images of a specimen with the fluorescence intensity data, the fluorescence emission spectrum (spectroscopic data in form of wavelength scans) is also collected which accompanies the images. On top of this, both the fluorescence intensity data and fluorescence emission spectrum of each pixel of the captured image can be individually analysed.

To develop the surface charge mapping technique, the relationship between zeta (ζ)-potential and fluorescence from PDMPO dye against the feature size of silica nanoparticles were explored. Hence, the technique is based on a calibration that uses zeta (ζ) potential from Stöber silica nanoparticles and emission ratios of PDMPO on

Stöber silica nanoparticles which when applied to the CSLM images through a ratiometric approach will provide local surface charge information on the biosilica features of a sample. As examples, the technique has been applied to study composite mixed silica structures produced by silicifying plant and diatoms.

Combining the calibration and CSLM's capability of spectral imaging allowed for the determination and quantification of the local surface charges of different biological samples found in nature. In addition to the chemical properties of biogenic silica nanostructures etc. providing beneficial information on the biosilicification process, this methodology also enables information on their structural/topographical information. An estimation of the relative size of silica structures can be made from the zeta potential values where a higher negative zeta potential means larger size of silica structure. Hence, the developed method was aimed at studying the chemical features as well as the structural features of a specimen.

4.1.1. Biologically relevant tissues

Equisetum species such as *Equisetum arvense* (horsetail) are ancient land plants and known biosilicifiers as they take up and accumulate patterned silica in different regions of plant. In addition, these silicified structures are built from spheres ranging from 5 – 120 nm in size (Perry and Fraser, 1991). A research done by Law and Exley, 2011 looked at silica depositions in different regions of the plant including rhizome, stem, leaf and spores where numerous silicified structures such as cell wall, cell plates, plasmodesmata, guard cells and stomata at varying stages of differentiation were reported through the aid of PDMPO dye using CSLM. Since it had been shown that PDMPO accumulated into the different areas of *Equisetum arvense* containing silica, the use of *Equisetum arvense* formed the starting point to explore and test the newly developed surface charge mapping technique on living tissue.

Diatoms are silicifying organisms which are unicellular and photosynthetic eukaryotes. The size of most diatom species ranges from 2 to 200 μm (Stoermer and Julius, 2003; Werner, 1977). Diatom cell walls consists of inorganic and organic components where around 97% of the cell wall is inorganic compounds (as almost pure hydrated amorphous

silica also ranging from nano- to micro-meter in size) (Kröger et al., 2000). The patterns of silica within cell wall with pores is termed as frustules where the patterning of the silica structures is species-specific and only seen replicated in diatom progeny (Sumper and Kröger, 2004). There are two general classes of diatoms which are based on their overall shape: Centrics (radially symmetrical) and Pennates (bilaterally symmetrical). The distal (towards the outside) frustules can be further classified into two interlocking parts, valves and griddle bands, that make up the cell wall of diatoms. To extend the use of the newly developed surface charge mapping technique on living tissue, different diatoms were also studied.

4.2. Development of the surface charge mapping method

The initial method development (calibration plot) was carried out by a previous colleague, from the research group which was applied to a non-living sample of *Equisetum arvense* (also included in this chapter – Figure 4.7) (Parambath, 2016). Production of a calibration plot was used as a tool for the analysis of the ratiometric imaging obtained from CSLM to study the surface charge density on silica. The adaptation of the techniques to different living samples and refining the image processing method through ImageJ was carried out in this PhD research.

4.2.1. Silica nanoparticle synthesis and characterisation

The first step was the preparation of silica nanoparticles (SNPs) through a modified Stöber process (Stöber et al, 1968; Roach et al, 2006). Stöber process is a sol-gel method which consists of the hydrolysis of silica precursor to form silicon hydroxide $\text{Si}(\text{OH})_4$ followed by their condensation into oligomers leading to formation of silica nanoparticles (Brinker and Scherer, 1990). The synthesised SNPs were then characterised for their sizes based on an average of multiple dynamic light scattering measurements. Differently sized SNPs with diameters of 22.0 ± 0.45 nm, 33.0 ± 1.4 nm, 55.0 ± 2.1 nm, 77.0 ± 1.2 nm and 133.0 ± 0.8 nm were selected.

4.2.2. Production of the calibration plot for surface charge mapping method development

There were a couple of steps involved in the surface charge mapping method development for determining the local surface charges which are briefly explained and discussed below.

a. Characterising silica-PDMPO interactions with varying sizes of SNPs

Spectroscopic data was collected for the interactions of each size of SNPs with PDMPO at pH 7.0 using CSLM. Using a 405 nm laser diode line for excitation of PDMPO dye, an xy plane with maximum fluorescence intensity corresponding to the PDMPO's interaction with SNPs along the z-axis was selected. The fluorescence emission intensity data and its associated fluorescence emission spectrum was collected from 420-650nm at room temperature which was subsequently used to study the behaviour of PDMPO with differently sized SNPs. For this purpose, point-by-point procedure was adapted where the fluorescence emission spectra of selected regions of the collected images were used. The spectra were fitted and decomposed by least squares minimisation into components corresponding to peaks of $(\text{PDMPOH}_2)^{2+}$ and PDMPOH^+ , the two excitation states of PDMPO. The relative amounts of $(\text{PDMPOH}_2)^{2+}$ and PDMPOH^+ estimated by this procedure was associated with the differently sized SNPs. For each SNPs, their corresponding zeta potential (ζ) was also measured using a MALVERN nanos Zetasizer at 25°C which was compared against the measured PDMPO (fluorescence) emission ratio $((\text{PDMPOH}_2)^{2+}/\text{PDMPOH}^+)$.

Since the surface charge properties of SNPs have been shown to be dependent on the size of the nanoparticle (Barisik et al., 2014), an increase in the negative zeta potential values was seen with increasing diameter of SNPs from 22 nm to 133 nm. This can be explained because of surface acidity of SNPs which increases with increasing diameter of SNPs (due to the increased silanol groups (Si-OH)) especially for SNP greater than approximately 10 nm in diameter (Puddu and Perry, 2013). With surface acidity being an indicator of the zeta potential, increased surface acidity then affects the interactions of PDMPO with SNPs through increasing the PDMPO emission ratio

$((\text{PDMPOH}_2)^{2+}/\text{PDMPOH}^+)$. Hence, the relationship between the PDMPO emission ratio and the zeta potential related to the differently sized SNPs were explored for the surface charge mapping analysis.

b. Effects of a charge neutralisation agent on a singly sized SNP

It was also shown that the behaviour observed for the PDMPO's interactions above was solely due to the variations in the surface charge and not size related effects of SNPs. A charge neutralisation experiment was carried out which utilised a varying amount of a chaotropic agent, guanidine hydrochloride (GHCl) with a fixed concentration of PDMPO dye and a singly sized SNP (133 nm) at pH 7.0 under room temperature. An increase in the zeta potential was observed with an increasing GHCl concentration as GHCl led to surface charge neutralisation of SNPs due to increased cation concentration disrupting the PDMPO's interaction (Salis et al., 2016) which can also be illustrated using the electrical double layer shown in Figure 4.1. A concentration dependent shift in the PDMPO emission ratio $((\text{PDMPOH}_2)^{2+}/\text{PDMPOH}^+)$ was observed with GHCl which demonstrated that the surface charge measurements are dependent on the PDMPO emission ratio and independent of the size and morphology of the SNPs. For each of the GHCl concentrations, CSLM fluorescence images along with the spectroscopic data were collected, processed and fitted in the same manner as the data was analysed for the study of the interactions of each SNP with PDMPO. For each of the GHCl concentration used (same composition as before but without PDMPO dye), their corresponding zeta potential was also measured using a MALVERN nanos Zetasizer at 25°C which was compared against the estimated PDMPO emission ratio $((\text{PDMPOH}_2)^{2+}/\text{PDMPOH}^+)$.

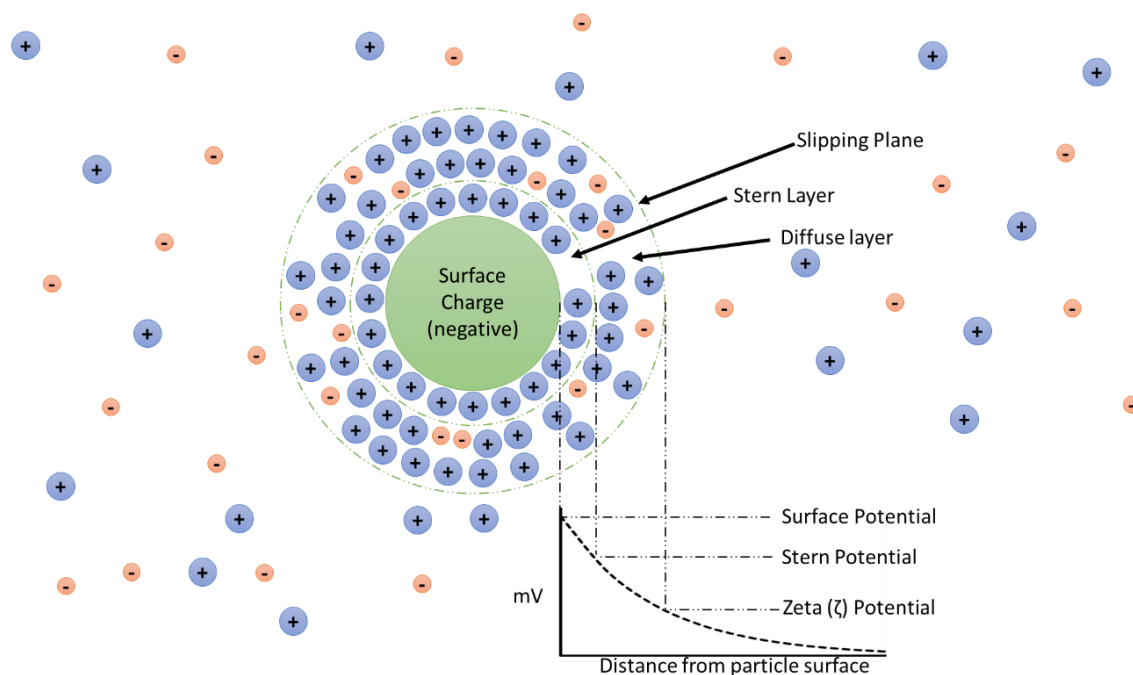


Figure 4.1 – Electrical double layer around a negatively charged particle surface.

Adapted and modified from Williams, 2016.

c. Integration of the PDMPO emission ratios to derive a calibration plot

From the above experiments, it was concluded that PDMPO could be used to study the local surface charge properties of a sample by using a fixed pH and monitoring PDMPO's fluorescence emission behaviour. Hence, the PDMPO emission ratio $((\text{PDMPOH}_2)^{2+}/\text{PDMPOH}^+)$ obtained for both the differently sized SNPs and effects of GHCl on a singly sized SNP through the analysis of their spectroscopic and imaging data obtained from CSLM and the zeta potential determined experimentally for the corresponding SNPs were used to produce the calibration plot of the zeta potential (ζ) values against the collective values of PDMPO emission ratio $((\text{PDMPOH}_2)^{2+}/\text{PDMPOH}^+)$ in log scale as shown in Figure 4.2 (left graph). This calibration plot was then used as a tool for surface charge mapping to measure the local surface charge of various samples. Figure 4.2 (right graph) also shows the relationship of zeta potential (ζ) against the differently sized SNPs.

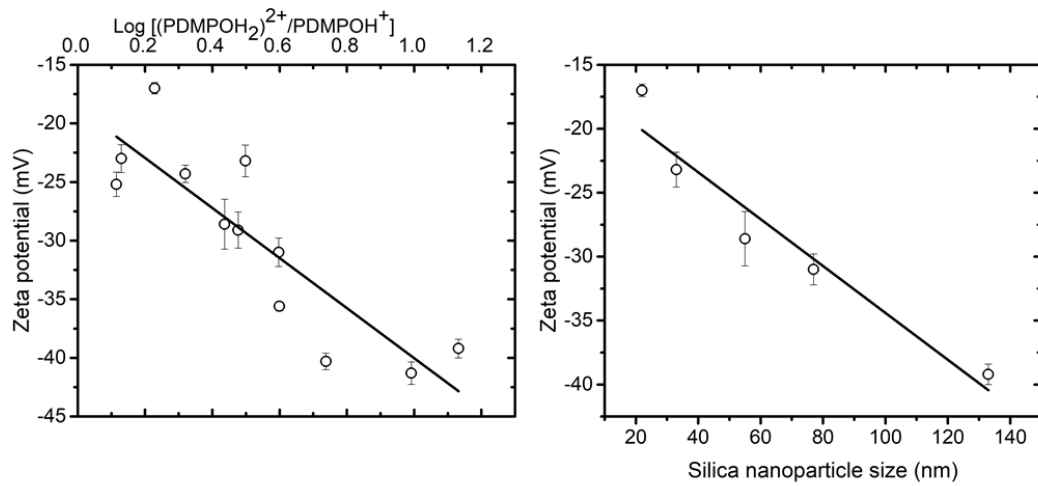


Figure 4.2 – Left: Calibration plot - zeta potential (ζ) against log of PDMPO emission ratio ($(\text{PDMPOH}_2)^{2+}/\text{PDMPOH}^+$), Right: Zeta potential (ζ) against the size (as diameter) of SNP

4.2.3. Calibration plot and related equations

The logarithm of PDMPO emission ratio ($(\text{PDMPOH}_2)^{2+}/\text{PDMPOH}^+$) followed an approximately linear relationship/correlation against zeta potential (ζ) (see Figure 4.2 left graph and Equation 4.1)

$$\zeta = -21.34 \text{ mV} \log \frac{[\text{PDMPOH}_2^{2+}]}{[\text{PDMPOH}^+]} - 18.67 \text{ mV} \quad (4.1)$$

Here, PDMPOH^+ and $(\text{PDMPOH}_2)^{2+}$ are derived from the fluorescence data as a ratio and form a representation of their ion's concentrations. The protonation equilibrium is $\text{PDMPOH}^+ + \text{H}^+ \rightleftharpoons (\text{PDMPOH}_2)^{2+}$.

It is noted that the protonation equilibrium is related to the potential, E , on the surface where the fluorophore adsorbs which can be explained by the Nernst equation (Equation 4.2). This understanding explained below was developed by another colleague, Dr. Igor Efimov, from the research group.

$$E = E^0 - \frac{2.3RT}{F} \log \frac{[\text{PDMPOH}_2^{2+}]}{[\text{PDMPOH}^+]a_{\text{H}^+}} \quad (4.2)$$

Here, E represents the surface potential at a given time with E^0 being the standard surface potential, R is the gas constant ($8.3144 \text{ J K}^{-1} \text{ mol}^{-1}$), T is the room temperature in Kelvin (K), F is the Faraday constant (96.5 kJ mol^{-1}) and a_{H^+} is the activity of protons (which is 1 for H^+). Also, $2.3RT/F$ is $\approx 60 \text{ mV}$ at room temperature.

Since the experimentally accessed zeta (ζ) potential is measured at the slip-plane, two boundary conditions can be considered: (i) if the slip-plane coincides with the surface of the particle, then $\zeta = \delta E$ and (ii) if the slip plane is infinitely remote from the surface, $\zeta = 0$. Between these two boundaries, ζ is a fraction $0 < \alpha < 1$ of the actual surface potential in Equation 4.2 which is constant to a first approximation with a particular value $\alpha = 0.36$ ($21.34/60=0.36$).

Upon integration of Equations 4.1 and 4.2, Equation 4.3 is obtained.

$$\zeta - \varphi^0 = -\alpha \frac{2.3RT}{F} \log \frac{[\text{PDMPOH}_2^{2+}]}{[\text{PDMPOH}^+]} \quad (4.3)$$

where all values except the concentrations of PDMPO species are included in φ^0 .

In cases where $[(\text{PDMPOH}_2)^{2+}] = [\text{PDMPOH}^+]$, the change in surface potential (and consequently surface charge) is equal to zero. The zeta potential that corresponds to this condition, can be called the zeta potential of zero charge, equals -18.67 mV . This means that there is preferable orientation of the dipoles of water molecules, facing the silica surface with hydrogen forming chemical bonds, and bulk solvent with oxygen, which results in the measured double layer jump.

The significance of Equation 4.3 is that it provides a theoretical basis for the proposed method. Usually, zeta potential is expressed through bulk concentrations of absorbing charged species. However, since their surface concentration is not known, only model-based assumptions are possible. For strong electric fields, for example the Stern layer, any model approximations fail and there is typically limited agreement with experiment. In the proposed method, the ratio of concentrations of adsorbed species is accessed directly, without any model assumptions.

4.3. Chemicals and Materials

PDMPO (LysoSensor™ yellow/blue DND-160, 1 mM in dimethyl sulfoxide) was obtained from Life Technologies. Type 1 grade water was used. The reagent ethanol, concentrated nitric acid, concentrated sulfuric acid, monobasic potassium phosphate monohydrate and dibasic potassium phosphate were obtained from Sigma-Aldrich.

Disposable glass coverslips (multiple) and microscope glass slides (Sail brand) were used. 96 microwell glass bottom black plates (Nunc 164588) were obtained from Nunc.

Plant material, *Equisetum arvense* and river water samples were collected locally from Nottingham Trent University. *Coscinodiscus Wailesii* diatoms were commercially sourced.

4.4. Experimental methodology

4.4.1. Scanning Electron Microscopy

Scanning Electron Microscopy (SEM) imaging of *Equisetum arvense*'s spores was conducted using a JEOL 7100FEG SEM. Samples were mounted on an aluminium stub with adhesive carbon tape (TAAB Laboratories, Aldermaston, UK) for imaging.

4.4.2. CSLM and experimental parameters

The CSLM used was from Leica microsystems (Leica TCS SP5 II) which is based on an inverted geometry. CSLM experiments were conducted using either a 96 microwell glass bottom black plate (Nunc 164588) or microscope slides and glass coverslips. Since the zeta potential is also affected by pH, the pH was kept similar to the living sample's pH. pH 7 was used as the cell walls of both plant and diatoms exhibit near to neutral pH. This then allowed for a comparison of differently sized silica structures in the same local environment. After the samples had been treated with PDMPO, they were subjected to CSLM.

A 405 nm laser diode line was used for excitation of PDMPO dye. The instrumental parameters that were kept the same throughout the imaging experiment of any one sample were as follows: the numerical aperture (0.5 or 0.7 NA), objective (Leica HCX PL Fluotar 20x or 63x), pinhole size (63 μm), photomultiplier tube (PMT) gain (up to 1250 V), offset (2.7 %), 4096 x 4096 or 8192 x 8192 pixels and a laser intensity (up to 100 %). For the purpose of this research, a different mode of image acquisition was adapted which was based on whole image analysis. The fluorescence emission intensity data was collected using CSLM with a 10 nm bandwidth for each of the wavelength scan ranges of 460-470 nm and 500-510 nm corresponding to peaks of PDMPOH^+ and $(\text{PDMPOH}_2)^{2+}$ respectively. For CSLM image acquisition for surface charge measurements and determination, either an xy plane with the maximum fluorescence intensity along the z-axis or stacks of xy planes along the z-axis were studied for different samples at room temperature.

To be able to utilise this surface charge mapping approach using intact biological tissues containing a range of other components such as carbohydrates, proteins and lipids etc. as well as silica, a fluorescence emission spectrum over the range of 420-600 nm was collected for each sample analysed to rule out the possibility of any other contributions and to ensure that the observed fluorescence is solely due to PDMPO prior to analysing them for producing the zeta potential images included in this chapter. This was more of a problem with plant materials as they also contain chlorophyll which is known to exhibit fluorescence. Hence, the fluorescence emission spectrum of chlorophyll was studied to confirm that it did not affect the analysis.

4.4.3. Processing the fluorescence emission intensity data collected using CSLM

The point-by-point decomposition procedure used for the spectral data during the derivation of the calibration plot was effective as specific regions of interest needed to be analysed to obtain the PDMPO emission ratio ($(\text{PDMPOH}_2)^{2+}/\text{PDMPOH}^+$). However, this mode of analysis when dealing with larger scale surface charge mapping is inconvenient and time consuming. Hence, a different mode of analysis needed to be sought to perform whole field local surface charge mapping. For this, two spectral images were collected using CSLM at different wavelengths corresponding to peaks of

PDMPOH⁺ and (PDMPOH₂)²⁺ to compute the PDMPO emission ratio which was then converted to surface charge units (zeta potential, ζ - mV). Since the exemplary samples used had not undergone any surface charge neutralisation, the measured local surface charge was a surrogate for local topography with the charge map indicating silica structures of different lengths.

The greyscale (fluorescence images captured at wavelength scan ranges of 460-470 nm and 500-510 nm corresponding to PDMPOH⁺ and (PDMPOH₂)²⁺ respectively) and bright field images collected were 16-bit images. The local surface charge measurements and assessment were achieved by ratiometric processing of the images obtained from CSLM. The processing of the images was obtained using ImageJ v1.50c. To improve the signal-to-noise ratio of the images, both the greyscale and bright field images were binned (adjusted to a size of 4096 x 4096 (if not already that size)), despeckled and filtered (4x4 Gaussian blur). The greyscale image at 500-510 nm was then divided by the greyscale image at 460-470 nm with subsequent application of the Log function and transformation into surface charge units (zeta potential, ζ - mV) using the Equation 4.1 obtained from the calibration plot shown in Figure 4.2 left graph.

To further refine the ratiometrically processed image, thresholding of the region of interest using the greyscale images was carried out which were then accounted for to produce the final ratiometrically processed images displayed in this chapter. Thresholding excludes the undesired regions detected within the images and improves the quality of the image and its analysis. The final ratiometrically processed image was colour mapped for the surface charge units (as zeta potential, ζ - mV) and the brightness and contrast of the image adjusted to obtain maximal structural features and information etc. A calibration bar representing the mapped colour is presented on the images. A scale bar as a visual indication of the size of features in the image has also been included. The greyscale images obtained after the improvement of signal to noise ratio were also colour mapped to blue and green for images at 460-470 nm and 500-510 nm corresponding to PDMPOH⁺ and (PDMPOH₂)²⁺ respectively. These false coloured images are included in this chapter to represent the fluorescence emission intensity from the two excited states of PDMPO.

4.5. Background fluorescence

To perfect this surface charge mapping method to effectively study the surface charge properties only without interferences from the confocal scanning laser microscope setup, additional data collection was carried out to confirm if any background fluorescence caused interferences that affected the ratiometric processing of the images. For this, the fluorescence emission intensity data and its associated fluorescence emission spectrum was collected from 420 - 600nm at room temperature. The following were studied:

- Microscope glass slide
- Microscope glass slide with glass coverslip
- Microscope glass slide with water
- Microscope glass slide with PDMPO

For water and PDMPO, aliquots were spotted onto the microscope glass slide which were covered by coverslip before image acquisition.

4.6. Exemplary samples for surface charge mapping

The surface charge mapping approach was applied to different living organisms to study and characterise the nature of silica structures of the heavily silicified plant and diatoms. The following were used as examples: Plant (*Equisetum arvense* – different parts of the branch) and Diatoms (*Coscinodiscus Wailesii*, *Cylindrotheca Closterium*, *Diatoma mesodon* and *Diatoma vulgaris bory*).

The concentration used for the PDMPO was 0.5 μM or 1 μM for the incubation of samples for surface charge mapping as previous studies using a concentration of 0.125 μM to 1 μM was shown to be enough for effective staining (Law and Exley, 2011; Shimizu et al., 2001). Initially, other lower concentrations of PDMPO were also tested using *Equisetum arvense* (data not used). To ensure effective staining, 0.5 μM and 1 μM concentrations were finally adopted for the living and non-living samples respectively.

4.6.1. *Equisetum arvense*

a. Collection and cultivation of *Equisetum arvense*

At start, several different samples of *Equisetum arvense* were sampled from the field of Clifton Campus, Nottingham Trent University. The samples were transferred to a pot which were placed under room temperature condition (25°C) next to a window towards south-west. The pots were watered daily to secure excessive wet conditions. Within the first week after sampling, stems started to appear. During the second to third week, new green stems started to grow for photosynthesis and produced fertile spore heads. After one to two months, the plants accomplished sporulation and moved into vegetative growth. During this period when the plants were growing most optimally, fluorescence microscopy of bio-inorganic structuring in branches of fully developed stems was started. Later in time depending on the need for the experiments, further *Equisetum arvense* samples were collected locally which had already developed stems including branches and were used straight away.

The silica samples of *Equisetum arvense* were studied both as intact plant material (living) and extracted silica from the plant material (non-living).

b. Sample preparation of non-living plant sample

A stem of *Equisetum arvense* plant was acid treated to remove the organic cell wall components with a mixture of 4:1 v/v of concentrated nitric and sulfuric acid (Perry et al., 1990). The sample was heated at 100°C for 24 hours, washed to remove the acid mixture and lyophilised. The extracted silica samples for imaging were treated with a solution of 1.0 µM PDMPO in 0.1 M Phosphate Buffer (pH 7.1) followed by an incubation with shaking (60 min, 10 RPM) at room temperature. Aliquots were spotted onto the microscope glass slide which were covered by coverslip before image acquisition.

The sample was then subject to CSLM imaging to capture the greyscale and bright field images followed by their treatment and processing for their local surface charge measurements as described in section 4.4.3.

c. Sample preparation of intact plant material

There were two methods utilised for the sample preparation of the living samples of *Equisetum arvense* (ca. 3mm diameter).

1. A small part of the stem of *Equisetum arvense* was submerged in an aqueous solution of 0.5 μM PDMPO for up to a period of 24-48 hours at room temperature. It was expected that the stem will uptake PDMPO from the solution due to transpiration process of the plants. The sample was removed and fixed onto a glass coverslip with the support of a coverslip holder. The sample was placed perpendicular to the optical axis.
2. A small part of the stem of *Equisetum arvense* was cut longitudinally and the sample was fixed onto a glass coverslip with the support of a coverslip holder. The sample was then immediately submerged in an aqueous solution of 0.5 μM PDMPO for up to a period of 24 hours at room temperature. The sample while submerged in the aqueous PDMPO was placed perpendicular to the optical axis.

The samples were then subject to CSLM imaging to capture the greyscale and bright field images followed by their treatment and processing for their local surface charge measurements as described in section 4.4.3.

Although the two sample preparation methods explained above were both used and are feasible options, it was found that the second method (which involved cutting the sample and submerging it into aqueous PDMPO while imaging) showed an improved uptake of PDMPO into the cellular compartments. This in turn led to capturing images with enhanced details of the silicified structures when processed for the surface charge mapping. Therefore, the method 2 was selected over the method 1 which was then used for the time dependent behaviour of PDMPO uptake and further image collections for zeta potential analysis.

For spore analysis, aqueous 0.5 μM PDMPO was added to the plant pot during the time when spore heads started to appear. Samples were collected after 2-4 weeks for surface charge measurements using CSLM.

d. Effects of chlorophyll on the surface charge mapping of *Equisetum arvense*

A stem of *Equisetum arvense* plant was chopped into small pieces and treated with 10 ml of ethanol for 4 hours at room temperature. Ethanol was used to disrupt the organic cell membrane increasing its fluidity and permeability (Goldstein, 1986; Patra et al., 2006) such that the chlorophyll could penetrate out of the cell membrane. After incubation, the ethanol containing the chlorophyll was aliquoted into a well of a 96 microwell glass bottom black plate. A fluorescence emission spectrum from 440 – 850 nm at room temperature using CSLM was studied to determine if the fluorescence from the chlorophyll (Maxwell and Johnson, 2000) interferes with the charge mapping of plant sample, *Equisetum arvense*.

e. Time dependent behaviour of PDMPO uptake into *Equisetum arvense*

Using the second method of sample preparation explained earlier in this section, a sample of *Equisetum arvense* was exposed to water followed by an aqueous solution of 0.5 μM PDMPO. Initially, an xy plane along the z-axis of the sample (while in water) was located and fluorescence emission intensity images at each wavelength range were collected along with a fluorescence emission spectrum over the range of 420-600 nm at room temperature. The water was then replaced with the aqueous solution of PDMPO. Further CSLM imaging was similarly acquired after 2, 4 and 22 hours of PDMPO exposure.

4.6.2. Diatoms

a. Collection and cultivation of diatoms

River water sample was collected and passed through 50 – 100 μm filters prior to its use for this research as soon as possible after. Examples of the diatoms collected is shown in Figure 4.3 b-d.

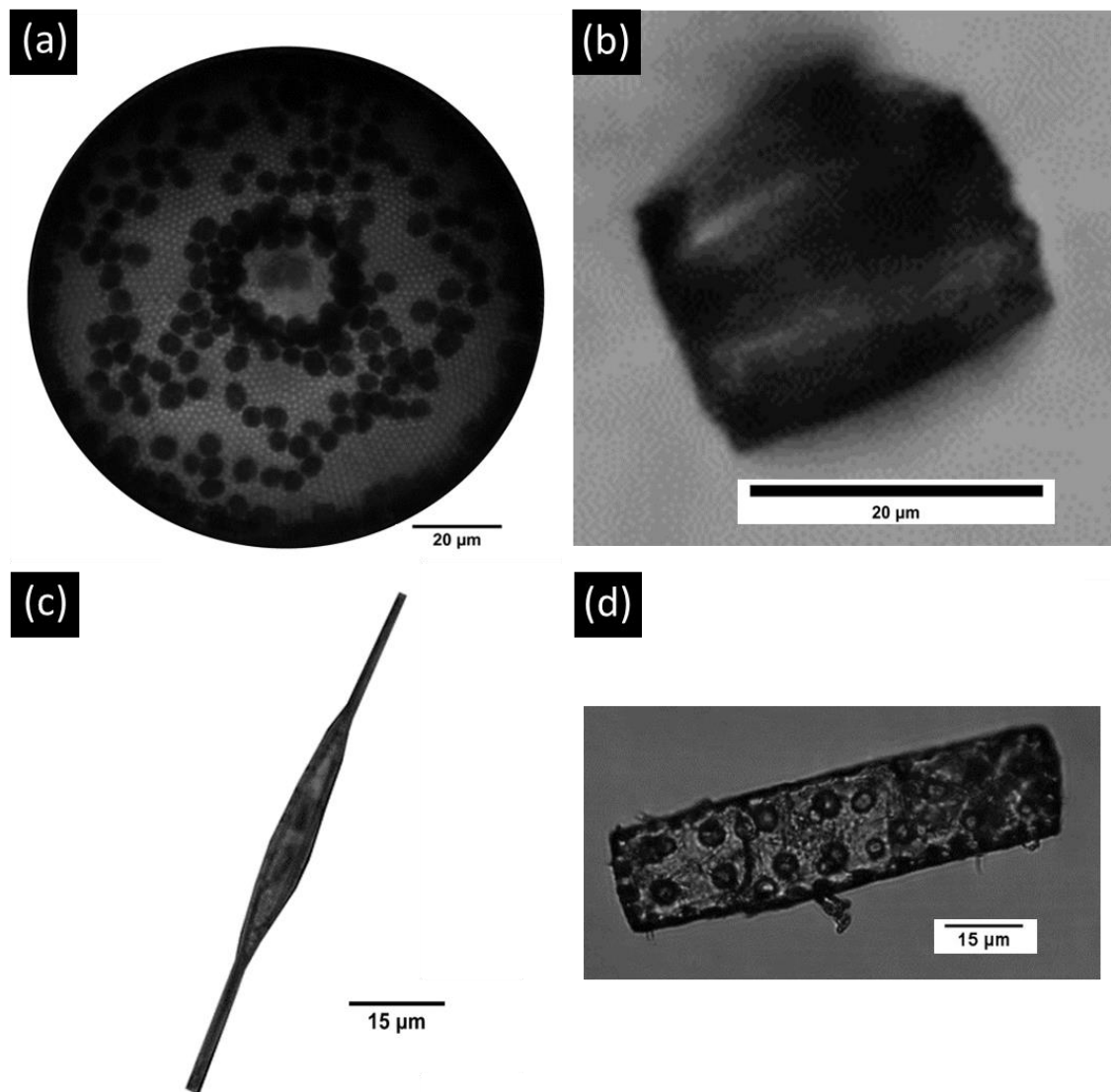


Figure 4.3 – Diatoms collected or used for the surface charge determination method. (a) *Coscinodiscus Wailesii* (b) *Diatoma vulgaris bory* (c) *Cylindrotheca Closterium* and (d) *Diatoma mesodon*

b. Sample preparation

The diatom river water sample or the *Coscinodiscus Wailesii* sample (see Figure 4.3 a) were prepared in a way such that a final concentration of 0.5 μM PDMPO in an aqueous solution was used. The samples were incubated for up to a period of 72 hours at room temperature. It has been demonstrated previously that diatoms deposit fluorescent dye, Rhodamine 19, within the cell walls of the rapidly replicating diatom cells within days (Kucki and Fuhrmann-Lieker, 2011); however, other modes such as internalisation by endocytosis can also be applicable as previously seen with another fluorescent dye, FM1-43 (Kühn and Brownlee, 2005). The samples were then subject to CSLM imaging to capture the greyscale and bright field images followed by their treatment and processing for their local surface charge measurements as described in section 4.4.3.

4.7. Results and Discussion

Zeta potential images with data analysis and key findings are included in this section.

4.7.1. Background fluorescence

Background fluorescence emission intensity data analysis of the empty CSLM (Figure 4.4 1 a-b), glass coverslip (Figure 4.4 2 a-b), water (Figure 4.4 3 a-b) and PDMPO (Figure 4.4 4 a-b) using a microscopic glass slide led to a confirmation that the instrument, materials and reagents (except PDMPO) used within the experiments have no contributory effect towards the fluorescence observed for the surface charge mapping images. Figure 4.4 1c, 2c, 3c and 4c show their corresponding brightfield images. Figure 4.4 graph 5 also displays the fluorescence emission spectrum for each of the tests above and the background fluorescence seen from CSLM, glass coverslip and water are stable throughout the fluorescence emission spectrum range. Therefore, no contributions were observed that would affect the method implementation to study the surface charge properties. The fluorescence emission spectrum for PDMPO was used as a comparison for the ones obtained for the images acquired for the surface charge mapping determinations.

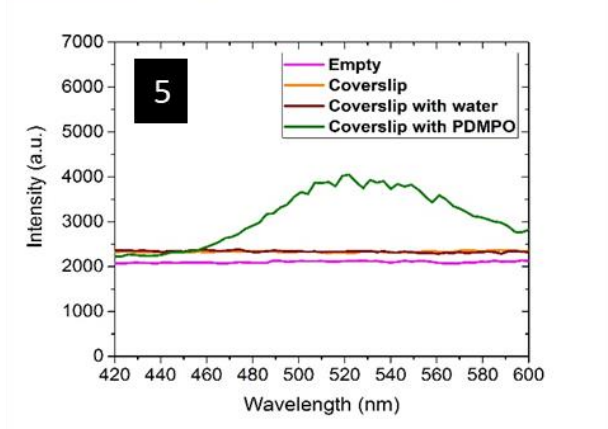
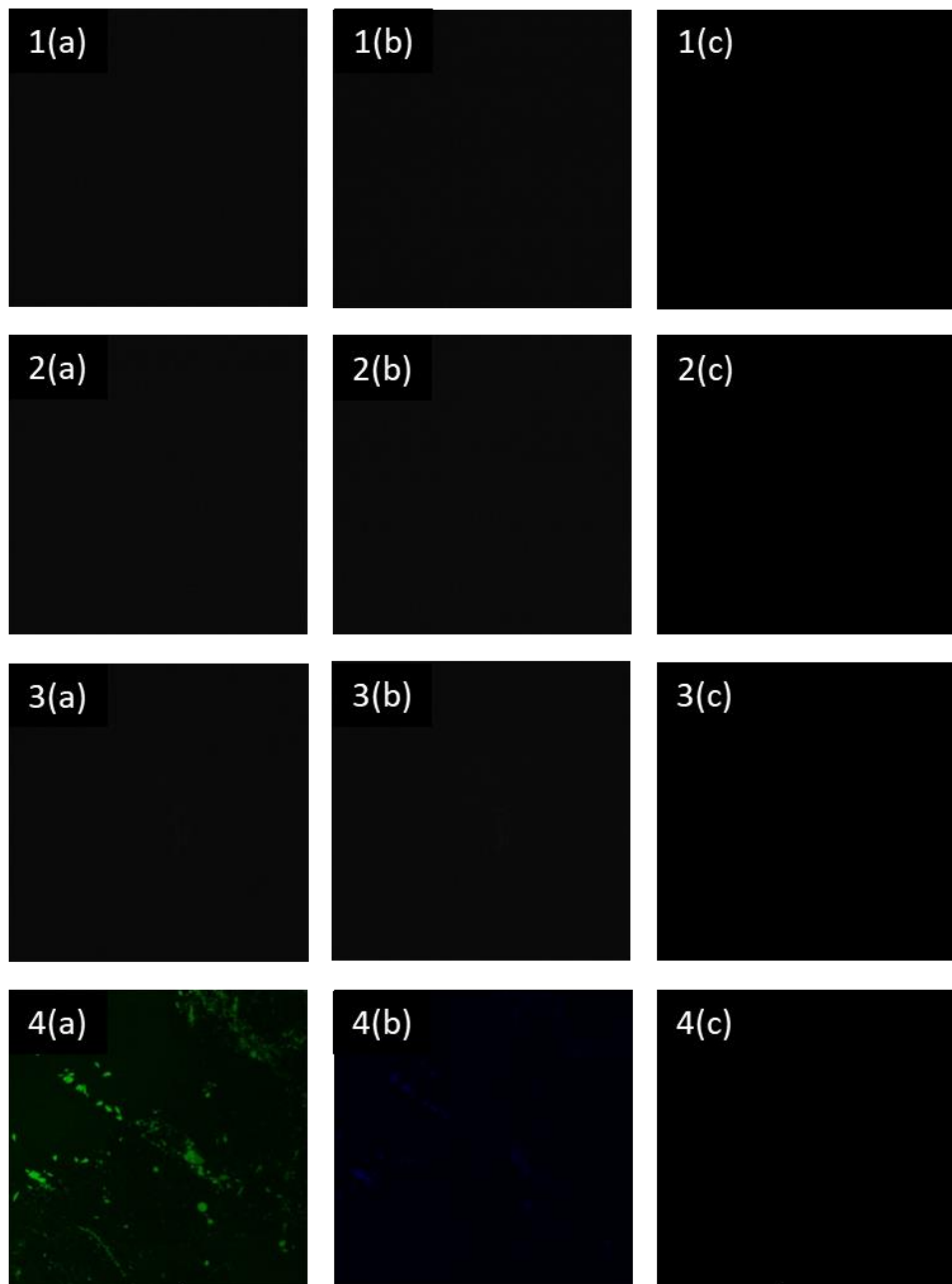


Figure 4.4 – Functional images showing the background fluorescence intensity under different circumstances within the confocal scanning laser microscope used.

Continued on next page

(a) $(\text{PDMPOH}_2)^{2+}$ imaging with data collected over the wavelength range 500-510 nm, (b) PDMPOH^+ imaging with data collected over the wavelength range 460-470 nm and (c) bright field image of same sample.

1 shows the background within the empty confocal scanning laser microscope (always present), 2 shows the fluorescence with a coverslip used for the experimentations, 3 shows fluorescence with water, 4 shows the fluorescence with PDMPO and 5 shows a graph displaying the varying fluorescence intensity under different circumstances in form of fluorescence emission spectrum.

4.7.2. *Equisetum arvense*

a. Effects of chlorophyll on the charge mapping of *Equisetum arvense*

From the fluorescence emission spectrum collected, two peaks at around 670 nm and 730 nm were observed (see Figure 4.5) which corresponded to chlorophyll (Pedrós et al., 2008). Since the contributions from chlorophyll start from after the wavelength of 630 nm, this confirmed that it would have no interference with the charge mapping measurements as the fluorescence emission spectrum data was collected within the wavelength scan ranges of 460-470 nm and 500-510 nm.

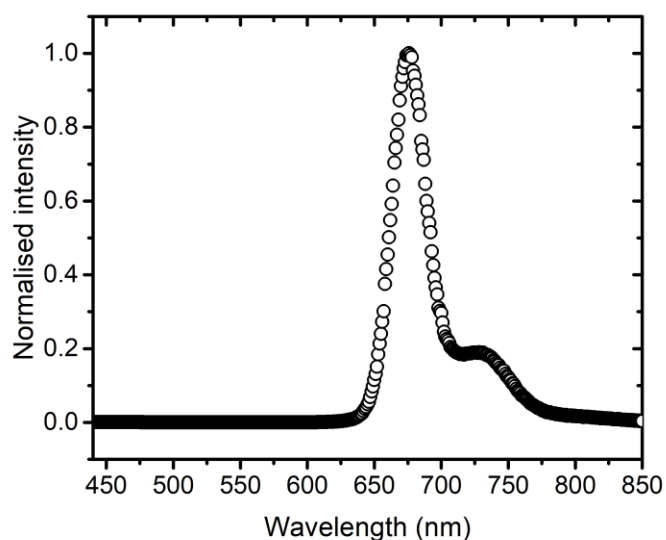


Figure 4.5 – A graph displaying the normalised fluorescence intensity in form of fluorescence emission spectrum for chlorophyll.

b. Time dependent behaviour of PDMPO uptake into *Equisetum arvense*

Studying the time dependent behaviour of PDMPO uptake into *Equisetum arvense* was a crucial step towards making an informed conclusion of smoothly transferring the application of the surface charge mapping determination method to living samples. Figure 4.6 shows the functional images illustrating the time dependent behaviour of PDMPO uptake into the stomata, star shaped rosette like structures (clustered pilulae) and a random array of pilulae covering the nodal plane of the cell wall of *Equisetum arvense*. Here, pilulae are bead-like hemispherical silica structures which are arranged in different patterns throughout. 1 shows the sample without PDMPO (in water) where any of the observed fluorescence emission spectrum is of the background present due to the CSLM (see Figure 4.6 graph 5). 2 shows the sample after two hours of PDMPO exposure where the silicified cell wall and other silicified structures start to fluoresce. This is due to the PDMPO accumulation in cellular compartments where the ratio of $(\text{PDMPOH}_2)^{2+}$ to (PDMPOH^+) are highly dependent on the surrounding pH and the particle size of silica. 3 and 4 show the sample after 4 and 22 hours of PDMPO exposure respectively. A visual increase in the fluorescence emission intensity is observed over time (see Figure 4.6 2 a-b, 3 a-b and 4 a-b). Figure 4.6 graph 5 displays the behaviour of PDMPO uptake through fluorescence emission spectrum where an increase in the fluorescence intensity is clearly seen. This confirms that the whole living tissue samples of *Equisetum arvense* are capable of up taking PDMPO depending on the silica nanostructures. Thus, this confirms that the surface charge mapping is a useful technique and can be applied to various other organisms.

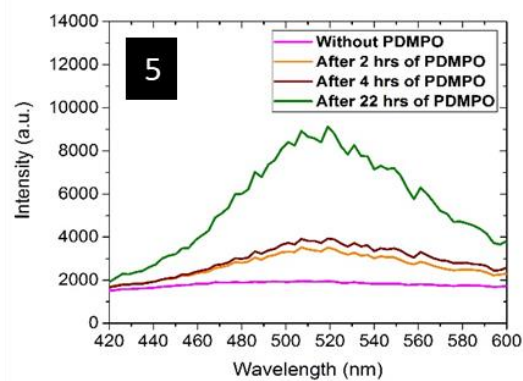
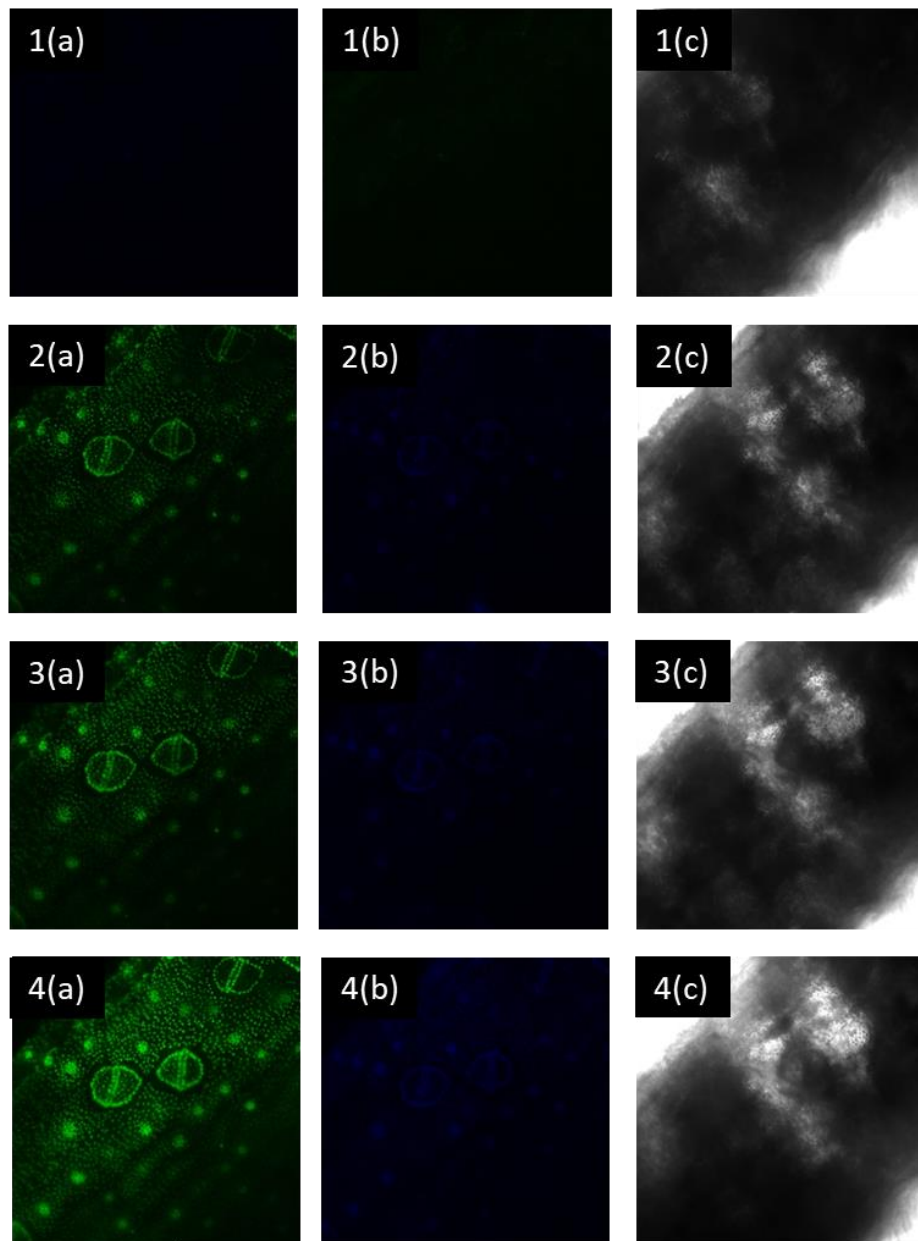


Figure 4.6 – Functional images illustrating the time dependent behaviour of PDMPPO uptake into the stomata and star shaped rosette like structures within *Equisetum arvense*.

Continued on next page

(a) $(\text{PDMPOH}_2)^{2+}$ imaging with data collected over the wavelength range 500-510 nm, (b) PDMPOH^+ imaging with data collected over the wavelength range 460-470 nm and (c) bright field image of same sample.

1 shows the sample without PDMPO, 2 shows the sample after 2 hours of PDMPO exposure, 3 shows the sample after 4 hours of PDMPO exposure, 4 shows the sample after 22 hours of PDMPO exposure and 5 shows a graph displaying the varying fluorescence intensity in form of fluorescence emission spectrum over time.

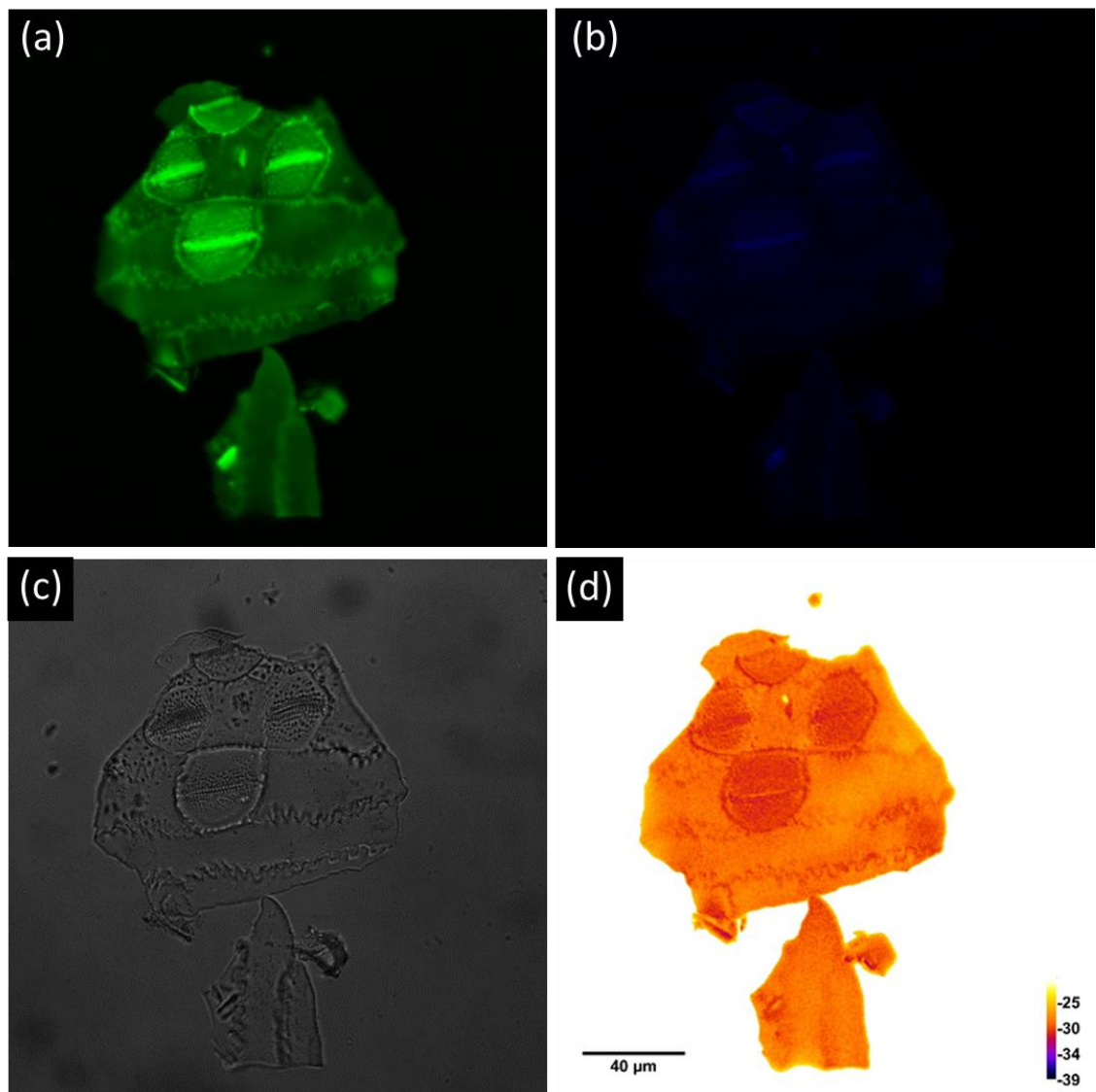


Figure 4.7 – Functional imaging of charge on stomata and ridges of *Equisetum arvense* (a) $(\text{PDMPOH}_2)^{2+}$ imaging with data collected over the wavelength range 500-510 nm, (b) PDMPOH^+ imaging with data collected over the wavelength range 460-470 nm, (c) Bright field image of same sample, (d) Zeta potential image calculated from the ratio of $(\text{PDMPOH}_2)^{2+}/(\text{PDMPOH})^+$ using ImageJ. The colours in (a) and (b) are false colours.

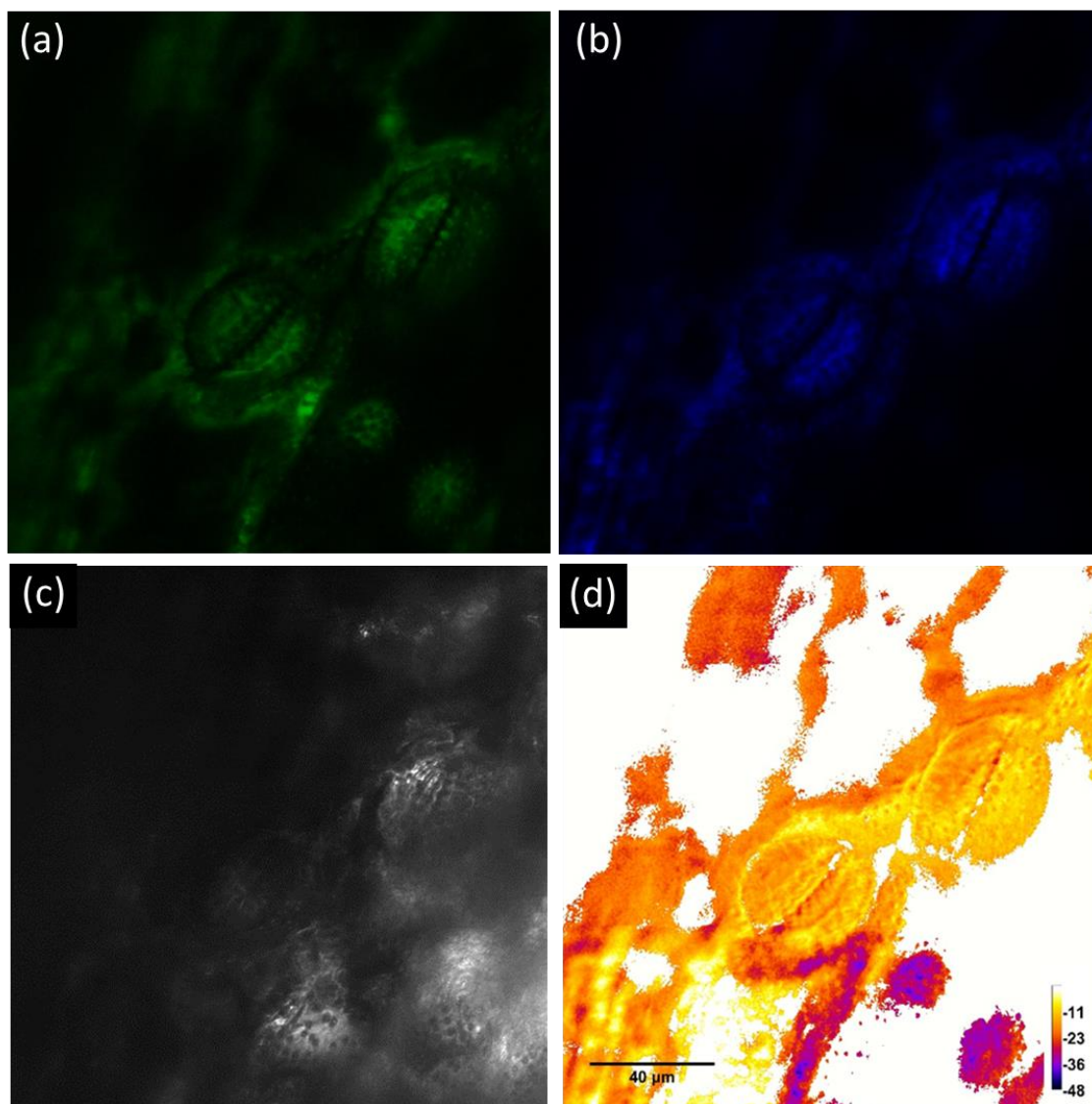


Figure 4.8 – Functional imaging of charge on stomata of *Equisetum arvense*

Sample preparation method 1 (Section 4.6.1) was used

(a) $(\text{PDMPOH}_2)^{2+}$ imaging with data collected over the wavelength range 500-510 nm, (b) PDMPOH^+ imaging with data collected over the wavelength range 460-470 nm, (c) Bright field image of same sample, (d) Zeta potential image calculated from the ratio of $(\text{PDMPOH}_2)^{2+}/(\text{PDMPOH})^+$ using ImageJ. The colours in (a) and (b) are false colours.

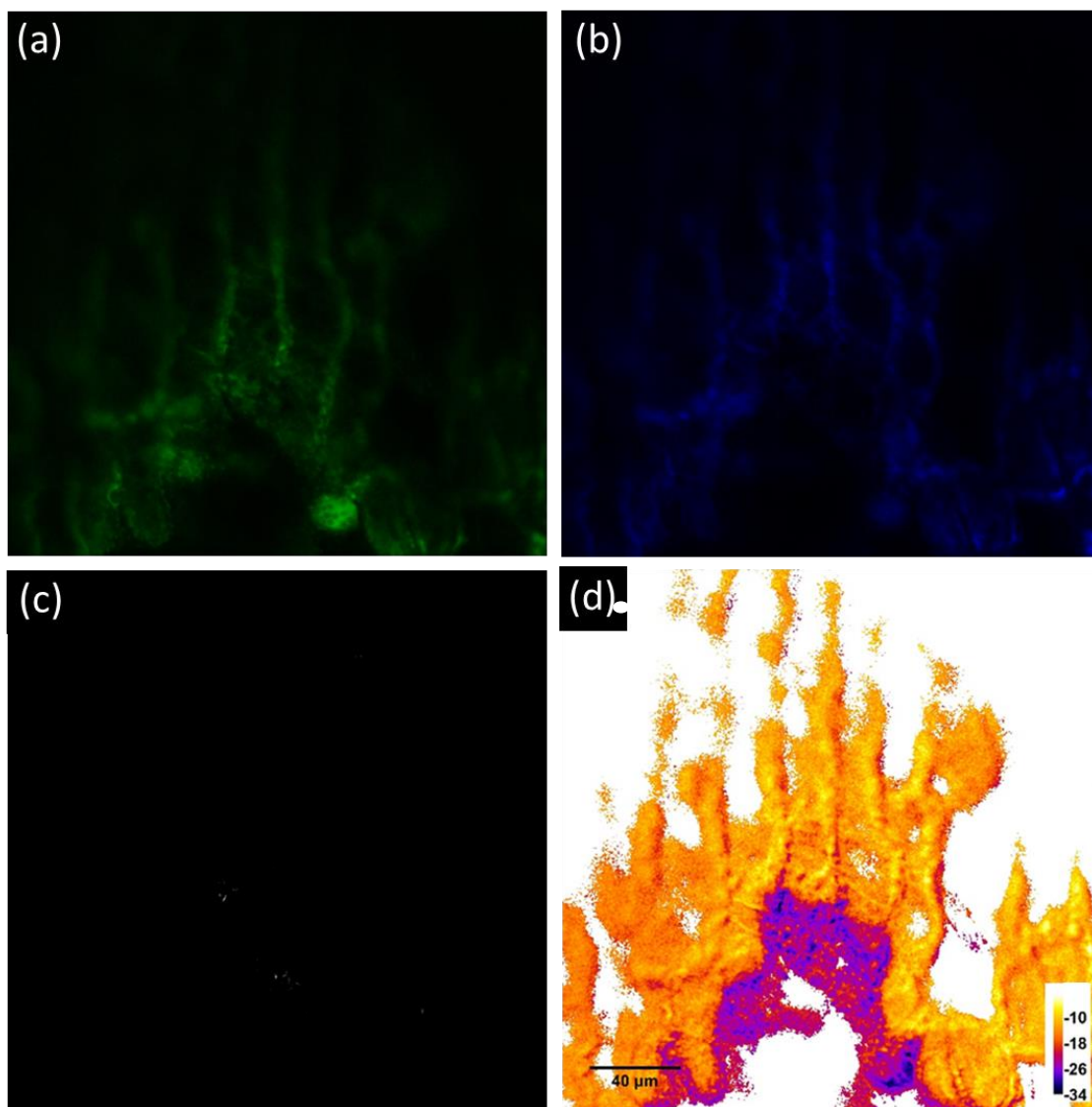


Figure 4.9 – Functional imaging of charge on stomata and ridges of *Equisetum arvense*

Sample preparation method 1 (Section 4.6.1) was used

(a) $(\text{PDMPOH}_2)^{2+}$ imaging with data collected over the wavelength range 500-510 nm, (b) PDMPOH^+ imaging with data collected over the wavelength range 460-470 nm, (c) Bright field image of same sample, (d) Zeta potential image calculated from the ratio of $(\text{PDMPOH}_2)^{2+}/(\text{PDMPOH})^+$ using ImageJ. The colours in (a) and (b) are false colours.

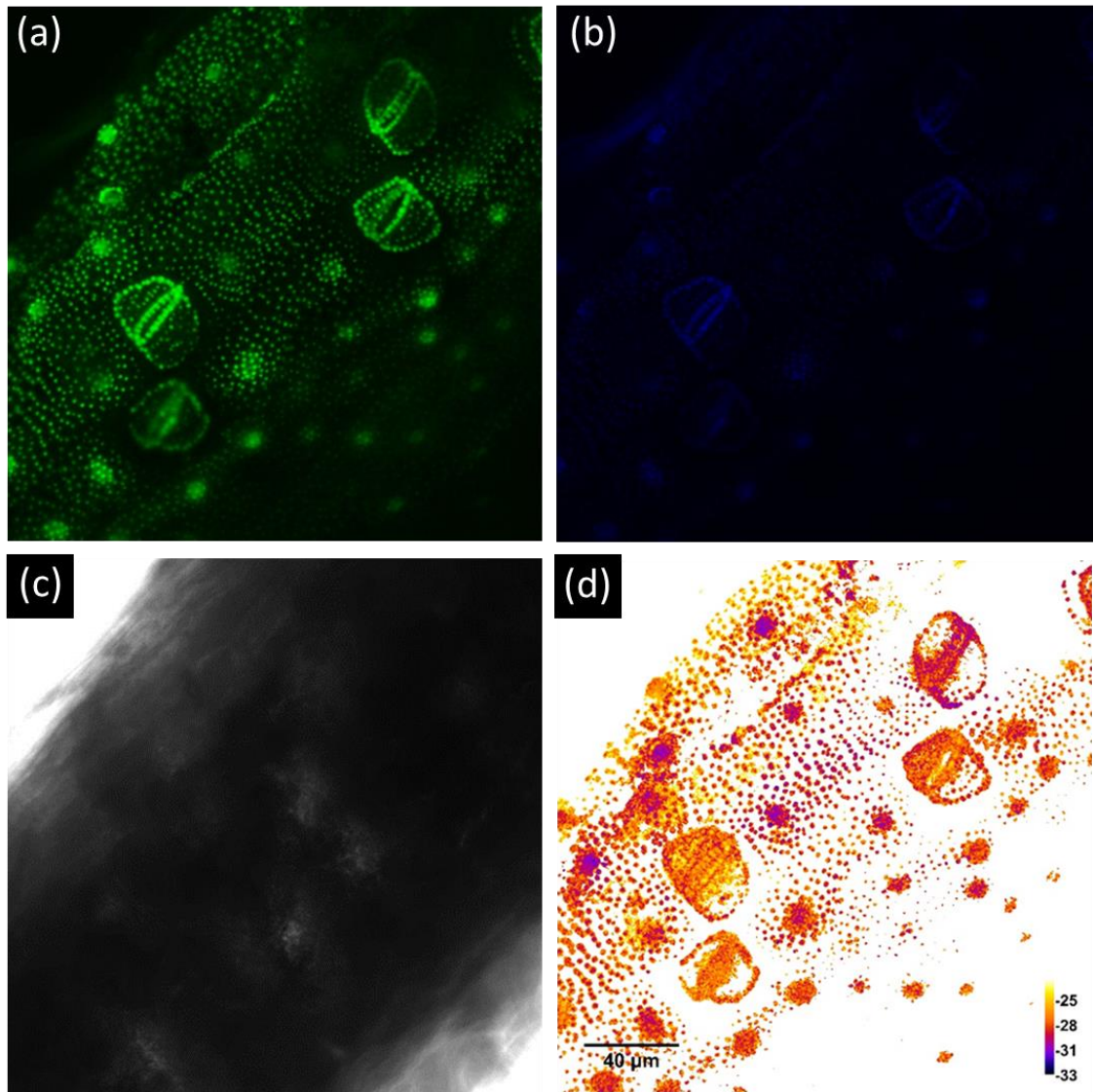


Figure 4.10 – Functional imaging of charge on stomata, star shaped rosettes like structures, and a random array of pilulae covering the nodal plane of the cell wall of *Equisetum arvense*

Sample preparation method 2 (Section 4.6.1) was used

(a) $(\text{PDMPOH}_2)^{2+}$ imaging with data collected over the wavelength range 500-510 nm, (b) PDMPOH^+ imaging with data collected over the wavelength range 460-470 nm, (c) Bright field image of same sample, (d) Zeta potential image calculated from the ratio of $(\text{PDMPOH}_2)^{2+}/(\text{PDMPOH})^+$ using ImageJ. The colours in (a) and (b) are false colours.

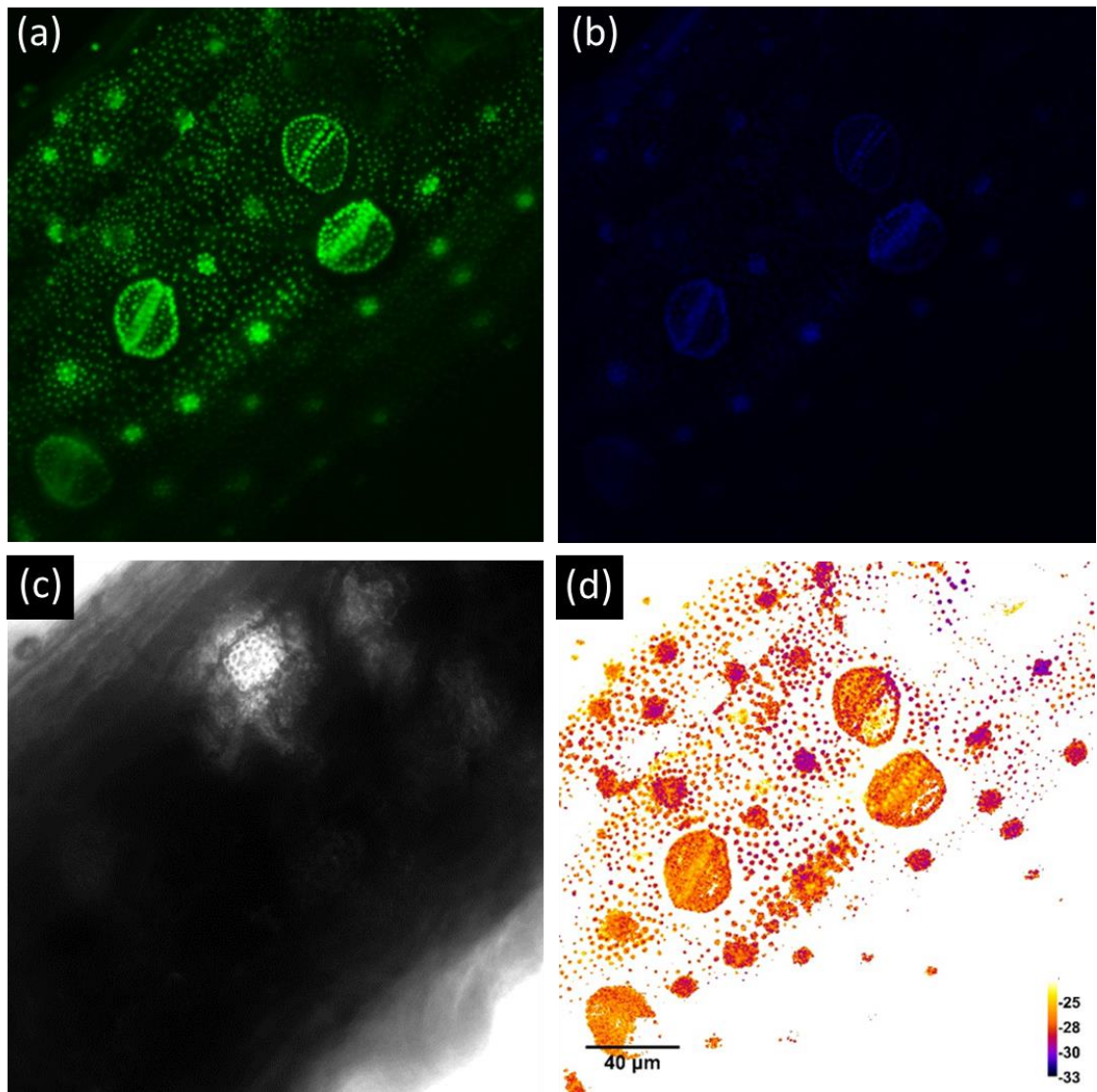


Figure 4.11 – Functional imaging of charge on stomata, star shaped rosettes like structures, and a random array of pilulae covering the nodal plane of the cell wall of *Equisetum arvense*

Sample preparation method 2 (Section 4.6.1) was used

(a) $(\text{PDMPOH}_2)^{2+}$ imaging with data collected over the wavelength range 500-510 nm, (b) PDMPOH^+ imaging with data collected over the wavelength range 460-470 nm, (c) Bright field image of same sample, (d) Zeta potential image calculated from the ratio of $(\text{PDMPOH}_2)^{2+}/(\text{PDMPOH})^+$ using ImageJ. The colours in (a) and (b) are false colours.

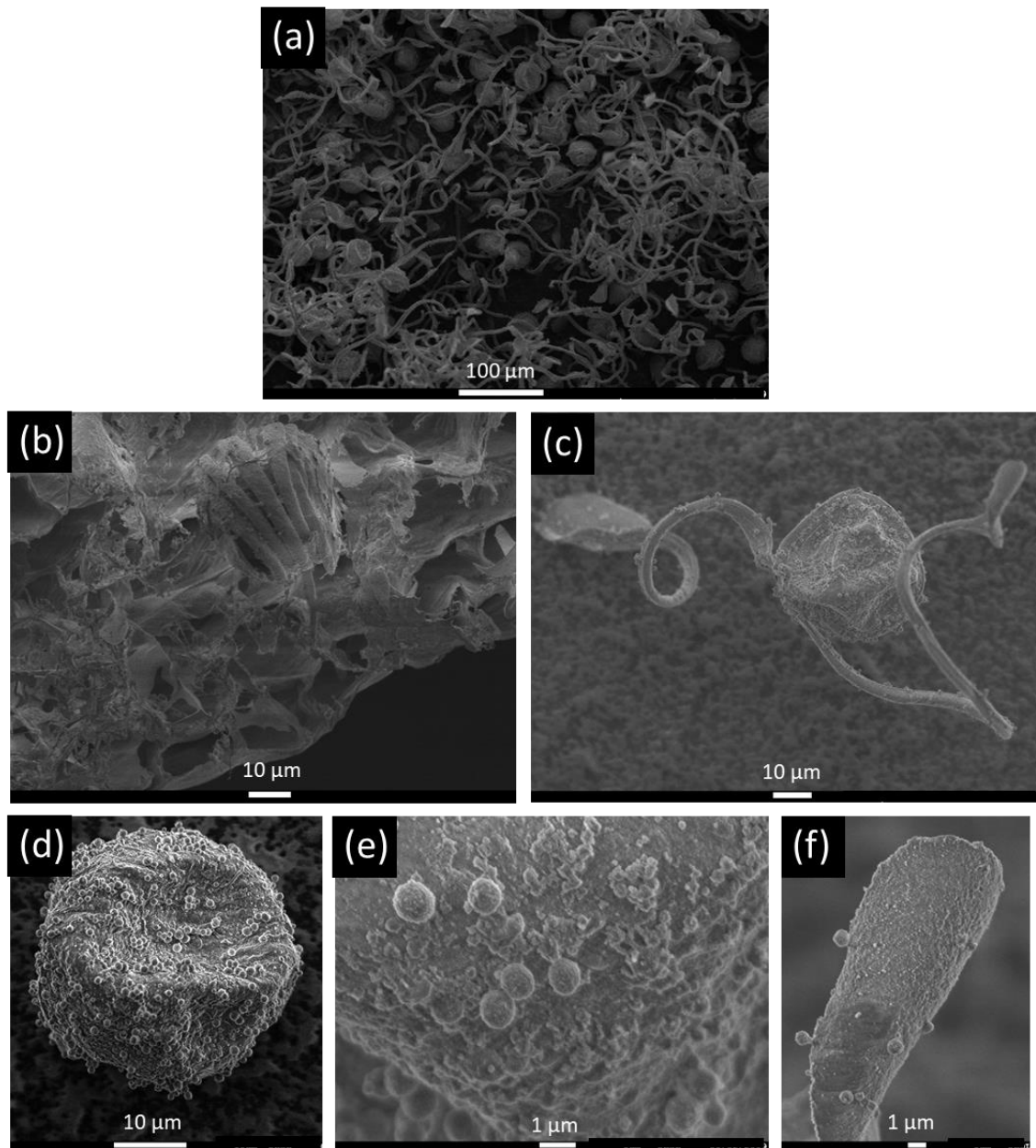


Figure 4.12 – SEM images of spores of *Equisetum arvense*

(a) Multiple spores, (b) Wrapped spore, (c) Spore with elaters, (d) Central body of spore, (e) Spherical silica structures on the central body of spore, (f) Elater paddle with spherical silica structures.

Note: the sample used was all badly affected by drying - especially the spore body as it should be round and not deflated.

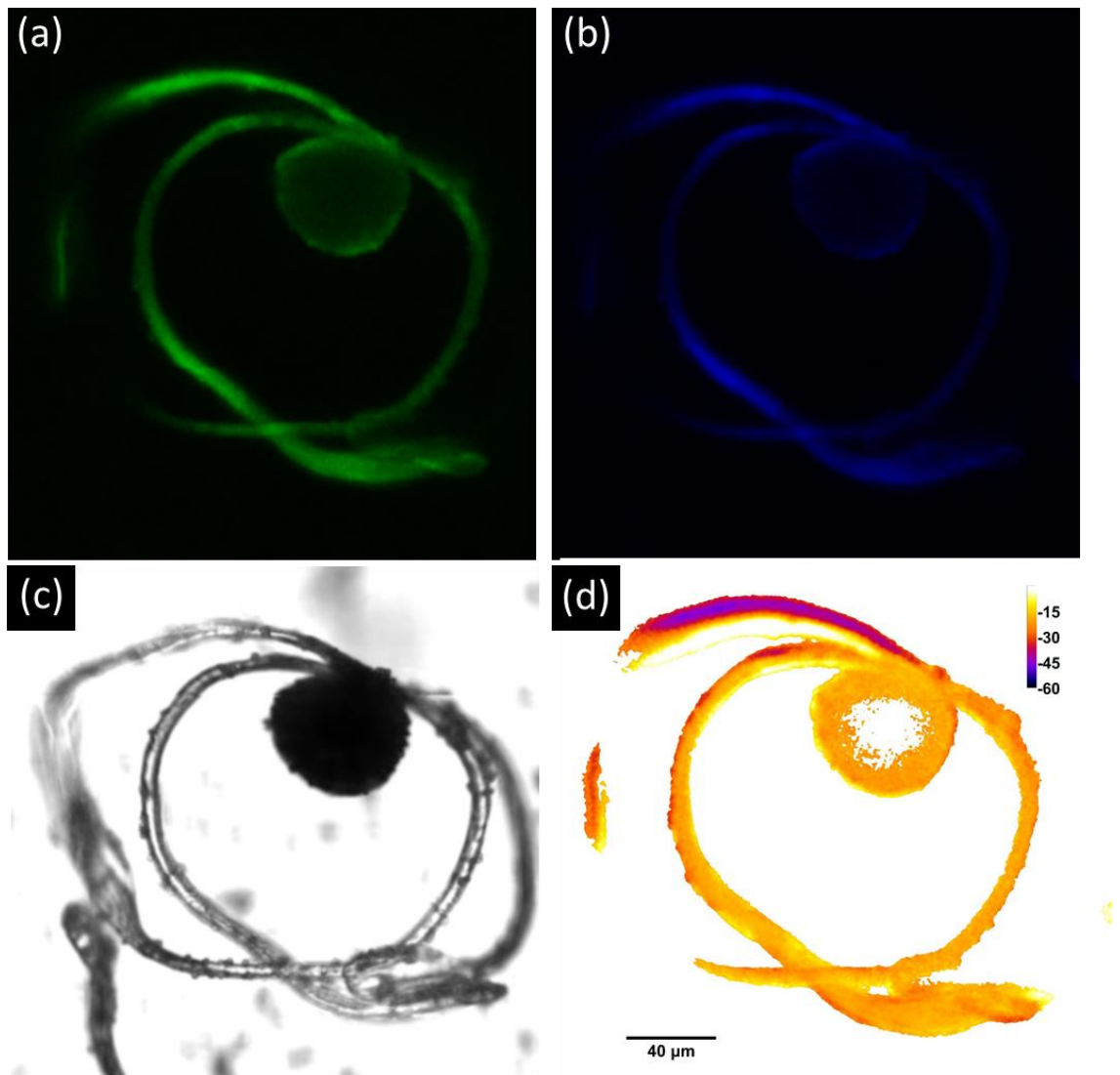


Figure 4.13 – Functional imaging of charge on a spore with elaters of *Equisetum arvense*

(a) $(\text{PDMPOH}_2)^{2+}$ imaging with data collected over the wavelength range 500-510 nm, (b) PDMPOH^+ imaging with data collected over the wavelength range 460-470 nm, (c) Bright field image of same sample, (d) Zeta potential image calculated from the ratio of $(\text{PDMPOH}_2)^{2+}/(\text{PDMPOH})^+$ using ImageJ. The colours in (a) and (b) are false colours.

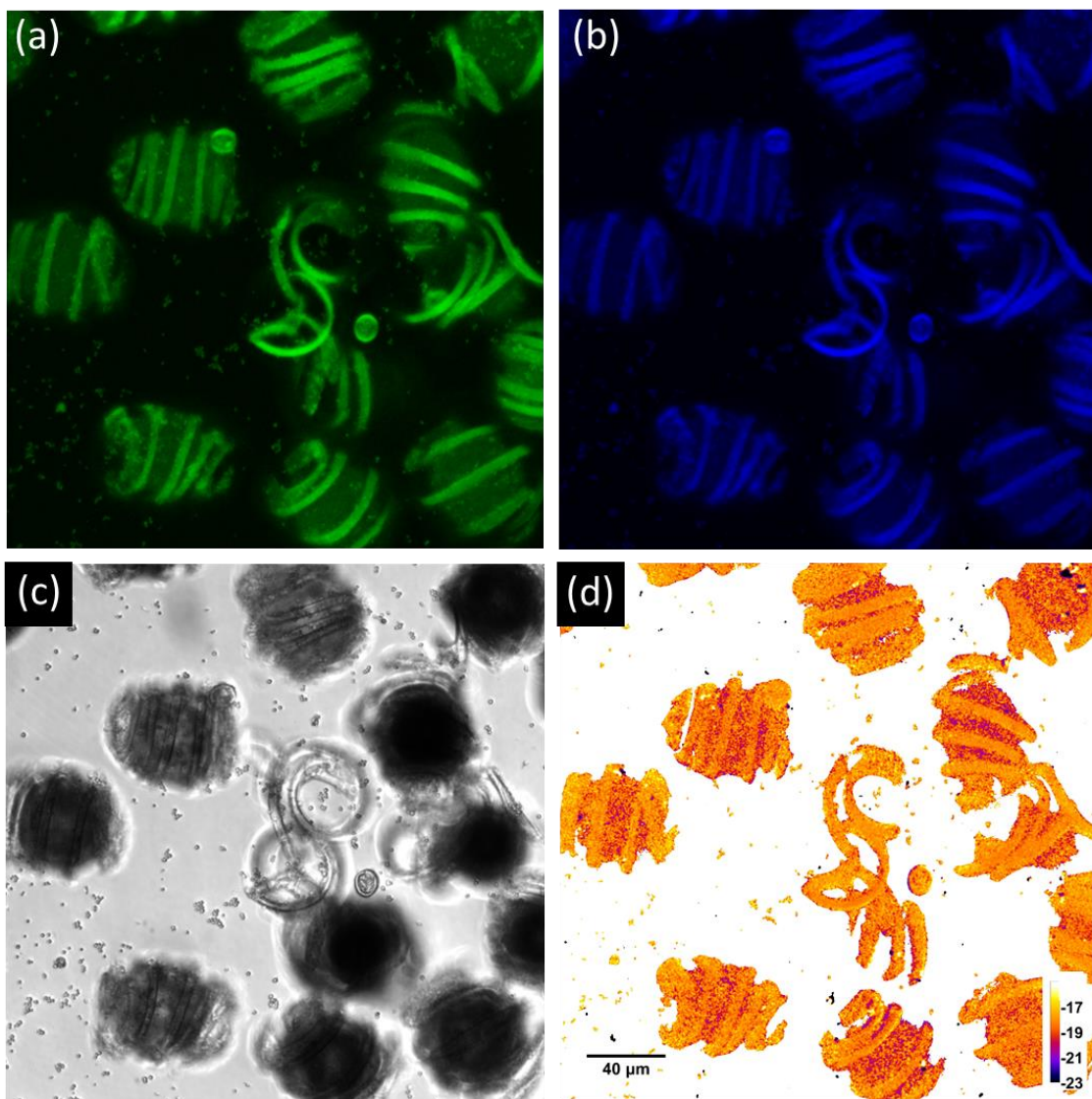


Figure 4.14 – Functional imaging of charge on multiple wrapped spores of *Equisetum arvense*

(a) $(\text{PDMPOH}_2)^{2+}$ imaging with data collected over the wavelength range 500-510 nm, (b) PDMPOH^+ imaging with data collected over the wavelength range 460-470 nm, (c) Bright field image of same sample, (d) Zeta potential image calculated from the ratio of $(\text{PDMPOH}_2)^{2+}/(\text{PDMPOH})^+$ using ImageJ. The colours in (a) and (b) are false colours.

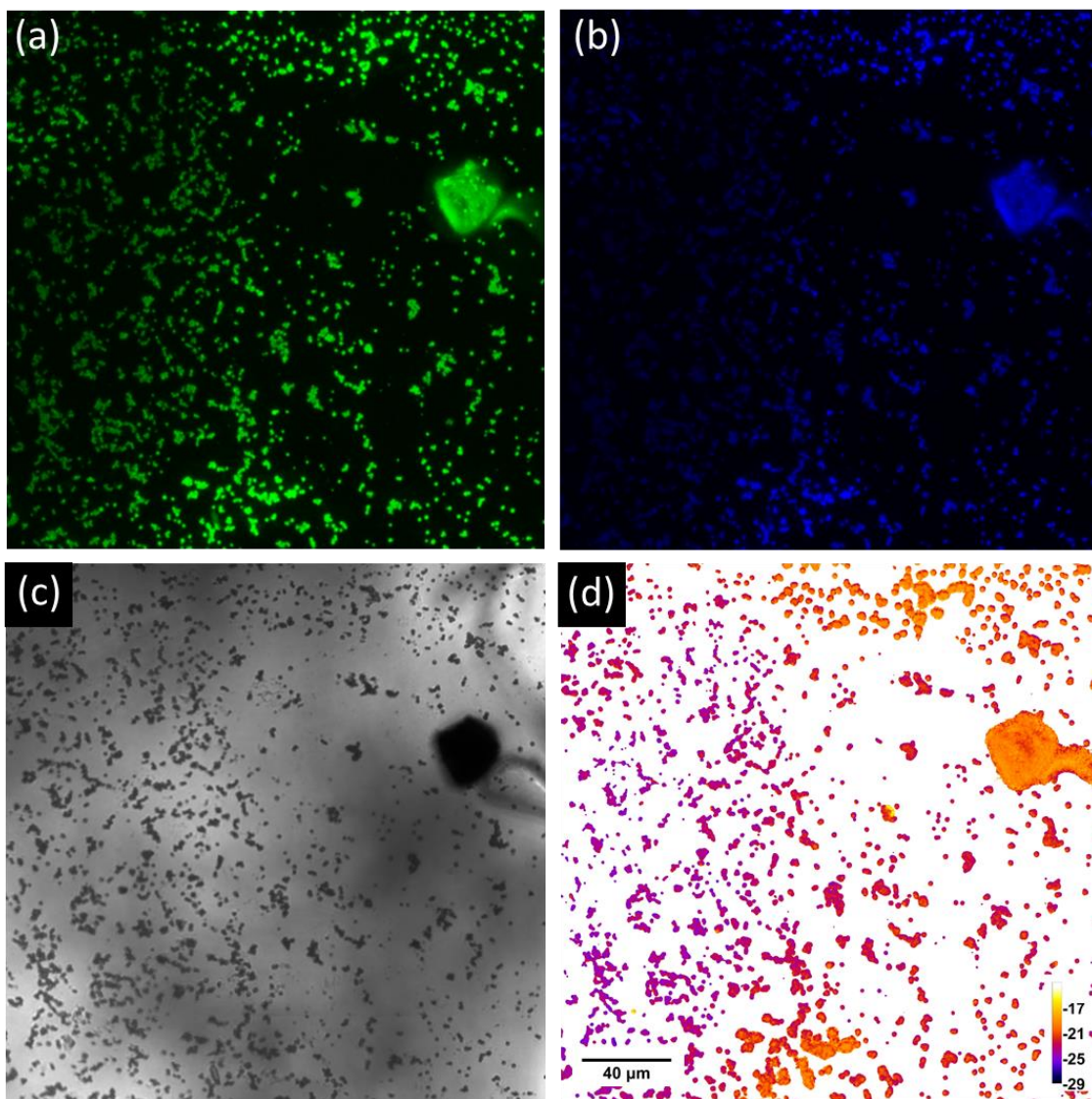


Figure 4.15 – Functional imaging of charge on spherical silica structures disassociated from the surface of the spores of *Equisetum arvense*

(a) $(\text{PDMPOH}_2)^{2+}$ imaging with data collected over the wavelength range 500-510 nm, (b) PDMPOH^+ imaging with data collected over the wavelength range 460-470 nm, (c) Bright field image of same sample, (d) Zeta potential image calculated from the ratio of $(\text{PDMPOH}_2)^{2+}/(\text{PDMPOH})^+$ using ImageJ. The colours in (a) and (b) are false colours.

c. Surface charge mapped images

From inspection of the fluorescence emission intensity data and fluorescence emission spectrum obtained from CSLM, it was noted that the areas of the samples analysed were dominated by the spectral behaviour of $(\text{PDMPOH}_2)^{2+}$ compared to PDMPOH^+ . In addition, the PDMPO emission ratio ($(\text{PDMPOH}_2)^{2+}/\text{PDMPOH}^+$) varied throughout the sample indicating differences in the local biochemistry and/or aqueous flow environment during the process of biosilicification (Perry and Fraser, 1991).

Figure 4.7 shows an application of the surface charge mapping method to basal portion of the branch (exhibiting stomata and ridges) of *Equisetum arvense* (non-living sample). The measured surface charge data shows that the silica structures delineating the stomata and the ridges have a higher zeta potential of - 28 mV when compared with adjacent epidermal silicified structures at zeta potential of - 25 mV. Analysing the local surface charge mapping as a surrogate for local topography indicated silica structures of different length scales consistent with approximately 40 - 60 nm which is well below the classical resolution limit of the confocal scanning laser microscope used. The data were found to be consistent with published data on the sizes of the globular silica aggregates that make up the silica structures found in the branches of *Equisetum arvense* (Perry and Fraser, 1991).

Application of the surface charge mapping approach to intact biological tissues extended its ability to investigate the nature of silica structures embedded within the cells of different silicifying organisms. For this purpose, young branches of heavily silicified plant, *Equisetum arvense* was used. Figures 4.8 – 4.11 show different parts of *Equisetum arvense*. Figures 4.8 and 4.9 were collected using the sample preparation method 1 whereas the Figures 4.10 and 4.11 were collected using the sample preparation method 2. As explained in section 4.6.1, method 2 was concluded to be the method of choice for the surface charge estimation measurements which are discussed below. However, the Figures 4.8 and 4.9 are included in this chapter as a reference that image quality is not maximised using method 1.

Figures 4.10 and 4.11 show samples of basal stem of the *Equisetum arvense* plant (exhibiting stomata, star shaped rosette like structures, and a random array of pilulae covering the nodal plane of the cell wall of *Equisetum arvense*) which is still growing as a varying range of zeta potential is observed which demonstrates varying sizes of silica present. A range of -25 to -33 mV zeta potential values leads to an estimation of varying silica particle sizes to up to around 100 nm which is consistent with particle sizes found from TEM studies of silica extracted from immature samples of *Equisetum arvense* (Perry and Fraser, 1991).

In *Equisetum arvense*, there are four ribbon-like attachments to the wall of spore's central body which are known as elaters and exhibit paddles at their ends. The central body of a spore is approximately 30 – 50 μm in diameter (Duckett, 1970). The elaters tightly curl around the central body of spore under moist conditions; however, the elaters uncoil to extend out from the central body of spore under dry conditions (Newcombe, 1888; Marmottant et al., 2013). The paddle like structure of the elater ensures the spore's survival and play a role in propagation (for germination) (Newcombe, 1888). The silica is mainly deposited on the surface of spores as thin layered amorphous structures along with some organic material (Volkov et al., 2019). Spherical structures (approximately 500 nm in size) present on the ridged surfaces of the elaters and central body of spores are found to have a relatively higher silica deposition (Volkov et al., 2019). Fluorescent labelling of *Equisetum* spores using PDMPO dye showed punctate deposits of silica on the spore surfaces (Law and Exley, 2011).

Figure 4.12 shows the SEM images of spores of *Equisetum arvense* where a wrapped and an extended spore with elaters are shown in b and c respectively. Figure 4.12 d, e and f show the central body of the spore, the spherical silica structures on the central body of spore and a paddle of an elater with a few spherical silica structures respectively. Note that the sample used was all badly affected by drying - especially the spore body as it should be round and not deflated.

Figures 4.13 and 4.14 show *Equisetum arvense* spores in wrapped and extended form respectively. The boundary of the elaters on the left in Figure 4.13 d show a relatively higher zeta potential value which is most likely due to the presence of silica structures.

However, the zeta potential value of -17 to -19 mV within the remaining structures may be observed due to the thin silica layers of silica nanostructures on the surface of the spore or due to the autofluorescence from the organic material present. Figure 4.14 show an example of wrapped spores with a slightly higher zeta potential on the surface of the central body of the spore or the elaters which may be again due to the thin silica layers of silica nanostructures on the surface of the spore or due to the autofluorescence from the organic material present. When imaging the spores, the spherical silica structures disassociated from the surface of the spores which were also studied (see Figure 4.15) as it was believed that they are the most silica rich structures within the spores. A varying range of zeta potential is observed which demonstrates varying sizes of silica present. A range of -20 to -26 mV zeta potential values leads to an estimation of varying silica particle sizes from 25 – 50 nm.

Some of the bright field images for the living plant samples (Figures 4.8 – 4.15 c) show poor resolution compared to the resolution of the bright field image for the extracted non-living silica sample (Figure 4.7 c). Little structural features could be seen in living plant samples which is because the area being analysed is within the sample and not on the surface. When comparing the bright field images (Figures 4.8 – 4.11 c) to the greyscale (fluorescence) images at different wavelength scan ranges (460 - 470 nm and 500 - 510 nm corresponding to PDMPOH^+ and $(\text{PDMPOH}_2)^{2+}$ respectively) (Figures 4.8 – 4.11 a-b) obtained through CSLM, it is clear that some of the structural features seen in bright field are not seen in the fluorescence images and vice versa. Surface charge mapped images are shown in Figures 4.7 – 4.15 d. The ability of CSLM to sample the fluorescence emission signal at different depths within the sample, and specifically not at the surface shows that the fluorescence observed is solely due to the PDMPO dye which accumulates where silica is present.

Through the application of this surface charge mapping approach to *Equisetum arvense*, it was concluded that both stomata and basal structures of the sample are hydrated at the local scale as water in the Stern layer is required for the PDMPO to interact with silica. Additionally, a highly charged fluorescence emission of $(\text{PDMPOH}_2)^{2+}$ from both stomata and basal structures of the samples confirms the silica-based environment of the area being analysed due to the presence of varying silica structures.

4.7.3. Diatoms

The focus of this surface charge determination method is to study the surface chemistry and obtain as much information as possible regarding the silica nanostructures within different living organisms. Although it also enables information on the structural/topographical features, this may not always be adequate when identifying the diatoms from the river water sample in this study. Although combining this method with another technique such as scanning or transmission electron microscopy would allow better identification of these diatoms, this may not be possible for the current river water samples and even in the future as it may be difficult to find another one of the same diatoms within the sample. Hence, efforts were made to identify the diatoms using the structural information available within the bright field images in this study.

For most of the diatoms, the fluorescence emission intensity data and fluorescence emission spectrum obtained from CSLM again showed that the areas of the samples analysed were dominated by the spectral behaviour of $(\text{PDMPOH}_2)^{2+}$ compared to PDMPOH^+ . In addition, the PDMPO emission ratio $((\text{PDMPOH}_2)^{2+}/\text{PDMPOH}^+)$ varied throughout the sample indicating differences in the local biochemistry.

a. *Coscinodiscus Wailesii*

Coscinodiscus genus are large centric diatoms (diameter up to 500 μm) where their species have a distinct cell wall morphology. It is characterised by a hexagonally porous array with 1 – 2 micrometre periodicity within valves and a square pattern of 250 – 300 nm periodicity within girdle (Kucki and Fuhrmann-Lieker, 2011). *Coscinodiscus* is rich in chloroplast which is located within vesicles directly next to the cell wall (Kucki and Fuhrmann-Lieker, 2011). In addition, species, *Coscinodiscus granii* and *Wailesii*, have shown to exhibit a relatively weak and stable autofluorescence below the wavelength of 500 nm (Kucki and Fuhrmann-Lieker, 2011). Though the origin of this fluorescence is not understood, it is most likely to arise from the organic matrix of cells and is always present even after its isolation and purification (Kucki and Fuhrmann-Lieker, 2011; Ingalls et al., 2010). The high fluorescence quantum yield of dyes such as Rhodamine 19 and PDMPO has previously enabled researchers to overcome this due to their higher

accumulation efficiencies within the newly developing frustules of different *Coscinodiscus* diatoms *in vivo* (Kucki and Fuhrmann-Lieker; Shimizu et al., 2001).

Figures 4.16 and 4.18 show the valve and griddle view respectively of a sample of *Coscinodiscus Wailesii* of around 110 μm size. A hexagonally porous array of frustules covering the valve and no details of griddles of *Coscinodiscus Wailesii* can be clearly observed in Figures 4.16 and 4.18 which means that it is still growing as a varying range of zeta potential is observed which demonstrates varying sizes of silica present. A range of -24 to -37 mV zeta potential values leads to an estimation of varying silica particle sizes as granular agglomerated nanostructures to up to around 110 nm which is consistent with particle sizes of 50-200 nm found from AFM studies of silica extracted from two similar species of *Coscinodiscus* genus (Noll et al., 2002; Losic et al., 2007; Hilderbrand et al., 2009).

To note, it was often difficult to image the fluorescence areas due to their fast bleaching/fading which was observed after a few seconds to minutes of the UV light exposure. As the vesicle like structures seen within the *Coscinodiscus Wailesii* images (Figures 4.16 – 4.19) do not display fluorescence, it confirms that they are likely to be the chloroplasts filled with chlorophyll (which fluoresces at higher wavelengths than the ones used for this surface charge determination method).

From the derived zeta potential image (Figure 4.16 d) for *Coscinodiscus Wailesii* (valve view), the central region did not show much structural details and it looked that the collected greyscale images (Figure 4.16 a-b) may be saturated such that the individual pixels cannot be differentiated. Initially, it was thought that zeta potential images produced using the processed greyscale images with reduced fluorescence intensity values by half (Figure 4.17 a) or quarter (Figure 4.17 b) could resolve this problem. However, no differences were observed in terms of observing the structural details of the diatom, *Coscinodiscus Wailesii* (see Figure 4.16 d in comparison to Figures 4.17 a - b). Later, the threshold of the greyscale images was modified in hope to obtain more structural details of the diatom, *Coscinodiscus Wailesii*. The zeta potential images, Figures 4.17 c - d, show the details of the hexagonally porous array and its interior (dots) within the valve in more detail.

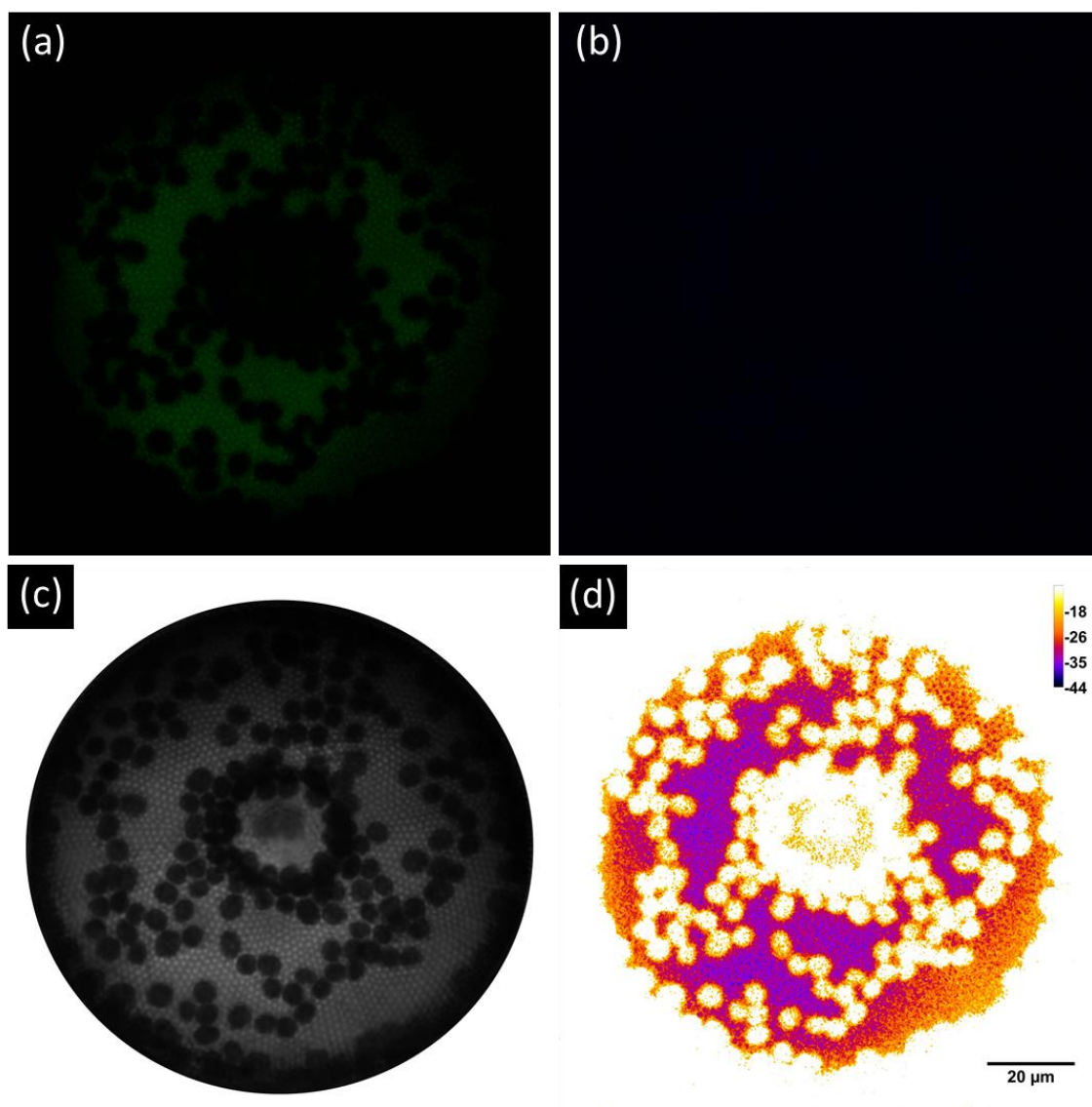


Figure 4.16 – Functional imaging of charge on diatom, *Coscinodiscus Wailesii* (valve view)

(a) $(\text{PDMPOH}_2)^{2+}$ imaging with data collected over the wavelength range 500-510 nm, (b) PDMPOH^+ imaging with data collected over the wavelength range 460-470 nm, (c) Bright field image of same sample, (d) Zeta potential image calculated from the ratio of $(\text{PDMPOH}_2)^{2+}/(\text{PDMPOH})^+$ using ImageJ. The colours in (a) and (b) are false colours.

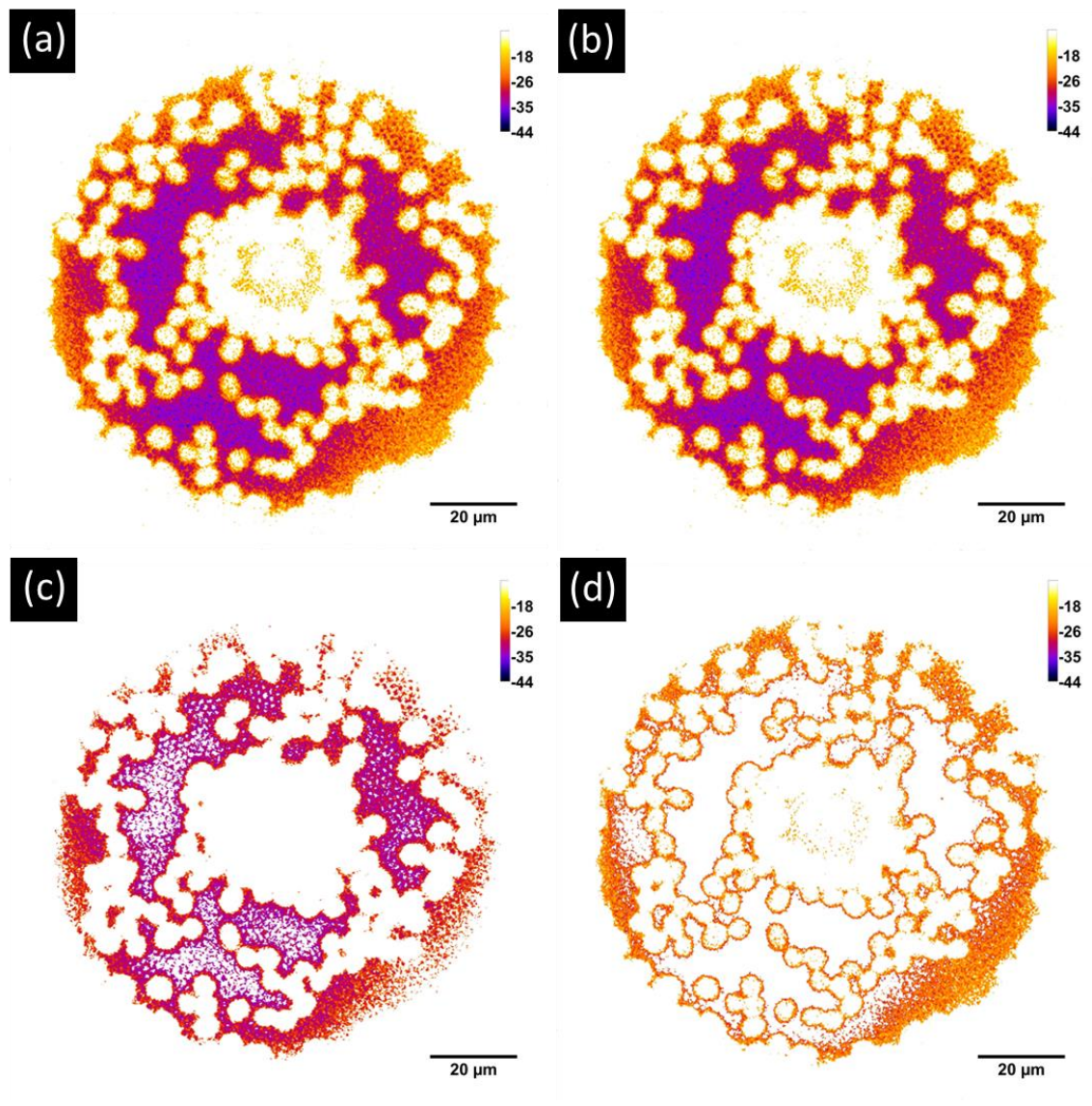


Figure 4.17 – Functional imaging of charge on diatom, *Coscinodiscus Wailesii* (valve view)

Zeta potential images calculated from the ratio of $(\text{PDMPOH}_2)^{2+}/(\text{PDMPOH})^+$ using ImageJ with different processing are included. (a) fluorescence intensity values of greyscale images reduced by half, (b) fluorescence intensity values of greyscale images reduced by quarter, (c) Another exemplary threshold of the greyscale images, (d) Another exemplary threshold of the greyscale images.

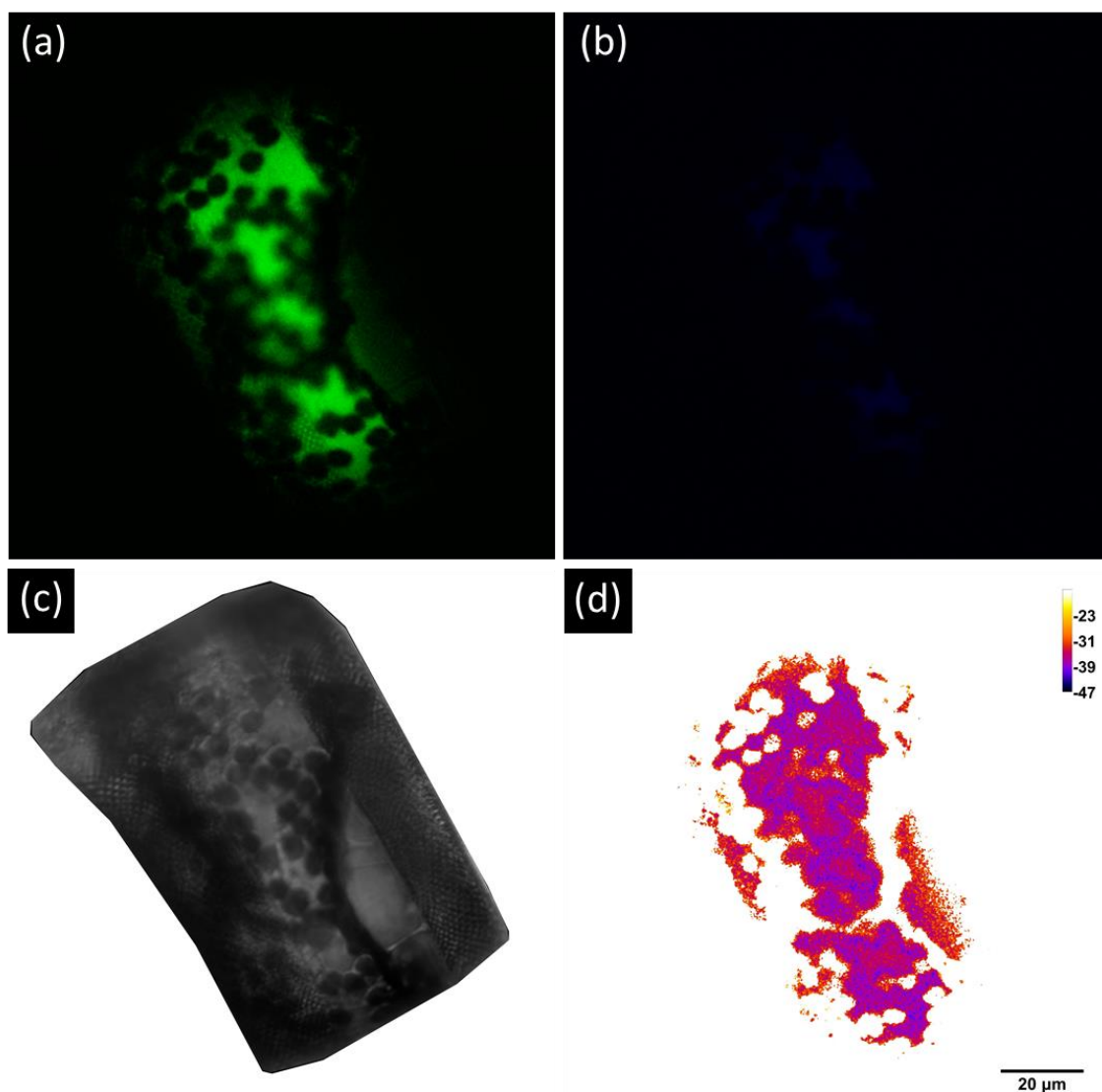


Figure 4.18 – Functional imaging of charge on diatom, *Coscinodiscus Wailesii* (girdle view)

(a) $(\text{PDMPOH}_2)^{2+}$ imaging with data collected over the wavelength range 500-510 nm, (b) PDMPOH^+ imaging with data collected over the wavelength range 460-470 nm, (c) Bright field image of same sample, (d) Zeta potential image calculated from the ratio of $(\text{PDMPOH}_2)^{2+}/(\text{PDMPOH})^+$ using ImageJ. The colours in (a) and (b) are false colours.

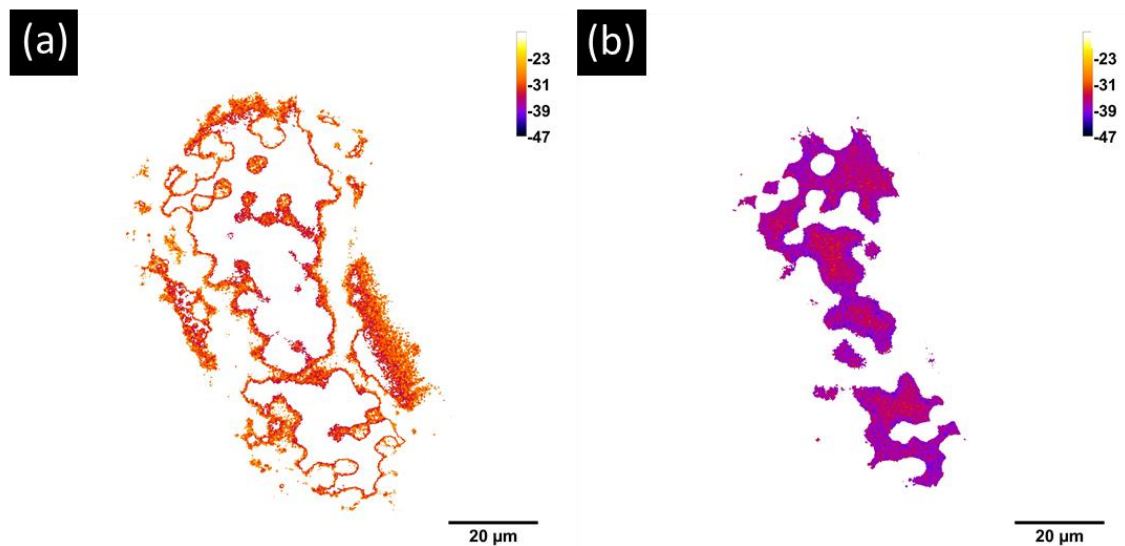


Figure 4.19 – Functional imaging of charge on diatom, *Coscinodiscus Wailesii* (girdle view)

Zeta potential images calculated from the ratio of $(\text{PDMPOH}_2)^{2+}/(\text{PDMPOH})^+$ using ImageJ with different processing are included. (a) Another exemplary threshold of the greyscale images, (b) Another exemplary threshold of the greyscale images.

From the derived zeta potential image (Figure 4.18 d) for *Coscinodiscus Wailesii* (girdle view), the central region again did not show much structural details for similar reasons as explained above for the valve view. As the zeta potential images produced using the processed greyscale images with reduced fluorescence intensity values did not resolve this problem; hence, different thresholds of the greyscale images were studied to obtain more structural details of the diatom, *Coscinodiscus Wailesii*. The zeta potential images, Figures 4.19 a - b, show the details of the hexagonally porous array and its interior (dots) within the valve (outer regions) in more detail. However, no details of the girdle band(s) can be observed.

b. *Cylindrotheca Closterium*

It was not easy to identify the diatom in Figure 4.20. Initially, it was thought that it could be any of the following: *Fragilaria Crotonensis*, *Fragilaria Nanana* or *Cylindrotheca Closterium* (also known as *Nitzschia Closterium*). Looking at the structural features, it was concluded that it is most likely *Cylindrotheca Closterium* which is a diatom with a weakly silicified frustule (Reimann and Lewin, 1964). It ranges from 25 to 98 µm in length

and 2 to 4 μm in width (Li et al., 2007). The cells have long projections with two equal chloroplasts in the middle of its body (Li et al., 2007). No striae (pores) are present (Li et al., 2007).

Figure 4.20 shows the valve view of *Cylindrotheca Closterium*. Since it only exhibits a weakly silicified structure, the fluorescence observed was also very weak. Hence, it can be concluded that the zeta potential observed demonstrates a presence of a relatively similarly sized silica. A -17 to -20 mV zeta potential values leads to an estimation of silica particle sizes to around 10 - 20 nm.

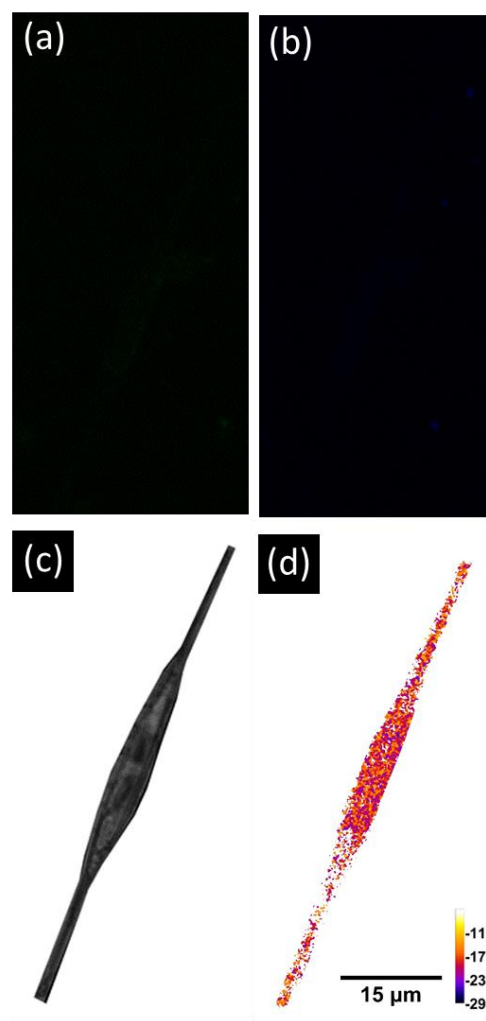


Figure 4.20 – Functional imaging of charge on diatom, *Cylindrotheca Closterium*
(a) $(\text{PDMPOH}_2)^{2+}$ imaging with data collected over the wavelength range 500-510 nm,
(b) PDMPOH^+ imaging with data collected over the wavelength range 460-470 nm, (c)
Bright field image of same sample, (d) Zeta potential image calculated from the ratio of
 $(\text{PDMPOH}_2)^{2+}/(\text{PDMPOH})^+$ using ImageJ. The colours in (a) and (b) are false colours.

c. *Diatoma mesodon*

Diatoma mesodon (also known as *Odontidium mesodon*) are pennate diatoms with 17 - 34 μm valves such that the frustules appear rectangular under valve view (Roy, 2016; Buysler, 2020). Rimoportulae (opening/extensions within the valve) and sometimes very small spines are also present in the periphery region of valves (Roy, 2016). Transapical costae are present across the griddle band area in a parallel or oblique manner (Roy, 2016). Girdle bands also has rows of pores.

Figure 4.21 show the valve view of *Diatoma mesodon* joined (slices through the sample also collected at every 1 μm which are shown in Figure 4.22). Rectangular frustule is seen with rimoportulae/spines present on the valve (also seen throughout the slices). The tendon like features known as transapical costae can also be observed (especially in Figure 4.21 and 4.22 d). Pore like features also seen on the boundary (griddle bands). A varying range of zeta potential is observed which demonstrates varying sizes of silica present. A range of -12 to -25 mV zeta potential values leads to an estimation of varying silica particle sizes to up to around 30 nm.

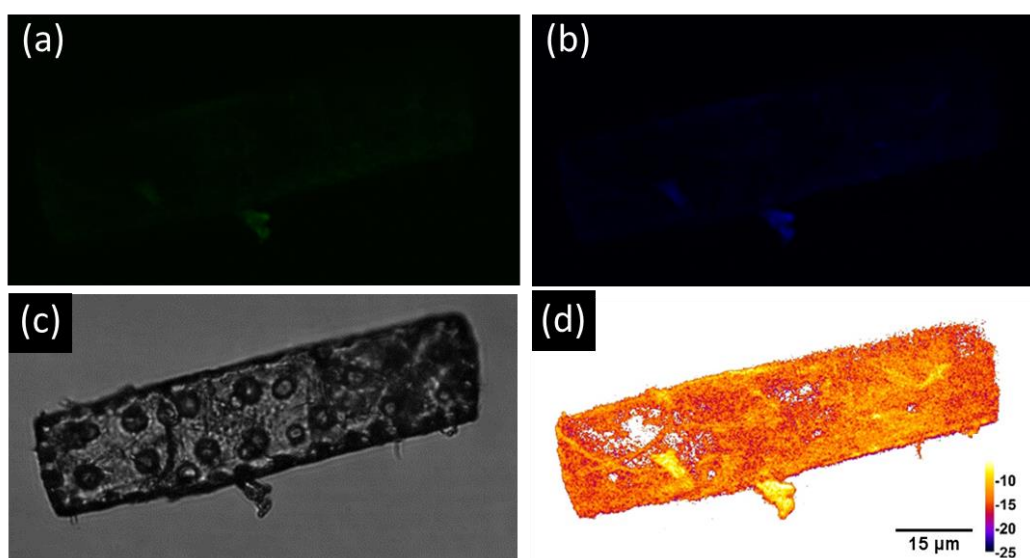


Figure 4.21 – Functional imaging of charge on diatom, *Diatoma mesodon*

(a) $(\text{PDMPOH}_2)^{2+}$ imaging with data collected over the wavelength range 500-510 nm, (b) PDMPOH^+ imaging with data collected over the wavelength range 460-470 nm, (c) Bright field image of same sample, (d) Zeta potential image calculated from the ratio of $(\text{PDMPOH}_2)^{2+}/(\text{PDMPOH})^+$ using ImageJ. The colours in (a) and (b) are false colours.

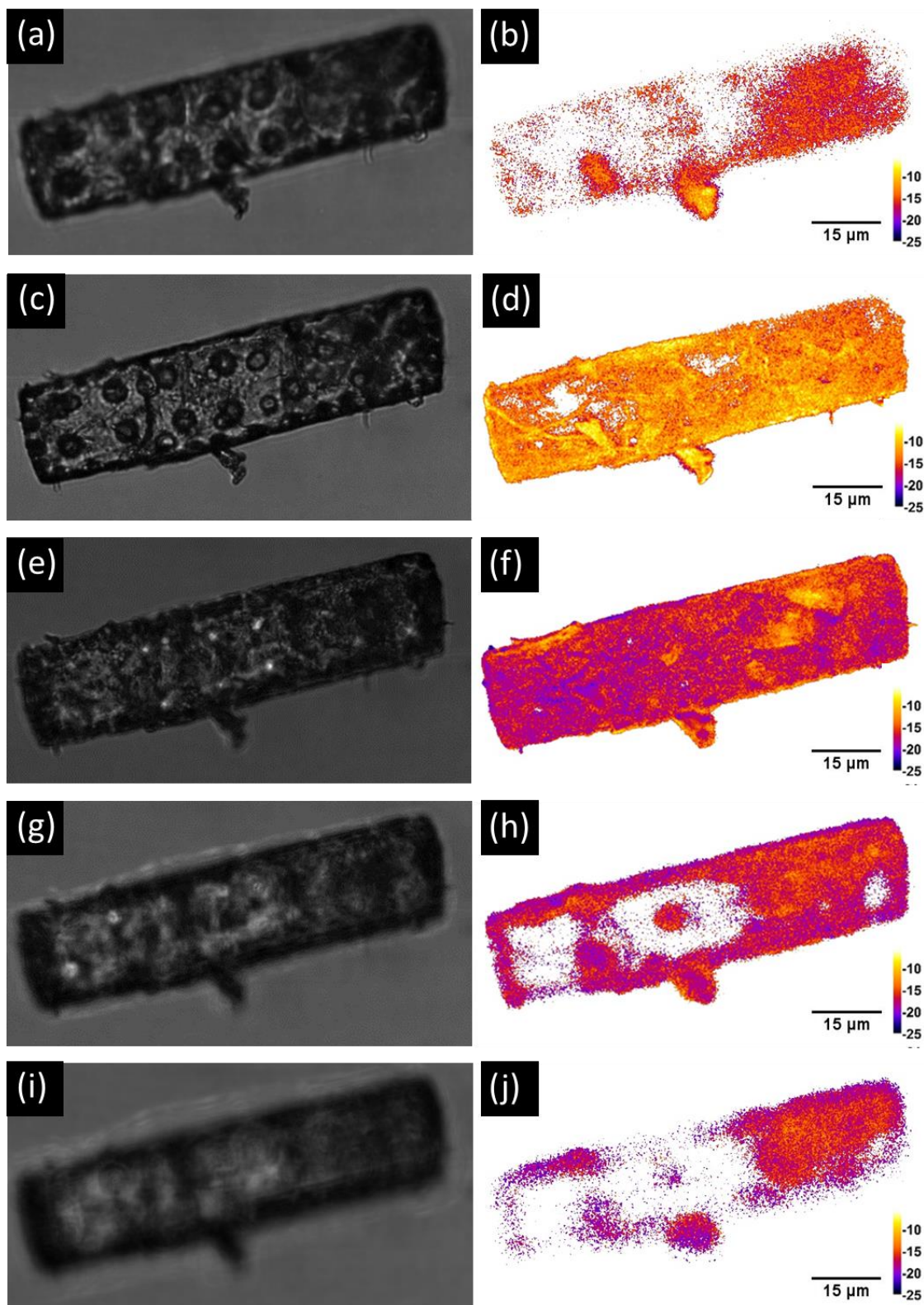


Figure 4.22 – Functional imaging of charge on diatom, *Diatoma mesodon*

Slices through the sample collected at every 1 μm - Bright field image and Zeta potential image calculated from the ratio of $(\text{PDMPOH}_2)^{2+}/(\text{PDMPOH})^+$ using ImageJ presented respectively for slice 1 (a) and (b), slice 2 (c) and (d), slice 3 (e) and (f), slice 4 (g) and (h) and slice 5 (i) and (j).

d. *Diatoma vulgare bory*

Diatoma vulgare bory are pennate diatoms with 8 – 75 µm valve length and 7 – 18 width such that the frustules appear like rectangles/squares under griddle view (Lee et al., 2019). The valve is elliptical in shape and striae are also present on them (Lee et al., 2019). Rimoportulae (opening/extensions within the valve) and very small spines may also be present in the periphery region of valves as they are seen within another diatom (*Diatoma mesodon*) of the same genus (Roy, 2016).

Figures 4.23 and 4.24 show the griddle view of two *Diatoma vulgare bory* diatoms close to separation and joined respectively (slices through the sample for Figure 4.24 also collected at every 0.5 µm which are shown in Figures 4.25 and 4.26). Frustule is seen with rimoportulae present on the valve (also seen throughout the slices). A varying range of zeta potential is observed which demonstrates varying sizes of silica present. A range of -15 to -30 mV zeta potential values leads to an estimation of varying silica particle sizes to up to around 50 nm.

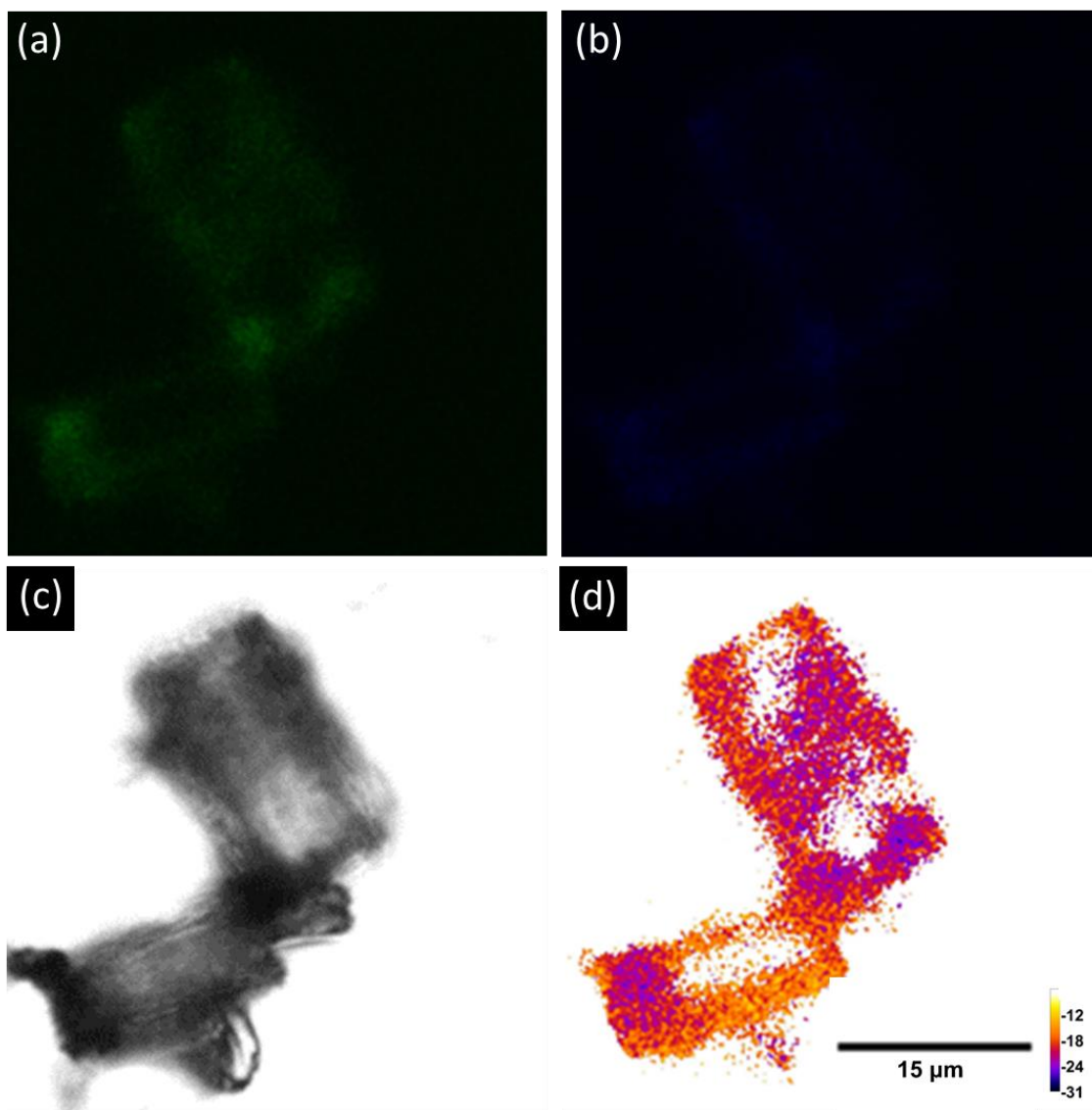


Figure 4.23 – Functional imaging of charge on diatom, *Diatoma vulgaris bory*
(separating diatoms)

(a) $(\text{PDMPOH}_2)^{2+}$ imaging with data collected over the wavelength range 500-510 nm,
 (b) PDMPOH^+ imaging with data collected over the wavelength range 460-470 nm, (c)
 Bright field image of same sample, (d) Zeta potential image calculated from the ratio of
 $(\text{PDMPOH}_2)^{2+}/(\text{PDMPOH})^+$ using ImageJ. The colours in (a) and (b) are false colours.

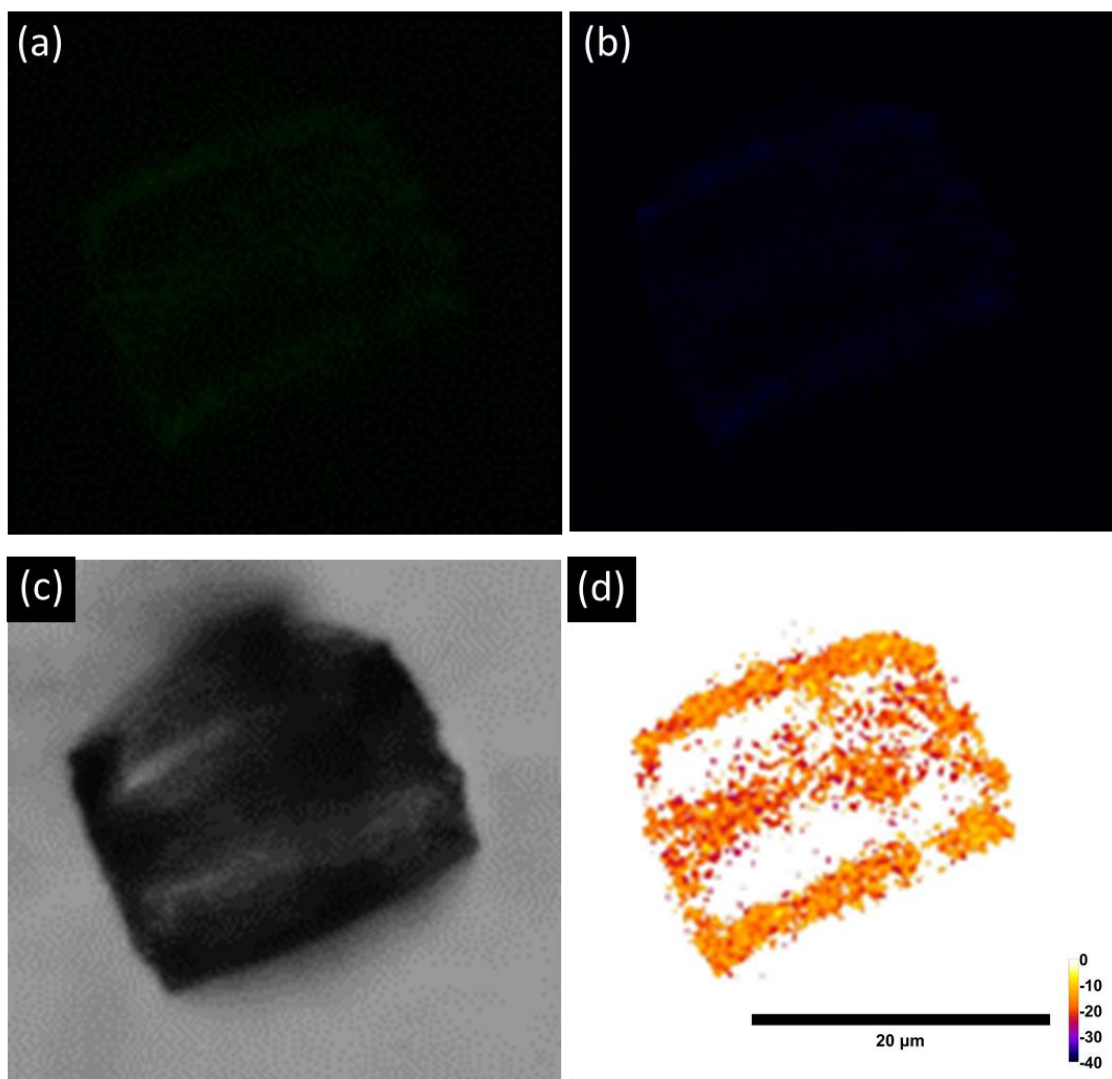


Figure 4.24 – Functional imaging of charge on diatom, *Diatoma vulgaris bory* (joined) (a) $(\text{PDMPOH}_2)^{2+}$ imaging with data collected over the wavelength range 500-510 nm, (b) PDMPOH^+ imaging with data collected over the wavelength range 460-470 nm, (c) Bright field image of same sample, (d) Zeta potential image calculated from the ratio of $(\text{PDMPOH}_2)^{2+}/(\text{PDMPOH})^+$ using ImageJ. The colours in (a) and (b) are false colours.

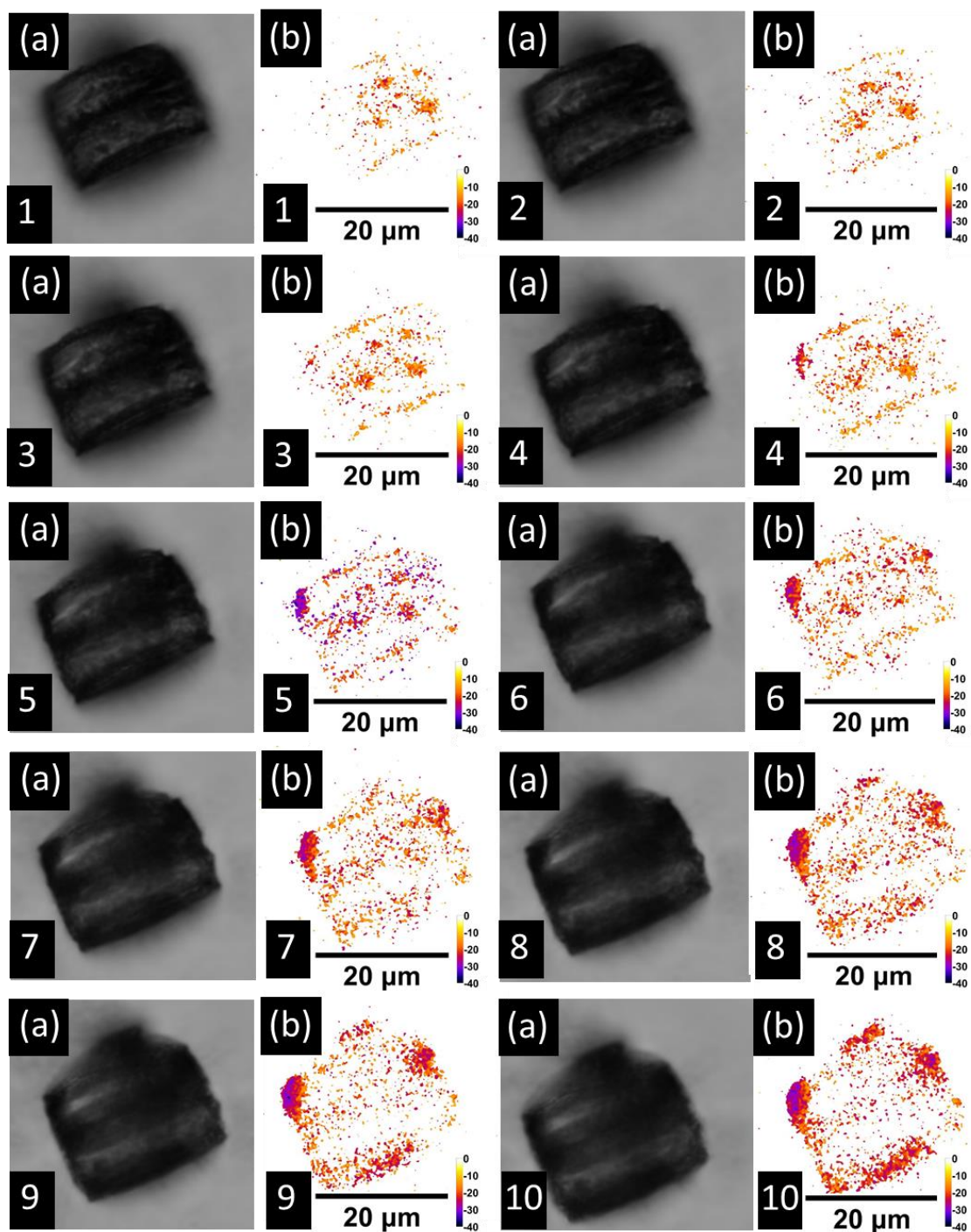


Figure 4.25 – Functional imaging of charge on diatom, *Diatoma vulgaris bory* (joined) Slices through the sample collected at every 0.5 μm - Bright field image and Zeta potential image calculated from the ratio of $(\text{PDMPOH}_2)^{2+}/(\text{PDMPOH})^+$ using ImageJ presented respectively for slice 1 (1a) and (1b), slice 2 (2a) and (2b), slice 3 (3a) and (3b), slice 4 (4a) and (4b), slice 5 (5a) and (5b), slice 6 (6a) and (6b), slice 7 (7a) and (7b), slice 8 (8a) and (8b), slice 9 (9a) and (9b), slice 10 (10a) and (10b).

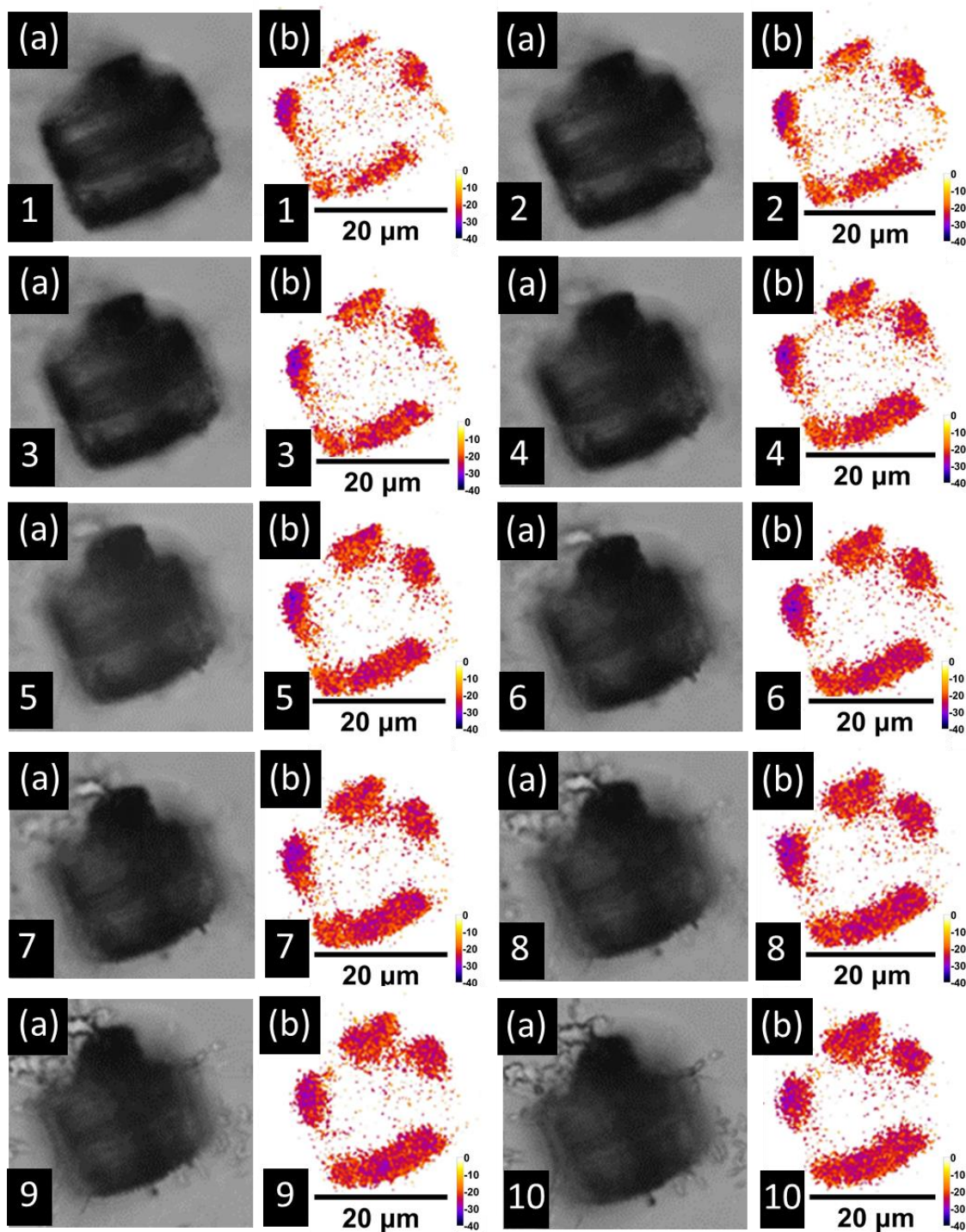


Figure 4.26 – Functional imaging of charge on diatom, *Diatoma vulgaris bory* (joined) Slices through the sample collected at every 0.5 μm continued - Bright field image and Zeta potential image calculated from the ratio of $(\text{PDMPOH}_2)^{2+}/(\text{PDMPOH})^+$ using ImageJ presented respectively for slice 11 (1a) and (1b), slice 12 (2a) and (2b), slice 13 (3a) and (3b), slice 14 (4a) and (4b), slice 15 (5a) and (5b), slice 16 (6a) and (6b), slice 17 (7a) and (7b), slice 18 (8a) and (8b), slice 19 (9a) and (9b), slice 20 (10a) and (10b).

4.8. Conclusion

In this chapter, it was demonstrated that the developed surface charge mapping method allows for determining and monitoring the surface charge density on heterogeneous silica structures using the calibration plot based on the PDMPO emission ratio $((\text{PDMPOH}_2)^{2+}/\text{PDMPOH}^+)$ and zeta potential (ζ) of differently sized SNPs. Since the PDMPO is a fluorescent pH indicator located in the Stern layer under aqueous environment and has a history of being used as a probe, it was shown that PDMPO is an excellent indicator to determine local surface charge on silica. Using the developed surface charge mapping method, both the chemical and topography features can simultaneously be monitored on silicified heterogeneous surfaces. The development of this method opens the possibility of using CSLM to map and determine surface charge on both inert and living biological samples where the process of biosilicification can be followed under a range of environmental conditions. Not only that this methodology will enable real-time surface charge measurements but its capability to provide biosilicification related information *in vivo* makes it a technique of choice as many organisms ranging from microorganism such as diatoms to higher plants such as *Equisetum arvense* can be studied.

Moreover, incorporation of the developed surface charge mapping method to adapt the existing technologies of ratiometric imaging of calcium (Schild et al., 1994) can add immense value to research when studying surface charges on living organisms. Application of such novel methods is desirable in biomedical engineering of materials with defined surface charge characteristics in instances such as materials for tissue replacement etc.

The reported method was based on a fixed pH where the different sizes of silica nanostructures can be studied. However, this method development is not limited to this purpose and can extend the applicability of the approach to wide range of environmental conditions. There is a possibility that it can be transferred to study changes in pH where a fixed size of SNPs can be used for the method development. In addition, it can also be applicable to other materials of interest where the surface exhibits hydroxylated moieties. To adapt this method and be able to apply for the other

purposes mentioned, further experimentation and simulation to extract surface charge will be required.

Chapter 5. Towards understanding the biological mechanisms involved in the role of silicon (as silicate) uptaken from dietary intake through transcriptome analysis using RNA sequencing

5.1. Introduction

Bone related disorders such as osteoporosis cost the UK healthcare economy around £1.8 billion in 2000 and has been estimated to increase to up to £2.2 billion by 2025 (Burge et al., 2001). The rise in bone related cases is a problem that requires enhancement of knowledge in relevant areas such that it can be tackled.

Silicon, as an element, most likely as orthosilicic acid, plays a role as an essential element responsible for many biological functions of several living organisms but its role as an essential mineral is still uncertain (Farooq and Dietz, 2015). One of the biological functions of silicon is its role in physiological bone growth and development (Wang et al., 2014; Carlisle, 1986); however, its mode of action is not yet fully understood. Nutritional intake of silicon has shown the beneficial health effects of silicon on bone mineral density (Jugdaohsingh, 2007; Macdonald et al., 2012). Research involving silicon is an area of interest that poses many challenges as it is not an easy element to tackle in biological tissues. However, enhancement of knowledge of the uptake of silicon from diet and/or supplements and mechanism of silicon on bone health and formation is desired as this could help in the development of further approaches to tackle bone related disorders in addition to calcium and vitamin D that are already available.

In this part of the PhD research, a focus on understanding the mechanisms of the effects of a dietary supplement, silicon as soluble component silicate, was made through an investigation of the parameters of the whole bird as well as variance in gene expression. For the purpose of this study, bone tissue was used from a broiler chicken (*Gallus gallus*, GRCg6a). The main aim was to carry out transcriptome analysis to understand and identify the mechanisms and the key biological pathways respectively which may be involved in utilising silicate (as sodium metasilicate) from dietary intake (supplemented feed) and/or incorporating it into the bone matrix which contribute towards the bone

and overall bird skeletal growth and strength. In other words, the effects of the silicate supplemented diet in comparison to a control diet in broilers was examined through transcriptome analysis using RNA sequencing.

5.1.1. Techniques available for transcriptome analysis

Sequencing techniques such as Microarray or RNA sequencing (transcriptome) are used to study an organism's RNA transcripts at a large scale such that a comparison of level of gene expression can be made. Advantages of RNA-Sequencing over Microarray in Transcriptome Profiling through various systems such as activated T Cells (Zhao et al., 2014) and anterior cruciate ligament tears (Rai et al., 2017) have been previously reported in the literature. Comparison of techniques through those systems have demonstrated that RNA-Sequencing was better in detecting low abundance transcripts, differentiating between biologically critical isoforms and identifying genetic variants. Unlike RNA-sequencing, Microarray limits the detection range due to its requirement of specific probes. Microarray is also limited to detection of known transcripts; whereas, RNA sequencing allows larger coverage and performs full sequencing of the whole transcriptome allowing identification of novel transcripts.

Although RNA-sequencing is found to be superior to Microarray, it may not always be the first choice for researchers due to it being more complex for data analysis. However, RNA-sequencing can provide much more useful information compared to the Microarray approach. Additional to the comparison using one of the two techniques (Microarray or RNA sequencing), an independent validation of transcript expression is usually performed through qPCR for selected genes identified through Microarray or RNA sequencing (Rai et al., 2017). Hence in literature, PCR is seen to form a validation step for techniques such as Microarray or RNA sequencing.

Reverse Transcription Polymerase Chain Reaction (RT-PCR) technique detects the differences in RNA expression between a control and treated sample where the knowledge of the transcripts of interest is required. RT-PCR gives qualitative gene expression information through creation of complementary DNA (cDNA) transcripts from RNA in a reaction catalysed by the enzyme reverse transcriptase. A Real-Time

Quantitative Polymerase Chain Reaction (q-PCR) is usually combined with RT-PCR to also access the quantitative information such that a comparison of level of gene expression can be made.

There is an uncertainty with regards to knowledge of the gene(s) contributing towards understanding the role and mechanism of silicon in bone growth and development within animals. This entailed exploring transcriptome evaluating techniques to better understand the contributions of the genes. Hence, RNA-sequencing formed the starting point for this study due to its ability to detect novel transcripts unlike Microarray. It also exhibits a better sensitivity towards gene detection and does not require species specific probes for the analysis as with PCR and Microarray.

5.1.2. Background to bone homeostasis

Bone homeostasis is a complex process where a lot of different nutrients and metabolic pathways regulate this process. Bone homeostasis is managed by osteoblasts and osteoclasts ensuring the coordinated process of bone remodelling which is the balance between the formation and resorption of bone carried out continuously to maintain its function. The osteoblasts are the bone forming cells capable of producing bone matrix. The osteoclasts are the bone resorption cells capable of resorbing bone matrix and are multinucleated cells that enter the bone through the blood vessels (Kahn and Simmons, 1975; Manolagas, 1995).

There are three distinct origins of the skeleton: somites (axial skeleton), lateral plate mesoderm (limb skeleton) and cranial neural crest (skull). There are two major modes that lead to osteogenesis (process of bone formation): intramembranous ossification and endochondral ossification.

a. Intramembranous ossification

Intramembranous ossification (Lonergan et al., 2018) involves the formation of bones such as the skull through the direct proliferation and condensation of neural crest-derived mesenchymal cells into compact nodules that go on to develop capillaries and

become osteoblasts which are the committed bone precursor cells. A collagen-proteoglycan (also known as pre-bone or osteoid) matrix is secreted by the osteoblasts that binds the calcium salts and becomes calcified. The osteoblasts then either become separated from the calcified matrix by a layer of osteoid matrix secreted by them or become embedded into the calcified matrix where they become osteocytes also known as bone cells. Ossification continues as calcification progresses leading to bone formation. A compact membrane of mesenchyme cells surrounds the calcified bone tissue which is known as the periosteum. Cells in the inner surface of the periosteum also develop into osteoblasts which deposit osteoid matrix parallel to the existing bone tissue in a layer manner leading to an increase in the thickness of the bone.

b. Endochondral ossification

Endochondral ossification involves formation of cartilage tissue from aggregated mesenchymal cells where the cartilage is subsequently replaced with bone tissue (Horton, 1990). This is applicable to mainly somites and lateral plate mesoderm lineages of the skeleton. Endochondral ossification is responsible for the growth of long bones of many mammals (including humans) after birth and it spreads outward in both directions from the centre of the bone contributing to the growth of mammals. The process of endochondral ossification can be explained in several phases.

Firstly, paracrine factors induce mesenchymal cells to commit to become cartilage cells, also known as chondrocytes, through expression of two transcription factors, Pax1 and Scleraxis, which activate cartilage-specific genes (Cserjesi et al., 1995; Šošić et al., 1997). Secondly, the committed mesenchymal cells initiate to condense into compact nodules which is controlled by N-cadherin and the compact nodules then differentiate into chondrocytes which is maintained by N-CAM (Oberlender and Tuan, 1994; Hall and Miyake, 1995). Thirdly, the rapid proliferation of chondrocytes leads to formation of the cartilage model which serves as a model for bone formation and a cartilage-specific extracellular matrix is secreted as chondrocytes divide. Fourthly, the proliferation of the chondrocytes stops, and the volume of chondrocytes increases rapidly leading to the formation of hypertrophic chondrocytes which produce an altered extracellular matrix containing collagen X and more fibronectin which allows mineralization by calcium

phosphate. Several small membrane-bound vesicles are secreted by hypertrophic chondrocytes into the extracellular matrix that contain enzymes that actively generate calcium and phosphate ions which lead to the mineralization process's induction within the cartilaginous matrix (Wu et al., 1997). Lastly, blood vessels invade the cartilage model and the hypertrophic chondrocytes die by apoptosis leading to recruitment and differentiation of osteoblasts that forms the bone matrix through replacement of degraded cartilage cells (Bruder and Caplan, 1989; Hatori et al., 2009). This region is known as the primary ossification centre as this is where bone development starts. The hypertrophic chondrocytes undergo a switch from aerobic to anaerobic respiration which affects the cell's metabolism and mitochondrial energy potential and membranes which is what leads to their death by apoptosis (Shapiro et al., 2009; Hatori et al. 2009; Rajpurohit et al. 1999). Over time, the hollow space invaded by blood vessels becomes the medullary cavity also known as bone marrow and the cartilage is eventually all replaced by bone. As the primary ossification front nears the ends of the cartilage model, the chondrocytes at the front proliferate before its conversion to hypertrophic chondrocytes which push the cartilaginous ends of the long bones and forms the site for the secondary ossification.

The cartilaginous ends towards the ends of the longitudinal bone are known as epiphyseal growth plates that contribute to the lengthening of bones. The growth plates consist of three regions: a region of chondrocyte proliferation, mature chondrocytes (in epiphysis) and hypertrophic (diaphysis) chondrocytes (Chen et al., 1995). The hypertrophic chondrocytes calcify and get replaced by the bone matrix on the diaphyseal side of the growth plate. Bone growth continues until the epiphyseal growth plates can produce chondrocytes, potentially until adolescence. Bone growth stops at a certain age in all mammals which is known as epiphyseal plate closure. This happens when the cartilage tissue stops proliferating and all the cartilage gets replaced with bone matrix. The epiphyseal growth plate fades which leave behind a structure called the epiphyseal line (epiphysis and diaphysis fuse).

An increase in bone width/diameter across the bone circumference is known as appositional growth. Appositional growth contributes towards the thickening of the long bones by deposition of bone cells on the surface of bones which is enclosed by

periosteum. The osteoblasts present on the surface secrete bone matrix and osteoclasts towards the inside break down the bone leading to bone resorption and further hollowing of the bone marrow cavity. The osteoblasts then differentiate into osteocytes leading to bone formation. A balance between these two processes including osteoblasts and osteoclasts allows the bone to thicken in width.

5.1.3. Bone metabolism or repair

The process and genes related to bone metabolism or repair after ossification are included later with reference to osteoimmunology etc. (see section 5.3.4.3).

5.2. Materials and Methods

5.2.1. Experimental design for animal trial

Ethical approval for the study outlined below was sought from a sub-group of the University's Animal Welfare and Ethical Review Board and was granted with approval code ARE636. A day-old male Ross 308 birds were ordered from PD Hook and collected from Cote (Oxford) hatchery to reduce travel stress. Birds were preferably selected from a flock aged approximately 40 weeks to optimize bird quality. Extra birds than needed were used so that poor birds could be excluded. The birds were placed in an environmentally controlled and preheated poultry room (as stipulated appropriate for birds of the age selected) in their respective pens through stratified random allocation and monitored regularly on daily basis. Water was available in the drinkers (both as bell and nipple drinkers) and trial diet (control and silicate supplemented feed) weighed into the feed troughs was available ad libitum. A basal starter diet for the 0-14 days phase was manufactured by RDS as a mash. Two batches of the feeds were then prepared for the control and silicate supplemented treatment groups (for each pen) using the basal starter diet. The feed intake was measured for the sampling days (day 7 and 14). On completion of the trial, disposal of birds was arranged via Crowdens.

Number of replicate birds per treatment at placement: 6

Birds were placed into adjacent, identical pens; one for Control and one for Treatment (silicate supplemented)

(Abbreviations were assigned for each pen: C for control and Si for silicate treated pen)

Sampling tissue: Right and left tibia bones

Sampling days: Days 7 and 14

5.2.2. Sample collection and preparation

For the purpose of this study, the tibia bone was selected. On sampling days, the following parameters were measured and recorded: bird's weight, right and left bone's weight, right and left bone's width and right and left bone's length. Weights were carried out by the difference method using a scale with an accuracy to 4 figures. The length and width were measured by a ruler or a calliper. The blood sample for each bird was collected immediately after death and stored in EDTA coated tubes at -20°C for serum silicon content analysis. Both the right and left bones were cleaned using a scalpel – all the muscles, tendons and articular cartilage etc. were carefully removed ensuring the bone was not affected. The left tibia bone was stored at -20°C until it will be used for bone breaking for bone strength analysis (to be completed in future). The right tibia bone was used for the RNA sequencing (transcriptome) analysis. At the time of selection, there was no specific reason as to why the right bone was chosen for the transcriptome analysis. It was only after the sample analysis was completed that it was noted that the right bone was slightly higher in bone weight compared to the left bone (see Table 5.5 and Figure 5.5).

5.2.2.1. Blood plasma silicon content analysis

The bioavailability tests were carried out through analysing the blood plasma of the chickens for the silicon content. An Optima™ 2100 DV ICP-OES (model PQ Excell VG Elemental Perkin Elmer®, USA) was used for this purpose.

a. Standard calibration graph for Si by ICP-OES

The standard curve was produced using the 1000 ppm SiO₂ stock obtained from BDH Laboratory Supplies. Deionised water was used to produce the different concentrations used for the standard calibration plot (shown in Figure 5.1) for ICP-OES analysis.

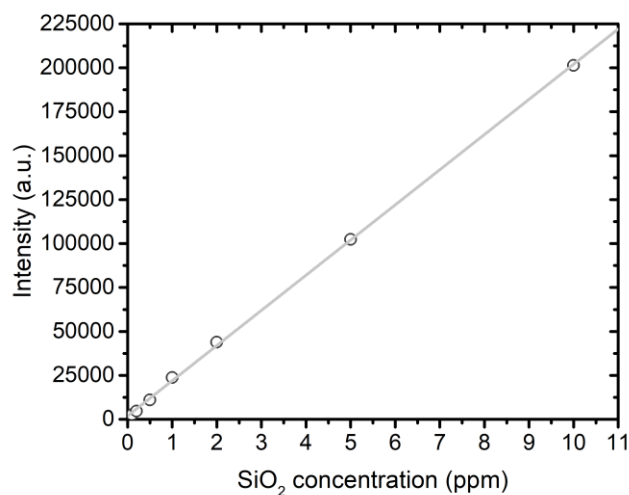


Figure 5.1 – Calibration curve for ICP-OES analysis

b. Sample analysis

At the time of analysis, the blood samples were defrosted at 4°C for couple of hours and then transferred to new 2 ml RNA/DNA free centrifuge tubes. The blood samples were centrifuged at 5400 rpm for 10-15 minutes to separate the blood into its different components. The blood plasma, top layer, was used for the silicon content analysis. 300 µl of the blood plasma was used and a 1 in 10 dilution was made with deionised water prior to performing ICP-OES (the method is discussed in chapter 2 section 2.9). Deionised water was used as a blank.

The standard calibration plot (Figure 5.1) was used for the ICP-OES analysis to determine the overall silicon concentration in ppm as SiO₂ of the blood samples.

5.2.2.2. *Disrupting bone (hard tissue) samples using liquid nitrogen*

For the right tibia bone for RNA analysis, two areas of the bone tissue, middle of bone diaphysis (approximately 5 mm) and both growth plates from proximal and distal epiphysis, were used. See Figure 5.2 for an example. A scalpel was used to cut these sections and a Dremel was used to cut the middle section of the bone where the scalpel was not adequate. Once the bone middle and growth plates were sampled, the sample was snap frozen using liquid nitrogen and gently ground into smaller pieces using a mortar and pestle. Further liquid nitrogen was utilised to grind the sample into powder. The ground sample was collected into an RNA/DNA free centrifuge tube containing RNAlater solution. The samples were stored at 4°C overnight before transferring it to -80°C on the following day until they were used for RNA extraction. Abbreviations were assigned for each bone regions: M for middle and GP for growth plates.

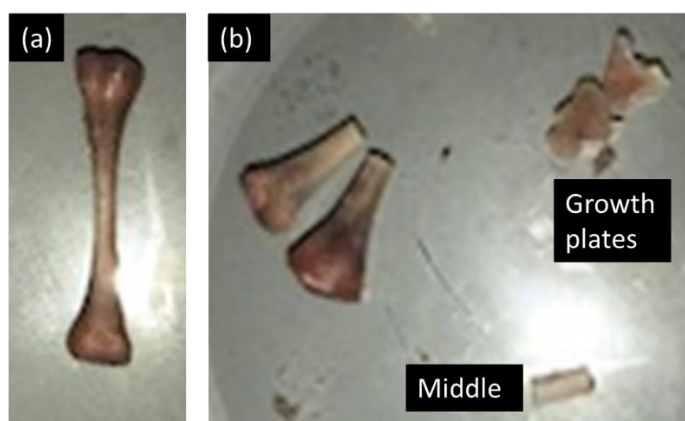


Figure 5.2 – Bone sampling of right tibia. (a) Whole bone with all the muscle, tendon and articular cartilage removed. (b) An example of growth plates and middle of bone.

RNAlater (RNA stabilising reagent) is commonly used to preserve RNA. For optimal RNA preservation, it is suggested to trim the tissue to less than 0.5 cm in at least one dimension and submerge it in 5 volumes of RNAlater solution (e.g., a 0.5 g sample requires about 2.5 mL of RNAlater solution). Since this study involved working with a hard tissue, the sample was ground to allow effective preservation of RNA. Through practising with differently aged bones available prior to the trial, it was estimated that the day 7 and day 14 bones' sections would not exceed 0.1 g and 0.2 g respectively.

Hence, the ground bone samples were stored in 0.5 ml and 1 ml of RNAlater solution on day 7 and day 14 samplings respectively.

Appropriate PPE (gloves, lab coat, goggles and a disposable face mask) were utilised throughout the process to minimise contamination from the human body and/or the environment. All precautions were also taken to prevent cross-contamination between samples when sampling for the bone tissue. The equipment/tools (mortar and pestle, scalpel and dremel blades) used for sample preparation was rinsed with or stored in ethanol to disinfect. RNAZap was used to remove any RNA contamination on the equipment/tools before use.

5.2.2.3. RNA extraction and purification

For RNA extraction, Qiagen RNeasy mini kit was initially sourced. However, the yield of the RNA was found to be very low with poor RNA quality. It was concluded that the buffer RLT to lyse the bone tissue was not sufficient solely for the RNA extraction from a hard tissue. Hence, another method using RNA STAT 60 was used which gave an over 15-fold increase in the RNA quantity with an improved RNA quality. See Table 5.1 for a comparison of the RNA yields. After evaluating the two methods for RNA extraction, RNA extraction was hence carried out using RNA stat 60 procedure followed by RNA clean up using Qiagen RNeasy mini kit to further purify the extracted RNA.

A comparison for the effects of the number of elution using RNeasy spin column from Qiagen RNeasy mini kit was also performed to maximise the chances of improving the RNA yield (see Table 5.1 again for a comparison). A second elution showed about a 2-fold increase in the RNA yield and hence this was adapted in the RNA extraction method.

Table 5.1 – A comparison of the RNA extraction methods and the effects of the number of elution on RNA yield.

Sample	RNA yield using Qiagen RNeasy mini kit		RNA yield using RNA STAT 60 followed by Qiagen RNeasy mini kit	
	First elution	Second elution	First elution	Second elution
	(ng/μl)	(ng/μl)	(ng/μl)	(ng/μl)
GP	14.00	21.77	289.2	536.1
M	19.88	29.80	303.6	1267

The Qiagen RNeasy mini kit (rejected method) and RNA STAT 60 followed by Qiagen RNeasy mini kit (accepted method) are compared for the RNA yield in Table 5.1. Please also note that the number of elution using RNeasy spin column from Qiagen RNeasy mini kit also influenced the RNA yield.

Figure 5.3 shows an overview of RNA extraction of a stabilised tissue in RNAlater. Generally, steps include lysing and homogenising the tissue, binding the separated total RNA, washing the bound RNA few times for a pure sample and then eluting it to obtain the RNA sample. The extraction method used during this PhD research is explained later.

All the RNA extraction experiments were carried out on ice and fume hood as much as possible. The bone tissue for RNA extraction was already disrupted and ground before storing in RNAlater. For extraction, the ground tissue was simply removed from RNAlater and treated as though it was just harvested. To remove RNAlater from the stabilized tissue, the RNA/DNA free centrifuge tube containing the bone tissue in RNAlater was defrosted and centrifuged at 13400 rpm and the supernatant removed.

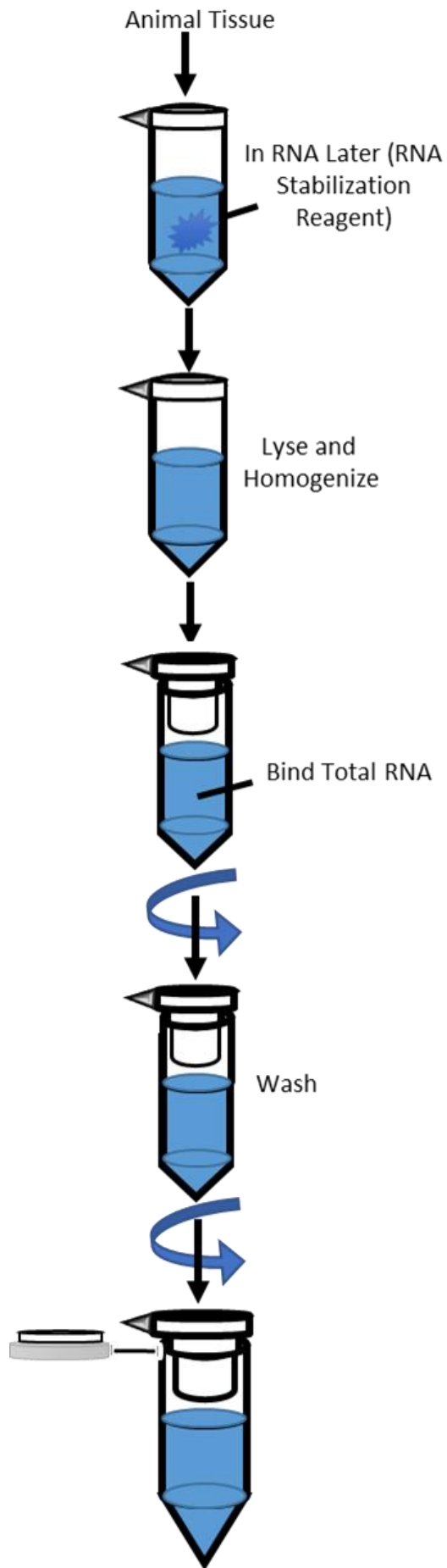


Figure 5.3 – An overview of RNA extraction process

a. Tissue homogenisation

It was suggested that 1 ml of RNA stat 60 was needed for 50-100 mg of tissue such that sample volume did not exceed 10% of the volume of the RNA STAT-60 used for homogenisation. The bone tissue was hence homogenised in 1 ml RNA STAT-60 through vortexing for 15 seconds followed by incubation for 2-5 minutes.

b. RNA isolation

Following homogenisation, the homogenate was vortexed for 5 minutes at room temperature to permit the complete dissociation of nucleoprotein complexes. 0.2 ml of chloroform per 1 ml of the RNA STAT 60 was added and the homogenate covered tightly and shaken vigorously using vortex for 15 seconds. The homogenate was further left to stand at room temperature for 2-3 minutes. The homogenate was then centrifuged at 10629 rpm for 15 minutes at 4°C. Following centrifugation, the homogenate separated into two phases: a lower red/pink phenol chloroform phase and a colourless upper aqueous phase. RNA remained exclusively in the colourless aqueous phase whereas DNA and proteins were in the interface and red/pink organic phase. The volume of the aqueous phase appeared to be about 60% of the volume of RNA STAT 60 used for homogenization.

c. RNA precipitation

The upper colourless aqueous phase was transferred to a fresh RNA/DNA free centrifuge tube and mixed with 0.5 ml of isopropanol per 1 ml of the RNA STAT 60 used for homogenization. The mixture was stored at room temperature for 5 - 10 minutes and centrifuged at 10629 rpm for 10 minutes at 4°C. From the observations, the precipitated RNA was often visible before centrifugation or a white pellet was observed at the bottom of the RNA/DNA free centrifuge tube upon centrifugation.

d. RNA wash

The supernatant was then removed, and the RNA pellet washed once with 1 ml 75% ethanol per 1 ml of the RNA STAT 60 used for the initial homogenization. The mixture was vortexed for 15 seconds with subsequent centrifugation at 10629 rpm for 5 minutes at 4°C. At the end of the procedure, the RNA pellet was briefly air-dried for 5-10 minutes. It was important not to let the RNA pellet dry completely as it would have greatly decreased its solubility. The RNA pellet was then dissolved in 50 µl RNase free water. The mixture was vortexed or passed a few times through a pipette tip for complete dissolution of RNA. Unless used immediately for the RNA clean up using Qiagen RNeasy mini kit, the extracted RNA was stored at -80 °C until the next step.

RNA clean up using Qiagen RNeasy mini kit

The protocol provided within the Qiagen RNeasy mini kit for RNA clean-up was utilised for this study (Qiagen.com., 2019).

a. Preparing working solutions of buffer

Since initially purifying RNA from tissue, 10 µl β-mercaptoethanol (β-ME) was added to every 1 ml buffer RLT (provided by Qiagen). Buffer RLT with β-ME was stored at room temperature for up to 1 month. Before using the buffer RPE for the first time, 4 volumes of ethanol (96–100%) was added to the concentrated buffer RPE (provided by Qiagen) to obtain a working solution for buffer RPE.

b. Components of the kit and their functions

β-mercaptoethanol (β-ME) is used to denature ribonucleases as numerous disulfide bonds make ribonuclease a very stable enzyme. Hence, it breaks these disulfide bonds which irreversibly denature the protein and prevents the digestion of RNA during the extraction procedure. Buffer RLT is a lysis buffer which is used to lyse cells and tissues prior to RNA isolation. Hence, this breaks the cell membrane which frees the RNA. Buffer RPE is a mild washing buffer which is exclusively a component of RNeasy kits. It contains

ethanol which plays the main function of removing any traces of salts which may be present on the column due to buffers used or impurities leaving only the nucleic acid bound to the column. Lastly, RNAase free water is used as the elution liquid to remove and dissolve the nucleic acid from the column.

The volume of the RNA sample from RNA STAT 60 method was adjusted to a total volume of 100 µl with RNase free water. 350 µl of buffer RLT was added and mixed well by vortexing for 15 seconds. 250 µl of ethanol (96–100%) was then added to the diluted RNA and mixed well by vortexing for 15 seconds. The mixture was not centrifuged, and the clean-up process immediately proceeded to the next step. The mixture (700 µl), including any precipitate, was transferred to a RNeasy Mini spin column placed in a 2 ml collection tube. The lid was closed, and the tube was centrifuged for 15 seconds at 10900 rpm. The flow-through was discarded.

500 µl of buffer RPE was added to the RNeasy spin column to wash the membrane. The lid was closed, and the tube was centrifuged for 15 seconds at 10900 rpm. The flow-through was discarded. 500 µl of buffer RPE was added to the RNeasy spin column to further wash the membrane. The lid was closed, and the tube was centrifuged for 2 minutes at 10900 rpm. The flow-through was discarded. The RNeasy spin column was then placed into a new 2 ml collection tube. The lid was closed, and the tube was centrifuged for 1 minute at maximum speed 13400 rpm to dry the membrane. Any flow-through was discarded.

The RNeasy spin column was then placed into a new 1.5 ml RNA/DNA free centrifuge tube. 30–50 µl of RNase free water was directly added to the spin column membrane. The lid was closed, and the tube was centrifuged for 1 minute at 10900 rpm to elute the RNA. To obtain a high RNA concentration or yield, the eluate was passed once more through the spin column membrane. Once the purified RNA was extracted, it was stored at -80°C until used.

5.2.2.4. DNA removal using Invitrogen DNA free kit

The protocol available online was used (Thermofisher.com., 2019).

The reactions were conducted in 0.5 mL tubes to facilitate the removal of the supernatant later in the treatment process. A starting reaction for the RNA sample was 50 μ L such that the RNA samples were diluted to a concentration of 200 μ g/ μ l. 0.1 volume of 10X DNase I Buffer to the RNA sample and 1 μ L rDNase I per every 10 μ g of RNA was added to the RNA sample and the reaction mixture was vortexed for 15 seconds prior to incubation at 37°C for 30 minutes. The DNase Inactivation Reagent was resuspended using vortex for 30 seconds before dispensing. 0.1 volume of the resuspended DNase Inactivation Reagent to the reaction mixture was added and incubated at room temperature for 2 minutes with vortexing 2-3 times during the incubation period to redisperse the DNase Inactivation Reagent. The reaction mixture was centrifuged at 11000 rpm for 1.5 minutes to remove the DNase Inactivation Reagent. The supernatant containing the DNA free RNA was transferred using a pipette to a new 0.5 ml RNA/DNA free centrifuge tube. The quantity and quality of the RNA was measured by Bioanalyzer. Once the purified DNA free RNA was extracted, it was stored at -80°C until used.

5.2.2.5. Zymo RNA clean up and concentrator

For the samples where the RIN value was under 8 after the RNA extraction using RNA stat 60 followed by Qiagen RNeasy mini kit and DNA removal using DNase Inactivation Reagent, Zymo RNA clean up and concentrator kit was utilised to further purify the samples where this method was used as this also concentrated the RNA. The following protocol was adapted (Zymoresearch.com., 2019).

a. Preparing working solutions of buffer

4 volumes of 100% ethanol were added to the concentrated RNA wash buffer provided by Zymo to obtain a working solution for the buffer.

b. DNA removal using DNase I set provided by Zymo

Although the RNA sample had been purified from DNA contamination using the Invitrogen DNA free kit, further treatment with DNase I was performed before Zymo clean up and concentrator kit which was also provided within the kit.

The DNase digestion procedure was performed using the DNase I set provided by Zymo. For DNase I digestion from samples, the following reaction mix was prepared which was mixed well by gentle inversion. An equivalent of 10 µg RNA sample in water was diluted with RNase free water to adjust the volume to 40 µl. DNase I (5 µl) and DNA digestion buffer (5 µl) were added to the diluted RNA sample to make the total volume of the reaction mixture to 50 µl. The reaction mix was incubated at room temperature for 15 minutes before starting the RNA purification using the RNA clean up and concentrator protocol provided by Zymo.

c. RNA clean up and concentrator

2 volumes of RNA binding buffer to the reaction mixture were added and mixed by vortexing for 15 seconds. An equal volume of ethanol (95-100%) to the reaction mixture was added and mixed by vortexing for 15 seconds. The mixture was transferred to the Zymo-Spin™ IC column placed in a 2 ml collection tube. The lid was closed, and the tube was centrifuged for 30 seconds at 13400 rpm. The flow-through was discarded. 400 µl of RNA prep buffer was added to the Zymo-Spin™ IC column. The lid was closed, and the tube was centrifuged for 30 seconds at 13400 rpm. The flow-through was discarded. 700 µl of RNA wash buffer was added to the Zymo-Spin™ IC column to wash the membrane. The lid was closed and the tube was centrifuged for 30 seconds at 13400 rpm. The flow-through was discarded. 400 µl of RNA wash buffer was added again to the Zymo-Spin™ IC column to wash the membrane further. The lid was closed, and the tube was centrifuged for 2 minutes at 13400 rpm to ensure complete removal of the wash buffer. The flow-through was discarded.

The Zymo-Spin™ IC column was then placed into a new 1.5 ml RNA/DNA free centrifuge tube. 15 µl of RNase free water was directly added to the spin column membrane. The

lid was closed, and the tube was centrifuged for 30 seconds at 13400 rpm to elute the RNA. To obtain a high RNA concentration or yield, the eluate was passed once more through the spin column membrane. The quantity and quality of the RNA was measured by Bioanalyzer. Once the purified DNA free RNA was extracted, it was stored at -80°C until used.

5.2.2.6. Quality control

Bioanalyzer

To perform adequate quality checks on the RNA samples before executing total RNA sequencing analysis using RNA transcriptome, an Agilent 2100 Bioanalyzer (Santa Clara, CA) using Agilent RNA 6000 nano kit protocol was carried out to determine information regarding the other parameters of RNA quality such as its integrity or degradation. A rRNA ratio as 28S/18S, RNA Integrity number (RIN) value and RNA concentration were delivered through the Agilent 2100 Bioanalyzer. A RIN value of 7 and above was assumed as adequate quality for the RNA and was used for this study.

The protocol below includes the pre-preparations (of reagents) and preparations for the RNA nanochip for the Agilent 2100 Bioanalyzer (Agilent.com, 2020). All the reagents were stored on ice when not in use.

a. Preparing the Gel

RNA 6000 Nano gel matrix - Red (provided in the Agilent RNA 6000 nano kit) was equilibrated to room temperature in dark for 30 minutes. The dye was handled in dark as it decomposes when exposed to light which can reduce the signal intensity and affect the analysis. 550 µl of RNA 6000 Nano gel matrix was pipetted into the top receptacle of a spin filter tube and placed into a microcentrifuge to centrifuge at 4000 rpm for 10 minutes. Aliquots of 65 µl were made for the filtered gel into 0.5 ml RNA/DNA free centrifuge tubes which were stored at 4°C for up to a month until used.

b. Preparing and loading the Gel-Dye mix

RNA 6000 Nano dye concentrate (provided in the Agilent RNA 6000 nano kit) – Blue binds to the nucleic acids. RNA 6000 Nano dye concentrate and filtered gel (pre-prepared) were equilibrated to room temperature in dark for 30 minutes. RNA 6000 Nano dye concentrate was vortexed for 10 seconds and centrifuged to collect all the content together at the bottom. 1 μ l of RNA 6000 Nano dye concentrate was added to 65 μ l aliquot of filtered gel and vortexed thoroughly before centrifuging it at 13000 g for 10 minutes at room temperature. The Gel-Dye mix was used immediately or stored at -80°C until used.

RNA nanochip (16 wells - 4X4) was placed into the chip priming station (a device with a syringe accompanied with a clip) with the lid open. Plunger of the syringe was pulled back to 1ml position and 9 μ l of Gel-Dye mix was pipetted at the bottom of the well marked in Figure 5.4 a. The prime station was closed and the plunger of the syringe pressed until it was held by the clip. After exactly 30 seconds, the plunger of the syringe was released for 5 seconds and then slowly pulled back to the 1 ml position. 9 μ l of Gel-Dye mix was also pipetted into the two wells marked in Figure 5.4 b.

c. Preparing and loading of RNA Ladder

The RNA Ladder tube (provided in the Agilent RNA 6000 nano kit) was centrifuged at 13000 g at 4°C to collect all the content together at the bottom. The content of the tube was heat denatured at 70°C for 2 minutes and cooled immediately on ice. 10 μ l aliquots were made and stored at -80°C until used. On the day of the running the samples, an RNA Ladder aliquot (pre-prepared) was defrosted on ice (extensive warming upon thawing process was avoided) and 1 μ l of RNA Ladder was pipetted into the well marked with ladder symbol (see Figure 5.4 d).

d. Loading the RNA 6000 Nano marker and samples

5 μ l of RNA 6000 Nano marker – Green (provided in the Agilent RNA 6000 nano kit) was pipetted into the wells (12 of the sample wells and 1 ladder symbol well) marked in

Figure 5.4 c. To minimise secondary structure, the RNA samples were also heat denatured at 70°C for 2 minutes before loading them on the chip. 1 µl of RNA sample was pipetted into each of the 12 of the sample wells marked in Figure 5.4 e.

e. Loading the RNA nanochip

Once the RNA nanochip was completely loaded, it was placed horizontally in the adapter of an IKA vortex mixer and vortexed for 60 seconds at 2400 rpm (initial lower speed was used to avoid spillages). The RNA nanochip was then placed carefully into the receptacle of the Agilent 2100 Bioanalyzer machine as soon as possible and the lid with electrode cartridge that fit well into the wells of the chip was closed. The checklist was checked within the software (Agilent 2100 Expert) for the electrode's detection within the wells and the Eukaryotic total RNA Nano series assay was run for the samples which lasted 20 - 30 minutes. The electrodes were decontaminated before and after the run.

f. Decontaminating electrodes

350 µl of RNaseZap was pipetted into a well of an electrode cleaner and placed into the Agilent 2100 Bioanalyzer. The lid was closed and the electrode cleaner left inside for 1 minute. The electrode cleaner was then replaced with another electrode cleaner where 350 µl of RNase free water was pipetted into a well. The lid was closed and the electrode cleaner left inside for 10 seconds before opening it to let the electrodes air dry (evaporate water) for 30 seconds.

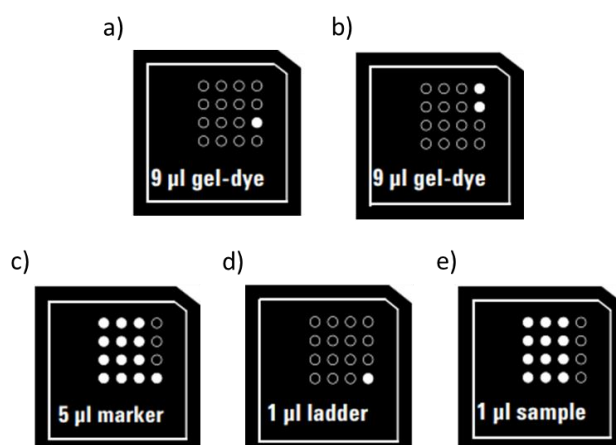


Figure 5.4 – RNA nanochip preparation

Adapted and modified from Agilent.com, 2020

5.2.3. RNA sequencing (transcriptome) and bioinformatics

See section 5.1.1 for the background on methods available for transcriptome analysis and the reason for choosing RNA sequencing for this study. The RNA samples were sent for RNA sequencing (transcriptome) to BGI Genomics with the relevant bioinformatic analysis to be completed as shown in chapter 2 Figure 2.12. The transcriptome method used by BGI was BGISEQ-500 Transcriptome for library construction which uses a DNBSEQ™ NGS technology platform, CA, USA.

The RNA sequencing data (detected reads) were filtered to get clean reads through removal of the low-quality reads, reads with adaptors and reads with unknown bases. The clean reads were mapped onto the reference genome (*Gallus gallus* (chicken), GRCg6a (Genome Reference Consortium Chicken Build 6a) based on female breed, Red Jungle fowl, with a reference GenBank assembly accession: GCA_000002315.5 (latest) on NCBI). This was achieved using HISAT (Kim, Langmead and Salzberg, 2015) which led to the detection of novel genes and spliced genes. The novel transcripts were merged with the reference transcripts to get a complete reference which was then used to map clean reads using Bowtie2 (Langmead and Salzberg, 2012) to calculate gene expression level for each sample with RSEM (Li and Dewey, 2011). Differentially Expressed Genes (DEGs) between the different groups in the comparisons studied were detected using the DEseq2 algorithms (Love, Huber and Anders, 2014) and PCA analysis carried out using princomp. Using the DEGs, KEGG pathway analysis was carried out providing functional annotations where the pathway functional enrichment was performed using phyper, a function of R.

5.2.3.1. Quality control by BGI

BGI's recommended RIN value for samples to be able to develop RNA transcriptome analysis was over 7. Hence, the samples with RIN value over 7.3 were chosen for this study and were sent to BGI. The rRNA ratio (28S/18S) of the samples used also ranged between 1.1 to 2.5. The samples were defrosted and homogenised by BGI which then experienced another quality control protocol by BGI which ensured that their RNA sequencing sample quality standards were met prior to transcriptome analysis. The

methods used by BGI for quality control analysis of the total RNA of samples were rRNA ratio and RIN value performed by Agilent 2100 Bioanalyzer (Agilent RNA 6000 Nano Kit).

The results based on these quality standards explain whether the testing sample meets the requirement of library construction and sequencing under the following three categories. Qualified means the requirements are met. Risky means the requirements are not totally met but it can be tried to construct library where the sequencing quality is not guaranteed. Unqualified means the requirements are not met and it is not suggested to use this sample. Based on historical statistics by BGI, the qualified samples have been shown to be linked with a 95% first success rate of Transcriptome Library construction as opposed to the risky or unqualified samples which carry some risks of failure.

Most of the samples used met the criteria as qualified (see Tables 5.2 and 5.3 – samples in black) with a few classified as risky (see Tables 5.2 and 5.3 – samples in red). Only one sample was unqualified as it did not meet the requirements (RIN value < 7) which was hence excluded from the further analysis and is not included in this chapter. For the samples classified as risky, their baseline was not smooth during the rRNA ratio analysis using Agilent 2100 Bioanalyzer. With the limitations present with the number of bird samples available in each pen, the risky samples were included for the Transcriptome Library construction. The RIN values have also been included in Tables 5.2 and 5.3.

Birds' allocation to pens (control diet and silicate supplemented diet) is shown in Tables 5.2 and 5.3. Row one shows the pens, row two shows the name given to the groups of the pens (growth plate and middle) and the rows 3-8 show the individual birds. Abbreviations were assigned for the bird: B for bird and Number 1, 2, 3 etc represent the number of birds out of 6 in that pen.

Although 6 birds were sampled for each pen, not all the 6 birds were selected from Day 7 of the control and silicate supplemented pens for RNA analysis due to inadequate RNA quality.

Table 5.2 – The birds' allocation to the groups for transcriptome analysis for the control pen.

Day 7 Control diet Pen		Day 14 Control diet Pen	
Day 7 GP C (RIN)	Day 7 M C (RIN)	Day 14 GP C (RIN)	Day 14 M C (RIN)
B2 C GP (8.1)	B2 C M (8.0)	B7 C GP (9.0)	B7 C M (8.2)
B3 C GP (7.8)	B3 C M (9.0)	B8 C GP (9.7)	B8 C M (7.5)
B4 C GP (7.9)	B4 C M (9.1)	B9 C GP (9.8)	B9 C M (8.4)
B6 C GP (7.5)	B6 C M (8.0)	B10 C GP (9.9)	B10 C M (8.6)
		B11 C GP (9.6)	B11 C M (8.6)
		B12 C GP (9.9)	B12 C M (8.7)

The birds in black are qualified and birds in red are risky as reported by the BGI quality control analysis.

GP – bone growth plates, M – bone middle and C – control sample

Table 5.3 – The bird's allocation to the groups for transcriptome analysis for the silicate treated pen.

Day 7 Silicate diet Pen		Day 14 Silicate diet Pen	
Day 7 GP Si (RIN)	Day 7 M Si (RIN)	Day 14 GP Si (RIN)	Day 14 M Si (RIN)
B3 Si GP (8.6)	B3 Si M (7.3)	B7 Si GP (8.9)	B7 Si M (8.3)
B4 Si GP (8.6)	B4 Si M (7.7)	B8 Si GP (9.8)	B8 Si M (8.0)
B6 Si GP (8.1)	B5 Si M (7.4)	B9 Si GP (9.6)	B9 Si M (8.7)
	B6 Si M (8.0)	B10 Si GP (9.9)	B10 Si M (8.4)
		B11 Si GP (9.8)	B11 Si M (8.4)
		B12 Si GP (9.8)	B12 Si M (8.5)

The birds in black are qualified and birds in red are risky as reported by the BGI quality control analysis.

GP – bone growth plates, M – bone middle and Si – silicon treated sample

5.2.3.2. Comparisons studied

The comparisons studied for the transcriptome analysis are shown below in Table 5.4.

Table 5.4 – Comparisons studied for the transcriptome analysis

Comparisons
<i>Day 7 GP Si vs Day 7 GP C</i>
<i>Day 7 M Si vs Day 7 M C</i>
<i>Day 14 GP Si vs Day 14 GP C</i>
<i>Day 14 M Si vs Day 14 M C</i>
<i>Day 7 M C vs Day 14 M C</i>
<i>Day 7 M Si vs Day 14 M Si</i>
<i>Day 7 GP C vs Day 14 GP C</i>
<i>Day 7 GP Si vs Day 14 GP Si</i>

5.3. Results and Discussion

5.3.1. Parameters studied

Bones' parameters, bird's weight and silicate blood plasma content are reported in Table 5.5 and Figure 5.5. To standardise between the birds as every individual would be different, right bone's parameters (used for RNA analysis) and silicate blood plasma content were normalised to the bird's weight (see Tables 5.6 and 5.7). Standardised values were used for the analysis of the different comparisons carried out to aid the transcriptome analysis later.

Independent sample t-test where equal variances between the silicate supplemented and control diets were not assumed was performed using IBM SPSS Statistics 26. T-test was performed on standardised right bone's parameters (used for RNA analysis) and silicate blood plasma content as well as the bird's weights. See Tables 5.6 and 5.7 for the p-values obtained through the t-test. P-value < 0.05 was considered significant.

Table 5.5 – Bone’s parameters, bird’s weight and blood plasma content on day 7 control and silicate treatment pen and day 14 control and silicate treatment pen.

Pen	Average Bone weight (g)		Average Bone length (cm)		Average Bone width (cm)		Average SiO ₂ in blood plasma (ppm)	Average Bird weight (g)
	Right	Left	Right	Left	Right	Left		
	Control day 7	1.19 ± 0.17	1.05 ± 0.15	4.46 ± 0.10	4.39 ± 0.14	0.36 ± 0.05		
Silicate Treatment day 7	1.27 ± 0.12	1.19 ± 0.13	4.48 ± 0.06	4.53 ± 0.15	0.35 ± 0.04	0.31 ± 0.02	4.52 ± 0.99	174.37 ± 11.02
Control day 14	3.78 ± 0.33	3.67 ± 0.29	6.19 ± 0.10	6.19 ± 0.14	0.46 ± 0.04	0.46 ± 0.04	0.67 ± 0.71	492.57 ± 30.43
Silicate Treatment day 14	3.93 ± 0.29	3.84 ± 0.32	6.14 ± 0.19	6.23 ± 0.19	0.46 ± 0.04	0.47 ± 0.04	3.15 ± 1.03	501.45 ± 36.38

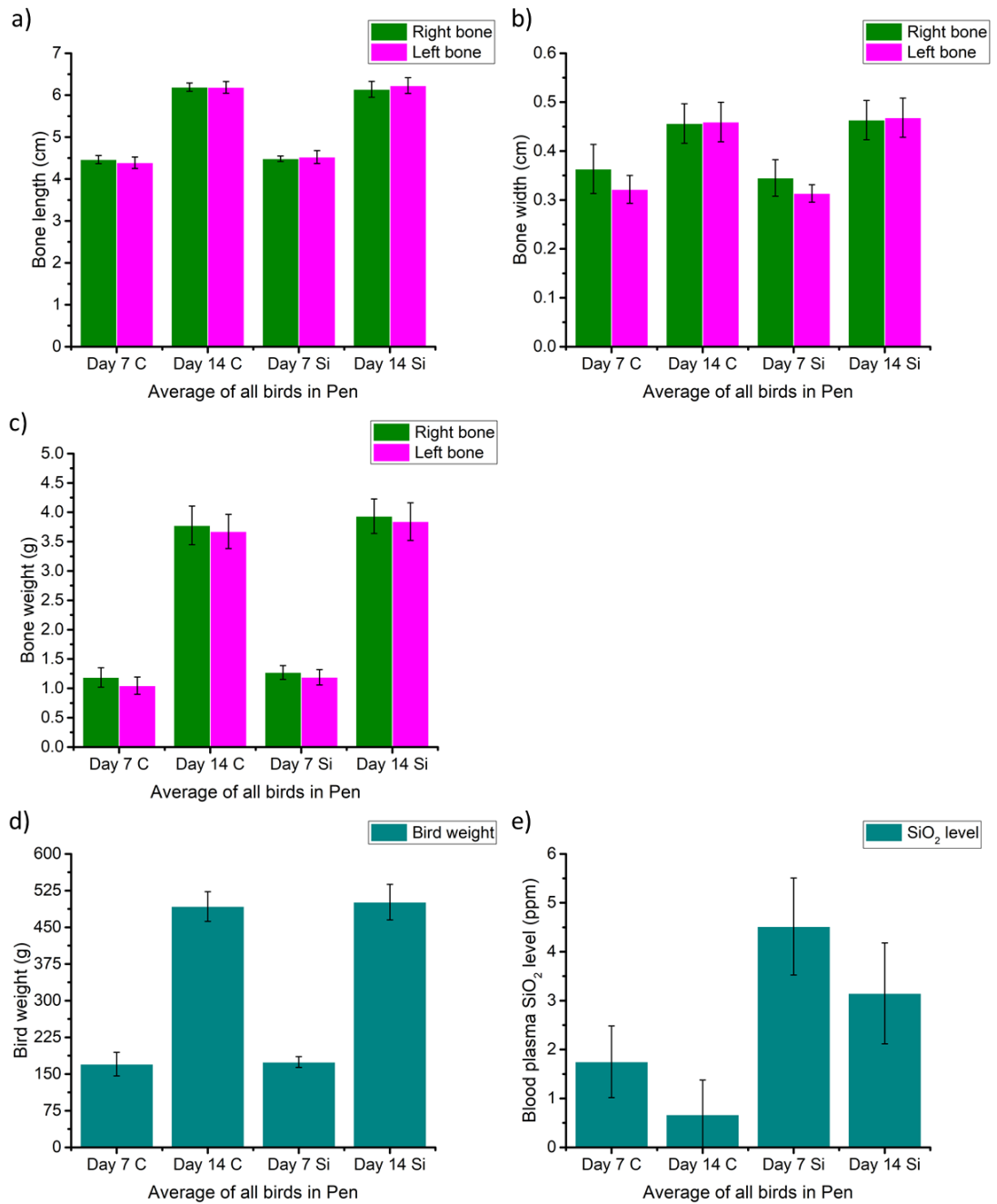


Figure 5.5 – Bone characteristics - a) height b) width c) weight and Bird characteristics - d) weight e) Blood plasma SiO₂ level

Table 5.6 – Bone’s parameters and blood plasma content normalised to bird weight on day 7 control and silicate treatment pen. *p*-value < 0.05 was considered significant.

Pen	Normalised to Average Bird weight (g)				Average Bird weight (g)
	Average Bone weight (mg/g)	Average Bone length (mm/g)	Average Bone width (mm/g)	Average SiO ₂ in blood plasma (ppm/g)	
	Right	Right	Right		
Control	6.97	0.2623	0.0214	0.0103	170.13
	±	±	±	±	±
day 7	0.98	0.0057	0.0030	0.0043	24.10
Silicate	7.47	0.2635	0.0203	0.0265	174.37
	±	±	±	±	±
Treatment	0.69	0.0038	0.0022	0.0058	11.02
day 7					
t-test	0.295	0.582	0.216	0.001	0.731
(p-value)					

Table 5.7 – Bone’s parameters and blood plasma content normalised to bird weight on day 14 control and silicate treatment pen. *p*-value < 0.05 was considered significant.

Pen	Normalised to Average Bird weight (g)				Average Bird weight (g)
	Average Bone weight (mg/g)	Average Bone length (mm/g)	Average Bone width (mm/g)	Average SiO ₂ in blood plasma (ppm/g)	
	Right	Right	Right		
Control	7.67	0.1257	0.0093	0.0014	492.57
	±	±	±	±	±
day 14	0.67	0.0020	0.0008	0.014	30.43
Silicate	7.98	0.1246	0.0094	0.0064	501.45
	±	±	±	±	±
Treatment	0.60	0.0039	0.0008	0.0021	36.38
day 14					
t-test	0.537	0.402	0.668	0.001	0.684
(p-value)					

The results for the transcriptome analysis are shown for the comparisons studied (Table 5.4) in the form of Venn diagrams, Principle Component Analysis (PCA), Differentially Expressed Genes (DEG) and enriched KEGG pathways (pathways that interlinks different biological interactions which has been generalised to different organisms through genomic information analysis) under their corresponding sub-sections. Two of the three types of DEG plots included for DEG analysis have been included in the appendix pertinent to this chapter as they displayed similar results to the one displayed within the DEGs plots section. A discussion of the results has also been included within each of these sections as appropriate.

5.3.2. Principle component analysis

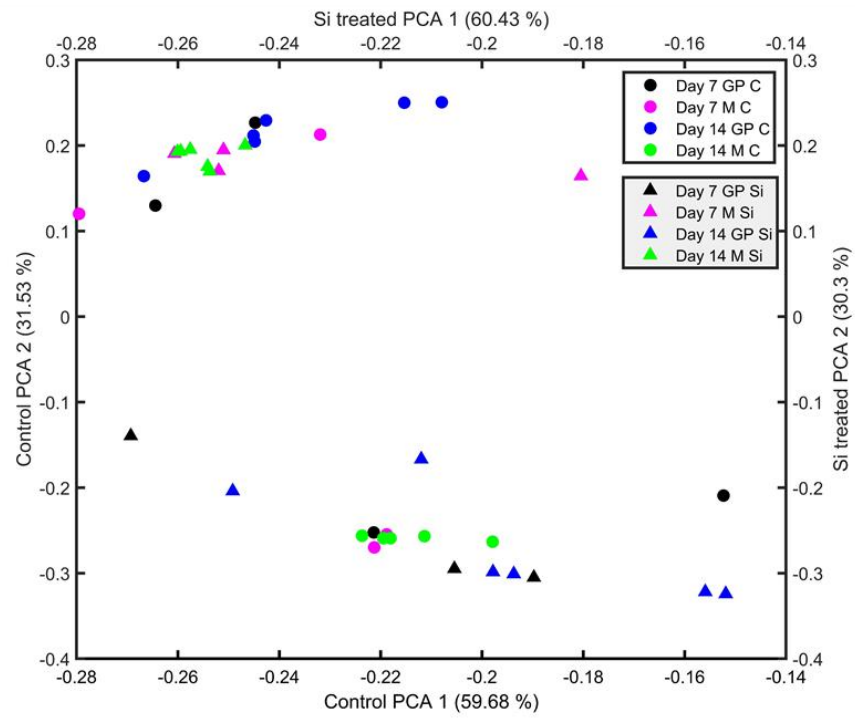
Principle component analysis, PCA, is a statistical procedure to visualise variability within a dataset through allowing analysis of gene expression correlation between samples (Ringnér, 2008). PCA uses a large dataset (gene expression values) as input and reduces the number of gene “dimensions” to a minimal set of linearly transformed dimensions to reflect the total intergroup variation within a dataset (Koch et al., 2018). Intergroup variation represents the differences between the experimental conditions in comparison to a control. PCA results are usually presented as two-dimensional plots of visualised data as principle components (PCs) along the axes which describe the variation within the dataset. PC1 describes the most variation within the data as a percentage, PC2 describes the second most, PC3 describes the third most and so on. Usually, the first two PCs can capture most of the variance; however, generating a further two PCs may also be helpful. The total variability of all PCs will always be 100%. Hence, PCA helps visualize groupings (including any among replicates) and aids in recognising technical or biological outliers. If a separation along the projected plane is observed between an experimental condition and a control, this shows that there is a treatment effect. The PCA analysis were carried out using princomp in this study.

Figure 5.6 shows the PCA plots generated using the gene expression, normalised mapped reads (RPKM), where both PC2 vs PC1 (Figure 5.6 a) and PC4 vs PC3 (Figure 5.6 b) were generated for all sample groups studied in both the control and silicon treated diets. Appendix figures 5.1 - 5.8 show the PCA plots generated using the gene

expression, normalised mapped reads (RPKM), where both PC2 vs PC1 and PC4 vs PC3 were generated (each figure shows the PC2 vs PC1 and PC4 vs PC3 plots for a comparison studied). X-axis and Y-axis represent the contributor rate of first and second principle components for PC2 vs PC1 and third and fourth principle components for PC4 vs PC3. Each sample is represented as a point where a different colour is used to represent each group.

The PCA results showed that some of the replicates of the same groups were dissimilar to the others within the same group indicating heterogeneity of samples as they are either found in a different region or plane of the plot. From the PC2 vs PC1 plots, differences between samples within the same group are seen for Day 7 GP C, Day 7 M C, Day 7 M Si, Day 14 M C, Day 14 GP Si and Day 14 M Si. Through comparing them with the risky samples (see Tables 5.2 and 5.3), it can be confirmed that this could be a source of the differences observed but is not definitive as groups Day 14 GP Si and Day 14 M Si had no risky samples but still showed differences within the samples in the group. For the purpose of this study, they were all used due to the limitations of the number of samples available. Hence, the groupings of samples within a group can be separated or simply not include the risky samples for future comparisons if they were to be repeated using another gene evaluating platform such as DAVID – bioinformatics database.

(a)



(b)

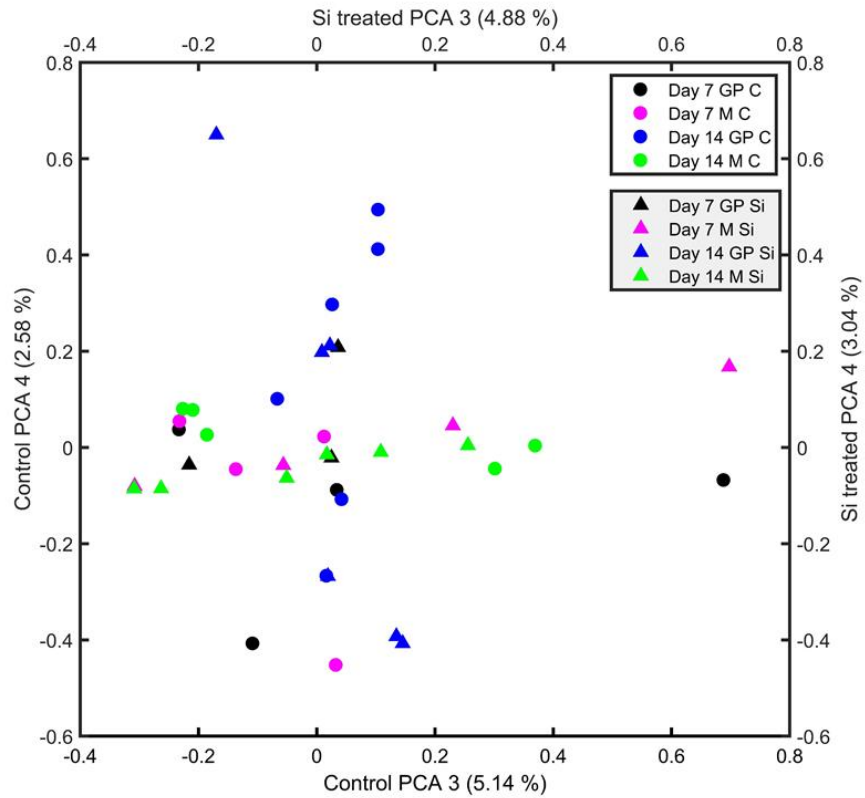


Figure 5.6 – PCA analysis for all sample groups studied in both the control and silicon treated diets (a) PC2 vs PC1 (b) PC4 vs PC3

5.3.3. Venn diagrams

Venn diagrams were used to study gene expression variations between groups. Venn diagrams show the number of genes expressed by the different groups of samples. Hence, the number of genes within each and multiple groups can be identified. See Figure 5.7 for the Venn diagrams of all the comparisons studied. It is seen that there are around 20,000 genes which were common amongst the comparisons with around 1000 - 2000 genes being different in each of the groups within the comparisons. The difference is most likely due to the different diets or due to growth of birds over time.

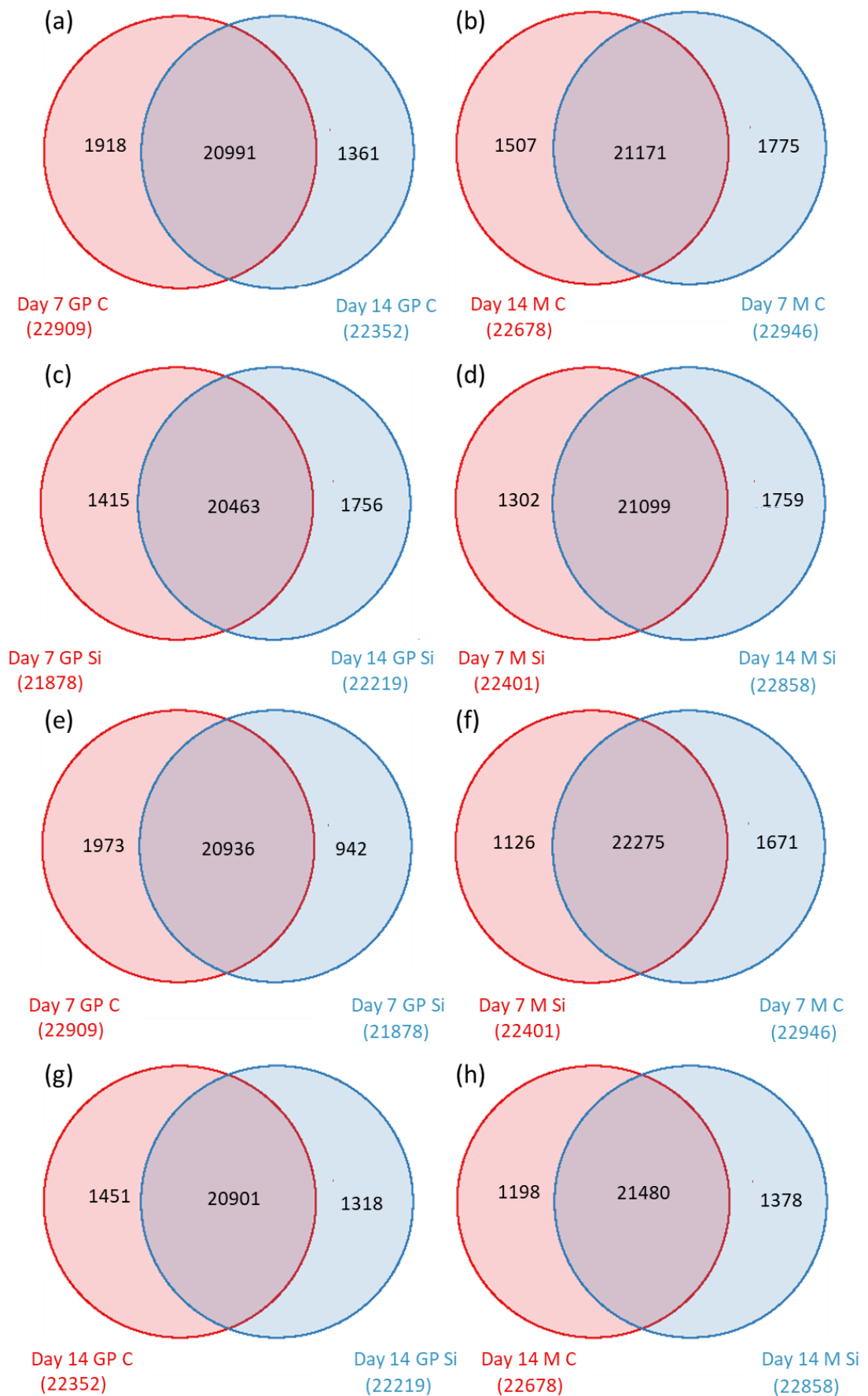


Figure 5.7 – Venn diagram of gene expression between the different comparisons studied

5.3.4. Differentially Expressed Genes

Based on the gene expression levels, Differentially Expressed Genes (DEGs) between different groups were detected and identified by using the DESeq2 algorithms (Love, Huber and Anders, 2014). DESeq2 algorithms involves normalization of the counts for a gene in each sample to the geometric mean calculated for each gene across all samples to identify the DEGs. A summary of statistics of DEGs is shown in Figure 5.8 for all the different comparisons studied (Table 5.4). DEGs were then used to identify the significantly enriched KEGG pathways (with q-value < 0.01).

The q-value is an adjusted p-value which takes into account the false discovery rate (FDR) (Lai, 2017). Applying an FDR becomes necessary when thousands of variables (e.g., gene expression levels) are measured from a small sample set (e.g., a couple of individuals). A p-value of 0.05 implies willingness to accept that 5% of all tests will be false positives. An FDR adjusted p-value (aka q-value) of 0.05 implies willingness to accept that 5% of the tests found to be statistically significant (by p-value) will be false positives. Such an adjustment becomes necessary when carrying out multiple tests on the same sample. BGI calculated FDR for each p-value (the q-value) of the enriched KEGG pathways where values below 0.01 were recommended to be significantly enriched.

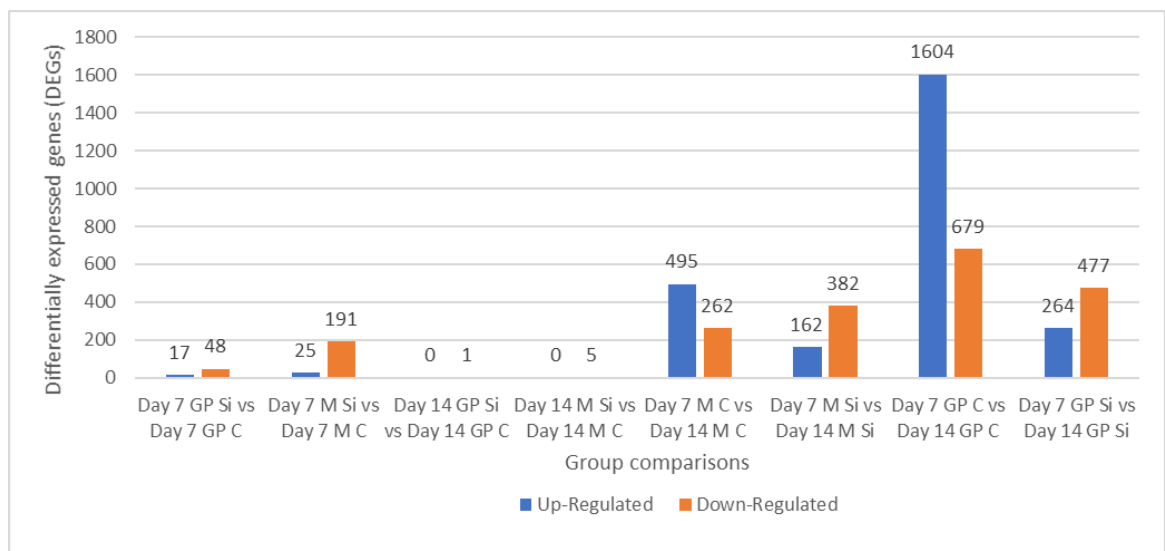


Figure 5.8 – Summary of statistics of DEGs for all the different comparisons studied.

Due to the large number of DEGs detected for the comparisons as seen in Figure 5.8, the individual genes will not be discussed. Instead, the significant genes identified through the enriched KEGG pathway of interest (osteoclast differentiation) are discussed later in the chapter under KEGG pathways.

5.3.4.1. DEG plots

Several different plots were created for DEG expression level analysis. MA plot is a plot of M (\log_2 transformed fold change (gene expression level of Group A over Group B)) against A (\log_2 transformed mean expression level of Group A and Group B). Volcano plot is a plot of $-\log_{10}$ transformed significance ($=-\log_{10}(P_{adj})$ where P_{adj} is the adjusted p-value for the significance of the DEG detected) against \log_2 transformed fold change. Scatter plot is a plot of \log_{10} transformed gene expression level of Group A against \log_{10} transformed gene expression level of Group B. The purpose of all these plots is to display the up-regulated, down-regulated and non-significant (non-)DEGs. Figures 5.9 - 5.11 show the scatter plots of the different comparisons studied (Table 5.4). The MA plots and Volcano plots are also included in Appendix Figures 5.9 - 5.11 and 5.12 - 5.14 respectively for a reference. Red, Blue and Grey dots represent up-regulated DEGs, down-regulated DEGs and non-DEGs respectively.

5.3.4.2. Heatmaps

Heatmaps were also created to show the distributions of DEGs amongst the comparisons studied (Table 5.4). See Figures 5.12 - 5.13 for the heatmaps. Heatmaps show the distribution of up and downregulated DEGs (on left y-axis) for each sample within the comparison (top x-axis showing the colour code for the samples of groups of interest within the comparison). Also, the colour code on right y-axis represents the \log_{10} transformed gene expression level of significant DEGs where a darker red or blue colour signify a higher expression level and lighter red or blue colour signify a lower expression level.

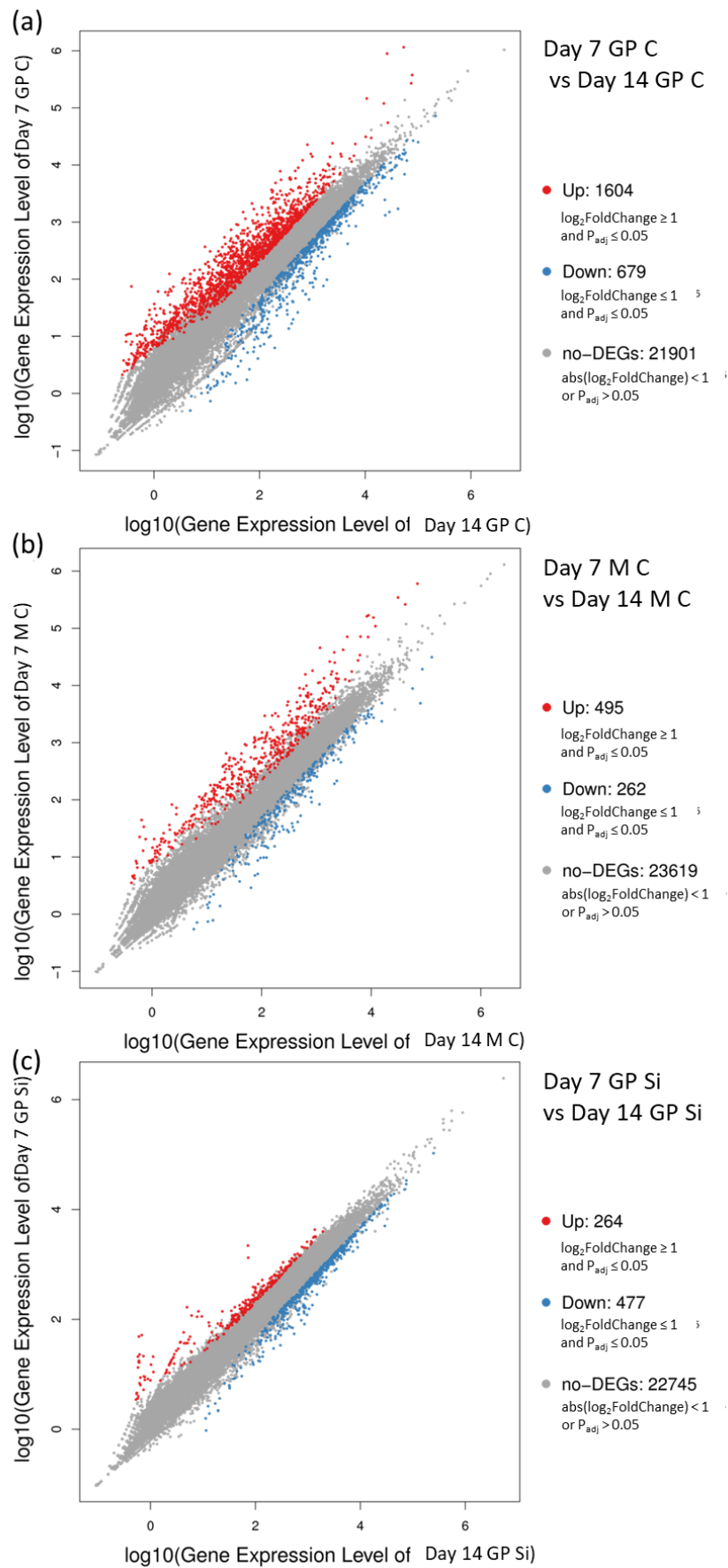


Figure 5.9 – Scatter plot of DEGs (a) Day 7 GP C vs Day 14 GP C (b) Day 7 M C vs Day 14 M C (c) Day 7 GP Si vs Day 14 GP Si

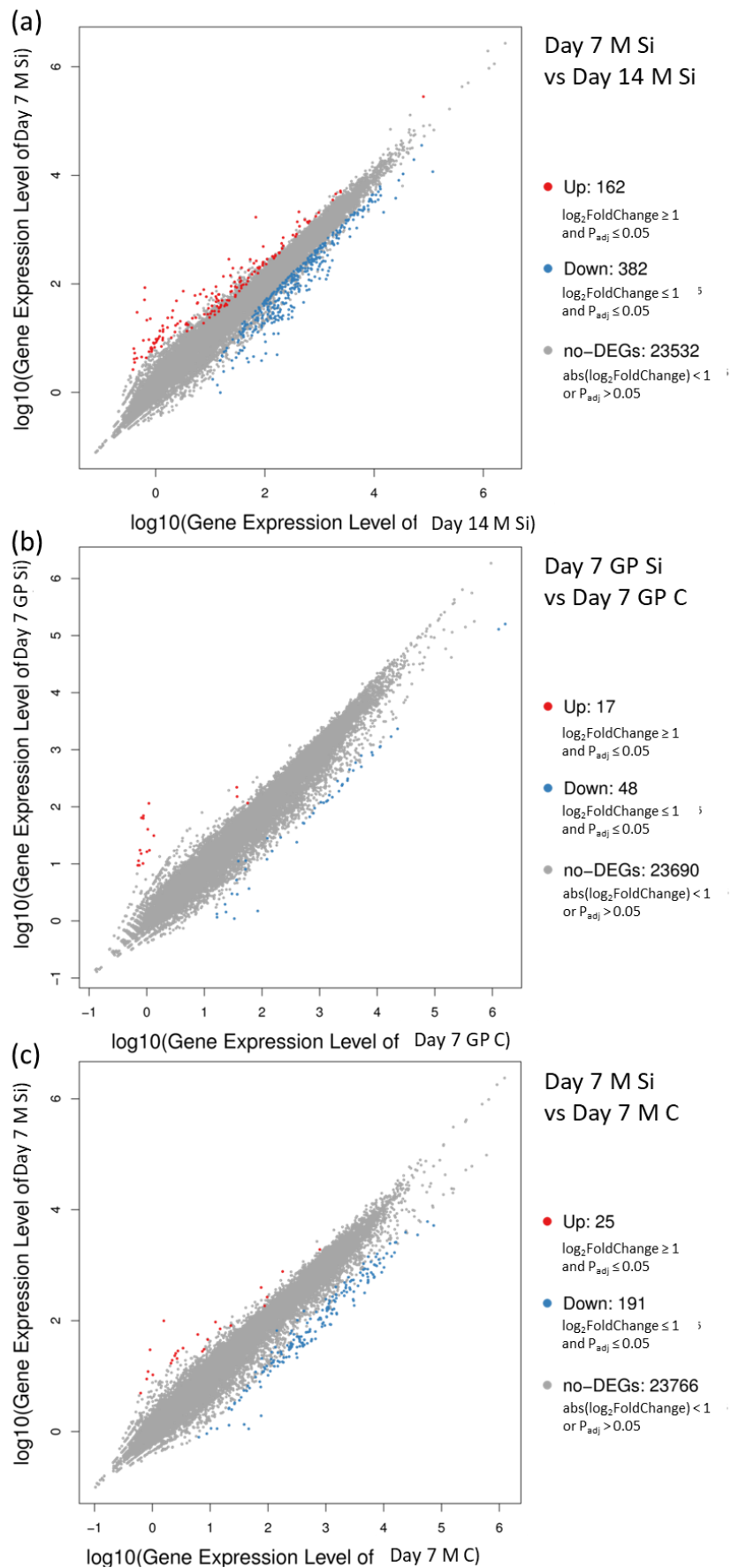


Figure 5.10 – Scatter plot of DEGs (a) Day 7 M Si vs Day 14 M Si (b) Day 7 GP Si vs Day 7 GP C (c) Day 7 M Si vs Day 7 M C

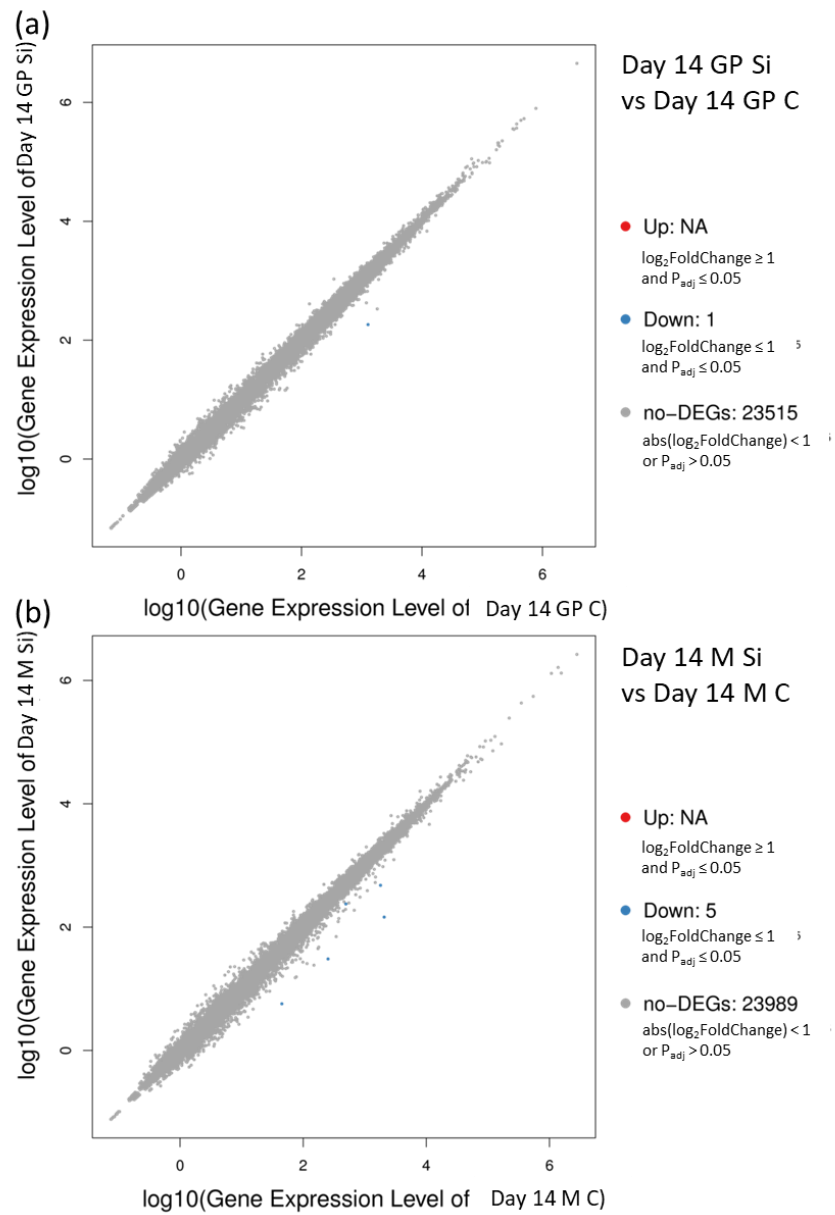


Figure 5.11 – Scatter plot of DEGs (a) Day 14 GP Si vs Day 14 GP C (b) Day 14 M Si vs Day 14 M C

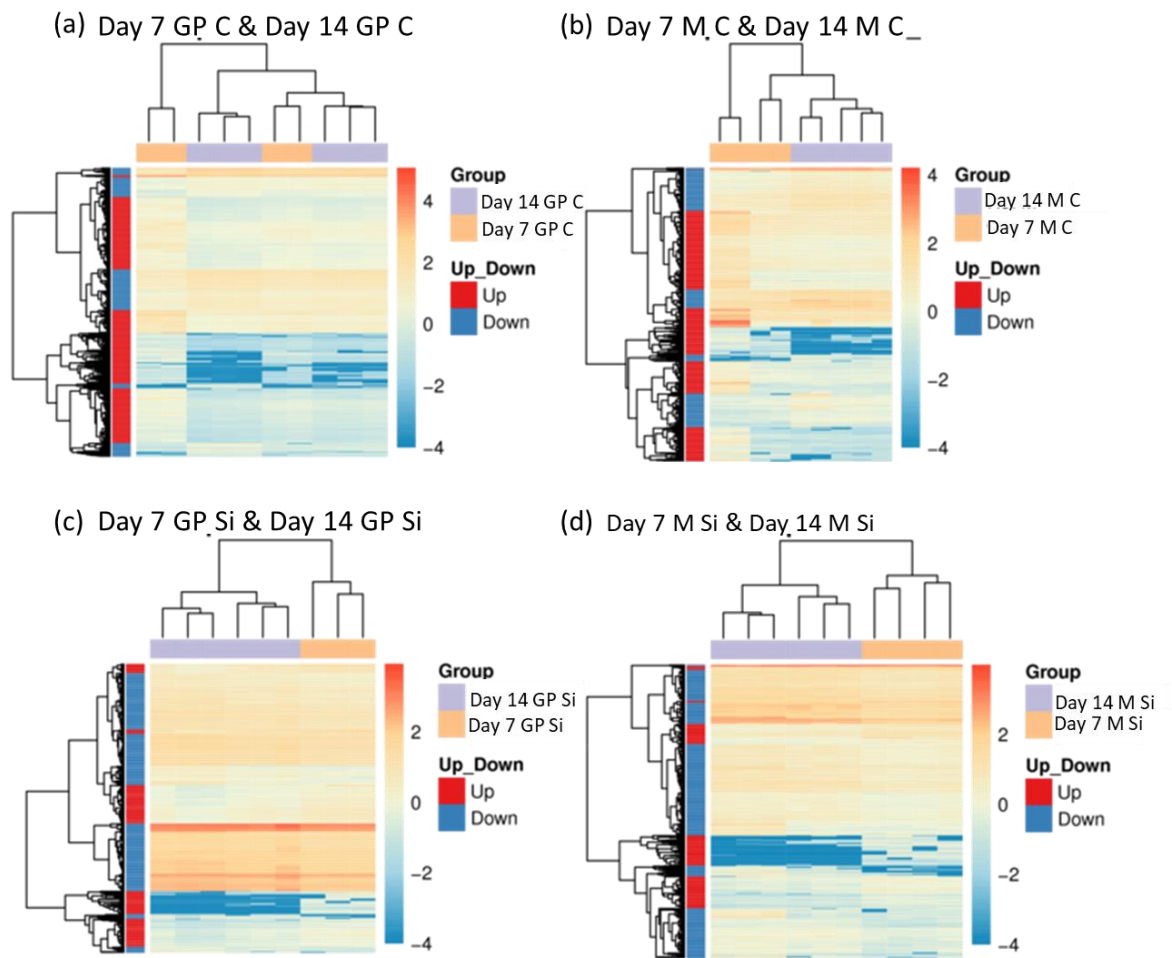


Figure 5.12 – Heatmap of DEGs (a) Day 7 GP C vs Day 14 GP C (b) Day 7 M C vs Day 14 M C (c) Day 7 GP Si vs Day 14 GP Si (d) Day 7 M Si vs Day 14 M Si

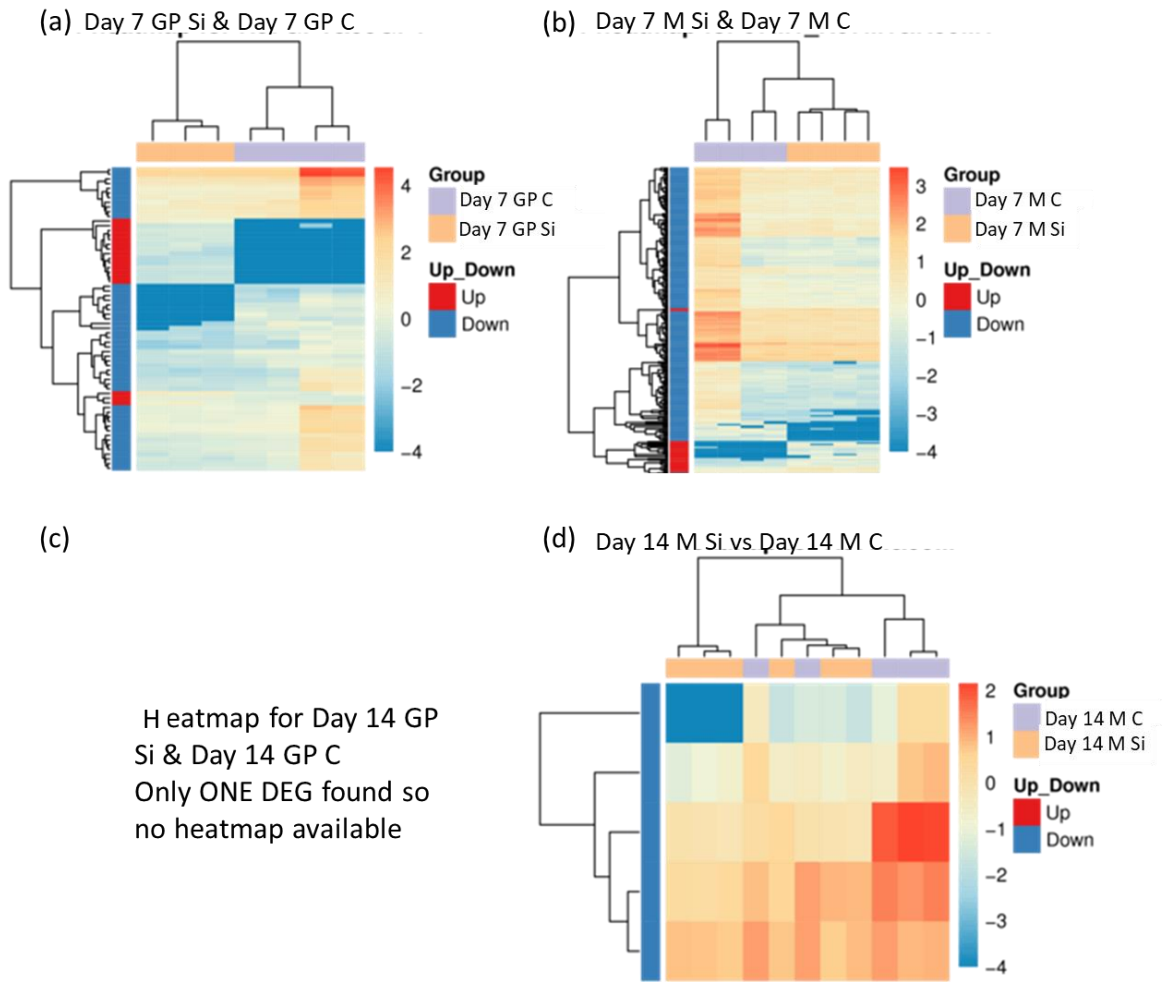


Figure 5.13 – Heatmap of DEGs (a) Day 7 GP Si vs Day 7 GP C (b) Day 7 M Si vs Day 7 M C (c) Day 14 GP Si vs Day 14 GP C (d) Day 14 M Si vs Day 14 M C

5.3.4.3. KEGG pathways and related findings

Pathway functional enrichment was performed using *phyper*, a function of R. Comparisons as stated in Table 5.4 will be discussed in this section with reference to the enriched KEGG pathways. Reference to the bone parameters, silicate blood plasma content and bird weight will also be made where appropriate. As mentioned earlier under section 5.3.1, the bone parameters (bone length, width and weight) and silicate blood plasma levels were standardised to the bird's weight in order to allow for the fact that individuals will be different. Hence, the reference to these parameters in this section will be the standardised values with units corresponding to per g of bird weight.

For the analysis of the enriched KEGG pathways ($q\text{-value} < 0.01$) from the comparisons, each of the enriched KEGG pathway will be discussed with regards to the genes involved and the cascade of different effects they may have. Many signalling cascades are usually present that affect a biological function for example where each of the cascades can either positively or negatively affect the pathway overall. Hence, cascades could either be contributing to the pathway or inhibiting it. The up or down regulation of the genes within the enriched KEGG pathways will be the main focus to conclude the likely mechanism involved for the comparisons. The pathways with diseases will not be discussed as part of the discussion as it is assumed that they are detected by chance due to the other genes being affected that also contribute to another pathway. Such pathways are included as red text within the pathway tables within the comparisons.

This paragraph explains how the enriched KEGG pathways will be discussed in this section. Within the overall discussion of the different cascades contributing to the enriched KEGG pathway (as found in the literature), a statement on the effects of the specific genes detected through the enriched KEGG pathway from a comparison will be made. A detailed key findings section will be presented towards the end of the discussion of the affected pathways which will focus on proposing the mechanism of action of the silicate supplement on bone health. As appropriate, other comparisons with the control etc. will be included to support the conclusions.

Blood plasma silicate content

Generally, it was noted that the blood plasma silicate level as SiO₂ in blood was reduced for both the control and the silicate treated diets over time where the levels were higher at day 7 compared to the day 14.

Day 7 GP Si vs Day 7 GP C and Day 7 M Si vs Day 7 M C

When comparing the bone's growth plates of silicate supplemented diet on day 7 (Day 7 GP Si) against the bone's growth plates of control diet on day 7 (Day 7 GP C), no significantly enriched KEGG pathways (q-value ≤ 0.01) were observed. Also, when comparing the bone middle of silicate supplemented diet on day 7 (Day 7 M Si) against the bone middle of control diet on day 7 (Day 7 M C), no significantly enriched KEGG pathways (q-value ≤ 0.01) were observed. This indicates that no genetic pathways are involved that indicate that silicate supplements fed to broilers compared to the control at day 7 show any significantly enriched alterations in the gene expression. This can be related to the measured bone and bird parameters.

The average bird weight at day 7 was 170.13 g \pm 24.10 g for the control pen as opposed to 174.37 g \pm 11.02 g which was slightly higher for the silicate treated pen but not significant (p-value = 0.295). The standardised silicate blood plasma content calculated as SiO₂ in blood at day 7 on the other hand was 0.0103 \pm 0.0043 ppm/g for the control pen as opposed to 0.0265 \pm 0.0058 ppm/g which was significantly higher for the silicate treated pen (p-value = 0.01). This also showcases that silicate supplement was absorbed from the silicate supplemented diet. The standardised average weight of the right bone at day 7 was 6.97 \pm 0.98 mg/g for the control pen as opposed to 7.47 \pm 0.69 mg/g which was slightly higher for the silicate treated pen but not significant (p-value = 0.731). The standardised average of the right bone length at day 7 was not affected when the control pen, 0.2623 \pm 0.0057 mm/g, was compared to the silicate treated pen, 0.2635 \pm 0.0038 mm/g (p-value = 0.582). The standardised average of the right bone width at day 7 was also not affected when the control pen, 0.0214 \pm 0.0030 mm/g, was compared to the silicate treated pen, 0.0203 \pm 0.0022 mm/g (p-value = 0.216).

Day 14 GP Si vs Day 14 GP C and Day 14 M Si vs Day 14 M C

When comparing the bone's growth plates of silicate supplemented diet on day 14 (Day 14 GP Si) against the bone's growth plates of control diet on day 14 (Day 14 GP C), no significantly enriched KEGG pathways ($q\text{-value} \leq 0.01$) were observed. Also, when comparing the bone middle of silicate supplemented diet on day 14 (Day 14 M Si) against the bone middle of control diet on day 14 (Day 14 M C), no significantly enriched KEGG pathways ($q\text{-value} \leq 0.01$) were observed. This indicates that no genetic pathways are involved that indicate that silicate supplements fed to broilers compared to the control at day 14 show any significantly enriched alterations in the gene expression. This can again be related to the measured bone and bird parameters.

The average bird weight at day 14 was $492.57 \text{ g} \pm 30.43 \text{ g}$ for the control pen as opposed to $501.45 \text{ g} \pm 36.38 \text{ g}$ which was slightly higher for the silicate treated pen but not significant ($p\text{-value} = 0.537$). The standardised silicate blood plasma content calculated as SiO_2 in blood at day 14 on the other hand was $0.0014 \pm 0.0014 \text{ ppm/g}$ for the control pen as opposed to $0.0064 \pm 0.0021 \text{ ppm/g}$ which was significantly higher for the silicate treated pen ($p\text{-value} = 0.001$). This again also showcases that silicate supplement was absorbed from the silicate supplemented diet. The standardised average weight of the right bone at day 14 was $7.67 \pm 0.67 \text{ mg/g}$ for the control pen as opposed to $7.98 \pm 0.60 \text{ mg/g}$ which was slightly higher for the silicate treated pen but not significant ($p\text{-value} = 0.684$). The standardised average of the right bone length at day 14 was not affected when the control pen, $0.1256 \pm 0.0020 \text{ mm/g}$, was compared to the silicate treated pen, $0.1265 \pm 0.0038 \text{ mm/g}$ ($p\text{-value} = 0.402$). The standardised average of the right bone width at day 14 was also not affected when the control pen, $0.0093 \pm 0.0008 \text{ mm/g}$, was compared to the silicate treated pen, $0.0095 \pm 0.0008 \text{ mm/g}$ ($p\text{-value} = 0.668$).

Day 7 M C vs Day 14 M C and Day 7 M Si vs Day 14 M Si

When comparing the bone's middle of control diet on day 7 (Day 7 M C) against day 14 (Day 14 M C), no significantly enriched KEGG pathways ($q\text{-value} \leq 0.01$) were observed. This indicates that no genetic pathways are involved that indicate that the control diet fed to broilers show any significantly enriched alterations in the gene expression when

the bone middles of control diet on day 7 (Day 7 M C) is compared to day 14 (Day 14 M C). Hence, a normal balanced diet shows no significant effects on the bone health of broiler chickens over time.

When comparing the bone middle of silicate supplemented diet on day 7 (Day 7 M Si) against day 14 (Day 14 M Si), five significantly enriched KEGG pathways (q-value ≤ 0.01) were observed. See Table 5.8 for the enriched KEGG pathways. This indicates that these genetic pathways are involved that demonstrate the effects of the silicate supplements fed to broilers when silicate supplemented diet at day 7 (Day 7 M Si) is compared to day 14 (Day 14 M Si) for bone middles. Hence, it can be concluded that these pathways affect how the bioavailable silicate is utilised to develop and strengthen bones contributing towards the bone health of the broiler chickens over time. No similar gene evaluating study has been carried out that documents the pathways that may be involved for the role of silicon in bone health. However, Kim et al., 2013 has shown that silicon exhibits antioxidative and anti-inflammatory properties which aligns with the kind of pathways observed in the current study.

Table 5.8 – Significantly enriched KEGG pathways involved for Day 14 M Si vs Day 7 M

Si

Pathway	Q-value
Rheumatoid arthritis	0.000000989
Th17 cell differentiation	0.000011896
Osteoclast differentiation	0.000011896
Phagosome	0.00235
Cytokine-cytokine receptor interaction	0.00353

a. Osteoclast differentiation pathway (see Figure 5.14 for the pathway)

The concept of osteoimmunology has been discussed in detail in reviews which explain the overlap between the skeletal and immune system and their regulatory mechanisms (Lorenzo et al., 2008; Walsh et al., 2006). Blood cells such as red and white blood cells, platelets and osteoclasts etc. originate from the same progenitor cells of the hematopoietic stem cells (HSCs) in a process called haematopoiesis which continuously

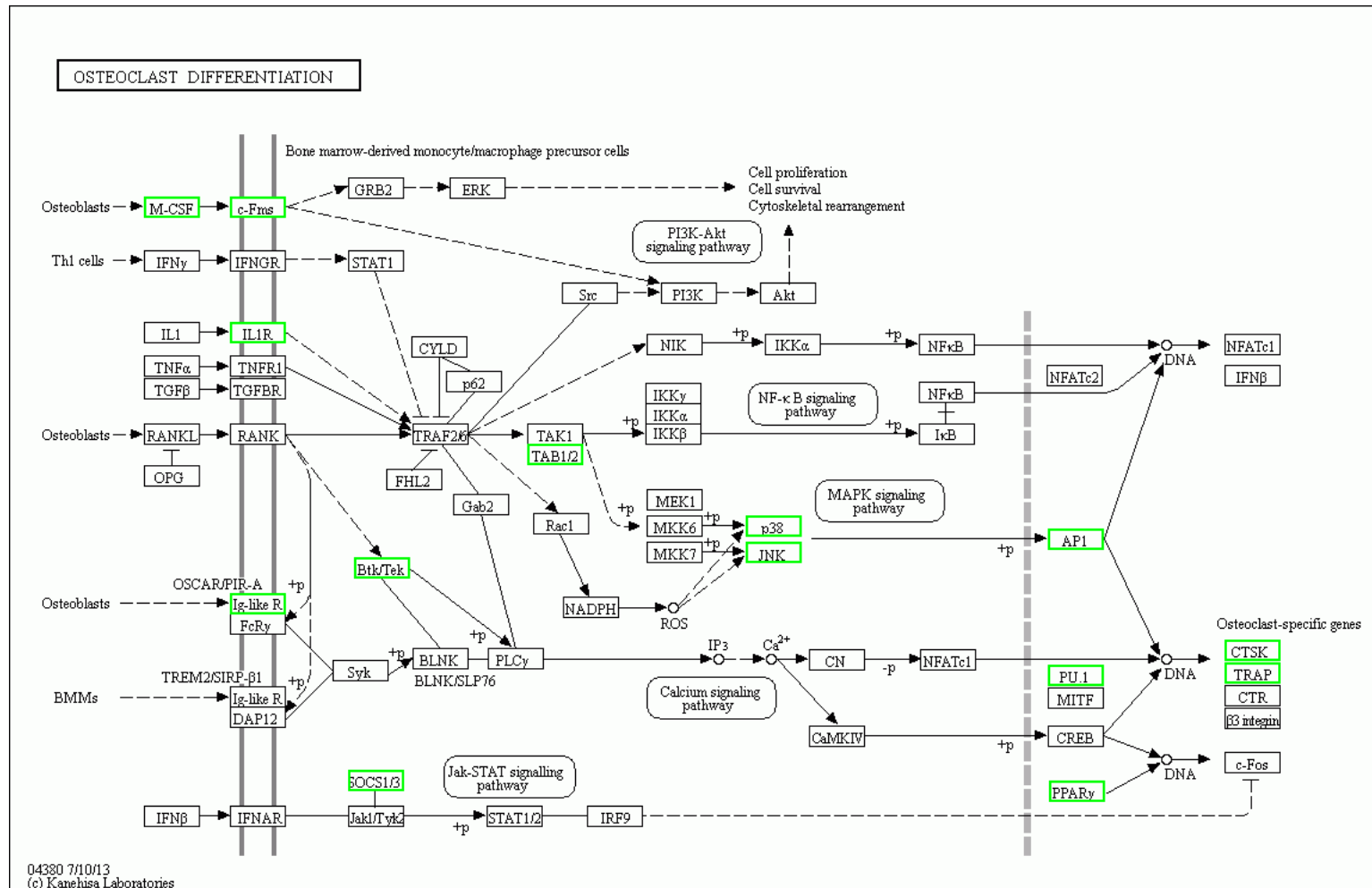


Figure 5.14 – Osteoclast differentiation pathway

Green boxes mean downregulation, red boxes mean up-regulation and black boxed genes are not affected.

replaces the cells due to their short life span throughout life (Birbrair and Frenette, 2016). Osteoclasts originate from the mononuclear precursor cells of the HSC (bone marrow), blood and spleen that fuse to form multinucleated cells such as macrophages and antigen presenting cells and dendritic cells (Miyamoto et al., 2001; Lorenzo et al., 2008; Guder et al., 2020). The environment where such differentiation occurs is termed the hematopoietic stem cell niche whose development is regulated by osteoblasts and rests in the bone marrow of living organisms (Birbrair and Frenette, 2016). Since bone provides a microenvironment for haematopoiesis, various cytokines produced by immune cells determines the fate of the bone cells leading to its regulatory effects.

Osteoblasts differentiate from a different progenitor called a multipotent mesenchymal stem cell which also differentiates to yield bone marrow stromal cells, chondrocytes and adipocytes (Walsh et al., 2006; Lee et al., 2008). Under the influence of cytokines, multipotent mesenchymal stem cells commit to the osteogenic lineage and differentiate to preosteoblasts before transforming to lining cells and mature osteoblasts. The regulatory signals responsible for osteoblast differentiation are not fully understood but several paracrine signals and cell-autonomous transcription factors at different time points during differentiation have been identified.

The existence of a physiological relationship between the normal immune system and bone metabolism was first emerged through the discovery of a cytokine, RANKL which later appeared under the field of osteoimmunology (Rho et al, 2004). RANKL is an essential factor for osteoclastogenesis which is derived from bone marrow stromal cells and osteoblasts (Wong et al., 1997; Anderson et al., 1997). RANKL expressed by activated T lymphocyte cells and dendritic cells is also known to promote dendritic cells function and survival (Yasuda et al., 1998; Lacey et al., 1998). In addition to RANKL/RANK/OPG signal axis, the relationship between the immune system and bone cells through many other cytokine molecules are implicated in the regulation of both the immune and skeletal system (D'Amelio and Isaia, 2009). The formation, maturation and survival process of osteoclasts is influenced by the activation of critical intracellular pathway and several osteoblast-derived specific cytokines. Many cytokines including the pro-inflammatory cytokines that have been shown to stimulate bone resorption include

primarily M-CSF and RANKL but also TNF- α , IL-1, IL-6, IL-7, IL-11, IL-17, IL-23, TGF β , and IFN γ (Rinaldis and De Martinis, 2016).

Bone marrow stromal cells (also known as mesenchymal stem cells) and osteoblasts produce M-CSF (Macrophage Colony Stimulating Factor) also known as CSF-1, homodimeric glycoprotein, that interacts and binds to high affinity receptors (c-fms) which are expressed on the cells of the monocyte/macrophage lineage. This induces the differentiation and proliferation of osteoclast precursors and leads to an increase in the survival of the mature osteoclasts through regulating apoptosis (Faccio et al., 2003). However, co-stimulation by both essential osteoclastogenic factors, M-CSF and RANKL, is what leads to osteoclast formation from monocytes (Faccio et al., 2003). Both M-CSF and c-fms were down-regulated for bone middle at day 7 of the silicate supplemented diet (Day 7 M Si) when compared to day 14 (Day 14 M Si) in the current study. See Figure 5.14. As mentioned above at the start of the KEGG pathways and related findings section that the affected genes in the current study will be stated within the literature discussion, this is the first time a reference to the current data is made. Similar references to the data will be made throughout the discussion of the pathways.

RANKL (also known as TNF-related activation-induced cytokine, TRANCE) is a type II membrane protein. It is a receptor activator of the NF- κ B ligand which activates its functional signalling receptor, RANK which is a trimeric protein encoded by a tumour necrosis factor receptor (TNFR) superfamily gene and is expressed on osteoclast precursors. The polypeptide RANKL is present both as a transmembrane and an extracellular receptor interacting domain expressed either bound to the surface of recruiting cells (osteoblasts) or as a proteolytically secreted soluble form (Anderson et al., 1997). The activation of RANK plays a central role in osteoclast formation and hence is essential for osteoclastogenesis and bone resorption (Hofbauer and Heufelder, 2001). RANK activation leads to the expression of osteoclast specific genes during differentiation. The stimulation of RANK leads to a decrease in osteoclast apoptosis and differentiation of osteoclast (myelomonocytic) precursors into mature multinucleated osteoclasts at the resorption site which promotes bone resorption by mature osteoclasts at neighbouring sites. A link with dwarfism has been reported due to defects with bone resorption and development of cartilaginous growth plates in mice that lack

RANK (Xing, Chen and Boyce, 2013). In mouse, RANK has also been shown to regulate calcium homeostasis through calcitropic hormones as hypocalcaemia was observed in mice lacking RANK (Li et al., 2000).

RANK pathway's activation involves interactions of TNFR-associated cytoplasmic factors (TRAFs) which are cytoplasmic adapter proteins involved in the mediation of several downstream cytokine-signalling pathways with various functions. The TRAFs protein family includes different members that bind to specific domains within the cytoplasmic domain of RANK and activate different transcriptional pathways (Darnay et al., 1998; Galibert et al., 1998). Among the TRAF family, TRAF member 6 plays an important role as an adaptor that assembles the signalling proteins required for directing osteoclast specific gene expression leading to osteoclast differentiation and activation.

TRAF members 2, 5, and 6 activate the NF- κ B, nuclear factor kappa beta signalling pathway through I κ B kinase (IKK) stimulation leading to NF- κ B activation. Three forms of IKK exist which are IKK α , IKK β and IKK γ . TRAF members 2, 5, and 6 also activate mitogen-activated protein kinases (MAPKs), including c-Jun-N-terminal kinase (JNK) through MAPK-related kinase MKK7 phosphorylation (Yamamoto et al., 2002), p38 (stress activated protein kinase) through MAPK-related kinase MKK6 phosphorylation (Li et al., 2002; Matsumoto et al., 2000), extracellular signal-regulated kinase (ERK) and Src pathway that lead to activation of activator protein-1, AP-1. Moreover, TRAF member 6 functions as a ubiquitin ligase that catalyses the formation of a poly Ubchain which also plays a role in the activation of IKK (phosphorylates to I κ B) and JNK (phosphorylates to Jun) through a proteasome-independent mechanism (Xu et al., 2009). p38, JNK and AP-1 are all down-regulated for bone middle at day 7 of the silicate supplemented diet (Day 7 M Si) when compared to day 14 (Day 14 M Si) in the current study. See Figure 5.14.

A decrease in the NF- κ B induction through TNF- α , tumour necrosis factor-alpha, was found with silicon *in vitro* which was shown to affect the signal transduction pathways that inhibits osteoblastic bone formation (Zhou et al., 2016). Hence, a reduction in the gene expression of inflammatory mediators especially TNF- α is seen with silicon (Zhou et al., 2016; Kim et al., 2013). In addition to stimulating osteoblastic differentiation and

collagen type 1 formation as shown *in vitro* (Reffitt et al., 2003), silicon has also been shown to affect the immune or inflammatory response and oxidative stress in murine macrophages (Kim et al., 2013) where silicon has been shown to reduce oxidative stress and act as an anti-inflammatory agent where the anti-inflammatory effects of silicon are due to its antioxidative properties.

The activated receptor complexes upon TRAF's interactions have shown the detection of the mitogen-activated protein kinase (MAPK)-related TGF- β -inducible kinase, TAK1 along with the TRAF-binding adapter protein, TAB1 or 2 within the complexes (Lee et al., 2002; Mizukami et al., 2002). These are important for the activation of the transcription factors AP-1 and NF- κ B which prompt osteoclast gene expression activities. Mutations in TAK1 have been associated with an inhibition of the RANK mediated activation of NF- κ B and AP-1 (Yamamoto et al., 2002). Osteoclast specific genes include CTSK, Tartrate Resistant Acid Phosphatase (TRAP), CTR and β 3-integrin from PU 1. p38 stimulation is shown to activate transcription regulator mi/Mitf which controls the expression of TRAP and CATK (Mansky et al., 2002). TAB 1 or 2, PU 1, CTSK and TRAP are all downregulated for bone middle at day 7 of the silicate supplemented diet (Day 7 M Si) when compared to day 14 (Day 14 M Si) in the current study. See Figure 5.14.

RANKL also stimulates bone synthesis through a non-genetic link through the assistance of the closely adjacent osteoblasts by a process called 'coupling' (Udagawa et al., 2000). RANKL/RANK pathway interaction is opposed by osteoprotegerin (OPG) which is a neutralizing soluble decoy receptor (TNFR related protein) produced by bone marrow stromal cells and osteoblasts (Grundt et al., 2009). Hence in RANKL/RANK/OPG signalling axis, OPG modulates the interactions between ligand and signalling receptor through blocking RANKL's binding to RANK. Anabolic agents such as oestrogens and transforming growth factor- β (TGF- β)-related bone morphogenic proteins (BMPs) also stimulate OPG's production (Udagawa et al., 2000; Schoppet et al., 2002). Mechanisms responsible for bone loss in case of estrogen deficiency (D'Amelio et al., 2008), inflammation (Leibbrandt and Penninger, 2008), and cancer induced (Fili, Karalaki and Schaller, 2009) has been linked with an imbalance between RANKL and OPG. OPG has been indicated in regulating bone density and bone mass through blocking bone resorption in various animal studies (Yasuda et al., 1998; Morony et al., 1999). RANKL

also induces the Tec tyrosine kinase, Btk, which regulates osteoclast maturation through promoting nucleation leading to osteoclastogenesis (Lee et al., 2008b). Btk/Tek is downregulated for bone middle at day 7 of the silicate supplemented diet (Day 7 M Si) when compared to day 14 (Day 14 M Si) in the current study. See Figure 5.14.

Various co-stimulatory molecules along with M-CSF and RANKL play a role in osteoclastogenesis through synergistically activating and differentiating osteoclasts (Walsh et al., 2006; Jacome-Galarza et al., 2013). The co-stimulatory adaptor proteins such as DNAX adaptor protein 12 (DAP12) and Fc receptor γ (FcRγ) that contain an immunoreceptor tyrosine based activation motif are associated with activating Ig-like R receptors expressed by myeloid cells-2 (TREM-2) and signal regulatory protein b1 (SIRPb1) and with osteoclast-associated receptor (OSCAR) and paired Ig-like receptor A (PIR-A), respectively (Mocsai et al., 2004; Koga et al., 2004). Osteoclastogenesis is promoted by OSCAR through interacting with specific motifs within fibrillar collagens of the extracellular matrix (Barrow et al., 2011) whereas the mechanism of the other factors is still unknown. Ig-like R is down-regulated for bone middle at day 7 of the silicate supplemented diet (Day 7 M Si) when compared to day 14 (Day 14 M Si) in the current study. See Figure 5.14.

Under M-CSF and RANKL treatment, the bone marrow derived and splenic dendritic cells of murine, that were activated by cytokines and presented antigens to T lymphocytes, develop into osteoclasts (Alnaeeli et al., 2006). M-CSF and RANKL also influenced the immature (as opposed to mature) dendritic cells to differentiate into osteoclast like cells through pro-inflammatory cytokines where Interleukin (IL)-1 β and (TNF- α) stimulated and Interferon (IFN)- α , IL-2, IFN- γ , and IL-4 inhibited this differentiation. (Speziani et al., 2007). Circulatory osteoclast precursor cells in blood identified as monocytes have been found to be stimulated through inducing inflammatory response with cytokines particularly TNF- α (Sørensen et al., 2006; Yao et al., 2006).

Peroxisome proliferator activated receptor (PPAR)- γ is a member of the nuclear hormone receptor superfamily which directly potentiates the induction of RANKL through c-fos, a transcriptional gene, which is an essential mediator of osteoclastogenesis (Wan et al., 2007). PPAR- γ is down-regulated for bone middle at day

7 of the silicate supplemented diet (Day 7 M Si) when compared to day 14 (Day 14 M Si). See Figure 5.14. RANKL also induces INF- β expression in osteoclast precursor cells which inhibits osteoclast differentiation through suppressing RANKL mediated c-Fos expression and hence osteoclastogenesis (Takayanagi et al., 2002). Interestingly, RANKL also induces the expression of suppressors of cytokine signalling (SOCS)-1 and SOCS-3 which act as suppressors of IFN- β signalling (Hayashi et al., 2002). The induction of such suppressors of IFN- β by RANKL may rescue the inhibitory effects of IFN- β on osteoclastogenesis. SOCS-1 and 3 are down-regulated for bone middle at day 7 of the silicate supplemented diet (Day 7 M Si) when compared to day 14 (Day 14 M Si) in the current study. See Figure 5.14.

Many cytokines and hormones induce and regulate RANKL which include IL-1, TNF- α , parathyroid hormone (PTH), prostaglandin E2 (PGE2), TGF- β , Wnt ligands, and lipopolysaccharide (Walsh and Choi, 2014). IL-1 plays a central role in the regulation of immunity and inflammation and is a potent stimulator of bone resorption through affecting osteoclastogenesis both directly and indirectly via RANKL production by osteoblasts (Lorenzo et al., 2008; Walsh et al., 2006; Lee et al., 2008). IL-1 stimulates the nucleation of the osteoclast precursors to form osteoclasts and inhibits osteoclast apoptosis leading to their survival (Jimi et al., 1999; Jimi et al., 1998). In addition, IL-1 inhibits osteoblastogenesis via modulation of MAPK through recruitment of TRAF adaptor proteins leading to a downregulation of new bone formation (Bradley and Pober, 2001). IL-1 β was also found to stimulate proliferation of osteoblasts and production of mineralized bone matrix without affecting the proliferation or differentiation of bone marrow derived mesenchymal stem cells during fracture healing process which included inflammation (Lange et al., 2009). IL-1R is down-regulated for bone middle at day 7 of the silicate supplemented diet (Day 7 M Si) when compared to day 14 (Day 14 M Si) in the current study. See Figure 5.14.

It is known that the lifespan of osteoclasts and osteoblasts is 2 weeks and 3 months respectively. From the scope of the transcriptome analysis in this study, a conclusion about osteoclast differentiation can be made. No metabolic pathway was significantly enriched that linked the role of silicon with osteoblasts directly. The much longer lifespan for osteoblasts may be the reason that no metabolic pathway was detected that

directly affected osteoblasts at day 7 compared to day 14 for bone middle of silicate supplemented diet. The high activity of osteoblasts is what is most likely recruiting osteoclast differentiation in the first place. It is also likely that the osteoblasts are unaffected by the silicate supplementation and the high activity of osteoblasts promoting bone formation is unaffected with the observed osteoclast differentiation at day 14 when compared to day 7 for bone middle of silica supplemented diet. Hence, the role of silicon in bone formation and/or health is through promoting or reducing osteoclast differentiation which depends on the blood silicon levels. Though the osteoblasts are not directly affected up to day 14 of the analysis of this study, osteoclast differentiation may indirectly affect the osteoblasts through coupling (Udagawa et al., 2000) or other regulatory mechanisms such as protein modifications that are out of the scope of the current study or genetic pathways which are not detectable this early in time and may become prominent later over the development of the bones.

The gene expression level of all the DEGs identified under the osteoclast differentiation pathway was also studied for all the sample groups used in the comparisons (see Figures 5.15 - 5.19). The genes include: CHIR-AB-600, LOC100857375, LOC101747711, MAPK9, PPARG, LOC107049514, CSF1R, MAPK11, CTSK, ACP5, LOC107050283, LOC112529962, CHIR-AB1, LOC107055386, LOC112531100, LOC107050017, SPI1, LOC100857409, LOC107050774, LOC107049125, CSF1, IL1R1, TEC, SOS3 and SYNGR3. The main finding that was interpreted is that the reads (FPKM) are higher for day 7 and 14 of the control middles (Day 7 M C and Day 14 M C) when compared to day 7 and 14 of the silicon supplemented middles (Day 7 M Si and Day 14 M Si) respectively. This is seen with many of the DEGs. This also explains that the bioavailable silicon levels reduce these levels significantly when day 7 is compared to day 14 for the silicate supplemented diet of bone middle. However, this is not the case with the control diet. For the DEGs that also show the significant fold change in the control diet comparisons of the bone middle day 7 compared to day 14 (see Figure 5.18 b - e and Figure 5.19 a - c), they are not enough to affect the osteoclast differentiation pathway in that comparison as no enriched KEGG pathways are observed. Also, the significant fold changes observed in other comparisons (see Figure 2.19 d and e) do not show any enriched KEGG pathways which mean that they are also not enough to affect the osteoclast differentiation pathway.

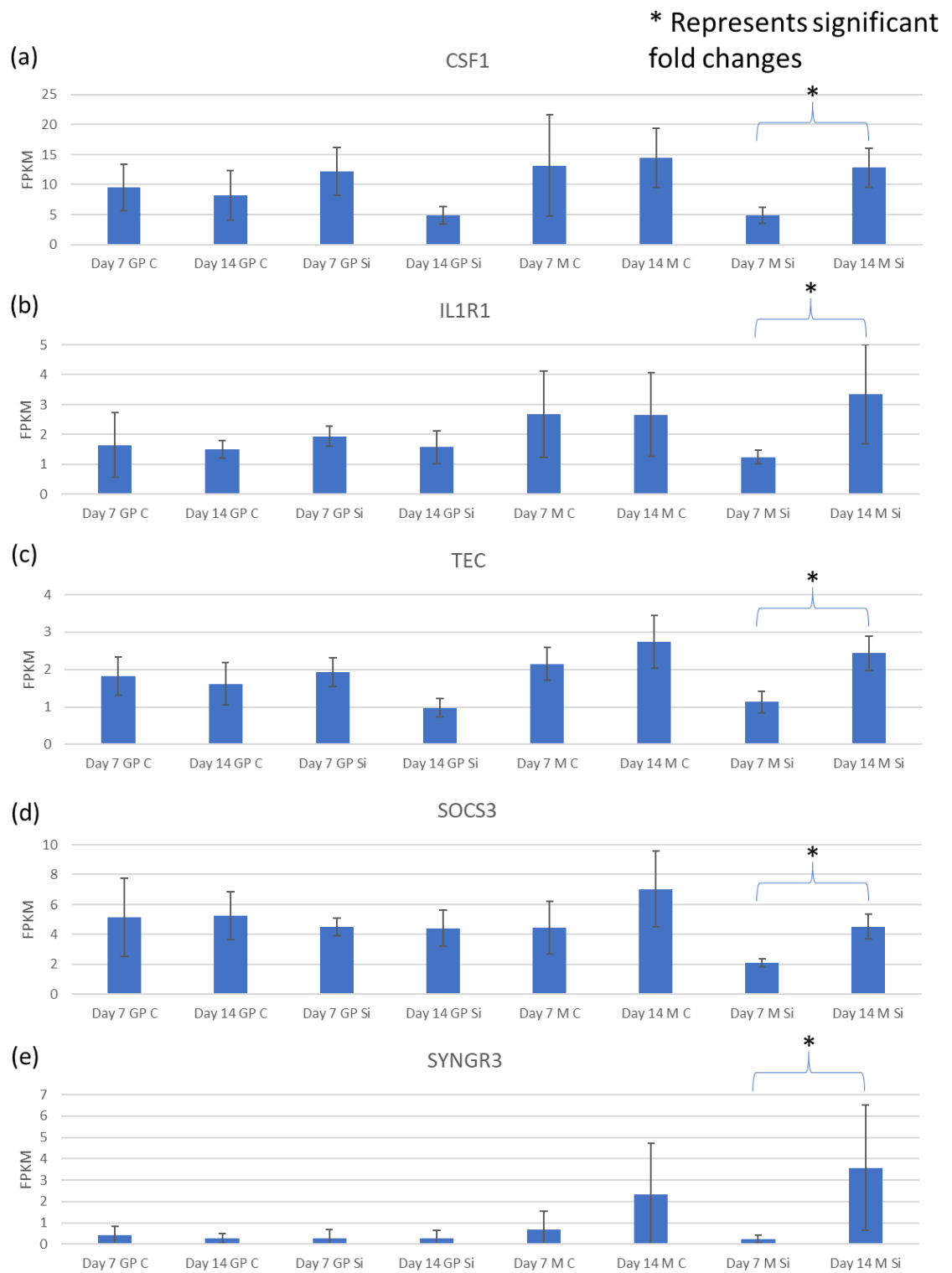


Figure 5.15 – Gene expression level of the DEGs identified under osteoblast differentiation pathway (a) CSF1 (b) IL1R1 (c) TEC (d) SOS3 (e) SYNGR3

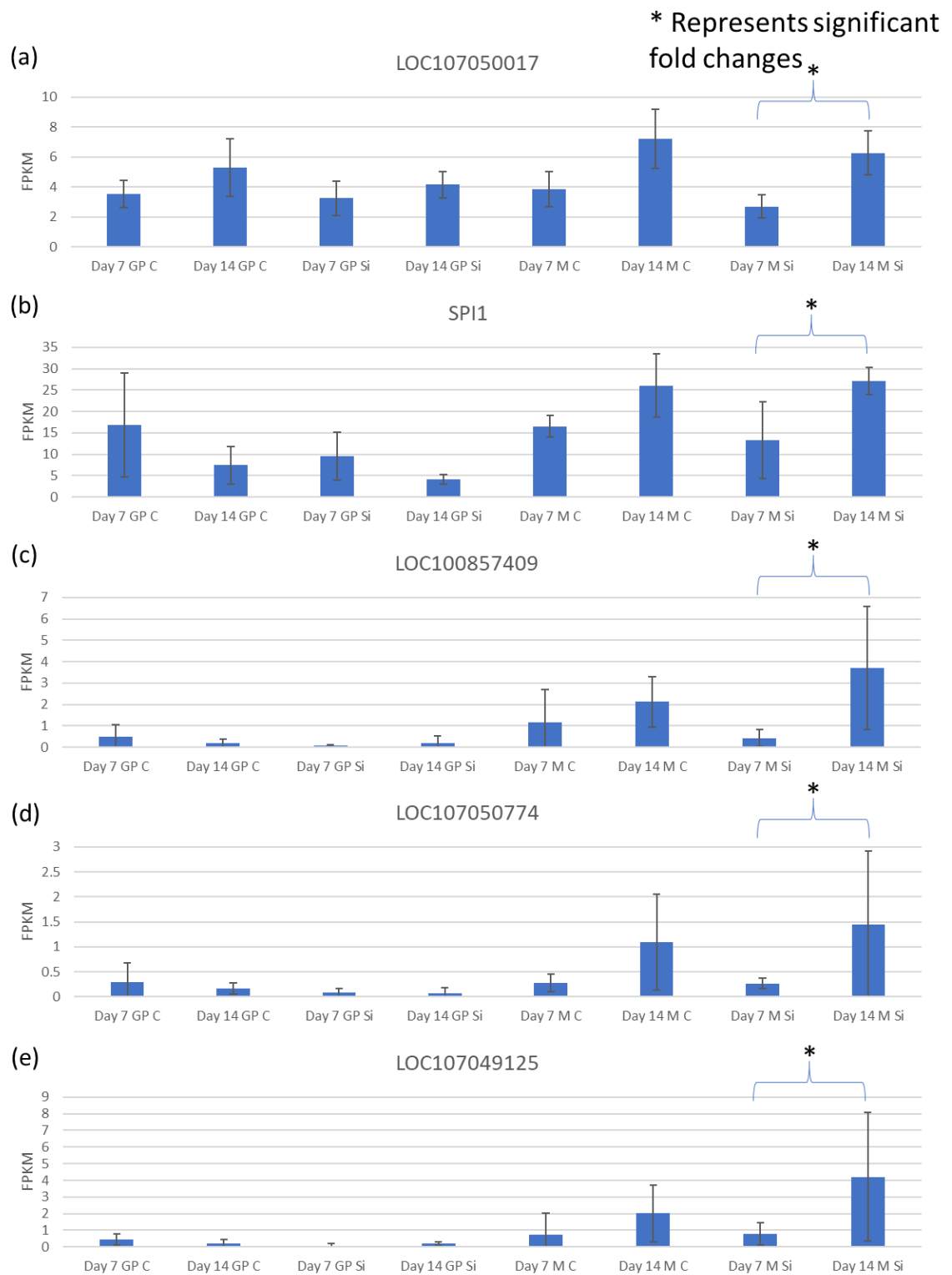


Figure 5.16 – Gene expression level of the DEGs identified under osteoblast differentiation pathway (a) LOC107050017 (b) SPI1 (c) LOC100857409 (d) LOC107050774 (e) LOC107049125

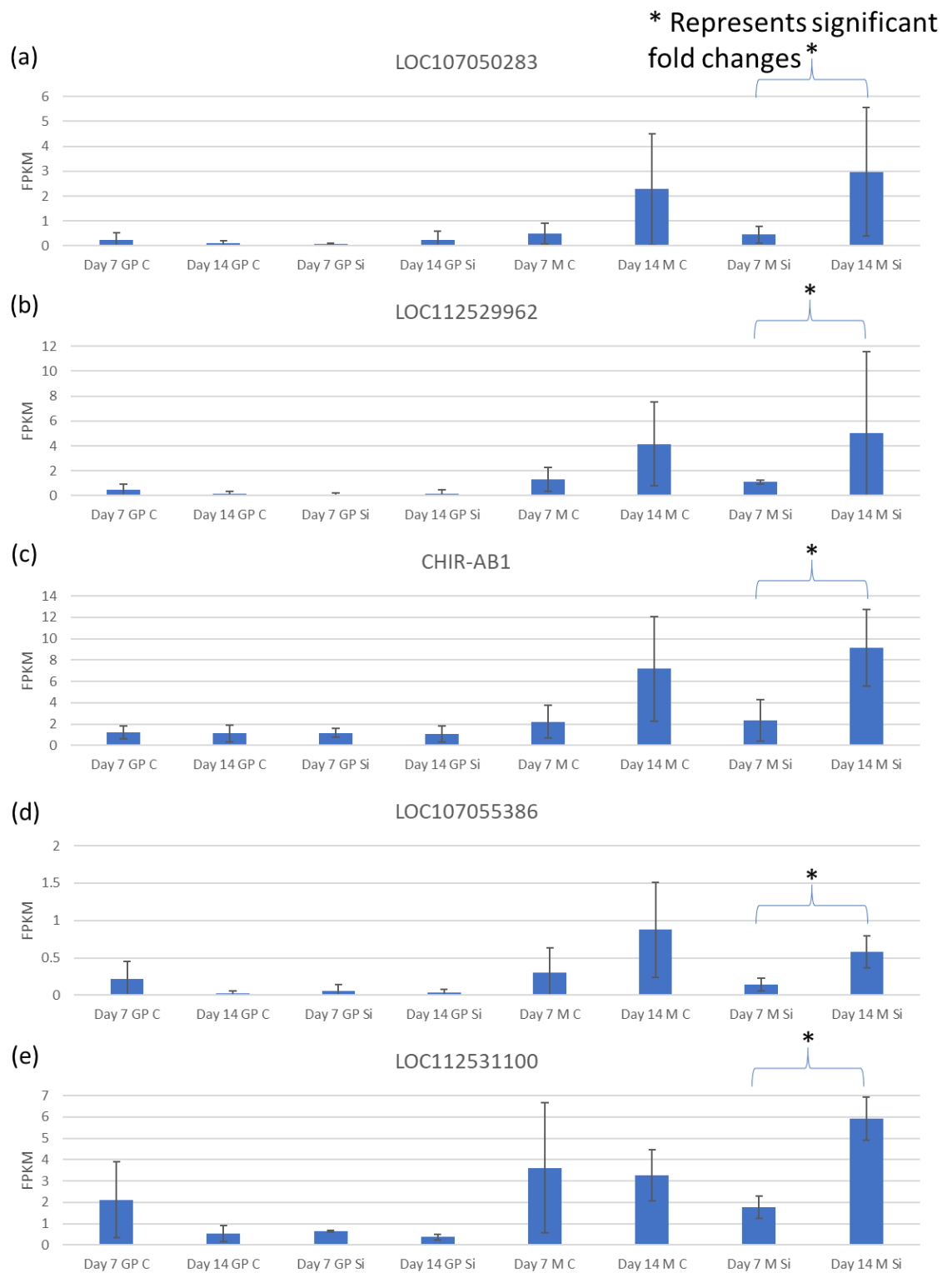


Figure 5.17 – Gene expression level of the DEGs identified under osteoblast differentiation pathway (a) LOC107050283 (b) LOC112529962 (c) CHIR-AB1 (d) LOC107055386 (e) LOC112531100

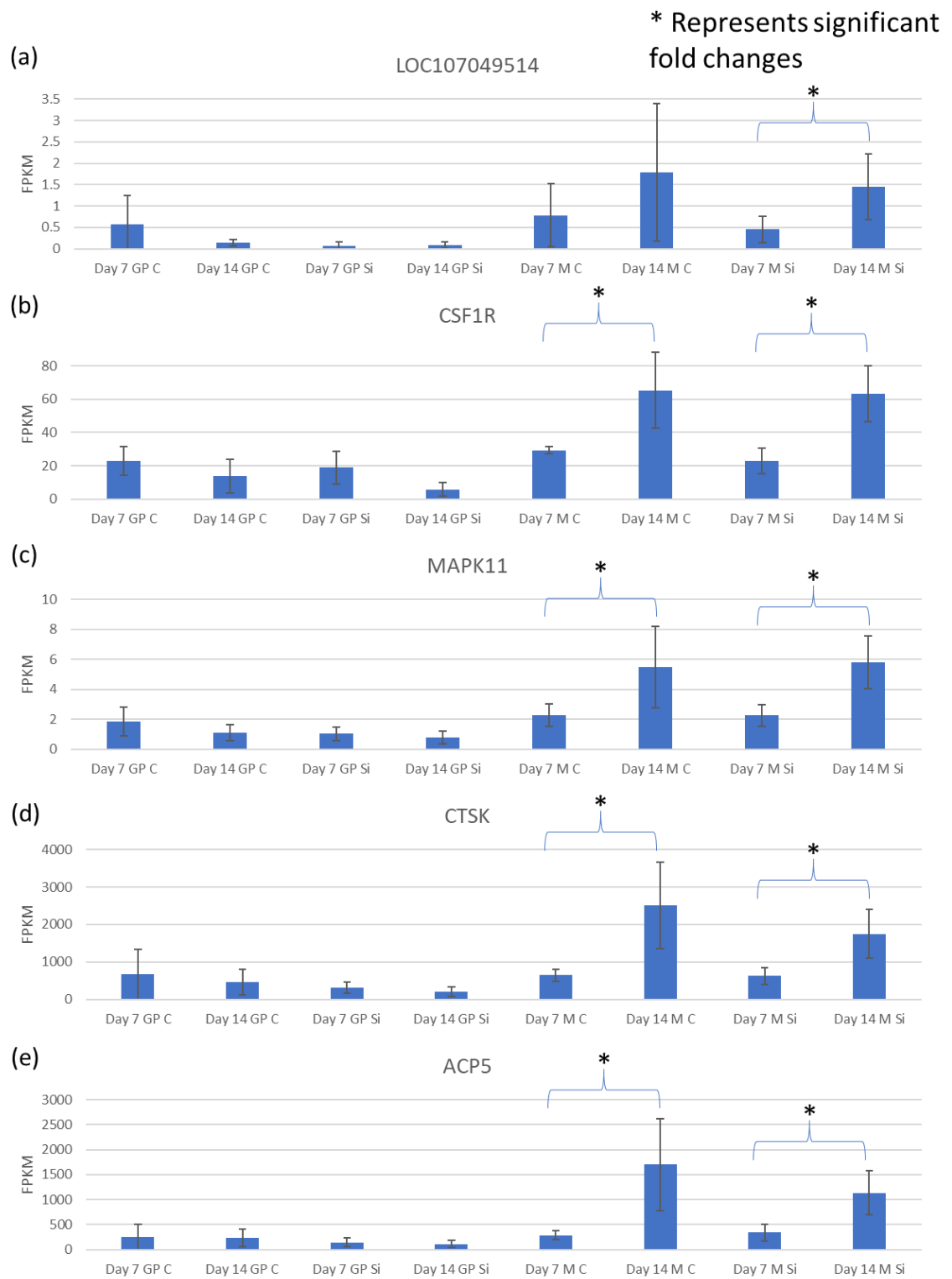


Figure 5.18 – Gene expression level of the DEGs identified under osteoblast differentiation pathway (a) LOC107049514 (b) CSF1R (c) MAPK11 (d) CTSK (e) ACP5

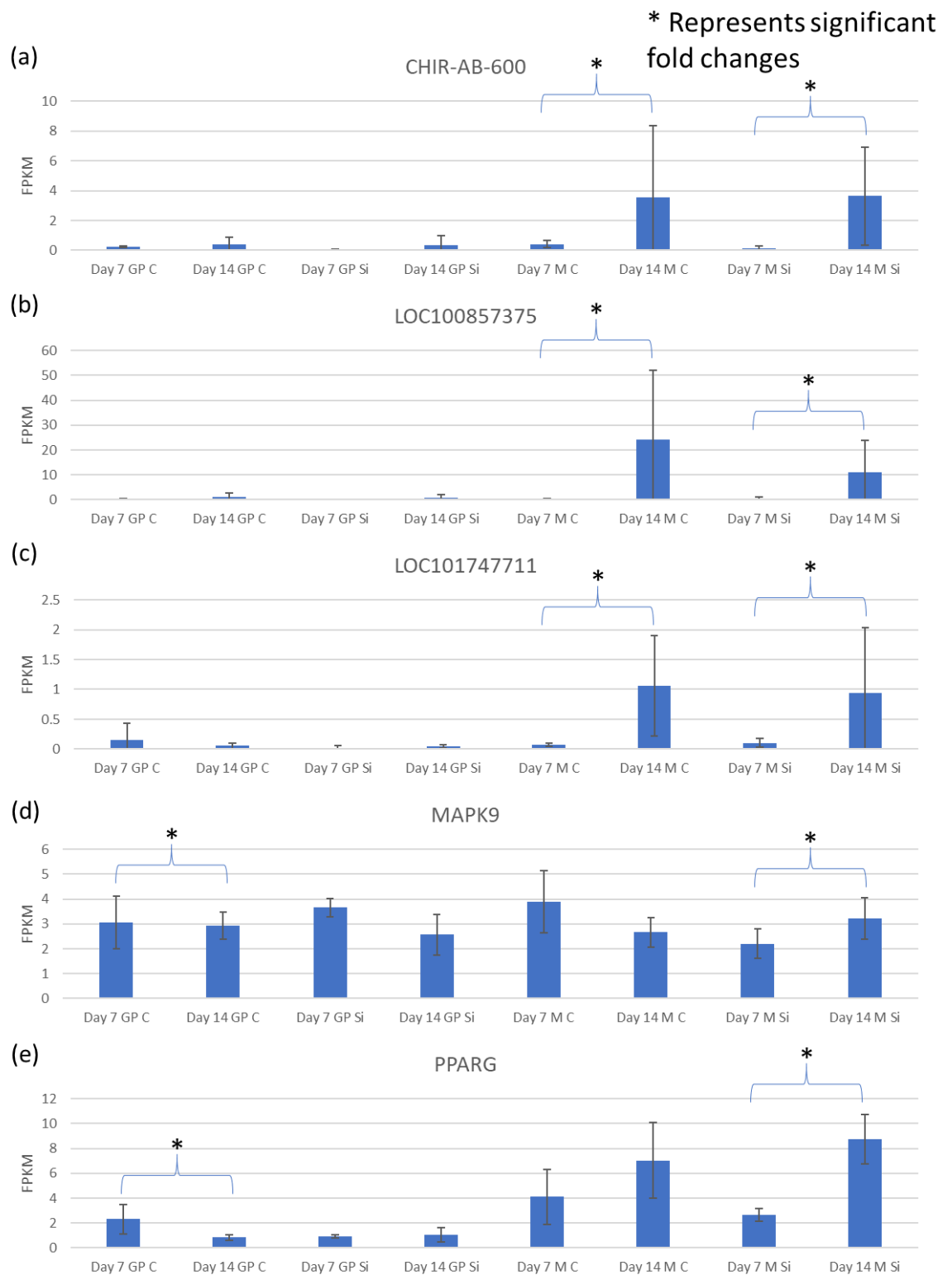


Figure 5.19 – Gene expression level of the DEGs identified under osteoblast differentiation pathway (a) CHIR-AB-600 (b) LOC100857375 (c) LOC101747711 (d) MAPK9 (e) PPARG

b. Th17 cell differentiation pathway (see Figure 5.20 for the pathway)

As stated earlier, the bone marrow derived and splenic dendritic cells are capable of presenting antigens to T-lymphocytes (Alnaeeli et al., 2006). The antigen presenting cells promote Th17 cell differentiation. Th17 cells produce cytokine IL-17A/IL-17F (Raphael et al., 2015). Different cascades either promote or inhibit the Th17 cell differentiation.

IL-1/IL-1R signalling and IL-6/IL-6R signalling are found to be critical for the commitment to and Th17 cell differentiation (Wilson et al., 2007; Acosta-Rodriguez et al., 2007). IL-6 is found to be the critical differentiation factor for Th17 cell generation (Bettelli et al., 2006). Stimulation of its corresponding receptor IL-6R on CD4 T cells leads to an activation of STAT 3 which induces the activation of lineage associated master transcription factor, retinoic acid-related orphan receptor gamma t (ROR γ t) (Zhou et al., 2007; Zeng et al., 2007). Though both STAT 3 and ROR γ t co-operatively induce Th17 cell differentiation leading to IL-17 production, the overexpression of ROR γ t as opposed to STAT 3 alone can induce Th17 cell differentiation (Zhou et al., 2007). IL-1 β R and IL-6R are down-regulated and ROR γ t is up-regulated for bone middle at day 7 of the silicate supplemented diet (Day 7 M Si) when compared to day 14 (Day 14 M Si) in the current study. See Figure 5.20.

JAKs are tyrosine kinases which are found bound to cytoplasmic regions of type I and II cytokine receptors (Darnell, Jr., 2012). Activation of those receptors initiate JAK transphosphorylation which leads to a subsequent recruitment of the phosphorylation of STATs in the cytoplasm (O'Shea and Murray, 2008). Phosphorylated STATs translocate to nucleus and activate or suppress the specific DNA expression (Levy and Darnell, 2002; O'Shea et al., 2013). Jak1/3 and STAT 6 are downregulated for bone middle at day 7 of the silicate supplemented diet (Day 7 M Si) when compared to day 14 (Day 14 M Si) in the current study. See Figure 5.20.

Activation of major histocompatibility complex (MHC) class II molecules by the antigen presenting cells activate the T-lymphocytes through T-cell receptor (TCR) such as TCR α and CD35 which are protein complexes found on its surface (Holling et al., 2004; Ono and Takayanagi, 2017). This leads to a series of steps to activate I κ B which also

stimulates the IL-17 production. In addition to the role of p38 and JNK mentioned under osteoclast pathway, p38 MAPK leads to nuclear translocation of interferon regulatory factor (IRF-4) which also stimulates the osteoclast formation (Nakashima and Haneji, 2013). Retinoid X receptors (RXR) are members of nuclear receptor superfamily of ligand dependent transcription factors that modulate immune responses and regulate physiological processes such as osteoclast differentiation leading to bone remodelling (Menéndez-Gutiérrez et al., 2015). On the other hand, Transcription factor, T-bet, inhibits the Th17 differentiation by preventing RUNX1 mediated activation of the ROR γ t gene (Lazarevic et al., 2010). MHCII, TCR α , CD35, p38, JNK, Jun, RXR, T-bet and I κ B are all down-regulated for bone middle at day 7 of the silicate supplemented diet (Day 7 M Si) when compared to day 14 (Day 14 M Si) in the current study. See Figure 5.20.

Amongst all T cells, Th17 cells are known as the most osteoclastogenic subset that produce IL-17 (Sato et al., 2006; Kotake et al., 1999). IL-17 is shown to stimulate the release of RANKL by osteoblasts and osteocytes (Li et al., 2015, Sato et al., 2006) which is responsible for the osteoclastogenic activity in bone. Hence, a link between the T cells and osteoblasts and osteocytes through the cytokine IL-17 is found which regulates RANKL production (Li et al., 2015). With all the up-regulation and down-regulation of the genes observed within the T cell differentiation pathway when the bone middle at day 7 of the silicate supplemented diet (Day 7 M Si) is compared to day 14 (Day 14 M Si), IL-17 is not affected even with the up-regulation of ROR γ t which is the main transcription factor of T cell differentiation. Without IL-17, this enriched KEGG pathway is most likely to have no effect on osteoclastogenesis or on bone health.

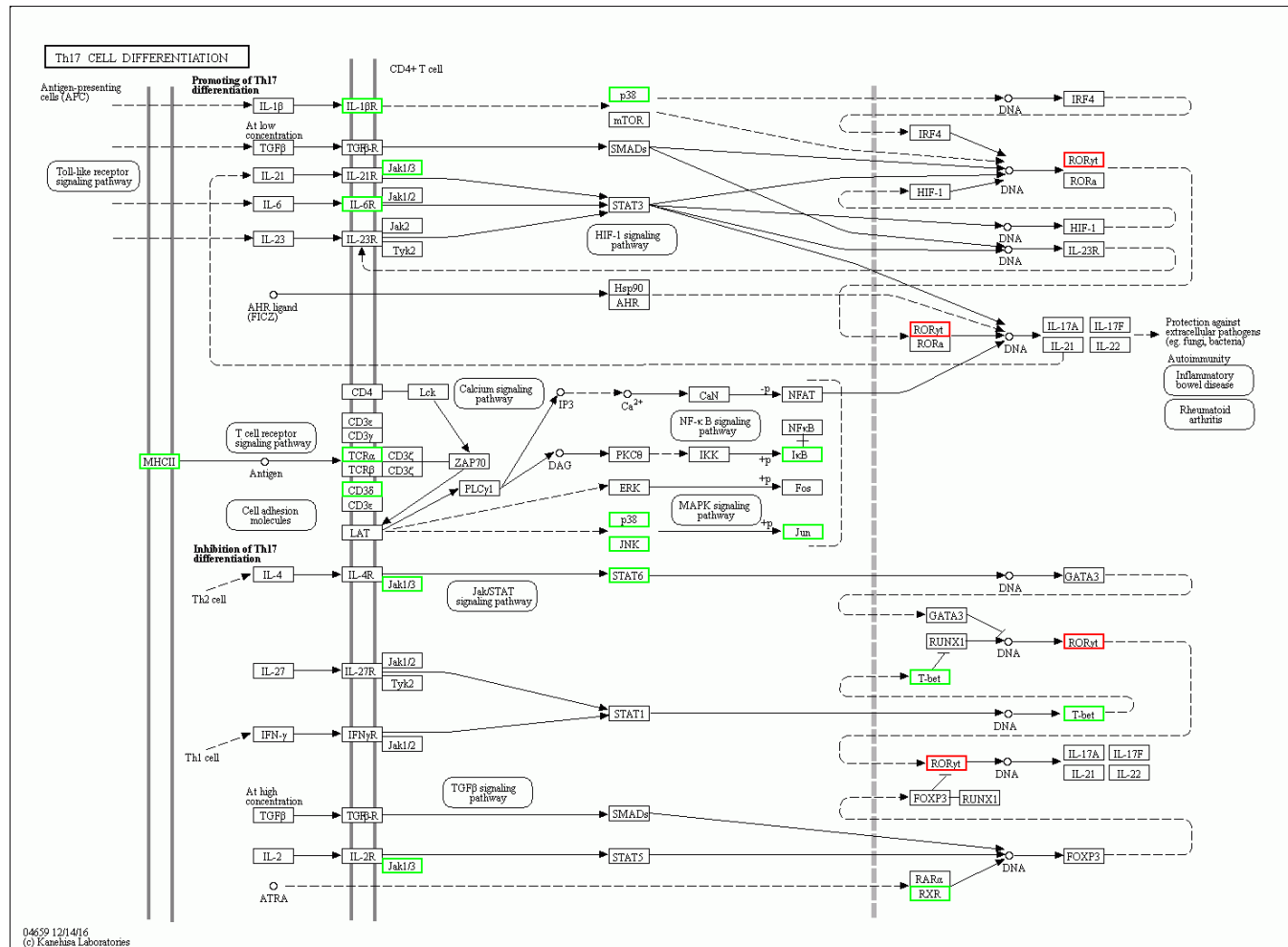


Figure 5.20 – Th17 cell differentiation pathway

Green boxes mean downregulation, red boxes mean up-regulation and black boxed genes are not affected.

c. Other enriched KEGG pathways

Of the enriched KEGG pathways when the bone middle at day 7 of the silicate supplemented diet (Day 7 M Si) is compared to day 14 (Day 14 M Si), the Osteoclast differentiation and Th17 cell differentiation are discussed in detail above as they appeared the most relevant towards understanding the role of silicon in animals. The other pathways were Rheumatoid arthritis, Phagosome and Cytokine-cytokine receptor interaction.

For the phagosome pathway, phagosomes play a role in remodelling, inflammation and fighting infectious agents (immune response) through ingesting and lysing foreign or apoptotic cells (Rosales and Uribe-Querol, 2017). A downregulation of genes associated with ER mediated phagocytosis and phagocytosis promoting receptors was observed when the bone middle at day 7 of the silicate supplemented diet (Day 7 M Si) is compared to day 14 (Day 14 M Si). Hence, it can be concluded that there is less phagocytosis happening or being promoted which may be due to reduced osteoclast differentiation leading to fewer osteoclasts (also act as phagocytes) reducing bone resorption which helps in the retention of bone.

For the Cytokine-cytokine receptor interaction pathway, there are up-regulated or downregulated genes corresponding to different cytokines when the bone middle at day 7 of the silicate supplemented diet (Day 7 M Si) is compared to day 14 (Day 14 M Si). Their role will again be linked to osteoimmunology where the cytokines (important ones already discussed above) either promote or inhibit osteoclastogenesis.

For the Rheumatoid arthritis pathway, a downregulation of genes has been observed which means an inhibition of the pathway when the bone middle at day 7 of the silicate supplemented diet (Day 7 M Si) is compared to day 14 (Day 14 M Si). Since it was a disease pathway, it has not been discussed. However, its downregulation shows that it complements the osteoclast differentiation pathway such that bone resorption is suppressed.

Key findings

The affected genes which are observed within the significantly enriched KEGG pathways were discussed above for comparison of bone middle at day 7 of the silicate supplemented diet (Day 7 M Si) compared to day 14 (Day 14 M Si). It can be concluded that there is less osteoclast differentiation, no effects on IL-17 production from Th17 cell differentiation and reduced phagocytosis at day 7 as opposed to day 14 which correlates with the blood silicon levels which are high at day 7 as opposed to day 14. Hence, relatively higher blood silicon levels lead to reduced osteoclast differentiation initiation which may promote osteoblast differentiation leading to osteogenesis. Also, most importantly, this significant enrichment of the pathways is not seen when bone middle at day 7 of the control diet (Day 7 M C) is compared to day 14 of the control diet (Day 14 M C). Hence, it can be concluded that these effects are only seen when a silicate supplemented diet is fed to the broiler chicken over a period of time. This study provides an insight into the genes that are responsible for silicon's role in bone health and homeostasis. Though no gene evaluating studies similar to the current study is available, other literature available show that silicon given over a period of time indeed reduces bone resorption (Kim et al., 2008).

Day 7 GP C vs Day 14 GP C and Day 7 GP Si vs Day 14 GP Si

When comparing the bone's growth plates of control diet on day 7 (Day 7 GP C) against day 14 (Day 14 GP C), no significantly enriched KEGG pathways ($q\text{-value} \leq 0.01$) were observed. This indicates that no genetic pathways are involved that indicate that the control diet fed to broilers does not show any significantly enriched alterations in the gene expression when the bone growth plates from control diet on day 7 (Day 7 GP C) is compared to day 14 (Day 14 GP C). Hence, a normal balanced diet shows no significant effects on the bone health of broiler chickens over time.

When comparing the growth plates of silicate supplemented diet on day 7 (Day 7 GP Si) against day 14 (Day 14 GP Si), four significantly enriched KEGG pathways ($q\text{-value} \leq 0.01$) were observed. See Table 5.9 for the enriched KEGG pathways. This indicates that these genetic pathways are involved that demonstrate the effects of the silicate supplements

fed to broilers when silicate supplemented diet at day 7 (Day 7 GP Si) is compared to day 14 (Day 14 GP Si) for growth plates. Hence, it can be concluded that these pathways affect how the bioavailable silicate is utilised to develop and strengthen bones contributing towards the bone health of the broiler chickens over time. Again, no similar gene evaluating study are available that documents the pathways that may be involved for the role of silicon in bone health. However, Kim et al., 2013 has shown that silicon exhibits antioxidative and anti-inflammatory properties which aligns with the kind of pathways observed in the current study.

Table 5.9 – Significantly enriched KEGG pathways involved for Day 14 GP Si vs Day 7 GP Si

Pathway	Q-value
Glutathione metabolism	0.00088
Ribosome	0.00089
Alzheimer's disease	0.00332
Huntington's disease	0.00859

a. Glutathione metabolism pathway (see Figure 5.21 for the pathway)

For Glutathione pathway, there are upregulated and downregulated genes corresponding to the synthesis or breakdown of Glutathione (GSH) in a cyclic manner when the bone growth plates at day 7 of the silicate supplemented diet (Day 7 GP Si) is compared to day 14 (Day 14 GP Si). The fold changes of the genes (1.11.1.12, 1.11.1.9, 1.8.1.7, 2.5.1.18, 3.4.19.13 and 2.3.2.2 – see Figure 5.21) were carefully considered to estimate the production of the GSH being up or down regulated. Although the other upregulated and downregulated genes may also affect the GSH, they do not form a direct link which would lead to any effects on GSH. A net fold change contributing towards a higher production or retention of GSH is observed.

GSH is an essential thiol compound naturally present in eukaryotic systems (Fahey and Newton, 1987). GSH plays many physiologically important roles such as iron metabolism, scavenger for free radicals, provides a reservoir for some amino acids and detoxifies the metal ions (electrophiles) (Meister and Anderson, 1983; Penninckx, 2002).

GSH is oxidised to Glutathione disulfide (GSSG) where their ratio acts as a redox buffer for the cells for their proper functioning (Kaplowitz et al., 1985). The cellular redox state is a balance of the reactive oxygen species (ROS) as either radicals or non-radicals and antioxidants (Valko et al., 2006; Valko et al., 2007). The redox state of the cell regulates the cellular processes such as proliferation, differentiation, repair and apoptosis (Ray et al., 2012).

The redox state changes also regulate the bone remodelling process which allows for bone homeostasis (Wauquier et al., 2009). An imbalance of the redox state generates oxidative stress which leads to cellular damage and affects the bone remodelling process such that an imbalance of the osteoblasts and osteoclasts occurs which has been linked with skeletal system disorders such as osteoporosis (Baek et al., 2010). A review discusses that ROS favours osteoclastogenesis through the activation of different pathways such as MAPK, p38, JNK and RANKL which has effects on bone resorption as discussed under the osteoclast differentiation pathway earlier where antioxidants such as GSH opposes this effect leading to bone formation through osteoblast activity (Domazetovic, 2017). Hence, an effect of GSH on the ROS system is what is responsible for the effects of silicon on bone health and homeostasis through the inhibition of osteoclastogenesis and possible promotion of osteoblast activity.

silicate supplemented diet (Day 7 GP Si) is compared to day 14 (Day 14 GP Si). This indicates a reduced ribosome activity. Since ribosomes are responsible for the synthesis of proteins for cellular functions such as repairing damage or directing chemical processes (Zhou et al., 2015), a downregulation would indicate that there is a lower demand of proteins for repairing damage to cells for example at day 7 of the silicate supplemented diet (Day 7 GP Si) when compared to day 14 (Day 14 GP Si) for growth plates. This aligns with the reduced bone resorption activity leading to a probable osteogenesis through osteoblasts.

For Alzheimer's disease and Huntington's disease pathways observed when the bone growth plates at day 7 of the silicate supplemented diet (Day 7 GP Si) is compared to day 14 (Day 14 GP Si), they were not considered in the discussion as they are disease pathways.

Key findings

The affected genes which are observed within the significantly enriched KEGG pathways were discussed above for the comparison of bone growth plates at day 7 of the silicate supplemented diet (Day 7 GP Si) to the day 14 (Day 14 GP Si). It can be concluded that there is reduced ROS activity through upregulation of GSH and reduced ribosome activity at day 7 as opposed to day 14 which correlates with the blood silicon levels which are high at day 7 as opposed to day 14. Hence, a relatively higher blood silicon level leads to a reduced ROS activity leading to reduced osteoclast activity which may promote osteoblast activity leading to osteogenesis. This can be confirmed with reduced ribosomal activity due to reduced repair of cells confirming reduced bone resorption. Also, most importantly, this significant enrichment of the pathways is not seen when bone growth plates at day 7 of the control diet (Day 7 GP C) is compared to day 14 of the control diet (Day 14 GP C). Hence, it can be concluded that these effects are only seen when the silicate supplemented diet is fed to the broiler chicken over a period of time. This study brings an insight into the genes that are probably responsible for the silicon's role in bone health and homeostasis. Though no gene evaluating studies similar to the current study is available, other literature available show that silicon given over a period of time indeed reduces bone resorption (Kim et al., 2008).

5.4. Conclusion

Silicon has previously been shown to affect the immune or inflammatory response and oxidative stress in murine macrophages (Kim et al., 2013) where it was found to reduce oxidative stress and act as an anti-inflammatory agent where the anti-inflammatory effects of silicon were due to its antioxidative properties. The findings of the current study align with this. Upon researching to understand the role of silicon in animals, a gap existed in the research which required gene evaluation analysis using an animal tissue. The current study has given great insight into the biological pathways that are involved in leading to the anti-inflammatory and antioxidative effects. From the current study, it can be concluded that Si supplementation suppresses the production of inflammatory cytokines and mediators through possibly suppressing the radical scavenger activity which directly or indirectly down-regulates gene expression of inflammatory mediators (as discussed earlier) when the silicate blood plasma levels are high. However, the levels needed to be able to see this effect cannot be estimated as it is out of scope of this study. Though an overall proposal for the role of silicon on bone health can be made, it is important to note that the mechanism of the role of silicon is understood to be different between the two parts (middle and growth plates) of the tibia bone studied which may or may not be interlinked.

Interestingly, the above results are only observed when the silicate supplemented diets are compared over time for both the bone middle and growth plates. No significant pathways are observed on the day 7 or day 14 when the silicate supplemented diet is compared to control diet for both the bone middle and growth plates. This means that the expression of genes affected is not significant enough to be observed on the day 7 or day 14 when the silicate supplemented diet is compared to control diet. Since the size of the bone was not seen to be affected during this research trial, it is likely that the average bone density may be affected.

If the above transcriptome analysis was to be repeated, it would be beneficial to have a larger set of birds for an increased number of samples per group. Due to the limited number of samples per group in the current study, the risky samples as identified by BGI were used for the Transcriptome library construction. As stated earlier, the risky samples

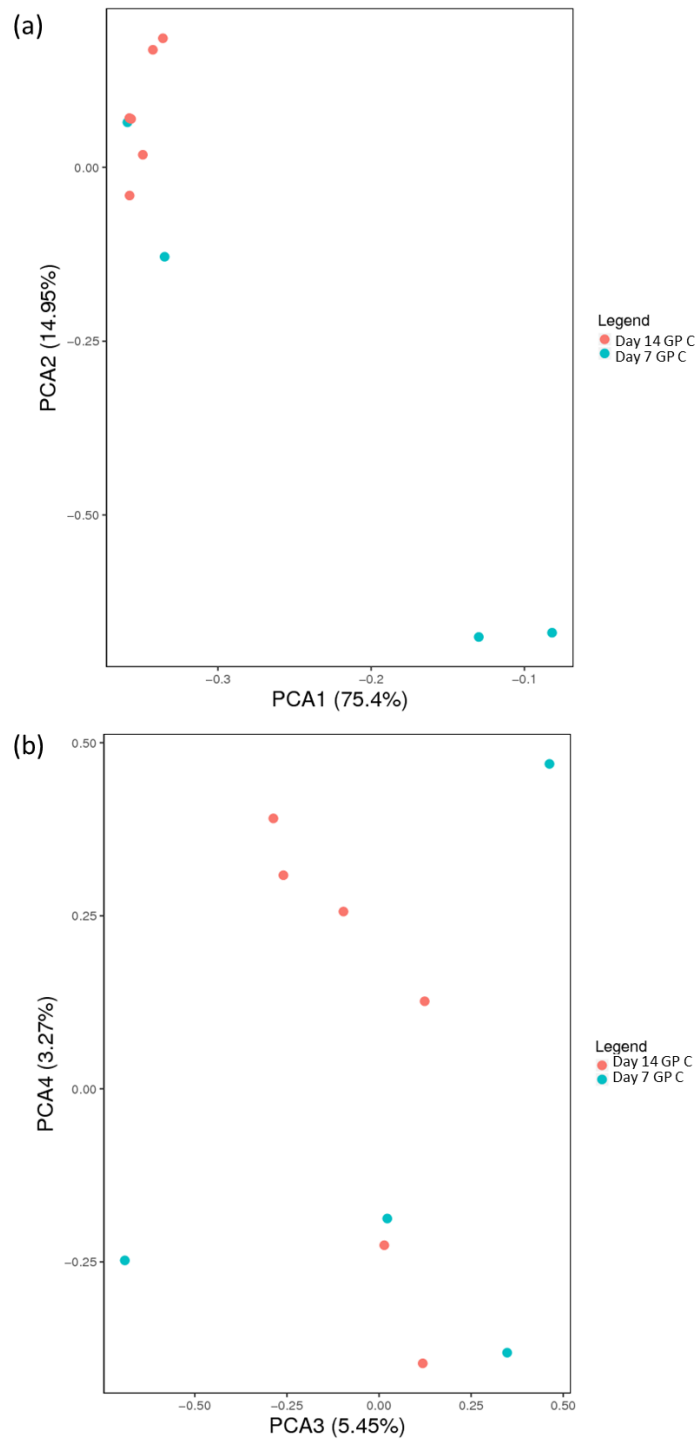
carry some risks of failure for the Transcriptome library construction where the sequencing quality is not guaranteed. Additionally, a longer time span for future trials is recommended as silicon may play a different role in bone health which may or may not be dependent on time.

The future aim will be to pair the analysed transcriptome data with PCR analysis where the PCR would be used as a source of validating the findings discussed above. The genes identified through osteoclast differentiation would form the beginning of this research aim which is when specific genes can be documented. As the principle component analysis showed heterogeneity of samples within the sample groups, it is believed that re-clustering of sample groups properly for both the control and the silicate supplemented diet should be considered. It is this clustering of particular bird(s) genetic data that might lead to a clearer picture being formed when specific genes are discussed. For this, some further analysis would need to be carried out using another bioinformatics database such as DAVID.

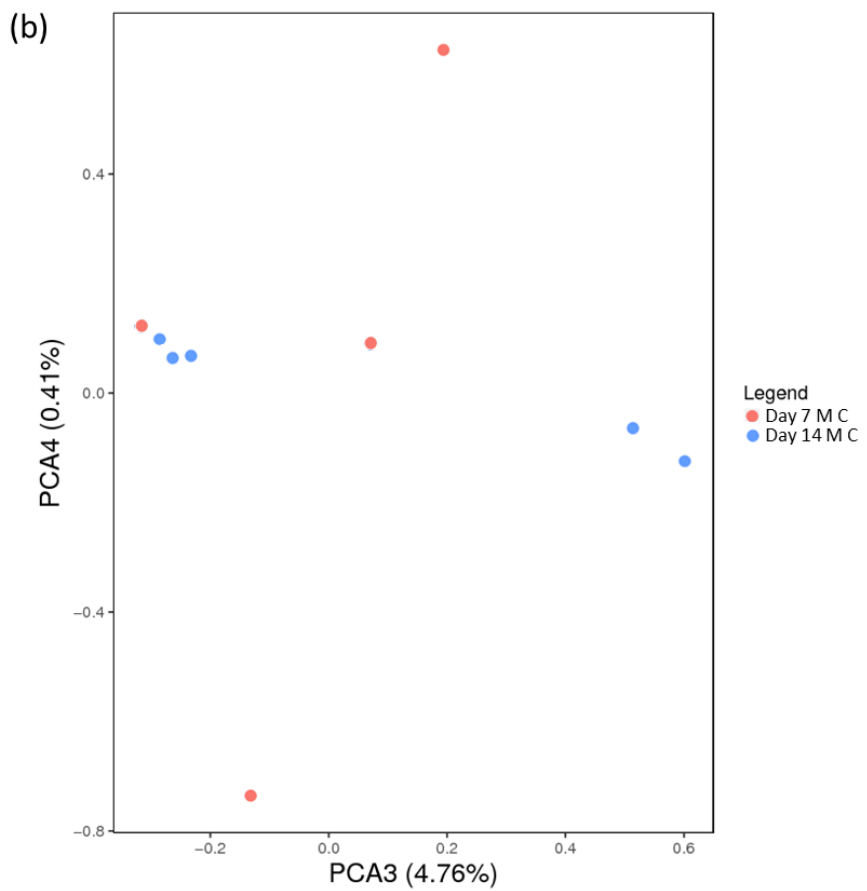
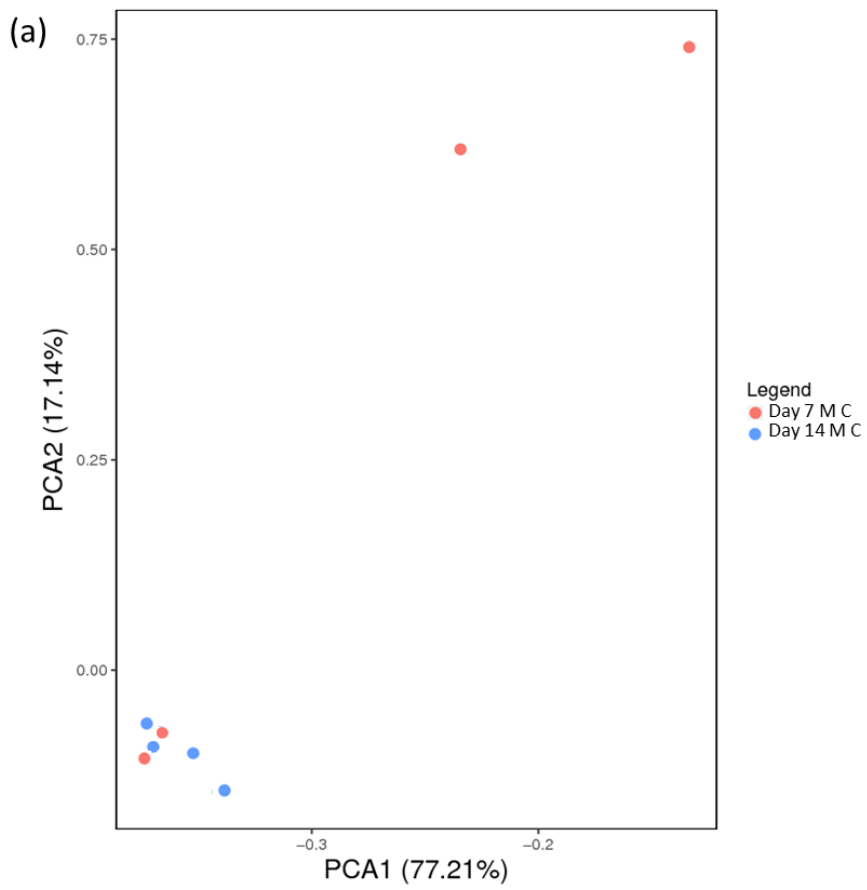
Another suggestion for future works would be to study the differences in protein expression to aid the above transcriptome analysis to confirm if the silicate supplements cause any modifications at the protein level. It is understood that this could have easily been done as RNA stat 60 used for RNA extraction could have also allowed for protein analysis. Since this was not planned during the initial stages of this work, the other bone (left tibia) could be utilised. To add further insight into the mechanism of the silicate supplement on bone health, carrying out bone strength analysis could also help understand the structural features of bone mineral crystallinity and average bone mineral density (which is expected to increase). Since none of the bone parameters or bird weight showed significant changes, bone breaking analysis would best enhance the current findings. A further contribution towards the understanding of the role of silicon on bone health will be made as it will help conclude that it is not just that silicon promotes osteogenesis but also if its incorporation within the bone matrix is what leads to strengthening of bone leading to improved bone density. However, it is also essential to note that there may be no significant differences observed for the average bone density this early in stage of the research study as the effects are usually observed after 3 weeks of supplementation (Burton et al., 2020). Due to the current availability of the

left tibia bone only, a careful consideration is essential for future work such that it would best complement the work shown in this chapter which will optimally progress the research further.

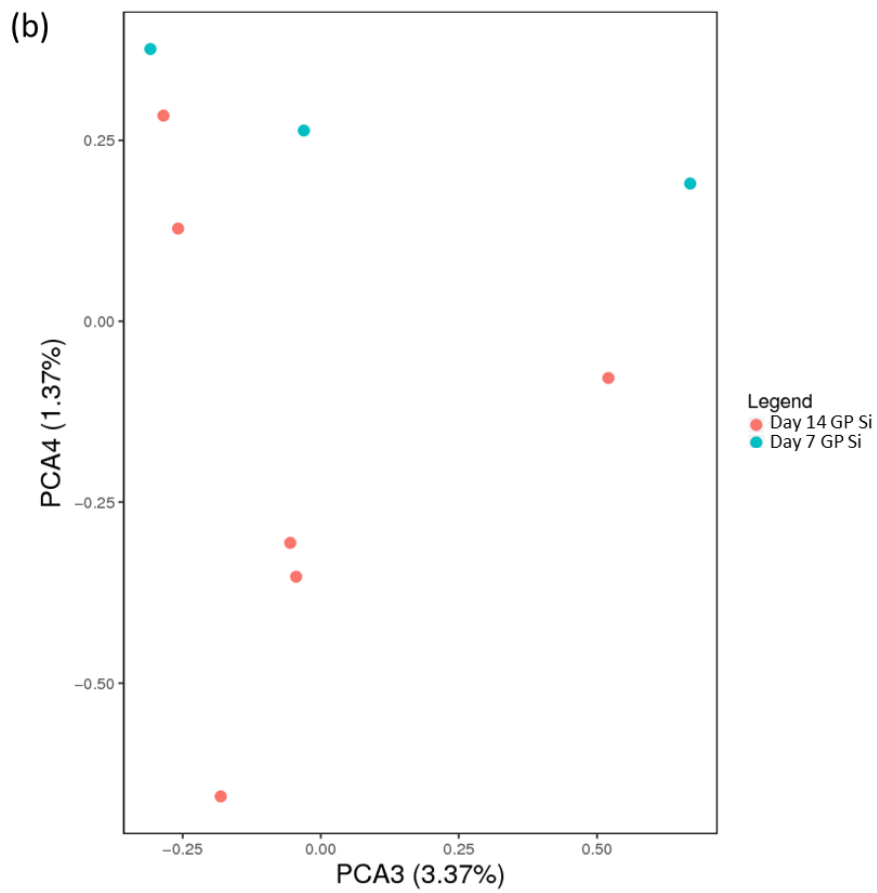
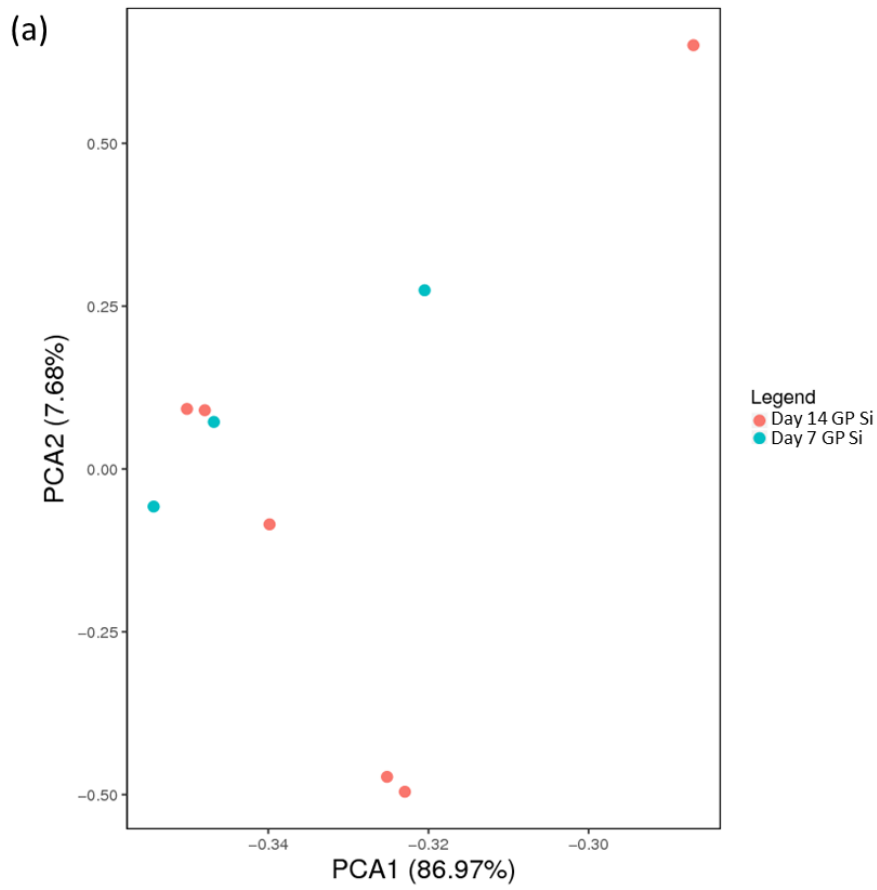
5.5. Appendix



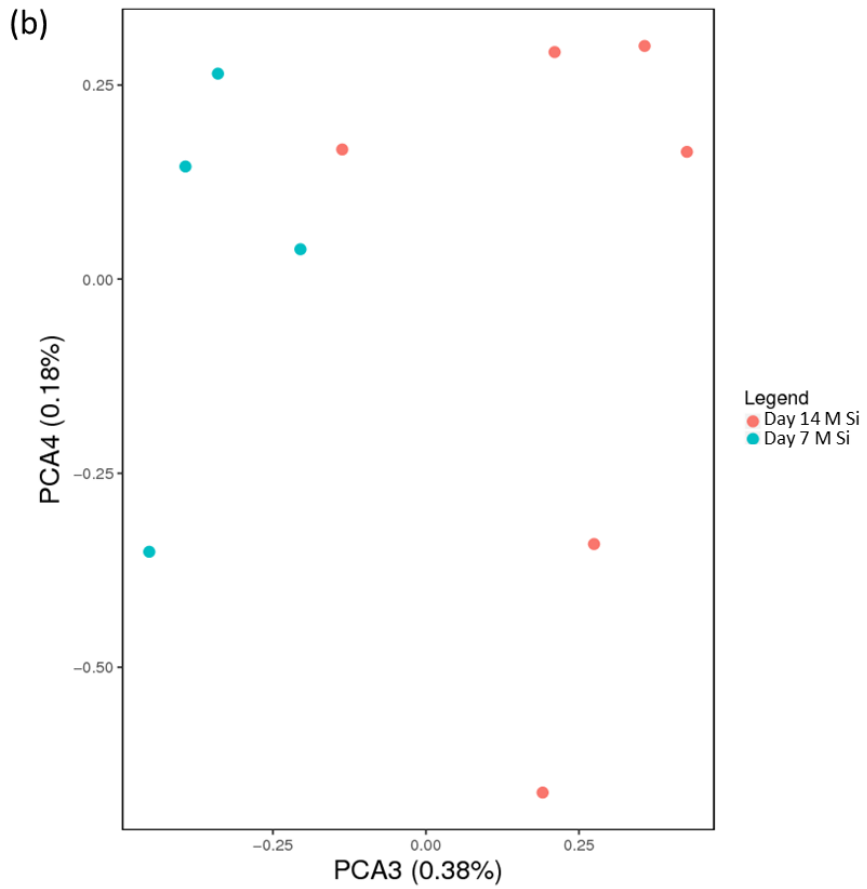
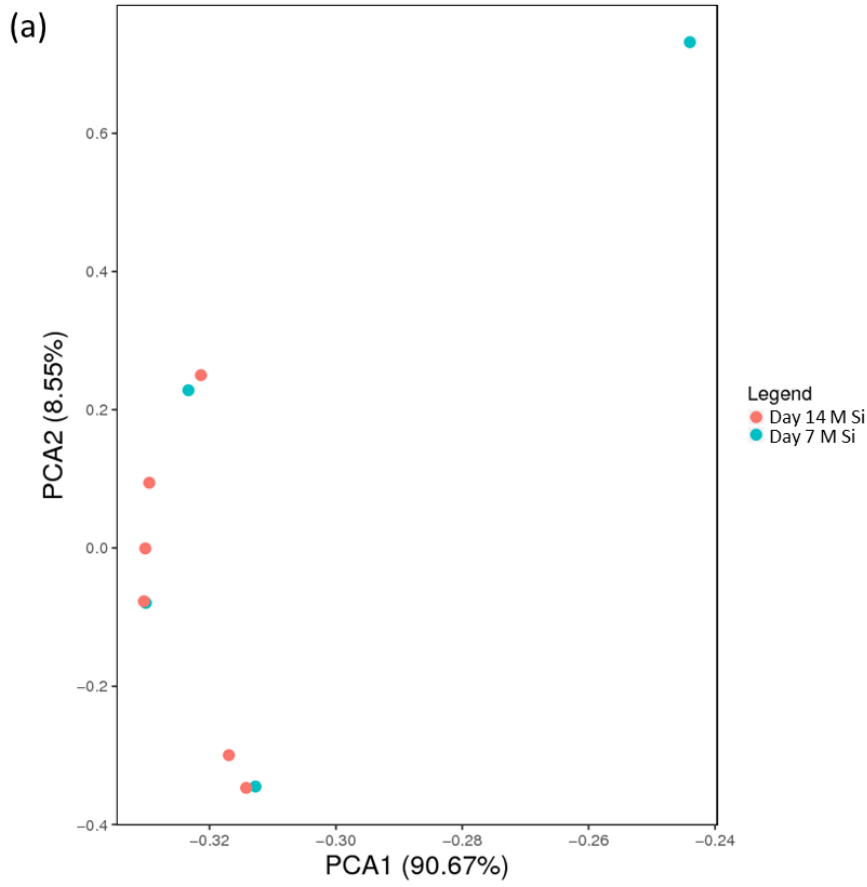
Appendix Figure 5.1 – PCA analysis for Day 7 GP C vs Day 14 GP C (a) PC2 vs PC1 (b) PC4 vs PC3



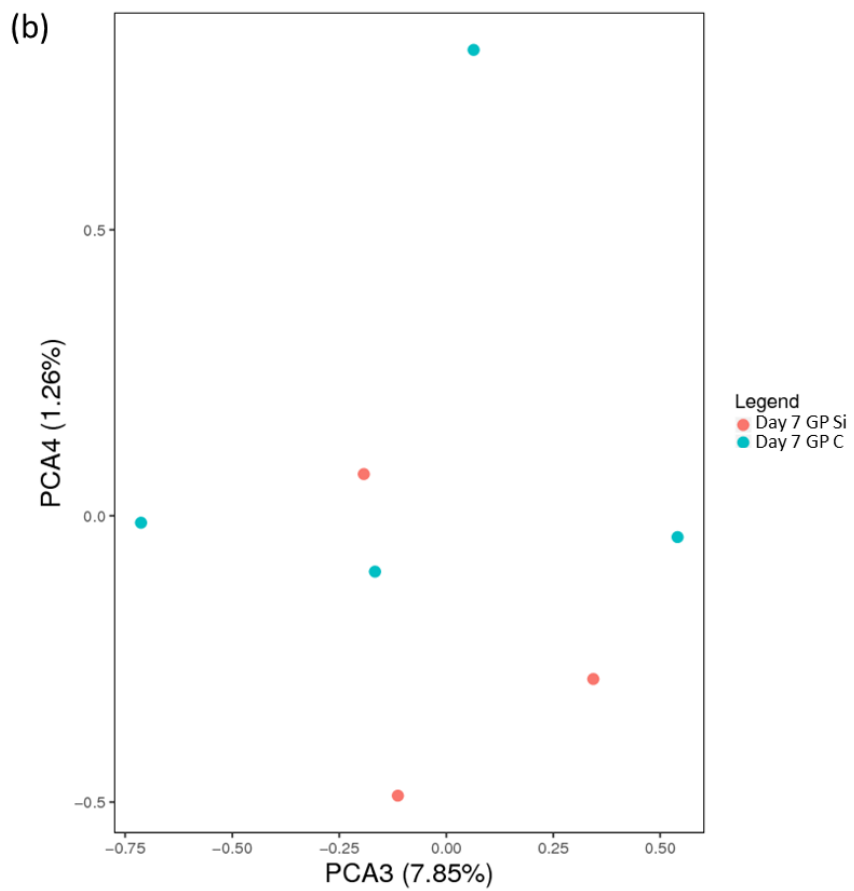
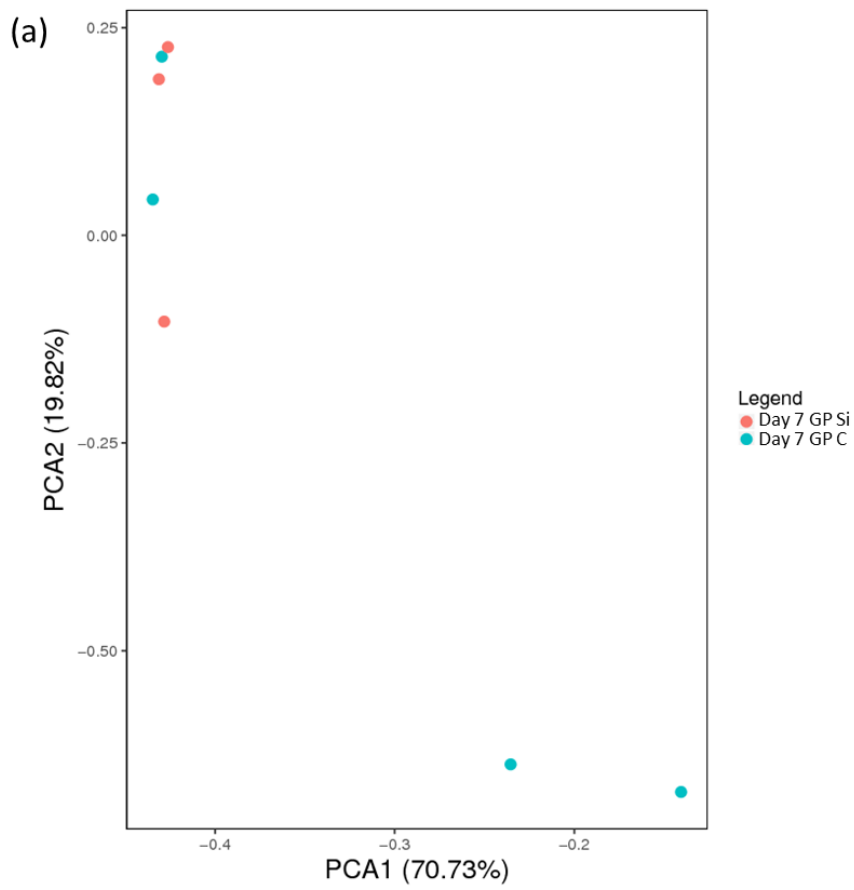
Appendix Figure 5.2 – PCA analysis for Day 7 M C vs Day 14 M C (a) PC2 vs PC1 (b) PC4 vs PC3



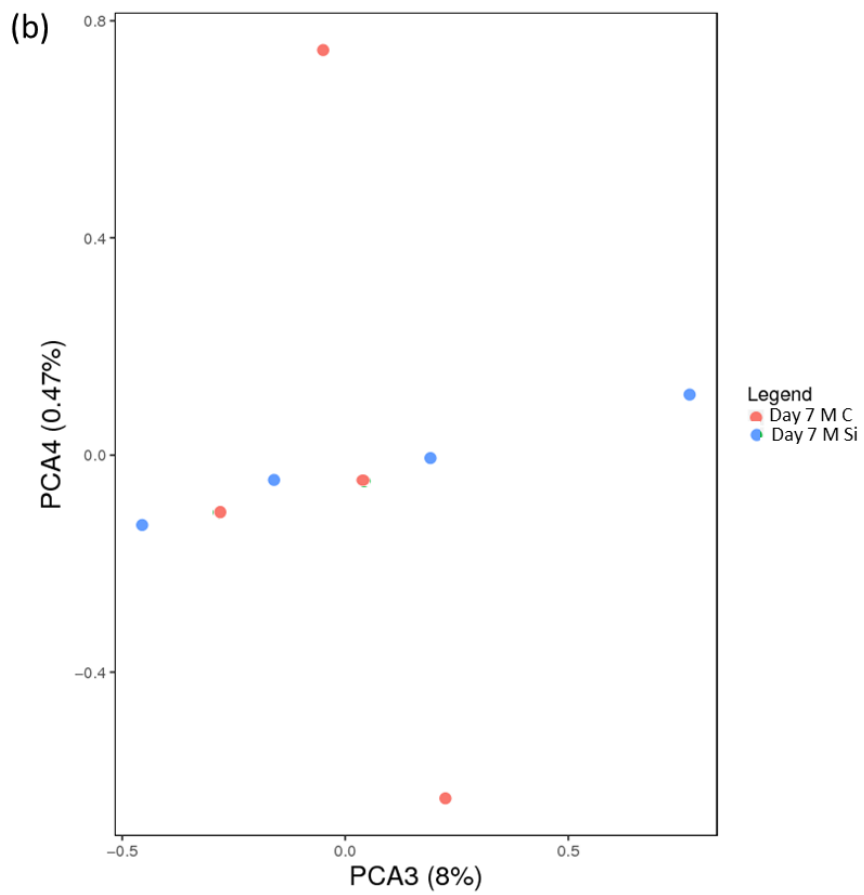
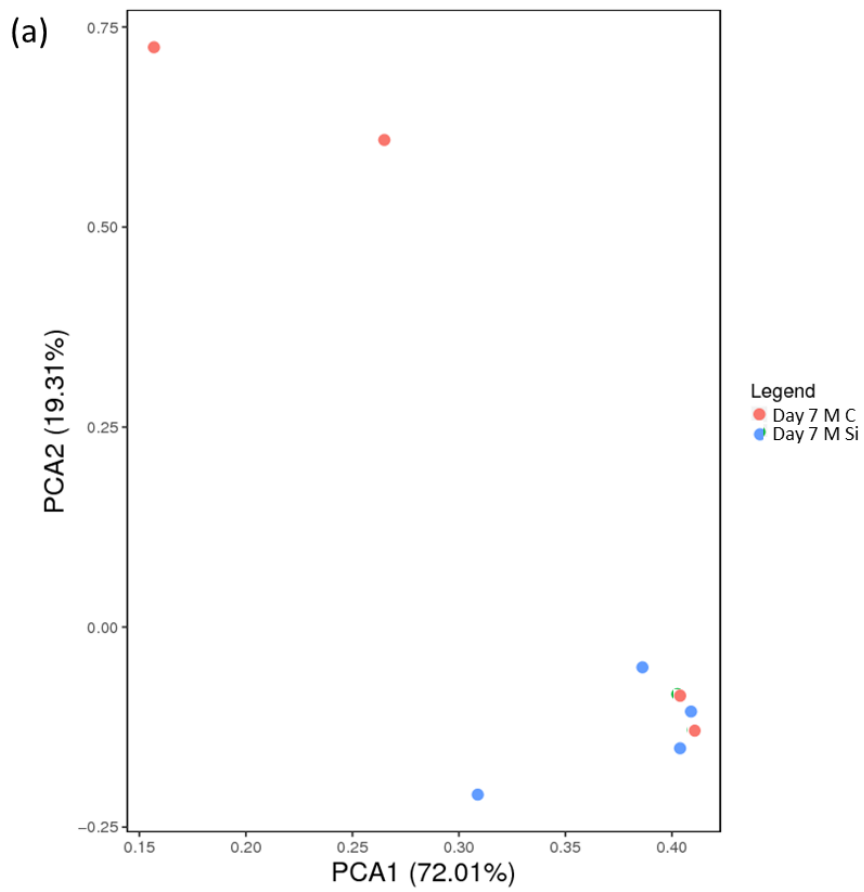
Appendix Figure 5.3 – PCA analysis for Day 7 GP Si vs Day 14 GP Si (a) PC2 vs PC1 (b) PC4 vs PC3



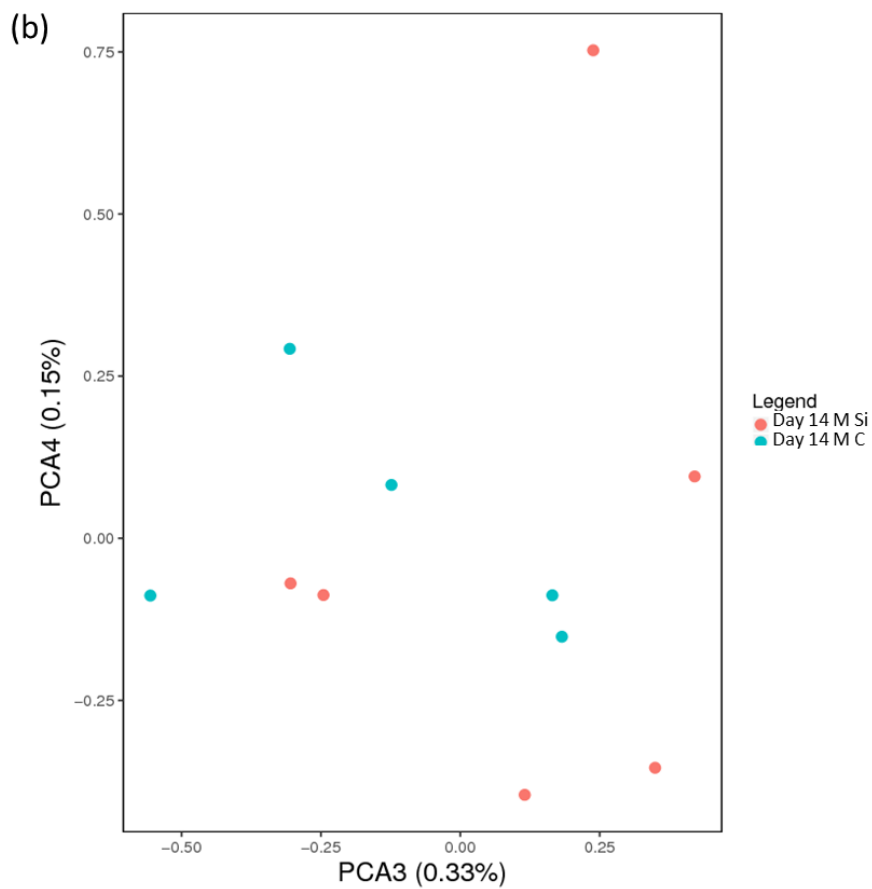
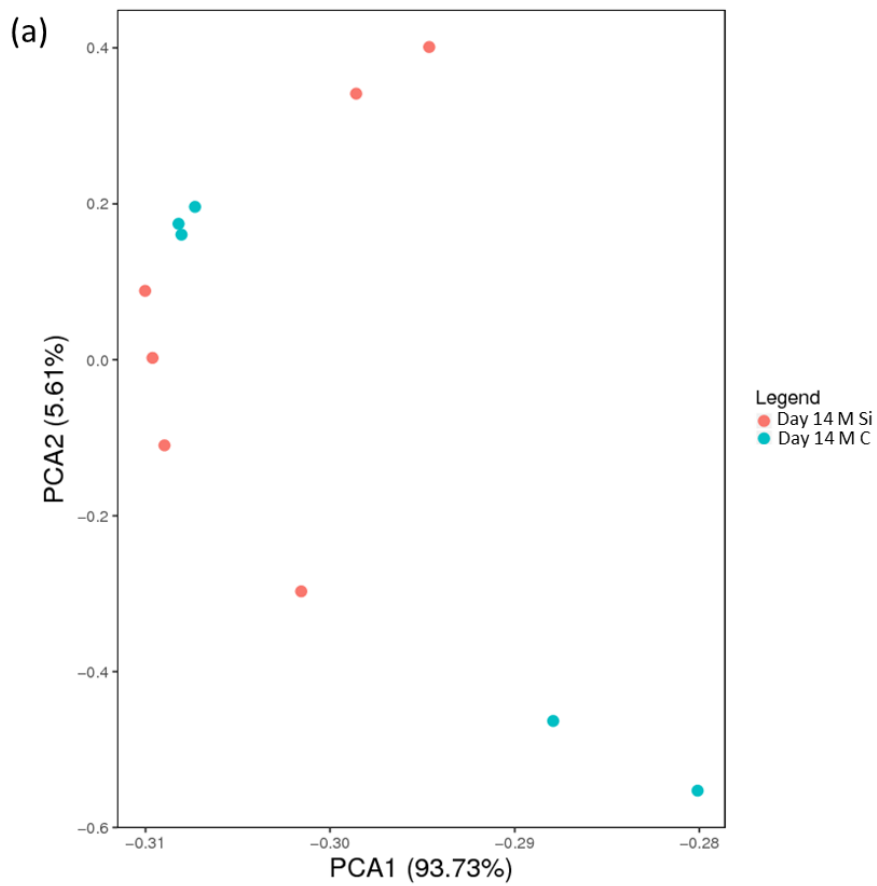
Appendix Figure 5.4 – PCA analysis for Day 7 M Si vs Day 14 M Si (a) PC2 vs PC1 (b) PC4 vs PC3



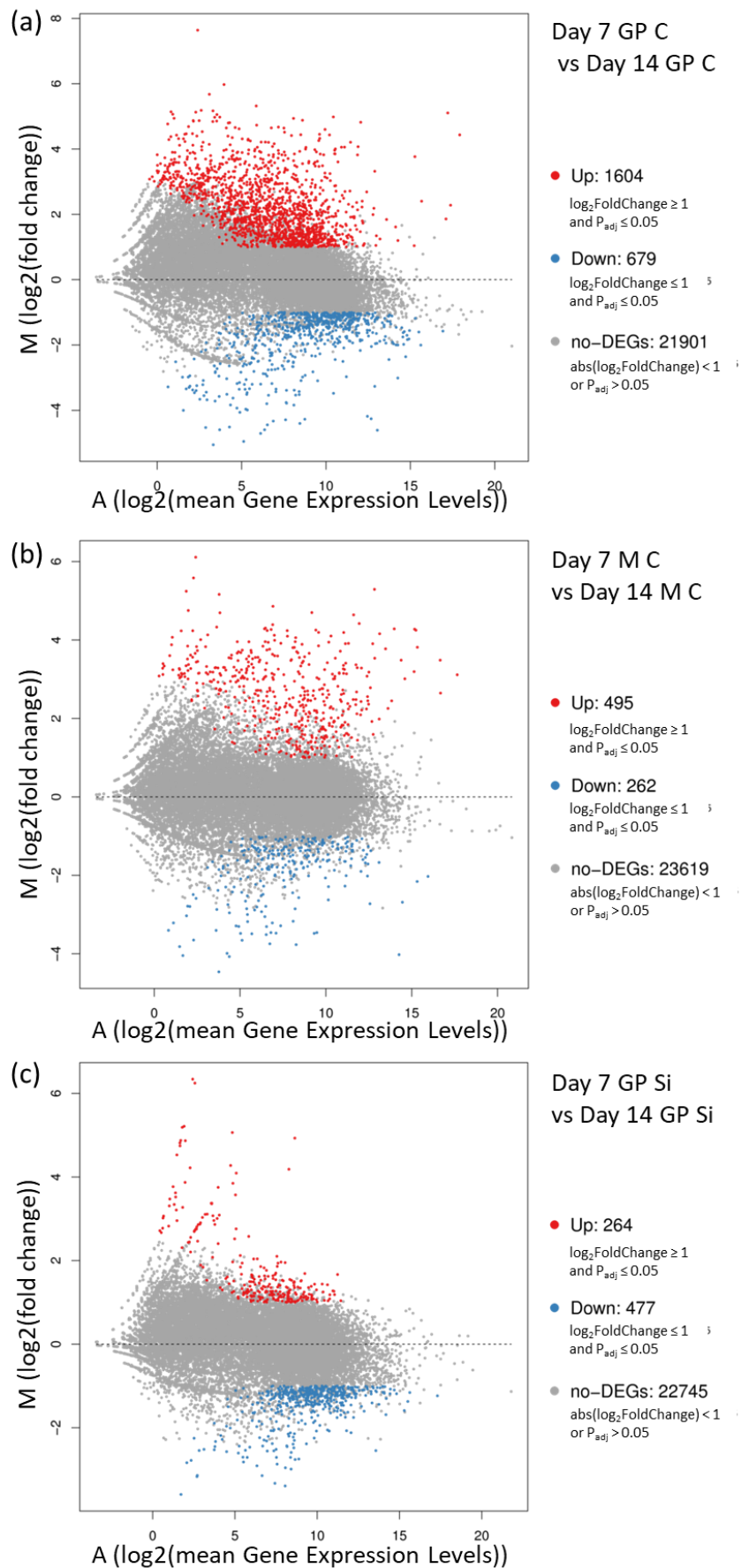
Appendix Figure 5.5 – PCA analysis for Day 7 GP Si vs Day 7 GP C (a) PC2 vs PC1 (b) PC4 vs PC3



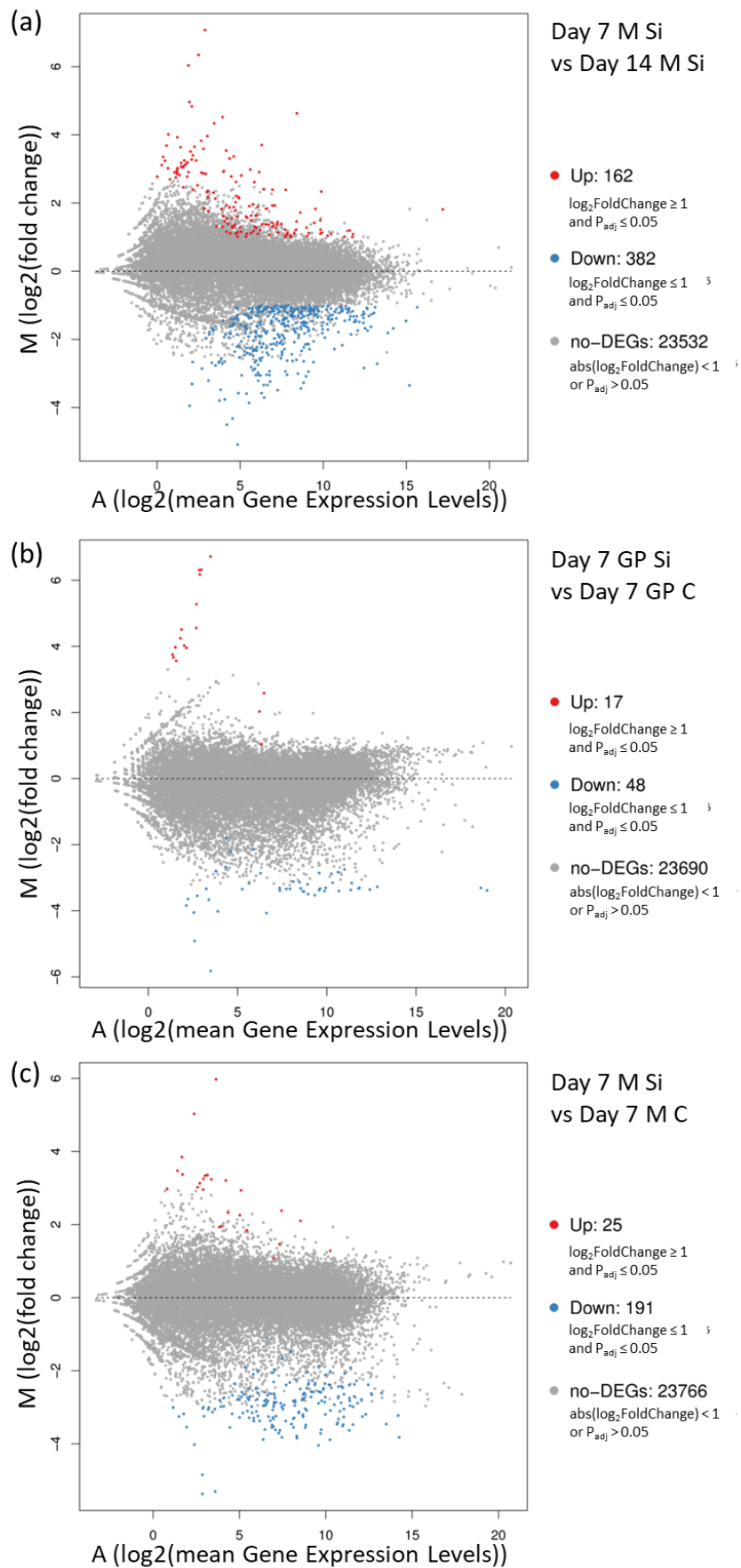
Appendix Figure 5.6 – PCA analysis for Day 7 M Si vs Day 7 M C (a) PC2 vs PC1 (b) PC4 vs PC3



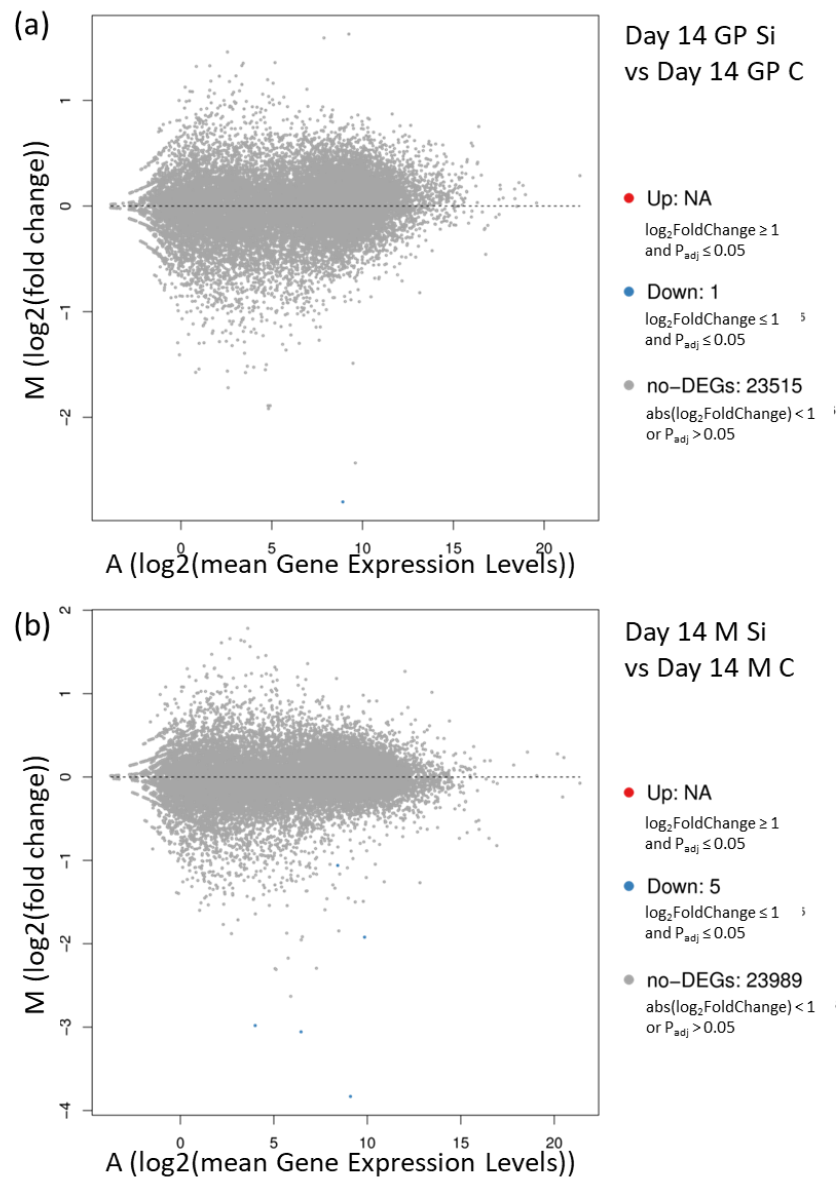
Appendix Figure 5.8 – PCA analysis for Day 14 M Si vs Day 14 M C (a) PC2 vs PC1 (b) PC4 vs PC3



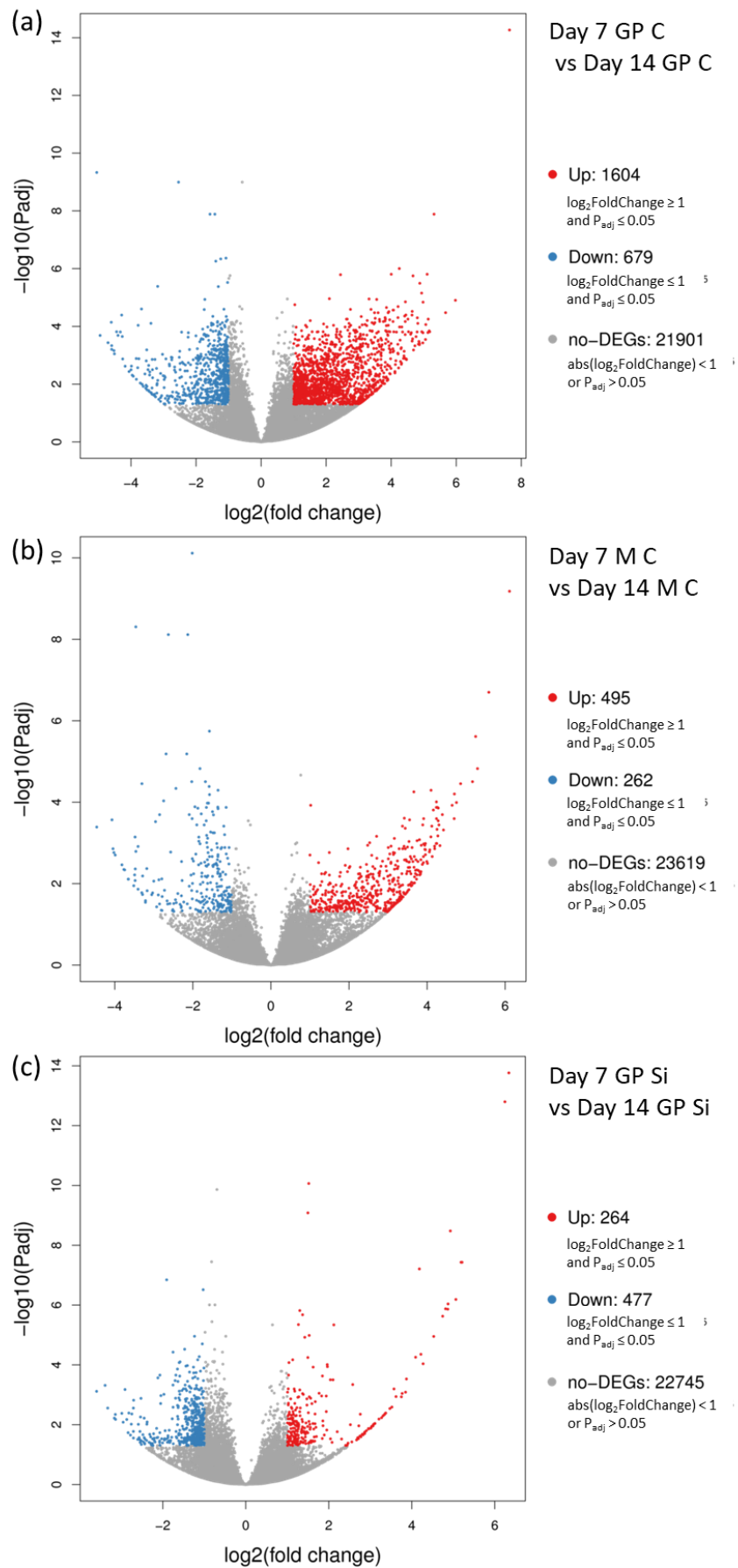
Appendix Figure 5.9 – MA plots of DEGs (a) Day 7 GP C vs Day 14 GP C (b) Day 7 M C vs Day 14 M C (c) Day 7 GP Si vs Day 14 GP Si



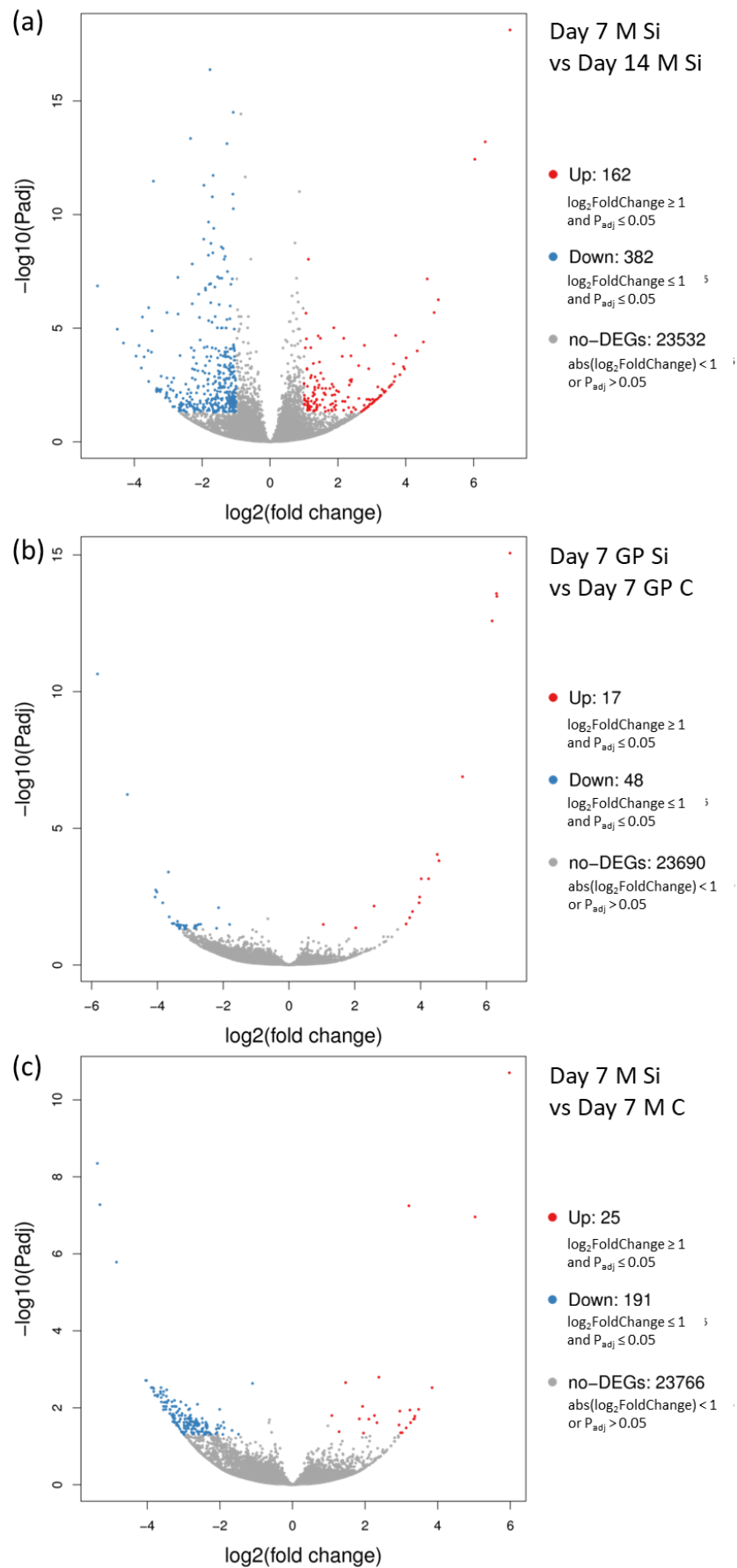
Appendix Figure 5.10 – MA plots of DEGs (a) Day 7 M Si vs Day 14 M Si (b) Day 7 GP Si vs Day 7 GP C (c) Day 7 M Si vs Day 7 M C



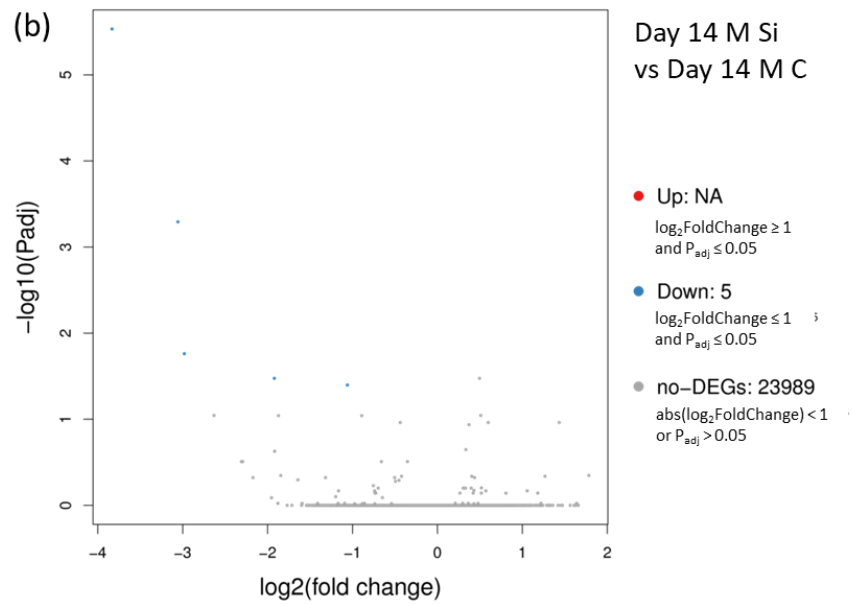
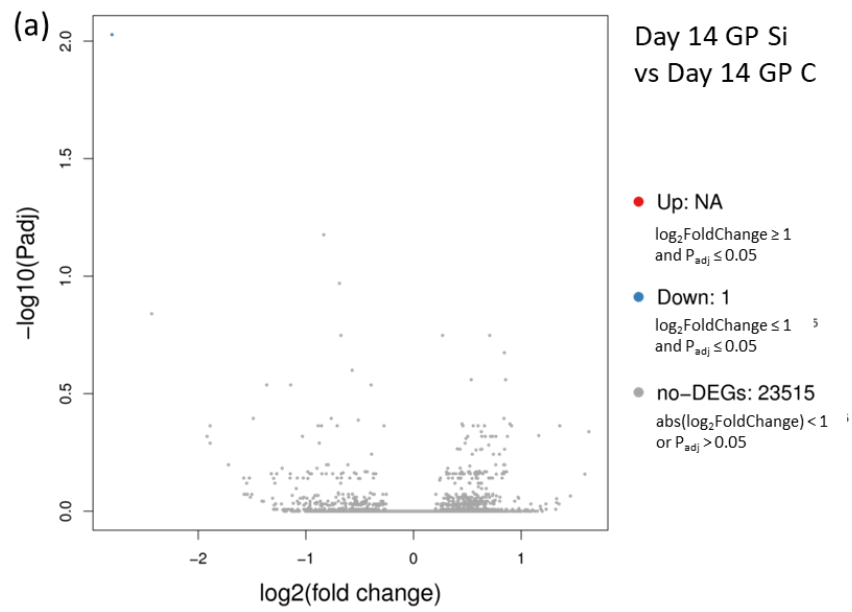
Appendix Figure 5.11 – MA plots of DEGs (a) Day 14 GP Si vs Day 14 GP C (b) Day 14 M Si vs Day 14 M C



Appendix Figure 5.12 – Volcano plot of DEGs (a) Day 7 GP C vs Day 14 GP C (b) Day 7 M C vs Day 14 M C (c) Day 7 GP Si vs Day 14 GP Si



Appendix Figure 5.13 – Volcano plot of DEGs (a) Day 7 M Si vs Day 14 M Si (b) Day 7 GP Si vs Day 7 GP C (c) Day 7 M Si vs Day 7 M C



Appendix Figure 5.14 – Volcano plot of DEGs(a) Day 14 GP Si vs Day 14 GP C (b) Day 14 M Si vs Day 14 M C

Chapter 6. Conclusion and Future works

Silicon is a trace element of interest and plays a role in many physiological functions of different living organisms. Hence, the main aims of this PhD research were to focus on understanding the role of silicon within some of the living organisms in life. Each of the aims (as titles of chapters 3 - 5) is discussed below with a conclusion containing key findings and/or contributions (including its importance) and possible future work with their benefit.

The first two aims (sections 6.1 and 6.2) were achieved through exploring knowledge of the silicaphilic nature of a fluorescent dye, PDMPO (2-(4-pyridyl)-5-((4-(2-dimethylaminoethylaminocarbonyl)methyl)phenyl)oxazole) (Parambath et al., 2016), and the availability of a specialised fluorescence microscopy technique, confocal scanning laser microscopy (CSLM) which allowed detection of fluorescence through a sample of interest.

6.1. Development of a novel Displacement Assay for screening abiotic/biotic interactions

6.1.1. Conclusion

In this chapter, knowledge of the interactions of PDMPO dye to silica was explored to develop a novel Optically Sectioned Planar Format Indicator Displacement Assay (O-IDA) to study silica biomolecule interactions *in vitro* using CSLM. Different amino acids, a polyamine and a drug were studied by this assay and aided its development. To further test the capability and limitations of the assay, it was extended and applied to larger biomolecules such as 7-mer peptides that have been identified as silica binders by Phage display (Puddu and Perry, 2012 and Patwardhan et al., 2012). From the example molecules explored, it can currently be assumed that no limitations exist in respect of the type of molecules that can be studied by the O-IDA method. Having successfully tested various biomolecules including peptides through O-IDA, this provides evidence that this technique has potential to be used as a tool to screen silica binders and could

provide valuable information on the type of silica-biomolecule interactions that may be present. The development of this assay can benefit a few areas of research (in answering unsolved questions) such as drug delivery involving silica-based delivery systems, materials for biomedical use and biosilicification.

6.1.2. Future work

Regardless of the successful application of O-IDA using various biomolecules, the current method requires an initial fitting of the data obtained from the CSLM to obtain a working fluorescence intensity which is what is used for the binding affinity analysis. It would be ideal to explore options to overcome this. One of the ways to overcome this is to carry out this assay using fluorescence polarization measurements. Fluorescence polarisation uses the information on molecular orientation of fluorescent molecules where the degree of polarization is determined from measurements of fluorescence intensities parallel and perpendicular to the plane of linearly polarized excitation light (Lakowicz, 2010). The output of this method can be utilised without any further interpretation or analysis. However, it is essential to know the interactions of the PDMPO dye to the silica surface for such methods. It is expected that the dye should exhibit a specific orientation and be aligned on the surface for this method to be a success. An understanding of the silicophilic behaviour of PDMPO has provided a considerable insight into PDMPO–silica interactions (Parambath et al., 2016). Both single point and multipoint alignment modes are seen which are dependent on pH (Parambath et al., 2016). At a pH of 7.2, a two-point binding of PDMPO on silica is observed as seen in Figure 6.1 where the interactions with negatively charged silica are stabilised through a proton from the surrounding bulk solution (Parambath et al., 2016).

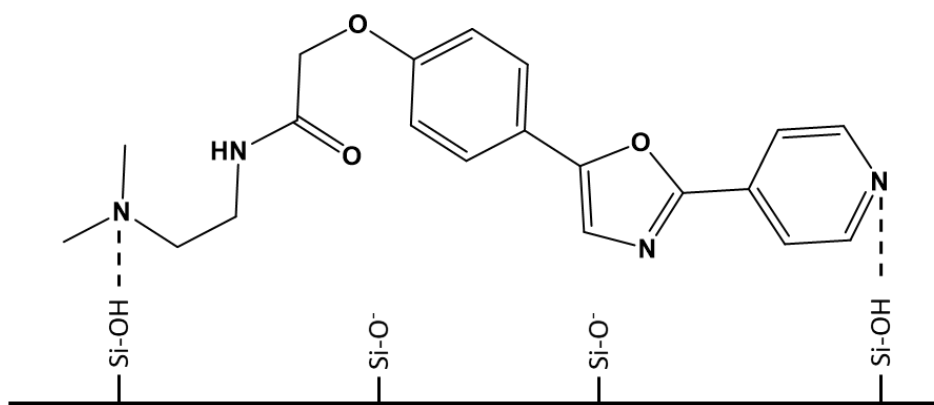


Figure 6.1 – Orientation of PDMPO dye on silica surface

Adapted and modified from Parambath et al., 2016

Considering the cost effectiveness of O-IDA at larger scale, it may also be beneficial to seek an indicator which is more cost effective than PDMPO. In addition, the developed assay can allow an easy transition of the methodology to any solvent and material/surface provided a relevant indicator can be sourced.

Since it is likely that a larger biomolecule (than 7-mer peptides studied) would displace more than one molecule of the PDMPO dye, it may be beneficial to study and confirm the presence of these multiple binding sites ($n > 1$) by another technique such as NMR to get greater insight into the interactions of larger biomolecules with silica. In addition, it can act as a source to validate the results obtained through O-IDA and will allow its extension to even larger biomolecules than 7-mer peptides.

6.2. Implementation of a fluorescence-based surface charge mapping method to study silica chemistry in biological tissues

6.2.1. Conclusion

In this chapter, the knowledge of the interactions of PDMPO dye with silica was further explored to develop an imaging method to understand the surface charge properties of silica microstructures within a cell wall. The method development was based on spectral imaging using CSLM which utilised the PDMPO emission ratio $(\text{PDMPOH}_2)^{2+}/\text{PDMPOH}^+$ as it is affected by the silica particle size (due to surface chemistry or acidity) and related

it to zeta potential (ζ) which is a proxy measure of surface charge. Hence, this technique allows a proxy measure of silica acidity through zeta potential estimation which leads to a prediction of particle sizes of the silica microstructures within a cell wall.

It has been successfully applied to different biologically relevant silicifying organisms (both living and non-living samples). A highly charged fluorescence emission of $(\text{PDMPOH}_2)^{2+}$ from the highly silicified regions of organisms was observed which confirms the silica-based environment of the area being analysed and this is a phenomenon previously shown for the interactions of PDMPO with silica (Parambath et al., 2016). A silica size dependent shift was observed through a varying PDMPO emission ratio $(\text{PDMPOH}_2)^{2+}/\text{PDMPOH}^+$. In addition, the sensitivity of this technique, observed through an estimation of varying zeta potential values obtained, also demonstrated that a range of silica structures of different sizes can be studied.

Application of the method to several organisms showcases the diversity of this technique which makes it a valuable tool to study surface charge properties in a variety of organisms. Surface charge mapping through this analytical tool will contribute towards an understanding of deposited biosilica and would play an essential role in understanding biosilicification processes. The chemical properties and morphology of silicifying organisms exhibiting silica microstructures within their cell wall can be explored. Not only will this methodology enable real-time surface charge measurements but its capability to provide biosilicification related information *in vivo* makes it a technique of choice for the study of many organisms in life.

6.2.2. Future work

Incorporation of the developed surface charge mapping method to adapt the existing technologies of ratiometric imaging of calcium (Schild et al., 1994) can add immense value to research when studying surface charge in living organisms. Application of such novel methods is desirable in biomedical engineering of materials with defined surface charge characteristics in instances such as materials for tissue replacement etc.

The reported method was based on a fixed pH where the different sizes of silica nanostructures can be studied. However, this method development is not limited to this purpose and the applicability of the approach could be extended to a wide range of environmental conditions. There is a possibility that it can be transferred to study changes in pH where a fixed size of SNPs can be used for the method development. Being able to monitor pH changes could further enhance understanding of biosilicification. In addition, it can also be applicable to other materials of interest where a surface exhibits hydroxylated moieties. To adapt this method and be able to apply it for the other purposes mentioned, further experimentation and simulation to extract surface charge will be required.

6.3. Towards understanding the biological mechanisms involved in the role of silicon (as silicate) uptaken from dietary intake through transcriptome analysis using RNA sequencing

6.3.1. Conclusion

Though silicon, an essential trace element, is shown to have a positive effect on mineralised tissues, the current research still lacks many aspects of the mechanisms involved. In this chapter, a transcriptome analysis was carried out to enhance the current knowledge of the mechanism of silicon in animals to help fulfil this research gap. RNA sequencing (transcriptome) was employed using a bone tissue from an animal trial with an aim to understand the mechanisms that may be involved in utilising silicon (as silicate) from dietary intake that play a role in bone health of animals. The findings from the transcriptome lead to identification of the biological pathways affected when the silicate supplement is fed over time which induces bone growth. Hence, this understanding of the role of silicon in animals could help towards a development of a novel approach for maintaining healthy bones in future.

A reduced osteoclastogenesis, no effects on IL-17 production from Th17 cell differentiation and reduced phagocytosis in earlier days (compared to later days) is observed with a high levels of silicate blood plasma levels for bone middle (diaphysis).

This would directly or indirectly promote osteoblast activity through possible modifications at protein level or by a coupling process (Udagawa et al., 2000) promoting osteogenesis. A reduced ROS activity through upregulation of glutathione activity and a reduced ribosome activity in earlier days (compared to later days) are observed with high levels of silicate blood plasma levels for bone growth plates (epiphysis). This would lead to reduced osteoclast activity which may promote osteoblast activity leading to osteogenesis. This can also be confirmed with reduced ribosomal activity due to reduced repair of cells as this would be needed during bone resorption.

As the time span of the current study was over 2 weeks, no direct genetic link was observed for osteoblast activity. This can be explained due to the long lifespan of osteoblast of 3 months which is why no biological pathways were observed that directly affect the osteoblasts necessary for osteogenesis.

It was also demonstrated that each part of the bone studied displays a different mechanism which promotes osteogenesis. Overall, it can be concluded that the pathways mentioned above are due to the effects of silicon on the immune or inflammatory response and oxidative stress within cells. It is highly likely that the anti-inflammatory and antioxidative properties of silicon are linked together as previously reported by Kim et al., 2013 through a genetic study using Reverse Transcription Polymerase Chain Reaction on murine macrophages. The mechanism behind these properties of silicon is not yet known. Research to understand this mechanism of Si is still ongoing and more evidence is required for its effect over time before anything can be proposed. At this stage, it can only be proposed that different genes or proteins may be affected in such a way that anti-inflammatory and antioxidative responses are observed but the exact mechanism cannot be concluded.

6.3.2. Future work

Due to the limited number of samples per group in the current study, the risky samples as identified by BGI were used for the Transcriptome library construction which may have compromised the sequencing quality. Future repeats of similar transcriptome analysis would be beneficial where a larger set of birds is used with an aim to have an

increased number of samples per group being ideal. Additionally, it would also be beneficial to increase the time span of the trial in future to observe the long-term effects of silicon (as silicate) in animals. This will also demonstrate if the bioavailable silicate gets stored within the mineralised tissue and plays a role different to what is observed in the current study with continued administration of supplementation over long term.

Another future aim will be to pair the analysed transcriptome data with PCR as a source of validating the findings discussed above. The genes identified through osteoclast differentiation could form the beginning of this research aim. However, this doesn't prevent one from exploring the genes in the other enriched pathways discussed.

Another suggestion would be to study the differences in protein expression to aid the transcriptome analysis in an hope to understand if the silicate supplements cause any modifications at the protein level. To add further insight into the mechanism of the silicate supplement on bone health, carrying out bone strength analysis could also help understand the structural features of bone mineral crystallinity.

Further analysis of samples within groups may be considered due to the heterogeneity seen within the samples of the same group. This could be carried out using an appropriate platform such as DAVID available to evaluate gene expression.

References

- Acosta-Rodriguez, E., Napolitani, G., Lanzavecchia, A. and Sallusto, F., 2007. Interleukins 1 β and 6 but not transforming growth factor- β are essential for the differentiation of interleukin 17-producing human T helper cells. *Nature Immunology*, 8(9), pp.942-949.
- Agilent.com., 2020. [online] Available at: <https://www.agilent.com/cs/library/usermanuals/Public/G2938-90034_RNA6000Nano_KG.pdf> [Accessed 27 September 2020].
- Akhtar K., Khan S.A., Khan S.B., Asiri A.M., 2018. Scanning Electron Microscopy: Principle and Applications in Nanomaterials Characterization. In: Sharma S. (eds) *Handbook of Materials Characterization*. Springer, Cham.
- Al Mahrouqi, D., Vinogradov, J. and Jackson, M., 2016. Temperature dependence of the zeta potential in intact natural carbonates. *Geophysical Research Letters*, 43(22).
- Albericio, F.; Kates, S. A (2000). In *Solid-phase synthesis: a practical guide*; Marcel Dekker: New York; pp 79-91.
- Alnaeeli, M., Penninger, J. and Teng, Y., 2006. Immune Interactions with CD4+ T Cells Promote the Development of Functional Osteoclasts from Murine CD11c+ Dendritic Cells. *The Journal of Immunology*, 177(5), pp.3314-3326.
- Alsteens, D., Pfreundschuh, M., Zhang, C., Spoerri, P., Coughlin, S., Kobilka, B. and Müller, D., 2015. Imaging G protein-coupled receptors while quantifying their ligand-binding free-energy landscape. *Nature Methods*, 12(9), pp.845-851.
- Amos, W. and White, J., 2003. How the Confocal Laser Scanning Microscope entered Biological Research. *Biology of the Cell*, 95(6), pp.335-342.
- Amsbio.com., 2019. [online] Available at: <<https://resources.amsbio.com/Datasheets/CS-110.pdf>> [Accessed 30 October 2019].
- Anderson, D., Maraskovsky, E., Billingsley, W., Dougall, W., Tometsko, M., Roux, E., Teepe, M., DuBose, R., Cosman, D. and Galibert, L., 1997. A homologue of the TNF receptor and its ligand enhance T-cell growth and dendritic-cell function. *Nature*, 390(6656), pp.175-179.

- Anderson, O., Perry, C. and Hughes, N., 1990. Transmission and scanning electron microscopic evidence for cytoplasmic deposition of strontium sulphate crystals in colonial radiolaria. *Philosophical Transactions of the Royal Society of London. Series B: Biological Sciences*, 329(1252), pp.81-86.
- Andersson, J., Rosenholm, J., Areva, S. and Lindén, M., 2004. Influences of Material Characteristics on Ibuprofen Drug Loading and Release Profiles from Ordered Micro- and Mesoporous Silica Matrices. *Chemistry of Materials*, 16(21), pp.4160-4167.
- Argyo, C., Weiss, V., Bräuchle, C. and Bein, T., 2013. Multifunctional Mesoporous Silica Nanoparticles as a Universal Platform for Drug Delivery. *Chemistry of Materials*, 26(1), pp.435-451.
- Azam, M. and Gibbs-Davis, J., 2013. Monitoring DNA Hybridization and Thermal Dissociation at the Silica/Water Interface Using Resonantly Enhanced Second Harmonic Generation Spectroscopy. *Analytical Chemistry*, 85(17), pp.8031-8038.
- Baek, K., Oh, K., Lee, W., Lee, S., Kim, M., Kwon, H., Rhee, E., Han, J., Song, K., Cha, B., Lee, K. and Kang, M., 2010. Association of Oxidative Stress with Postmenopausal Osteoporosis and the Effects of Hydrogen Peroxide on Osteoclast Formation in Human Bone Marrow Cell Cultures. *Calcified Tissue International*, 87(3), pp.226-235.
- Baeza, A., Colilla, M. and Vallet-Regí, M., 2014. Advances in mesoporous silica nanoparticles for targeted stimuli-responsive drug delivery. *Expert Opinion on Drug Delivery*, 12(2), pp.319-337.
- Barbé, C., Bartlett, J., Kong, L., Finnie, K., Lin, H., Larkin, M., Calleja, S., Bush, A. and Calleja, G., 2004. Silica Particles: A Novel Drug-Delivery System. *Advanced Materials*, 16(21), pp.1959-1966.
- Barel, A., Calomme, M., Timchenko, A., Paepe, K., Demeester, N., Rogiers, V., Clarys, P. and Vanden Berghe, D., 2005. Effect of oral intake of choline-stabilized orthosilicic acid on skin, nails and hair in women with photodamaged skin. *Archives of Dermatological Research*, 297(4), pp.147-153.
- Barisik, M., Atalay, S., Beskok, A. and Qian, S., 2014. Size Dependent Surface Charge Properties of Silica Nanoparticles. *The Journal of Physical Chemistry C*, 118(4), pp.1836-1842.

- Barrow, A., Raynal, N., Andersen, T., Slatter, D., Bihan, D., Pugh, N., Cella, M., Kim, T., Rho, J., Negishi-Koga, T., Delaisse, J., Takayanagi, H., Lorenzo, J., Colonna, M., Farndale, R., Choi, Y. and Trowsdale, J., 2011. OSCAR is a collagen receptor that costimulates osteoclastogenesis in DAP12-deficient humans and mice. *Journal of Clinical Investigation*, 121(9), pp.3505-3516.
- Belton, D., Deschaume, O. and Perry, C., 2012. An overview of the fundamentals of the chemistry of silica with relevance to biosilicification and technological advances. *FEBS Journal*, 279(10), pp.1710-1720.
- Belton, D., Deschaume, O., Patwardhan, S. and Perry, C., 2010. A Solution Study of Silica Condensation and Speciation with Relevance to in Vitro Investigations of Biosilicification. *The Journal of Physical Chemistry B*, 114(31), pp.9947-9955.
- Belton, D., Mieszawska, A., Currie, H., Kaplan, D. and Perry, C., 2012. Silk–Silica Composites from Genetically Engineered Chimeric Proteins: Materials Properties Correlate with Silica Condensation Rate and Colloidal Stability of the Proteins in Aqueous Solution. *Langmuir*, 28(9), pp.4373-4381.
- Belton, D., Paine, G., Patwardhan, S. and Perry, C., 2004. Towards an understanding of (bio)silicification: the role of amino acids and lysine oligomers in silicification. *Journal of Materials Chemistry*, 14(14), p.2231-2241.
- Belton, D., Patwardhan, S. and Perry, C., 2005. Spermine, spermidine and their analogues generate tailored silicas. *Journal of Materials Chemistry*, 15(43), p.4629-4638.
- Belton, D., Patwardhan, S., Annenkov, V., Danilovtseva, E. and Perry, C., 2008. From biosilicification to tailored materials: Optimizing hydrophobic domains and resistance to protonation of polyamines. *Proceedings of the National Academy of Sciences*, 105(16), pp.5963-5968.
- Bernecker, A., Ziolkowska, J., Heitmüller, S., Wieneke, R., Geyer, A. and Steinem, C., 2010. Formation of Silica Precipitates on Membrane Surfaces in Two and Three Dimensions. *Langmuir*, 26(16), pp.13422-13428.
- Bettelli, E., Carrier, Y., Gao, W., Korn, T., Strom, T., Oukka, M., Weiner, H. and Kuchroo, V., 2006. Reciprocal developmental pathways for the generation of pathogenic effector TH17 and regulatory T cells. *Nature*, 441(7090), pp.235-238.
- Birbrair, A. and Frenette, P., 2016. Niche heterogeneity in the bone marrow. *Annals of the New York Academy of Sciences*, 1370(1), pp.82-96.

- Boss, C. and Fredeen, K., 2004. Concepts, Instrumentation and Techniques in Inductively Coupled Plasma Optical Emission Spectrometry. [Shelton, CT]: PerkinElmer Instruments.
- Boss, C., and Fredeen, K., 1997. Concepts, instrumentation and techniques in inductively coupled plasma optical emission spectrometry. 2nd ed. U.S.A: Perkin Elmer Norwalk.
- Bradley, J. and Pober, J., 2001. Tumor necrosis factor receptor-associated factors (TRAFs). *Oncogene*, 20(44), pp.6482-6491.
- Brinker, C. J., Scherer, G. W., 1990. Sol-gel science: the physics and chemistry of sol-gel processing; Academic Press: London.
- British Orthopaedic Association, 2007. The care of patients with fragility fracture [online]. Available at: [http://www.bgs.org.uk/fallsresources-307/subjectreference/fallsandbones/bluebookfragility fracture](http://www.bgs.org.uk/fallsresources-307/subjectreference/fallsandbones/bluebookfragility%20fracture). [Accessed 28 Mar. 2018].
- Brown, M., Bossa, G. and May, S., 2015. Emergence of a Stern Layer from the Incorporation of Hydration Interactions into the Gouy–Chapman Model of the Electrical Double Layer. *Langmuir*, 31(42), pp.11477-11483.
- Bruder, S. and Caplan, A., 1989. Cellular and Molecular Events During Embryonic Bone Development. *Connective Tissue Research*, 20(1-4), pp.65-71.
- Burge, R.T., Worley, D., Johansen, A., Bhattacharyya, S. and Bose, U., 2001. 'The cost of osteoporotic fractures in the UK: Projections for 2000–2020', *Journal of Medical Economics*, 4(1-4), pp. 51–62.
- Burton, E., Scholey, D., Belton, D., Bedford, M. and Perry, C., 2020. Efficacy and stability of a novel silica supplement for improving bone development in broilers. *British Poultry Science*, 61(6), pp.719-724.
- Butch, A., 2000. Dilution Protocols for Detection of Hook Effects/Prozone Phenomenon. *Clinical Chemistry*, 46(10), pp.1719-1720.
- Buyser, D., 2020. Bacillariales. [online] Natureineu.blob.core.windows.net. Available at: <<http://natureineu.blob.core.windows.net/natureineu/bacillariales.html>> [Accessed 21 September 2020].
- Cambi, A. and Lidke, D., 2011. Nanoscale Membrane Organization: Where Biochemistry Meets Advanced Microscopy. *ACS Chemical Biology*, 7(1), pp.139-149.

- Carlisle EM. 1997. Silicon. In O'Dell BL, Sunde RA, editors: Handbook of nutritionally essential minerals, New York, , Marcel Dekker, pp 603–618.
- Carlisle, E.M., 1972. 'Silicon: An essential element for the chick', *Science*, 178(4061), pp. 619–621.
- Carlisle, E.M., 1981. 'Silicon: A requirement in bone formation independent of vitamin D1', *Calcified Tissue International*, 33(1), pp. 27–34.
- Carlisle, E.M., 1986. 'Silicon as an essential trace element in animal nutrition', *Ciba Foundation Symposium*, 121, pp. 123–139.
- Cazes, J. and Ewing, G. W., 2005. In *Ewing's analytical instrumentation handbook*. Marcel Dekker: New York, pp 57-71.
- Chen, Q., Johnson, D., Haudenschild, D. and Goetinck, P., 1995. Progression and Recapitulation of the Chondrocyte Differentiation Program: Cartilage Matrix Protein Is a Marker for Cartilage Maturation. *Developmental Biology*, 172(1), pp.293-306.
- Cheng, H., 2001. The power issue: determination of KB or Ki from IC50. *Journal of Pharmacological and Toxicological Methods*, 46(2), pp.61-71.
- Cheng, H., 2004. The influence of cooperativity on the determination of dissociation constants: examination of the Cheng–Prusoff equation, the Scatchard analysis, the Schild analysis and related power equations. *Pharmacological Research*, 50(1), pp.21-40.
- Cho, G., Lee, D., Lim, H., Lee, S., Kim, C. and Kim, D., 2014. Characterization of surface charge and zeta potential of colloidal silica prepared by various methods. *Korean Journal of Chemical Engineering*, 31(11), pp.2088-2093.
- Clark, A. J., 1933. *Mode of Action of Drugs on Cells*; Edward Arnold: London.
- Colquhoun, D., 2006. The quantitative analysis of drug–receptor interactions: a short history. *Trends in Pharmacological Sciences*, 27(3), pp.149-157.
- Craig, D., 1993. The Cheng-Prusoff relationship: something lost in the translation. *Trends in Pharmacological Sciences*, 14(3), pp.89-91.
- Cserjesi, P., Brown, D., Ligon, L., Lyons, E., Copeland, G., Gilbert, J., Jenkins, A., & Olson, N., 1995. Scleraxis: a basic helix-loop-helix protein that prefigures skeletal formation during mouse embryogenesis. *Development*, 121(4), pp. 1099–1110.
- Cudic, M., and Fields, G.B., 2008. Solid-Phase Peptide Synthesis. In: *Solid-Phase Peptide Synthesis*. *Molecular Biomethods Handbook*. Springer, 2008, pp. 515-546.

- Currie, H.A. and Perry, C.C., 2007. 'Silica in plants: Biological, biochemical and chemical studies', *Annals of Botany*, 100(7), pp. 1383–1389.
- D'Amelio, P. and Isaia, G., 2009. Immune System and Postmenopausal Bone Loss. *Clinical Reviews in Bone and Mineral Metabolism*, 7(4), pp.262-268.
- D'Amelio, P., Grimaldi, A., Di Bella, S., Brianza, S., Cristofaro, M., Tamone, C., Giribaldi, G., Ulliers, D., Pescarmona, G. and Isaia, G., 2008. Estrogen deficiency increases osteoclastogenesis up-regulating T cells activity: A key mechanism in osteoporosis. *Bone*, 43(1), pp.92-100.
- Darnay, B., Haridas, V., Ni, J., Moore, P. and Aggarwal, B., 1998. Characterization of the Intracellular Domain of Receptor Activator of NF- κ B (RANK). *Journal of Biological Chemistry*, 273(32), pp.20551-20555.
- Darnell, J., 2012. The JAK-STAT pathway at 20. *JAK-STAT*, 1(1), pp.2-5.
- De Jong, W. and Borm, P., 2008. Drug delivery and nanoparticles: Applications and hazards. *International Journal of Nanomedicine*, 3(2), p.133-149.
- Delle Piane, M., Corno, M. and Ugliengo, P., 2016. Propionic acid derivatives confined in mesoporous silica: monomers or dimers? The case of ibuprofen investigated by static and dynamic ab initio simulations. *Theoretical Chemistry Accounts*, 135(3), pp.1-10.
- Delle Piane, M., Corno, M., Pedone, A., Dovesi, R. and Ugliengo, P., 2014. Large-Scale B3LYP Simulations of Ibuprofen Adsorbed in MCM-41 Mesoporous Silica as Drug Delivery System. *The Journal of Physical Chemistry C*, 118(46), pp.26737-26749.
- Delle Piane, M., Vaccari, S., Corno, M. and Ugliengo, P., 2014b. Silica-Based Materials as Drug Adsorbents: First Principle Investigation on the Role of Water Microsolvation on Ibuprofen Adsorption. *The Journal of Physical Chemistry A*, 118(31), pp.5801-5807.
- Delle Piane, M.; Corno, M.; Ugliengo, P., 2018. Ab Initio Modeling of Hydrogen Bond Interaction at Silica Surfaces with Focus on Silica/ Drugs Systems. In *Modelling and Simulation in the Science of Micro and Meso-Porous Materials*; Catlow, C. R. A., van Speybroeck, V., van Santen, R. A., Eds.; Elsevier, pp 297–328.
- Demertzis, M., 2004. Low detection limit spectrophotometry. *Analytica Chimica Acta*, 505(1), pp.73-76.
- Dieudonné, S., van den Dolder, J., de Ruijter, J., Paldan, H., Peltola, T., van 't Hof, M., Happonen, R. and Jansen, J., 2002. Osteoblast differentiation of bone marrow

- stromal cells cultured on silica gel and sol–gel-derived titania. *Biomaterials*, 23(14), pp.3041-3051.
- Diwu, Z., Chen, C., Zhang, C., Klaubert, D. and Haugland, R., 1999. A novel acidotropic pH indicator and its potential application in labeling acidic organelles of live cells. *Chemistry & Biology*, 6(7), pp.411-418.
- Domazetovic, V., 2017. Oxidative stress in bone remodeling: role of antioxidants. *Clinical Cases in Mineral and Bone Metabolism*, 14(2), p.209.
- Duckett, J., 1970. Spore size in the genus *Equisetum*. *New Phytologist*, 69(2), pp.333-346.
- Dudko, O., Filippov, A., Klafter, J. and Urbakh, M., 2003. Beyond the conventional description of dynamic force spectroscopy of adhesion bonds. *Proceedings of the National Academy of Sciences*, 100(20), pp.11378-11381.
- Ellis, S., Brown, S., in het Panhuis, M., Blanksby, S. and Mitchell, T., 2013. Surface analysis of lipids by mass spectrometry: More than just imaging. *Progress in Lipid Research*, 52(4), pp.329-353.
- Emami, F., Puddu, V., Berry, R., Varshney, V., Patwardhan, S., Perry, C. and Heinz, H., 2014. Prediction of Specific Biomolecule Adsorption on Silica Surfaces as a Function of pH and Particle Size. *Chemistry of Materials*, 26(19), pp.5725-5734.
- Emami, F., Puddu, V., Berry, R., Varshney, V., Patwardhan, S., Perry, C. and Heinz, H., 2014a. Force Field and a Surface Model Database for Silica to Simulate Interfacial Properties in Atomic Resolution. *Chemistry of Materials*, 26(8), pp.2647-2658.
- Emami, F., Puddu, V., Berry, R., Varshney, V., Patwardhan, S., Perry, C. and Heinz, H., 2014b. Prediction of Specific Biomolecule Adsorption on Silica Surfaces as a Function of pH and Particle Size. *Chemistry of Materials*, 26(19), pp.5725-5734.
- Faccio, R., Takeshita, S., Zallone, A., Ross, F. and Teitelbaum, S., 2003. c-Fms and the $\alpha\beta3$ integrin collaborate during osteoclast differentiation. *Journal of Clinical Investigation*, 111(5), pp.749-758.
- Fahey, R. C. and Newton, G. L., 1987. Determination of low molecular weight thiols using monobromobimane fluorescent labeling and high performance liquid chromatography. *Methods in Enzymology*, 143, pp.85–96.
- Farooq, M. and Dietz, K., 2015. Silicon as Versatile Player in Plant and Human Biology: Overlooked and Poorly Understood. *Frontiers in Plant Science*, 6.

- Fernandez-Fernandez, A., Manchanda, R. and McGoron, A., 2011. Theranostic Applications of Nanomaterials in Cancer: Drug Delivery, Image-Guided Therapy, and Multifunctional Platforms. *Applied Biochemistry and Biotechnology*, 165(7-8), pp.1628-1651.
- Fili, S., Karalaki, M. and Schaller, B., 2009. Mechanism of bone metastasis: The role of osteoprotegerin and of the host-tissue microenvironment-related survival factors. *Cancer Letters*, 283(1), pp.10-19.
- Földes-Papp, Z., Demel, U. and Tilz, G., 2003. Laser scanning confocal fluorescence microscopy: an overview. *International Immunopharmacology*, 3(13-14), pp.1715-1729.
- Freire, E.; Mayorga, O. L.; Straume, M., 1990. Isothermal Titration Calorimetry. *Analytical Chemistry*, 62(18), pp.950A-959A.
- Friedrichs, L., Maier, M. and Hamm, C., 2012. A new method for exact three-dimensional reconstructions of diatom frustules. *Journal of Microscopy*, 248(2), pp.208-217.
- Fuller, J., Zugates, G., Ferreira, L., Ow, H., Nguyen, N., Wiesner, U. and Langer, R., 2008. Intracellular delivery of core-shell fluorescent silica nanoparticles. *Biomaterials*, 29(10), pp.1526-1532.
- Galibert, L., Tometsko, M., Anderson, D., Cosman, D. and Dougall, W., 1998. The Involvement of Multiple Tumor Necrosis Factor Receptor (TNFR)-associated Factors in the Signaling Mechanisms of Receptor Activator of NF- κ B, a Member of the TNFR Superfamily. *Journal of Biological Chemistry*, 273(51), pp.34120-34127.
- Gan, Y. and Franks, G., 2006. Charging Behavior of the Gibbsite Basal (001) Surface in NaCl Solution Investigated by AFM Colloidal Probe Technique. *Langmuir*, 22(14), pp.6087-6092.
- Gell, C., Brockwell, D. and Smith, A., 2006. *Handbook of single molecule fluorescence spectroscopy*. Oxford: Oxford University Press.
- Ghafari, H., Parambath, M. and Hanley, Q., 2012. Macromolecular binding and kinetic analysis with optically sectioned planar format assays. *The Analyst*, 137(20), pp.4809-4814.
- Ghafari, H., Zhou, Y., Ali, S. and Hanley, Q., 2009. Confocal detection of planar homogeneous and heterogeneous immunosorbent assays. *Journal of Biomedical Optics*, 14(6), pp.064022(1-10).

- Ginaldi, L. and De Martinis, M., 2016. Osteoimmunology and Beyond. *Current Medicinal Chemistry*, 23(33), pp.3754-3774.
- Girelli, A. and Mattei, E., 2005. Application of immobilized enzyme reactor in on-line high performance liquid chromatography: A review. *Journal of Chromatography B*, 819(1), pp.3-16.
- Goldstein, D., 1986. Effect of alcohol on cellular membranes. *Annals of Emergency Medicine*, 15(9), pp.1013-1018.
- Goldstein, J., Newbury, E., Joy, C., Echlin, P., Lyman, E., Lifeshin, E., and Sawyer, L., 2003. *Scanning electron microscopy and x-ray microanalysis*. 3rd ed. New York: Plenum Publishers.
- Gray, J., 2004. The Interaction of Proteins with Solid Surfaces. *ChemInform*, 35(26), pp.110-115.
- Grundt, A., Grafe, I., Liegibel, U., Sommer, U., Nawroth, P. and Kasperk, C., 2009. Direct effects of osteoprotegerin on human bone cell metabolism. *Biochemical and Biophysical Research Communications*, 389(3), pp.550-555.
- Guder, C., Gravius, S., Burger, C., Wirtz, D. and Schildberg, F., 2020. Osteoimmunology: A Current Update of the Interplay Between Bone and the Immune System. *Frontiers in Immunology*, 11.
- Guo, S., Kalinin, S. and Jesse, S., 2012. Open-loop band excitation Kelvin probe force microscopy. *Nanotechnology*, 23(12), p.125704.
- Hall, K., & Miyake, T., 1995. Divide, accumulate, differentiate: cell condensation in skeletal development revisited. *The International journal of developmental biology*, 39(6), pp. 881–893.
- Han, J. and Sholl, D., 2009. Enantiospecific Adsorption of Amino Acids on Hydroxylated Quartz (0001). *Langmuir*, 25(18), pp.10737-10745.
- Han, J. and Sholl, D., 2010. Enantiospecific adsorption of amino acids on hydroxylated quartz (1010). *Physical Chemistry Chemical Physics*, 12(28), p.8024-8032.
- Hatori, M., Klatte, K., Teixeira, C. and Shapiro, I., 2009. End labeling studies of fragmented DNA in the Avian growth plate: Evidence of apoptosis in terminally differentiated chondrocytes. *Journal of Bone and Mineral Research*, 10(12), pp.1960-1968.
- Hayashi, T., Kaneda, T., Toyama, Y., Kumegawa, M. and Hakeda, Y., 2002. Regulation of Receptor Activator of NF- κ B Ligand-induced Osteoclastogenesis by Endogenous

- Interferon- β (INF- β) and Suppressors of Cytokine Signaling (SOCS). *Journal of Biological Chemistry*, 277(31), pp.27880-27886.
- Hennessy, T.P., Boysen, R.I., Huber, M.I., Unger, K.K. and Hearn, M.T.W., 2003. Peptide mapping by reversed-phase high-performance liquid chromatography employing silica rod monoliths. *Journal of Chromatography A*, 1009 (1–2), 15-28.
- Hennig, A., Bakirci, H. and Nau, W., 2007. Label-free continuous enzyme assays with macrocycle-fluorescent dye complexes. *Nature Methods*, 4(8), pp.629-632.
- Hickman, G., Boocock, D., Pockley, A. and Perry, C., 2016. The Importance and Clinical Relevance of Surfaces in Tissue Culture. *ACS Biomaterials Science & Engineering*, 2(2), pp.152-164.
- Hickman, G., Rai, A., Boocock, D., Rees, R. and Perry, C., 2012. Fabrication, characterisation and performance of hydrophilic and super-hydrophilic silica as cell culture surfaces. *Journal of Materials Chemistry*, 22(24), p.12141-12148.
- Hickman, G., Rees, R., Boocock, D., Pockley, A. and Perry, C., 2014. Controlling the Dynamics of Cell Transition in Heterogeneous Cultures using Surface Chemistry. *Advanced Healthcare Materials*, 4(4), pp.593-601.
- Hildebrand, M., 2003. 'Biological processing of nanostructured silica in diatoms', *Progress in Organic Coatings*, 47(3-4), pp. 256–266.
- Hildebrand, M., 2008. Diatoms, Biomineralization Processes, and Genomics. *Chemical Reviews*, 108(11), pp.4855-4874.
- Hildebrand, M., Holton, G., Joy, D., Doktycz, M. and Allison, D., 2009. Diverse and conserved nano- and mesoscale structures of diatom silica revealed by atomic force microscopy. *Journal of Microscopy*, 235(2), pp.172-187.
- Hill, A. V., 1910. The Possible Effects of the Aggregation of the Molecules of Haemoglobin on Its Dissociation Curves. *The Journal of Physiology*, 40, pp. 4–7.
- Hodson, M. J., Smith, R. J., Vanblaaderen, A., Crafton, T. and Oneill, C.H., 1994. Detecting plant silica fibers in animal tissue by confocal fluorescence microscopy. *Annals of Occupational Hygiene*, 38 (2), pp. 149-160.
- Hofbauer, L. and Heufelder, A., 2001. Role of receptor activator of nuclear factor- κ B ligand and osteoprotegerin in bone cell biology. *Journal of Molecular Medicine*, 79(5-6), pp.243-253.
- Hoffmann E., Stroobant V., 2007. *Mass Spectrometry Principals and Applications*. John Wiley & Sons, Inc. United States of America, 3rd Edition, ISBN 978-0-470-03311-1

- Holling, T., Schooten, E. and van Den Elsen, P., 2004. Function and regulation of MHC class II molecules in T-lymphocytes: of mice and men. *Human Immunology*, 65(4), pp.282-290.
- Holzhter, G., Narayanan, K. and Gerber, T., 2003. Structure of silica in *Equisetum arvense*. *Analytical and Bioanalytical Chemistry*, 376(4), pp.512-517.
- Homola, J., Yee, S. and Gauglitz, G., 1999. Surface plasmon resonance sensors: review. *Sensors and Actuators B: Chemical*, 54(1-2), pp.3-15.
- Hornig, S., Biskup, C., Gräfe, A., Wotschadlo, J., Liebert, T., Mohr, G. and Heinze, T., 2008. Biocompatible fluorescent nanoparticles for pH-sensing. *Soft Matter*, 4(6), p.1169.
- Horton, A., 1990. The biology of bone growth. *Growth Genet. Horm*, 6 (2), pp 1–3.
- Hou, T., Chiang-Ni, C. and Teng, S., 2019. Current status of MALDI-TOF mass spectrometry in clinical microbiology. *Journal of Food and Drug Analysis*, 27(2), pp.404-414.
- Hou, X., and Jones, B., 2000. Inductively Coupled Plasma-Optical Emission Spectrometry. *Encyclopedia of Analytical Chemistry*.
- Ikuma, K., Madden, A., Decho, A. and Lau, B., 2014. Deposition of nanoparticles onto polysaccharide-coated surfaces: implications for nanoparticle–biofilm interactions. *Environ. Sci.: Nano*, 1(2), pp.117-122.
- Iler, R. K., 1979. *The Chemistry of Silica: Solubility, Polymerization, Colloid and Surface Properties and Biochemistry of Silica*. Wiley: New York
- Ingalls, A., Whitehead, K. and Bridoux, M., 2010. Tinted windows: The presence of the UV absorbing compounds called mycosporine-like amino acids embedded in the frustules of marine diatoms. *Geochimica et Cosmochimica Acta*, 74(1), pp.104-115.
- Institute of Medicine., 2001. *Dietary Reference Intakes for vitamin A, vitamin K, arsenic, boron, chromium, copper, iodine, iron, manganese, molybdenum, nickel, silicon, vanadium, and zinc*. Washington, DC: National Academy Press.
- Iversen P., Beck B., Chen Y, Dere W., Devanarayan V., Eastwood B. et al., 2012. "HTS assay validation." In *Assay Guidance Manual* [Internet]. Eli Lilly & Company and the National Center for Advancing Translational Sciences.

- Izutsu, H., Mizukami, F., Nair, P., Kiyozumi, Y. and Maeda, K., 1997. Preparation and characterization of porous silica spheres by the sol-gel method in the presence of tartaric acid. *Journal of Materials Chemistry*, 7(5), pp.767-771.
- Jacome-Galarza, C., Lee, S., Lorenzo, J. and Aguila, H., 2013. Identification, characterization, and isolation of a common progenitor for osteoclasts, macrophages, and dendritic cells from murine bone marrow and periphery. *Journal of Bone and Mineral Research*, 28(5), pp.1203-1213.
- Jimi, E., Nakamura, I., Duong, L., Ikebe, T., Takahashi, N., Rodan, G. and Suda, T., 1999. Interleukin 1 Induces Multinucleation and Bone-Resorbing Activity of Osteoclasts in the Absence of Osteoblasts/Stromal Cells. *Experimental Cell Research*, 247(1), pp.84-93.
- Jimi, E., Nakamura, I., Ikebe, T., Akiyama, S., Takahashi, N. and Suda, T., 1998. Activation of NF- κ B Is Involved in the Survival of Osteoclasts Promoted by Interleukin-1. *Journal of Biological Chemistry*, 273(15), pp.8799-8805.
- Johnell, O. and Kanis, J.A., 2006. 'An estimate of the worldwide prevalence and disability associated with osteoporotic fractures', *Osteoporosis International*, 17(12), pp. 1726-1733.
- Jugdaohsingh, R., 2007. 'Silicon and bone health', *Silicon and bone health*, 11(2), pp. 99-110.
- Jugdaohsingh, R., Pedro, L., Watson, A. and Powell, J., 2015. Silicon and boron differ in their localization and loading in bone. *Bone Reports*, 1, pp.9-15.
- Jugdaohsingh, R., Tucker, K., Qiao, N., Cupples, L., Kiel, D. and Powell, J., 2003. Dietary Silicon Intake Is Positively Associated with Bone Mineral Density in Men and Premenopausal Women of the Framingham Offspring Cohort. *Journal of Bone and Mineral Research*, 19(2), pp.297-307.
- Jurinke, C., Oeth, P. and van den Boom, D., 2004. MALDI-TOF mass spectrometry. *Molecular Biotechnology*, 26(2), pp.147-163.
- Kaehr, B., Townson, J., Kalinich, R., Awad, Y., Swartzentruber, B., Dunphy, D. and Brinker, C., 2012. Cellular complexity captured in durable silica biocomposites. *Proceedings of the National Academy of Sciences*, 109(43), pp.17336-17341.
- Kahn, A. and Simmons, D., 1975. Investigation of cell lineage in bone using a chimaera of chick and quail embryonic tissue. *Nature*, 258(5533), pp.325-327.

- Kaplowitz N., Aw T. Y. and Ookhtens M., 1985. The regulation of hepatic GSH. *Annual Review of Pharmacology and Toxicology*, 25, pp.714–744.
- Karmakar, B., De, G. and Ganguli, D., 2000. Dense silica microspheres from organic and inorganic acid hydrolysis of TEOS. *Journal of Non-Crystalline Solids*, 272(2-3), pp.119-126.
- Kawaguchi, T. and Ono, K., 1990. Spherical silica gels precipitated from acid catalyzed TEOS solutions. *Journal of Non-Crystalline Solids*, 121(1-3), pp.383-388.
- Kicman, A., Parkin, M. and Iles, R., 2007. An introduction to mass spectrometry based proteomics—Detection and characterization of gonadotropins and related molecules. *Molecular and Cellular Endocrinology*, 260-262, pp.212-227.
- Kim, D., Langmead, B. and Salzberg, S., 2015. HISAT: a fast spliced aligner with low memory requirements. *Nature Methods*, 12(4), pp.357-360.
- Kim, E., Bu, S., Sung, M., Kang, M. and Choi, M., 2013. Analysis of Antioxidant and Anti-inflammatory Activity of Silicon in Murine Macrophages. *Biological Trace Element Research*, 156(1-3), pp.329-337.
- Kim, I., Joachim, E., Choi, H. and Kim, K., 2015. Toxicity of silica nanoparticles depends on size, dose, and cell type. *Nanomedicine: Nanotechnology, Biology and Medicine*, 11(6), pp.1407-1416.
- Kim, M., Bae, Y., Choi, M. and Chung, Y., 2008. Silicon Supplementation Improves the Bone Mineral Density of Calcium-Deficient Ovariectomized Rats by Reducing Bone Resorption. *Biological Trace Element Research*, 128(3), pp.239-247.
- Kirkland, J., Truszkowski, F., Dilks, C. and Engel, G., 2000. Superficially porous silica microspheres for fast high-performance liquid chromatography of macromolecules. *Journal of Chromatography A*, 890(1), pp.3-13.
- Koch, C., Chiu, S., Akbarpour, M., Bharat, A., Ridge, K., Bartom, E. and Winter, D., 2018. A Beginner's Guide to Analysis of RNA Sequencing Data. *American Journal of Respiratory Cell and Molecular Biology*, 59(2), pp.145-157.
- Koga, T., Inui, M., Inoue, K., Kim, S., Suematsu, A., Kobayashi, E., Iwata, T., Ohnishi, H., Matozaki, T., Kodama, T., Taniguchi, T., Takayanagi, H. and Takai, T., 2004. Costimulatory signals mediated by the ITAM motif cooperate with RANKL for bone homeostasis. *Nature*, 428(6984), pp.758-763.
- Korzeniowska, B., Nooney, R., Wencel, D. and McDonagh, C., 2013. Silica nanoparticles for cell imaging and intracellular sensing. *Nanotechnology*, 24(44), p.442002.

- Kotake, S., Udagawa, N., Takahashi, N., Matsuzaki, K., Itoh, K., Ishiyama, S., Saito, S., Inoue, K., Kamatani, N., Gillespie, M., Martin, T. and Suda, T., 1999. IL-17 in synovial fluids from patients with rheumatoid arthritis is a potent stimulator of osteoclastogenesis. *Journal of Clinical Investigation*, 103(9), pp.1345-1352.
- Kotcherlakota, R., Barui, A., Prashar, S., Fajardo, M., Briones, D., Rodríguez-Diéguez, A., Patra, C. and Gómez-Ruiz, S., 2016. Curcumin loaded mesoporous silica: an effective drug delivery system for cancer treatment. *Biomaterials Science*, 4(3), pp.448-459.
- Kröger, N. and Poulsen, N., 2008. Diatoms—From Cell Wall Biogenesis to Nanotechnology. *Annual Review of Genetics*, 42(1), pp.83-107.
- Kröger, N., Deutzmann, R. and Sumper, M., 1999. Polycationic Peptides from Diatom Biosilica That Direct Silica Nanosphere Formation. *Science*, 286(5442), pp.1129-1132.
- Kröger, N., Deutzmann, R., Bergsdorf, C. and Sumper, M., 2000. 'Species-specific polyamines from diatoms control silica morphology', *Proceedings of the National Academy of Sciences*, 97(26), pp. 14133–14138.
- Kroutil, O., Chval, Z., Skelton, A. and Předota, M., 2015. Computer Simulations of Quartz (101)–Water Interface over a Range of pH Values. *The Journal of Physical Chemistry C*, 119(17), pp.9274-9286.
- Kubo, W. and Tatsuma, T., 2005. Conversion of a solid surface from super-hydrophobic to super-hydrophilic by photocatalytic remote oxidation and photocatalytic lithography. *Applied Surface Science*, 243(1-4), pp.125-128.
- Kucki, M. and Fuhrmann-Lieker, T., 2011. Staining diatoms with rhodamine dyes: control of emission colour in photonic biocomposites. *Journal of The Royal Society Interface*, 9(69), pp.727-733.
- Kühn, S. and Brownlee, C., 2005. Membrane organisation and dynamics in the marine diatom *Coscinodiscus wailesii* (Bacillariophyceae). *Botanica Marina*, 48(4), pp.297-305.
- Kupiec, T., 2004. Quality-control analytical methods: High-performance liquid chromatography. *International journal of pharmaceutical compounding*, 8, pp.223-227.

- Kwok, D., Ng, H. and Neumann, A., 2000. Experimental Study on Contact Angle Patterns: Liquid Surface Tensions Less Than Solid Surface Tensions. *Journal of Colloid and Interface Science*, 225(2), pp.323-328.
- Lacey, D., Timms, E., Tan, H., Kelley, M., Dunstan, C., Burgess, T., Elliott, R., Colombero, A., Elliott, G., Scully, S., Hsu, H., Sullivan, J., Hawkins, N., Davy, E., Capparelli, C., Eli, A., Qian, Y., Kaufman, S., Sarosi, I., Shalhoub, V., Senaldi, G., Guo, J., Delaney, J. and Boyle, W., 1998. Osteoprotegerin Ligand Is a Cytokine that Regulates Osteoclast Differentiation and Activation. *Cell*, 93(2), pp.165-176.
- Lai, Y., 2017. A statistical method for the conservative adjustment of false discovery rate (q-value). *BMC Bioinformatics*, 18(S3), pp.155-163.
- Lakowicz J.R., 2010. *Principals of Fluorescence Spectrometry*. Springer Science & Business Media. United States of America, 3rd Edition.
- Lange, J., Sapozhnikova, A., Lu, C., Hu, D., Li, X., Miclau, T. and Marcucio, R., 2009. Action of IL-1 β during fracture healing. *Journal of Orthopaedic Research*, 28(6), pp.778-784.
- Langmead, B. and Salzberg, S., 2012. Fast gapped-read alignment with Bowtie 2. *Nature Methods*, 9(4), pp.357-359.
- Latterini, L. and Amelia, M., 2009. Sensing Proteins with Luminescent Silica Nanoparticles. *Langmuir*, 25(8), pp.4767-4773.
- Law, C. and Exley, C., 2011. New insight into silica deposition in horsetail (*Equisetum arvense*). *BMC Plant Biology*, 11(1), p.112.
- Lazareno, S. and Birdsall, N., 1993. Estimation of competitive antagonist affinity from functional inhibition curves using the Gaddum, Schild and Cheng-Prusoff equations. *British Journal of Pharmacology*, 109(4), pp.1110-1119.
- Lazarevic, V., Chen, X., Shim, J., Hwang, E., Jang, E., Bolm, A., Oukka, M., Kuchroo, V. and Glimcher, L., 2010. T-bet represses TH17 differentiation by preventing Runx1-mediated activation of the gene encoding ROR γ t. *Nature Immunology*, 12(1), pp.96-104.
- Leblanc, K. and Hutchins, D., 2005. New applications of a biogenic silica deposition fluorophore in the study of oceanic diatoms. *Limnology and Oceanography: Methods*, 3(10), pp.462-476.

- Lee, S., Han, S., Kim, H. and Lee, Z., 2002. TAK1-dependent Activation of AP-1 and c-Jun N-terminal Kinase by Receptor Activator of NF- κ B. *BMB Reports*, 35(4), pp.371-376.
- Lee, S., Kim, T., Choi, Y. and Lorenzo, J., 2008. Osteoimmunology: cytokines and the skeletal system. *BMB Reports*, 41(7), pp.495-510.
- Lee, S., Kim, T., Jeong, D., Kim, N. and Choi, Y., 2008b. The Tec Family Tyrosine Kinase Btk Regulates RANKL-induced Osteoclast Maturation. *Journal of Biological Chemistry*, 283(17), pp.11526-11534.
- Lee, S., Yun, S., Cho, P., Yand, H. and Kim, O., 2019. Newly Recorded Species of Diatoms in the Source of Han and Nakdong Rivers, South Korea. *Phytotaxa*, 403(3), p.143.
- Leff, P. and Dougall, I., 1993. Further concerns over Cheng-Prusoff analysis. *Trends in Pharmacological Sciences*, 14(4), pp.110-112.
- Leibbrandt, A. and Penninger, J., 2008. RANK/RANKL: Regulators of Immune Responses and Bone Physiology. *Annals of the New York Academy of Sciences*, 1143(1), pp.123-150.
- Levy, D. and Darnell, J., 2002. STATs: transcriptional control and biological impact. *Nature Reviews Molecular Cell Biology*, 3(9), pp.651-662.
- Li, B. and Dewey, C., 2011. RSEM: accurate transcript quantification from RNA-Seq data with or without a reference genome. *BMC Bioinformatics*, 12(1).
- Li, C., Chu, S. and Lee, M., 1989. Characterizing the silica deposition vesicle of diatoms. *Protoplasma*, 151(2-3), pp.158-163.
- Li, H., Yang, G., Sun, Y., Wu, S. and Zhang, X., 2007. *Cylindrotheca closterium* is a species complex as was evidenced by the variations of *rbcl* gene and SSU rDNA. *Journal of Ocean University of China*, 6(2), pp.167-174.
- Li, J., D'Amelio, P., Robinson, J., Walker, L., Vaccaro, C., Luo, T., Tyagi, A., Yu, M., Reott, M., Sassi, F., Buondonno, I., Adams, J., Weitzmann, M., Isaia, G. and Pacifici, R., 2015. IL-17A Is Increased in Humans with Primary Hyperparathyroidism and Mediates PTH-Induced Bone Loss in Mice. *Cell Metabolism*, 22(5), pp.799-810.
- Li, J., Sarosi, I., Yan, X., Morony, S., Capparelli, C., Tan, H., McCabe, S., Elliott, R., Scully, S., Van, G., Kaufman, S., Juan, S., Sun, Y., Tarpley, J., Martin, L., Christensen, K., McCabe, J., Kostenuik, P., Hsu, H., Fletcher, F., Dunstan, C., Lacey, D. and Boyle, W., 2000. RANK is the intrinsic hematopoietic cell surface receptor that controls

- osteoclastogenesis and regulation of bone mass and calcium metabolism. *Proceedings of the National Academy of Sciences*, 97(4), pp.1566-1571.
- Li, X., Udagawa, N., Itoh, K., Suda, K., Murase, Y., Nishihara, T., Suda, T. and Takahashi, N., 2002. p38 MAPK-Mediated Signals Are Required for Inducing Osteoclast Differentiation but Not for Osteoclast Function. *Endocrinology*, 143(8), pp.3105-3113.
- Lonergan, S., Topel, D. and Marple, D., 2018. *The Science of Animal Growth and Meat Technology*. San Diego: Elsevier Science & Technology.
- Lorenzo, J., Horowitz, M. and Choi, Y., 2008. Osteoimmunology: Interactions of the Bone and Immune System. *Endocrine Reviews*, 29(4), pp.403-440.
- Losic, D., Short, K., Mitchell, J., Lal, R. and Voelcker, N., 2007. AFM Nanoindentations of Diatom Biosilica Surfaces. *Langmuir*, 23(9), pp.5014-5021.
- Love, M., Huber, W. and Anders, S., 2014. Moderated estimation of fold change and dispersion for RNA-seq data with DESeq2. *Genome Biology*, 15(12).
- Lovingood, D., Owens, J., Seeber, M., Kornev, K. and Luzinov, I., 2013. Preparation of Silica Nanoparticles Through Microwave-assisted Acid-catalysis. *Journal of Visualized Experiments*, (82) pp. e51022-e51022.
- Lowenstam H. A., Weiner S., 1989. *On Biomineralization*. Oxford University Press, New York.
- Macdonald, H., Hardcastle, A., Jugdaohsingh, R., Fraser, W., Reid, D. and Powell, J., 2012. Dietary silicon interacts with oestrogen to influence bone health: Evidence from the Aberdeen Prospective Osteoporosis Screening Study. *Bone*, 50(3), pp.681-687.
- Malvern Instruments, 2004. *Zetasizer Nano Series User Manual*. Worcestershire, United Kingdom: Malvern Instruments Ltd.
- Manolagas, S., 1995. Bone marrow, cytokines, and bone remodeling. *Biomedicine & Pharmacotherapy*, 49(10), p.473.
- Mansky, K., Sankar, U., Han, J. and Ostrowski, M., 2002. Microphthalmia Transcription Factor Is a Target of the p38 MAPK Pathway in Response to Receptor Activator of NF- κ B Ligand Signaling. *Journal of Biological Chemistry*, 277(13), pp.11077-11083.
- Marmottant, P., Ponomarenko, A. and Bienaimé, D., 2013. The walk and jump of Equisetum spores. *Proceedings of the Royal Society B: Biological Sciences*, 280(1770), p.20131465.

- Mathé, C., Devineau, S., Aude, J., Lagniel, G., Chédin, S., Legros, V., Mathon, M., Renault, J., Pin, S., Boulard, Y. and Labarre, J., 2013. Structural Determinants for Protein adsorption/non-adsorption to Silica Surface. *PLoS ONE*, 8(11), p.e81346.
- Matsumoto, M., Sudo, T., Saito, T., Osada, H. and Tsujimoto, M., 2000. Involvement of p38 Mitogen-activated Protein Kinase Signaling Pathway in Osteoclastogenesis Mediated by Receptor Activator of NF- κ B Ligand (RANKL). *Journal of Biological Chemistry*, 275(40), pp.31155-31161.
- Maxwell, K. and Johnson, G., 2000. Chlorophyll fluorescence—a practical guide. *Journal of Experimental Botany*, 51(345), pp.659-668.
- McCafferty, J., Griffiths, A., Winter, G. and Chiswell, D., 1990. Phage antibodies: filamentous phage displaying antibody variable domains. *Nature*, 348(6301), pp.552-554.
- McMahon, G., 2007. Analytical instrumentation: A guide to laboratory, portable and miniaturized instruments. 1st ed. Chichester: Wiley.
- McNair, H., Brzezinski, M. and Krause, J., 2015. Quantifying diatom silicification with the fluorescent dye, PDMPPO. *Limnology and Oceanography: Methods*, 13(10), pp.587-599.
- Meister, A. and Anderson, M. E., 1983. Glutathione. *Annual Review of Biochemistry*, 52, pp.711–760.
- Menéndez-Gutiérrez, M., Rószler, T., Fuentes, L., Núñez, V., Escolano, A., Redondo, J., De Clerck, N., Metzger, D., Valledor, A. and Ricote, M., 2015. Retinoid X receptors orchestrate osteoclast differentiation and postnatal bone remodeling. *Journal of Clinical Investigation*, 125(2), pp.809-823.
- Meng, M., Stievano, L. and Lambert, J., 2004. Adsorption and Thermal Condensation Mechanisms of Amino Acids on Oxide Supports. 1. Glycine on Silica. *Langmuir*, 20(3), pp.914-923.
- Menzel, H., Horstmann, S., Behrens, P., Bärnreuther, P., Krueger, I. and Jahns, M., 2003. Chemical properties of polyamines with relevance to the biomineralization of silica. *Chem. Commun.*, (24), pp.2994-2995.
- Merrifield, R. B., 1963. 'Solid Phase Peptide Synthesis. I. The Synthesis of a Tetrapeptide', *Journal of the American Chemical Society*, 85, 2149-2154.
- Michaelis, M., 2018. Binding Affinities and Adhesion Phenomena of Binding Peptides at The Interface to Zinc Oxide. PhD. UNIVERSITÄT BREMEN.

- Michaelis, M., Fayyaz, A., Parambath, M., Koeppen, S., Ciacchi, L., Hanley, Q. and Perry, C., 2019. Platform for Screening Abiotic/Biotic Interactions Using Indicator Displacement Assays. *Langmuir*, 35(44), pp.14230-14237.
- Minsky, M., 1961. Microscopy apparatus US patent 3013467. USP Office, Ed. US.
- Minsky, M., 1988. Memoir on inventing the confocal scanning microscope. *Scanning*, 10(4), pp.128-138.
- Miyamoto, T., Ohneda, O., Arai, F., Iwamoto, K., Okada, S., Takagi, K., Anderson, D. and Suda, T., 2001. Bifurcation of osteoclasts and dendritic cells from common progenitors. *Blood*, 98(8), pp.2544-2554.
- Mizukami, J., Takaesu, G., Akatsuka, H., Sakurai, H., Ninomiya-Tsuji, J., Matsumoto, K. and Sakurai, N., 2002. Receptor Activator of NF- κ B Ligand (RANKL) Activates TAK1 Mitogen-Activated Protein Kinase through a Signaling Complex Containing RANK, TAB2, and TRAF6. *Molecular and Cellular Biology*, 22(4), pp.992-1000.
- Mocsai, A., Humphrey, M., Van Ziffle, J., Hu, Y., Burghardt, A., Spusta, S., Majumdar, S., Lanier, L., Lowell, C. and Nakamura, M., 2004. The immunomodulatory adapter proteins DAP12 and Fc receptor γ -chain (FcR γ) regulate development of functional osteoclasts through the Syk tyrosine kinase. *Proceedings of the National Academy of Sciences*, 101(16), pp.6158-6163.
- Monton, M., Forsberg, E. and Brennan, J., 2011. Tailoring Sol–Gel-Derived Silica Materials for Optical Biosensing. *Chemistry of Materials*, 24(5), pp.796-811.
- Morony, S., Capparelli, C., Lee, R., Shimamoto, G., Boone, T., Lacey, D. and Dunstan, C., 1999. A Chimeric Form of Osteoprotegerin Inhibits Hypercalcemia and Bone Resorption Induced by IL-1 β , TNF- α , PTH, PTHrP, and 1,25(OH) $_2$ D $_3$. *Journal of Bone and Mineral Research*, 14(9), pp.1478-1485.
- Motulsky, H. and Christopoulos, A., 2004. *Fitting Models to Biological Data Using Linear and Nonlinear Regression*. Oxford: Oxford Univ. Press.
- Müller, W., Krasko, A., Le Penec, G. and Schröder, H., 2003. Biochemistry and cell biology of silica formation in sponges. *Microscopy Research and Technique*, 62(4), pp.368-377.
- Murray, J., Appleton, P., Swedlow, J. and Waters, J., 2007. Evaluating performance in three-dimensional fluorescence microscopy. *Journal of Microscopy*, 228(3), pp.390-405.

- Naik, R., Brott, L., Clarson, S. and Stone, M., 2002. Silica-Precipitating Peptides Isolated from a Combinatorial Phage Display Peptide Library. *Journal of Nanoscience and Nanotechnology*, 2(1), pp.95-100.
- Nakashima, Y. and Haneji, T., 2013. Stimulation of Osteoclast Formation by RANKL Requires Interferon Regulatory Factor-4 and Is Inhibited by Simvastatin in a Mouse Model of Bone Loss. *PLoS ONE*, 8(9), p.e72033.
- Napierska, D., Thomassen, L., Rabolli, V., Lison, D., Gonzalez, L., Kirsch-Volders, M., Martens, J. and Hoet, P., 2009. Size-Dependent Cytotoxicity of Monodisperse Silica Nanoparticles in Human Endothelial Cells. *Small*, 5(7), pp.846-853.
- Newcombe, F., 1888. Spore-Dissemination of Equisetum. *Botanical Gazette*, 13(7), pp.173-178.
- Nguyen, B. and Anslyn, E., 2006. Indicator–displacement assays. *Coordination Chemistry Reviews*, 250(23-24), pp.3118-3127.
- Nguyen, B., Wiskur, S. and Anslyn, E., 2004. Using Indicator-Displacement Assays in Test Strips and To Follow Reaction Kinetics. *Organic Letters*, 6(15), pp.2499-2501.
- Nicklin, M., Rees, R., Pockley, A. and Perry, C., 2014. Development of an hydrophobic fluoro-silica surface for studying homotypic cancer cell aggregation–disaggregation as a single dynamic process in vitro. *Biomater. Sci.*, 2(10), pp.1486-1496.
- Nielsen, F., 2014. Update on the possible nutritional importance of silicon. *Journal of Trace Elements in Medicine and Biology*, 28(4), pp.379-382.
- Noll, F., Sumper, M. and Hampp, N., 2002. Nanostructure of Diatom Silica Surfaces and of Biomimetic Analogues. *Nano Letters*, 2(2), pp.91-95.
- O’Sullivan, C. and Guilbault, G., 1999. Commercial quartz crystal microbalances – theory and applications. *Biosensors and Bioelectronics*, 14(8-9), pp.663-670.
- Oberlender, A., & Tuan, S., 1994. Expression and functional involvement of N-cadherin in embryonic limb chondrogenesis. *Development*, 120(1), pp.177–187.
- Oliver, D., Michaelis, M., Heinz, H., Volkov, V. and Perry, C., 2019. From phage display to structure: an interplay of enthalpy and entropy in the binding of the LDHSLHS polypeptide to silica. *Physical Chemistry Chemical Physics*, 21(8), pp.4663-4672.
- Ono, T. and Takayanagi, H., 2017. Osteoimmunology in Bone Fracture Healing. *Current Osteoporosis Reports*, 15(4), pp.367-375.

- Ons.gov.uk., 2018. Annual mid-year population estimates, UK - Office for National Statistics. [online] Available at: <https://www.ons.gov.uk/peoplepopulationandcommunity/populationandmigration/populationestimates/bulletins/annualmidyearpopulationestimates/2015-06-25> [Accessed 21 Mar. 2017].
- O'Shea, J. and Murray, P., 2008. Cytokine Signaling Modules in Inflammatory Responses. *Immunity*, 28(4), pp.477-487.
- O'Shea, J., Holland, S. and Staudt, L., 2013. JAKs and STATs in Immunity, Immunodeficiency, and Cancer. *New England Journal of Medicine*, 368(2), pp.161-170.
- Osseo-Asare, K. and Arriagada, F., 1990. Preparation of SiO₂ nanoparticles in a non-ionic reverse micellar system. *Colloids and Surfaces*, 50, pp.321-339.
- Otzen, D., 2012. The Role of Proteins in Biosilicification. *Scientifica*, 2012, pp.1-22.
- Ovanesyan, Z., Aljzmi, A., Almusaynid, M., Khan, A., Valderrama, E., Nash, K. and Marucho, M., 2016. Ion-ion correlation, solvent excluded volume and pH effects on physicochemical properties of spherical oxide nanoparticles. *Journal of Colloid and Interface Science*, 462, pp.325-333.
- Ozcelik, H. and Barisik, M., 2019. Electric charge of nanopatterned silica surfaces. *Physical Chemistry Chemical Physics*, 21(14), pp.7576-7587.
- Paddock, S., 2000. Principles and Practices of Laser Scanning Confocal Microscopy. *Molecular Biotechnology*, 16(2), pp.127-150.
- Paddock, S., Fellers, T. and Davidson, M., 2020. Introductory Confocal Concepts. [online] Nikon's MicroscopyU. Available at: <https://www.microscopyu.com/techniques/confocal/introductory-confocal-concepts> [Accessed 20 July 2020].
- Parambath, M., 2016. Development of new fluorescence spectroscopy approaches for the study of silica. PhD, Nottingham Trent University.
- Parambath, M., Hanley, Q., Martin-Martinez, F., Giesa, T., Buehler, M. and Perry, C., 2016. The nature of the silicophilic fluorescence of PDMPO. *Physical Chemistry Chemical Physics*, 18(8), pp.5938-5948.
- Patra, M., Salonen, E., Terama, E., Vattulainen, I., Faller, R., Lee, B., Holopainen, J. and Karttunen, M., 2006. Under the Influence of Alcohol: The Effect of Ethanol and Methanol on Lipid Bilayers. *Biophysical Journal*, 90(4), pp.1121-1135.

- Patwardhan, S. and Clarson, S., 2005. Bioinspired mineralisation: macromolecule mediated synthesis of amorphous germania structures. *Polymer*, 46(12), pp.4474-4479.
- Patwardhan, S., Clarson, S. and Perry, C., 2005. On the role(s) of additives in bioinspired silicification. *Chemical Communications*, (9), p.1113.
- Patwardhan, S., Emami, F., Berry, R., Jones, S., Naik, R., Deschaume, O., Heinz, H. and Perry, C., 2012. Chemistry of Aqueous Silica Nanoparticle Surfaces and the Mechanism of Selective Peptide Adsorption. *Journal of the American Chemical Society*, 134(14), pp.6244-6256.
- Pedersen, S.L., Tofteng, A.P., Malik, L. and Jensen, K.J., 2012. Microwave heating in solid-phase peptide synthesis. *Chemical Society Reviews*, 41 (5), 1826-1844.
- Pedrós, R., Moya, I., Goulas, Y. and Jacquemoud, S., 2008. Chlorophyll fluorescence emission spectrum inside a leaf. *Photochemical & Photobiological Sciences*, 7(4), p.498.
- Pegg, A., 2016. Functions of Polyamines in Mammals. *Journal of Biological Chemistry*, 291(29), pp.14904-14912.
- Penninckx, M., 2002. An overview on glutathione in *Saccharomyces* versus non-conventional yeasts. *FEMS Yeast Research*, 2(3), pp.295-305.
- Perry, C. and Fraser, M., 1991. Silica deposition and ultrastructure in the cell wall of *Equisetum arvense*: the importance of cell wall structures and flow control in biosilicification?. *Philosophical Transactions of the Royal Society of London. Series B: Biological Sciences*, 334(1269), pp.149-157.
- Perry, C. and Keeling-Tucker, T., 2000. Biosilicification: the role of the organic matrix in structure control. *JBIC Journal of Biological Inorganic Chemistry*, 5(5), pp.537-550.
- Perry, C. and Keeling-Tucker, T., 2003. Model studies of colloidal silica precipitation using biosilica extracts from *Equisetum telmateia*. *Colloid & Polymer Science*, 281(7), pp.652-664.
- Perry, C. and Lu, Y., 1992. Preparation of silicas from silicon complexes: role of cellulose in polymerisation and aggregation control. *Journal of the Chemical Society, Faraday Transactions*, 88(19), p.2915.
- Perry, C., Moss, E. and Williams, R., 1990. A staining agent for biological silica. *Proceedings of the Royal Society of London. Series B: Biological Sciences*, 241(1300), pp.47-50.

- Perry, C.C., 2003. 'Silicification: The processes by which organisms capture and Mineralize silica', *Reviews in Mineralogy and Geochemistry*, 54(1), pp. 291–327.
- Pottle, D., 2021. Leica TCS SP5 Confocal Laser Scanning Microscope User Guide. [online] Umassmed.edu. Available at: <https://www.umassmed.edu/globalassets/three-dimensional-microscopy/files/resources/tcs-sp5_editedforcellbio-userguide1-basicimageacquisition.pdf> [Accessed 30 June 2021].
- Puddu, V. and Perry, C., 2012. Peptide Adsorption on Silica Nanoparticles: Evidence of Hydrophobic Interactions. *ACS Nano*, 6(7), pp.6356-6363.
- Puddu, V. and Perry, C., 2013. Interactions at the Silica–Peptide Interface: The Influence of Particle Size and Surface Functionality. *Langmuir*, 30(1), pp.227-233.
- Puddu, V. and Perry, C., 2014. Interactions at the Silica–Peptide Interface: The Influence of Particle Size and Surface Functionality. *Langmuir*, 30(1), pp.227-233.
- Pusch, W., Flocco, M. T., Leung, S. M., Thiele, H., Kostrzewa, M., 2003. Mass spectrometry-based clinical proteomics. *Pharmacogenomics*, 4(4), pp463-476.
- Qiagen.com., 2019. Rneasy Mini Handbook - (EN) - QIAGEN. [online] Available at: <<https://www.qiagen.com/es/resources/resourcedetail?id=14e7cf6e-521a-4cf7-8cbc-bf9f6fa33e24&lang=en>> [Accessed 30 October 2019].
- Rabe, M., Verdes, D. and Seeger, S., 2011. Understanding protein adsorption phenomena at solid surfaces. *Advances in Colloid and Interface Science*, 162(1-2), pp.87-106.
- Rai, A. and Perry, C., 2010. Facile Fabrication of Uniform Silica Films with Tunable Physical Properties Using Silicatein Protein from Sponges. *Langmuir*, 26(6), pp.4152-4159.
- Rai, A. and Perry, C., 2009. Fabrication of Tuneable Thickness Silica Films on Solid Surfaces Using Amines and Proteins. *Silicon*, 1(2), pp.91-101.
- Rai, A. and Perry, C., 2012. Mussel adhesive protein inspired coatings: a versatile method to fabricate silica films on various surfaces. *Journal of Materials Chemistry*, 22(11), p.4790.
- Rai, M., Tycksen, E., Sandell, L. and Brophy, R., 2017. Advantages of RNA-seq compared to RNA microarrays for transcriptome profiling of anterior cruciate ligament tears. *Journal of Orthopaedic Research*, 36(1), pp.384-397.

- Rajpurohit, R., Mansfield, K., Ohyama, K., Ewert, D. and Shapiro, I., 1999. Chondrocyte death is linked to development of a mitochondrial membrane permeability transition in the growth plate. *Journal of Cellular Physiology*, 179(3), pp.287-296.
- Raphael, I., Nalawade, S., Eagar, T. and Forsthuber, T., 2015. T cell subsets and their signature cytokines in autoimmune and inflammatory diseases. *Cytokine*, 74(1), pp.5-17.
- Ray, P., Huang, B. and Tsuji, Y., 2012. Reactive oxygen species (ROS) homeostasis and redox regulation in cellular signaling. *Cellular Signalling*, 24(5), pp.981-990.
- Reffitt, D., Ogston, N., Jugdaohsingh, R., Cheung, H., Evans, B., Thompson, R., Powell, J. and Hampson, G., 2003. Orthosilicic acid stimulates collagen type 1 synthesis and osteoblastic differentiation in human osteoblast-like cells in vitro. *Bone*, 32(2), pp.127-135.
- Reimann, E. F. and Lewin, J. C., 1964. The diatom genus *Cylindrotheca* Rabenhorst (with a reconsideration of *Nitzschia closterium*). *Journal of the Royal Microscopical Society*, 83(3), pp. 283–296.
- Rho, J.; Takami, M and Choi, Y., 2004. Osteoimmunology: interactions of the immune and skeletal systems. *Molecular Cell*, 17(1), pp.1–9.
- Rimola, A., Costa, D., Sodupe, M., Lambert, J. and Ugliengo, P., 2013. Silica Surface Features and Their Role in the Adsorption of Biomolecules: Computational Modeling and Experiments. *Chemical Reviews*, 113(6), pp.4216-4313.
- Rimola, A., Sodupe, M. and Ugliengo, P., 2009. Affinity Scale for the Interaction of Amino Acids with Silica Surfaces. *The Journal of Physical Chemistry C*, 113(14), pp.5741-5750.
- Ringnér, M., 2008. What is principal component analysis?. *Nature Biotechnology*, 26(3), pp.303-304.
- Roach, P., Farrar, D. and Perry, C., 2005. Interpretation of Protein Adsorption: Surface-Induced Conformational Changes. *Journal of the American Chemical Society*, 127(22), pp.8168-8173.
- Roach, P., Farrar, D. and Perry, C., 2006. Surface Tailoring for Controlled Protein Adsorption: Effect of Topography at the Nanometer Scale and Chemistry. *Journal of the American Chemical Society*, 128(12), pp.3939-3945.
- Rosales, C. and Uribe-Querol, E., 2017. Phagocytosis: A Fundamental Process in Immunity. *BioMed Research International*, 2017, pp.1-18.

- Roy, S. and Keshri, J., 2016. Studies on four araphid taxa (Bacillariophyta) from Srikhola River, Eastern. *Phykos* 46(1), pp. 7-16.
- Ruffolo, R., 1982. Important Concepts of Receptor Theory. *Journal of Autonomic Pharmacology*, 2(4), pp.277-295.
- Salis, A., Medda, L., Cugia, F. and Monduzzi, M., 2016. Effect of electrolytes on proteins physisorption on ordered mesoporous silica materials. *Colloids and Surfaces B: Biointerfaces*, 137, pp.77-90.
- Salonen, J., Laitinen, L., Kaukonen, A., Tuura, J., Björkqvist, M., Heikkilä, T., Vähä-Heikkilä, K., Hirvonen, J. and Lehto, V., 2005. Mesoporous silicon microparticles for oral drug delivery: Loading and release of five model drugs. *Journal of Controlled Release*, 108(2-3), pp.362-374.
- Sambrook, J., Fritsch, E. and Maniatis, T., 1989. *Molecular Cloning: A Laboratory Manual*. 2nd ed. Cold Spring Harbor: Cold Spring Harbor Laboratory Press, USA.
- Sanchez, C., Arribart, H. and Giraud Guille, M., 2005. Biomimetism and bioinspiration as tools for the design of innovative materials and systems. *Nature Materials*, 4(4), pp.277-288.
- Sato, K., Suematsu, A., Okamoto, K., Yamaguchi, A., Morishita, Y., Kadono, Y., Tanaka, S., Kodama, T., Akira, S., Iwakura, Y., Cua, D. and Takayanagi, H., 2006. Th17 functions as an osteoclastogenic helper T cell subset that links T cell activation and bone destruction. *The Journal of Cell Biology*, 175(4), pp.i8-i8.
- Schermelleh, L., Heintzmann, R. and Leonhardt, H., 2010. A guide to super-resolution fluorescence microscopy. *The Journal of Cell Biology*, 190(2), pp.165-175.
- Schild, D., Jung, A. and Schultens, H., 1994. Localization of calcium entry through calcium channels in olfactory receptor neurones using a laser scanning microscope and the calcium indicator dyes Fluo-3 and Fura-Red. *Cell Calcium*, 15(5), pp.341-348.
- Schoppet, M., Preissner, K. and Hofbauer, L., 2002. RANK Ligand and Osteoprotegerin. *Arteriosclerosis, Thrombosis, and Vascular Biology*, 22(4), pp.549-553.
- Schwarz, K., 1973. 'A bound form of silicon in Glycosaminoglycans and Polyuronides', *Proceedings of the National Academy of Sciences*, 70(5), pp. 1608–1612.
- Schwarz, K. and Milne, D.B., 1972. 'Growth-promoting effects of silicon in rats', *Nature*, 239(5371), pp. 333–334.
- Scottish Intercollegiate Guidelines Network (SIGN), 2015. 'Management of osteoporosis and the prevention of fragility fractures'. A national clinical guideline, no. 142.

- Shah, F., Ruscsák, K. and Palmquist, A., 2019. 50 years of scanning electron microscopy of bone—a comprehensive overview of the important discoveries made and insights gained into bone material properties in health, disease, and taphonomy. *Bone Research*, 7(1).
- Shapiro, I., Debolt, K., Funanage, V., Smith, S. and Tuan, R., 2009. Developmental regulation of creatine kinase activity in cells of the epiphyseal growth cartilage. *Journal of Bone and Mineral Research*, 7(5), pp.493-500.
- Shimizu, K., Del Amo, Y., Brzezinski, M., Stucky, G. and Morse, D., 2001. A novel fluorescent silica tracer for biological silicification studies. *Chemistry & Biology*, 8(11), pp.1051-1060.
- Silva, F., Aguiar-Dias, A. and Mendonça, M., 2014. Silicified crystal concretions and rosettes in Piper (Piperaceae): unpublished reports on their macropatterns. *Acta Amazonica*, 44(4), 435-446.
- Singhal, N., Kumar, M., Kanaujia, P. and Viridi, J., 2015. MALDI-TOF mass spectrometry: an emerging technology for microbial identification and diagnosis. *Frontiers in Microbiology*, 6.
- Smith, G., 1985. Filamentous fusion phage: novel expression vectors that display cloned antigens on the virion surface. *Science*, 228(4705), pp.1315-1317.
- Solà Rabadà, A., 2016. Experimental studies of zinc oxide and silica peptide interactions. Ph.D. thesis. Nottingham Trent University.
- Sola-Rabada, A., Michaelis, M., Oliver, D., Roe, M., Colombi Ciacchi, L., Heinz, H. and Perry, C., 2018. Interactions at the Silica–Peptide Interface: Influence of the Extent of Functionalization on the Conformational Ensemble. *Langmuir*, 34(28), pp.8255-8263.
- Sola-Rabada, A., Rinck, J., Belton, D., Powell, A. and Perry, C., 2016. Isolation of a wide range of minerals from a thermally treated plant: *Equisetum arvense*, a Mare’s tale. *JBIC Journal of Biological Inorganic Chemistry*, 21(1), pp.101-112.
- Sola-Rabada, A., Sahare, P., Hickman, G., Vasquez, M., Canham, L., Perry, C. and Agarwal, V., 2018. Biogenic porous silica and silicon sourced from Mexican Giant Horsetail (*Equisetum myriochaetum*) and their application as supports for enzyme immobilization. *Colloids and Surfaces B: Biointerfaces*, 166, pp.195-202.

- Song, Y., Wu, L., Tannenbaum, S., Wishnok, J. and Han, J., 2013. Tunable Membranes for Free-Flow Zone Electrophoresis in PDMS Microchip Using Guided Self-Assembly of Silica Microbeads. *Analytical Chemistry*, 85(24), pp.11695-11699.
- Sørensen, M., Henriksen, K., Schaller, S., Henriksen, D., Nielsen, F., Dziegiel, M. and Karsdal, M., 2006. Characterization of osteoclasts derived from CD14+ monocytes isolated from peripheral blood. *Journal of Bone and Mineral Metabolism*, 25(1), pp.36-45.
- Šošić, D., Brand-Saberi, B., Schmidt, C., Christ, B. and Olson, E., 1997. Regulation of praxis Expression and Somite Formation by Ectoderm- and Neural Tube-Derived Signals. *Developmental Biology*, 185(2), pp.229-243.
- Spector, T., Calomme, M., Anderson, S., Clement, G., Bevan, L., Demeester, N., Swaminathan, R., Jugdaohsingh, R., Berghe, D. and Powell, J., 2008. Choline-stabilized orthosilicic acid supplementation as an adjunct to Calcium/Vitamin D3 stimulates markers of bone formation in osteopenic females: a randomized, placebo-controlled trial. *BMC Musculoskeletal Disorders*, 9(1), article 85.
- Speziani, C., Rivollier, A., Gallois, A., Coury, F., Mazzorana, M., Azocar, O., Flacher, M., Bella, C., Tebib, J., Jurdic, P., Roubourdin-Combe, C. and Delprat, C., 2007. Murine dendritic cell transdifferentiation into osteoclasts is differentially regulated by innate and adaptive cytokines. *European Journal of Immunology*, 37(3), pp.747-757.
- Stern, O., 1924. Zur theorie der elektrolytischen doppelschicht. *Zeitschrift für Elektrochemie und Angew. Phys. Chemie* 30(21-22), pp.508–516.
- Stöber, W., Fink, A. and Bohn, E., 1968. Controlled growth of monodisperse silica spheres in the micron size range. *Journal of Colloid and Interface Science*, 26(1), pp.62-69.
- Stoermer E. F. and Julius M. L., 2003. Centric diatoms. *Freshwater Algae of North America: Ecology and Classification*, Eds Wehr JD, Sheath RG (Elsevier, San Diego), pp 559–594.
- Stokes, G., 1854. On the change of refrangibility of light. *Abstracts of the Papers Communicated to the Royal Society of London*, 6, pp.195-200.
- Strasser, F., Offterdinger, M., Piestun, R., and Jesacher, A., 2019. Spectral image scanning microscopy. *Biomedical optics express*, 10(5), 2513–2527.

- Sumper, M. and Kröger, N., 2004. Silica formation in diatoms: the function of long-chain polyamines and silaffins. *J. Mater. Chem.*, 14(14), pp.2059-2065.
- Swedlow, J., Hu, K., Andrews, P., Roos, D. and Murray, J., 2002. Measuring tubulin content in *Toxoplasma gondii*: A comparison of laser-scanning confocal and wide-field fluorescence microscopy. *Proceedings of the National Academy of Sciences*, 99(4), pp.2014-2019.
- Takayanagi, H., Kim, S., Matsuo, K., Suzuki, H., Suzuki, T., Sato, K., Yokochi, T., Oda, H., Nakamura, K., Ida, N., Wagner, E. and Taniguchi, T., 2002. RANKL maintains bone homeostasis through c-Fos-dependent induction of interferon- β . *Nature*, 416(6882), pp.744-749.
- Thermofisher.com. 2019. [online] Available at: <https://assets.thermofisher.com/TFS-Assets/LSG/manuals/cms_055739.pdf> [Accessed 30 October 2019].
- Townson, J., Lin, Y., Chou, S., Awad, Y., Coker, E., Brinker, C. and Kaehr, B., 2014. Synthetic fossilization of soft biological tissues and their shape-preserving transformation into silica or electron-conductive replicas. *Nature Communications*, 5(1).
- Udagawa, N., Takahashi, N., Yasuda, H., Mizuno, A., Itoh, K., Ueno, Y., Shinki, T., Gillespie, M., Martin, T., Higashio, K. and Suda, T., 2000. Osteoprotegerin Produced by Osteoblasts Is an Important Regulator in Osteoclast Development and Function*. *Endocrinology*, 141(9), pp.3478-3484.
- Valeur, B., 2002. *Molecular fluorescence: Principles and Applications*. Weinheim: Wiley-VCH.
- Valko, M., Leibfritz, D., Moncol, J., Cronin, M., Mazur, M. and Telser, J., 2007. Free radicals and antioxidants in normal physiological functions and human disease. *The International Journal of Biochemistry & Cell Biology*, 39(1), pp.44-84.
- Valko, M., Rhodes, C., Moncol, J., Izakovic, M. and Mazur, M., 2006. Free radicals, metals and antioxidants in oxidative stress-induced cancer. *Chemico-Biological Interactions*, 160(1), pp.1-40.
- Vallet-Regí, M., Balas, F., & Arcos, D., 2007. Mesoporous materials for drug delivery. *Angewandte Chemie (International ed. in English)*, 46(40), 7548–7558.
- Van Blaaderen, A., Van Geest, J. and Vrij, A., 1992. Monodisperse colloidal silica spheres from tetraalkoxysilanes: Particle formation and growth mechanism. *Journal of Colloid and Interface Science*, 154(2), pp.481-501.

- Vansant, E., Voort, P. and Vrancken, K., 1995. Characterization And Chemical Modification of The Silica Surface. Amsterdam: Elsevier.
- Volkov, V., Hickman, G., Sola-Rabada, A. and Perry, C., 2019. Distributions of Silica and Biopolymer Structural Components in the Spore Elater of *Equisetum arvense*, an Ancient Silicifying Plant. *Frontiers in Plant Science*, 10, pp.1-10.
- Vrieling, E., Beelen, T., Sun, Q., Hazelaar, S., van Santen, R. and Gieskes, W., 2004. Ultrasmall, small, and wide angle X-ray scattering analysis of diatom biosilica: interspecific differences in fractal properties. *Journal of Materials Chemistry*, 14(13), pp.1970-1975.
- Vrieling, E., Beelen, T., Van Santen, R. and Gieskes, W., 2000. Nanoscale uniformity of pore architecture in diatomaceous silica: a combined small and wide angle x-ray scattering study. *Journal of Phycology*, 36(1), pp.146-159.
- Walsh, M. and Choi, Y., 2014. Biology of the RANKL/RANK/OPG System in Immunity, Bone, and Beyond. *Frontiers in Immunology*, 5.
- Walsh, M., Kim, N., Kadono, Y., Rho, J., Lee, S., Lorenzo, J. and Choi, Y., 2006. OSTEOIMMUNOLOGY: Interplay Between the Immune System and Bone Metabolism. *Annual Review of Immunology*, 24(1), pp.33-63.
- Wan, Y., Chong, L. and Evans, R., 2007. PPAR- γ regulates osteoclastogenesis in mice. *Nature Medicine*, 13(12), pp.1496-1503.
- Wang, S., Wang, X., Draenert, F., Albert, O., Schröder, H., Mailänder, V., Mitov, G. and Müller, W., 2014. Bioactive and biodegradable silica biomaterial for bone regeneration. *Bone*, 67, pp.292-304.
- Wang, X., Schröder, H. C., Wiens, M., Schloßmacher, U., & Müller, W. E., 2012. Biosilica: Molecular Biology, Biochemistry and Function in Demosponges as well as its Applied Aspects for Tissue Engineering. *Advances in marine biology*, 62, 231–271.
- Wauquier, F., Leotoing, L., Coxam, V., Guicheux, J. and Wittrant, Y., 2009. Oxidative stress in bone remodelling and disease. *Trends in Molecular Medicine*, 15(10), pp.468-477.
- Wenzl, S., Hett, R., Richthammer, P. and Sumper, M., 2008. Silacidins: Highly Acidic Phosphopeptides from Diatom Shells Assist in Silica Precipitation In Vitro. *Angewandte Chemie*, 120(9), pp.1753-1756.
- Werner D., 1977. *The Biology of Diatoms* (Blackwell, Oxford).

- WHO Technical Report Series no. 532, World Health Organization, 1973. 'Trace elements in human nutrition, pp. 168-170 [online]. Available at: http://apps.who.int/iris/bitstream/handle/10665/41057/WHO_TRS_532_eng.pdf?sequence=1. [Accessed 28/03/2018].
- Wieneke, R., Bernecker, A., Riedel, R., Sumper, M., Steinem, C. and Geyer, A., 2011. Silica precipitation with synthetic silaffin peptides. *Organic & Biomolecular Chemistry*, 9(15), p.5482.
- Williams P.M., 2016. Zeta Potential. In: Drioli E., Giorno L. (eds) *Encyclopedia of Membranes*. Springer, Berlin, Heidelberg.
- Wilson, N., Boniface, K., Chan, J., McKenzie, B., Blumenschein, W., Mattson, J., Basham, B., Smith, K., Chen, T., Morel, F., Lecron, J., Kastelein, R., Cua, D., McClanahan, T., Bowman, E. and de Waal Malefyt, R., 2007. Development, cytokine profile and function of human interleukin 17-producing helper T cells. *Nature Immunology*, 8(9), pp.950-957.
- Wong, B., Josien, R., Lee, S., Sauter, B., Li, H., Steinman, R. and Choi, Y., 1997. TRANCE (Tumor Necrosis Factor [TNF]-related Activation-induced Cytokine), a New TNF Family Member Predominantly Expressed in T cells, Is a Dendritic Cell-specific Survival Factor. *Journal of Experimental Medicine*, 186(12), pp.2075-2080.
- World Health Organ Technical Report Series no. 921, 2003. 'Prevention and management of osteoporosis'.
- Wright, L. and Walsh, T., 2012. Facet Selectivity of Binding on Quartz Surfaces: Free Energy Calculations of Amino-Acid Analogue Adsorption. *The Journal of Physical Chemistry C*, 116(4), pp.2933-2945.
- Wu, L., Genge, B., Dunkelberger, D., LeGeros, R., Concannon, B. and Wuthier, R., 1997. Physicochemical Characterization of the Nucleational Core of Matrix Vesicles. *Journal of Biological Chemistry*, 272(7), pp.4404-4411.
- Wu, Z., Li, C., Guo, X., Li, B., Zhang, D., Xu, Y. and Fang, F., 2012. Nanofracture on fused silica microchannel for Donnan exclusion based electrokinetic stacking of biomolecules. *Lab on a Chip*, 12(18), p.3408.
- Xing, L., Chen, D. and Boyce, B., 2013. Mice Deficient in NF- κ B p50 and p52 or RANK Have Defective Growth Plate Formation and Post-natal Dwarfism. *Bone Research*, 1(4), pp.336-345.

- Xu, J., Wu, H., Ang, E., Yip, K., Woloszyn, M., Zheng, M. and Tan, R., 2009. NF- κ B modulators in osteolytic bone diseases. *Cytokine & Growth Factor Reviews*, 20(1), pp.7-17.
- Xu, T., Fu, R. and Yan, L., 2003. A new insight into the adsorption of bovine serum albumin onto porous polyethylene membrane by zeta potential measurements, FTIR analyses, and AFM observations. *Journal of Colloid and Interface Science*, 262(2), pp.342-350.
- Yamamoto, A., Miyazaki, T., Kadono, Y., Takayanagi, H., Miura, T., Nishina, H., Katada, T., Wakabayashi, K., Oda, H., Nakamura, K. and Tanaka, S., 2002. Possible Involvement of κ B Kinase 2 and MKK7 in Osteoclastogenesis Induced by Receptor Activator of Nuclear Factor κ B Ligand. *Journal of Bone and Mineral Research*, 17(4), pp.612-621.
- Yao, Z., Li, P., Zhang, Q., Schwarz, E., Keng, P., Arbini, A., Boyce, B. and Xing, L., 2006. Tumor Necrosis Factor- α Increases Circulating Osteoclast Precursor Numbers by Promoting Their Proliferation and Differentiation in the Bone Marrow through Up-regulation of c-Fms Expression. *Journal of Biological Chemistry*, 281(17), pp.11846-11855.
- Yasuda, H., Shima, N., Nakagawa, N., Mochizuki, S., Yano, K., Fujise, N., Sato, Y., Goto, M., Yamaguchi, K., Kuriyama, M., Kanno, T., Murakami, A., Tsuda, E., Morinaga, T. and Higashio, K., 1998. Identity of Osteoclastogenesis Inhibitory Factor (OCIF) and Osteoprotegerin (OPG): A Mechanism by which OPG/OCIF Inhibits Osteoclastogenesis in Vitro¹. *Endocrinology*, 139(3), pp.1329-1337.
- Yasuda, H., Shima, N., Nakagawa, N., Yamaguchi, K., Kinoshita, M., Mochizuki, S., Tomoyasu, A., Yano, K., Goto, M., Murakami, A., Tsuda, E., Morinaga, T., Higashio, K., Udagawa, N., Takahashi, N. and Suda, T., 1998. Osteoclast differentiation factor is a ligand for osteoprotegerin/osteoclastogenesis-inhibitory factor and is identical to TRANCE/RANKL. *Proceedings of the National Academy of Sciences*, 95(7), pp.3597-3602.
- Yuan, Y., and Lee, T. R., 2013. Contact angle and wetting properties, in *Surface Science Techniques*, Springer Series (Berlin Heidelberg) in Surface Sciences, vol. 51, edited by G. Bracco and B. Holst, pp. 3– 34.

- Yung-Chi, C. and Prusoff, W., 1973. Relationship between the inhibition constant (KI) and the concentration of inhibitor which causes 50 per cent inhibition (I50) of an enzymatic reaction. *Biochemical Pharmacology*, 22(23), pp.3099-3108.
- Zemanová, L., Schenk, A., Valler, M., Nienhaus, G. and Heilker, R., 2003. Confocal optics microscopy for biochemical and cellular high-throughput screening. *Drug Discovery Today*, 8(23), pp.1085-1093.
- Zeng, R., Spolski, R., Casas, E., Zhu, W., Levy, D. and Leonard, W., 2007. The molecular basis of IL-21-mediated proliferation. *Blood*, 109(10), pp.4135-4142.
- Zhao, S., Fung-Leung, W., Bittner, A., Ngo, K. and Liu, X., 2014. Comparison of RNA-Seq and Microarray in Transcriptome Profiling of Activated T Cells. *PLoS ONE*, 9(1), p.e78644.
- Zhao, X., Tapeç-Dytioco, R. and Tan, W., 2003. Ultrasensitive DNA Detection Using Highly Fluorescent Bioconjugated Nanoparticles. *Journal of the American Chemical Society*, 125(38), pp.11474-11475.
- Zhou, L., Ivanov, I., Spolski, R., Min, R., Shenderov, K., Egawa, T., Levy, D., Leonard, W. and Littman, D., 2007. IL-6 programs TH-17 cell differentiation by promoting sequential engagement of the IL-21 and IL-23 pathways. *Nature Immunology*, 8(9), pp.967-974.
- Zhou, X., Liao, W., Liao, J., Liao, P. and Lu, H., 2015. Ribosomal proteins: functions beyond the ribosome. *Journal of Molecular Cell Biology*, 7(2), pp.92-104.
- Zhou, X., Moussa, F., Mankoci, S., Ustriyana, P., Zhang, N., Abdelmagid, S., Molenda, J., Murphy, W., Safadi, F. and Sahai, N., 2016. Orthosilicic acid, Si(OH)₄, stimulates osteoblast differentiation in vitro by upregulating miR-146a to antagonize NF-κB activation. *Acta Biomaterialia*, 39, pp.192-202.
- Zolkov, C., Avnir, D. and Armon, R., 2004. Tissue-derived cell growth on hybrid sol-gel films. *J. Mater. Chem.*, 14(14), pp.2200-2205.
- Zucca, P. and Sanjust, E., 2014. Inorganic Materials as Supports for Covalent Enzyme Immobilization: Methods and Mechanisms. *Molecules*, 19(9), pp.14139-14194.
- Zymoresearch.com., 2019. [online] Available at: <https://files.zymoresearch.com/protocols/_r1080_zr-96_rna_clean_concentrator.pdf> [Accessed 30 October 2020].

Michaelis, M.‡, Fayyaz, A‡., Parambath, M.‡, Koeppen, S., Ciacchi, L., Hanley, Q. and Perry, C., 2019. Platform for Screening Abiotic/Biotic Interactions Using Indicator Displacement Assays. *Langmuir*, 35(44), pp.14230-14237. (‡Authors contributed equally to this paper).

Platform for Screening Abiotic/Biotic Interactions Using Indicator Displacement Assays

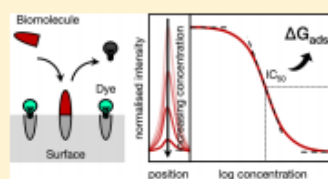
Monika Michaelis,^{†,‡} Aneeqa Fayyaz,[†] Mithun Parambath,[†] Susan Koeppen,^{‡,§} Lucio Colombi Ciacchi,^{‡,§} Quentin S. Hanley,[§] and Carole C. Perry^{†,§}

[†]Biomolecular and Materials Interface Research Group, School of Science and Technology and [‡]The Analytical Chemistry Research Group, School of Science and Technology, Nottingham Trent University, Clifton Lane, NG11 8NS Nottingham, U.K.

[§]Hybrid Materials Interfaces Group, Faculty of Production Engineering, Bremen Center for Computational Material Science (BCCMS), Center for Environmental Research and Sustainable Technology (UFT) and MAPEX Centre for Materials and Processes, University of Bremen, D-28359 Bremen, Germany

Supporting Information

ABSTRACT: This paper describes novel adaptations of optically sectioned planar format assays to screen compounds for their affinities to materials surfaces. The novel platform, which we name optically sectioned indicator displacement assays (O-IDA), makes use of displaceable dyes in a format adaptable to high-throughput multiwell plate technologies. We describe two approaches: the first being where the dye exhibits fluorescence in both the surface bound and unbound state and the second, where fluorescence is lost upon displacement of the dye from the surface. Half maximal inhibitory concentration (IC_{50}), binding affinity (K_d), and binding free energy (ΔG_{ads}) values can be extracted from the raw data. Representative biomolecules were tested for interactions with silica in an aqueous environment and ZnO(0001)-Zn and (10–10) facets in a nonaqueous environment. We provide the first experimental values for both the binding of small molecules to silica and the facet-dependent ZnO binding affinity of key amino acids associated with ZnO-specific oligopeptides. The specific data will be invaluable to those studying interactions at interfaces both experimentally and computationally. O-IDA provides a general framework for the high-throughput screening of molecule binding to materials surfaces, which has important applications in drug delivery, (bio-) catalysis, biosensing, and biomaterial engineering.



INTRODUCTION

Interactions at the abiotic/biotic interface are of fundamental interest in medical devices, drug delivery, and catalysis and have wide applications ranging from polypeptide adsorption,^{1–4} cell adhesion,^{5,6} biomaterials,^{7–10} and biosensors.^{11,12} Common methods for the experimental quantification of interactions at materials' surfaces include quartz crystal microbalance (QCM),¹³ surface plasmon resonance (SPR),¹⁴ or single molecule force spectroscopy.¹⁵ These techniques take an indirect measure of the interactions and heavily rely on the models applied during data analysis. Furthermore, the experimental procedure and the associated analysis can be very time-consuming. A direct measurement of binding enthalpies can be achieved using isothermal titration calorimetry,¹⁶ but the method is limited to stable suspensions.

Indicator displacement assays (IDAs)^{17–19} provide measurements of interactions based on the direct observation of competitive binding between a reference compound and the analyte of interest to a given interaction site. Although they are used in drug discovery and high throughput screening, to the best of our knowledge, they have not previously been applied to screening of molecules that bind to abiotic material surfaces. Adapting this approach into the field of abiotic/biotic interactions would represent an important advance and could

enable comprehensive screening of interactions at the analyte/material interface. Screenable displacement assays in a planar format²⁰ have been described for receptor ligand interaction studies and this approach can indeed be adapted to measure molecular interactions with abiotic/biotic surfaces, as we will prove in this paper.

We establish the novel approach using two representative functional oxides with important applications in nanotechnology and biomedicine. The first system is silica, for which knowledge of important binding interactions can lead to a deeper understanding of silica-based drug-delivery systems,^{21,22} the synthesis of new materials for biomedical use,²³ and processes such as biosilicification^{24,25} in mineralizing organisms.^{26–28} Advancements in this research area will have direct implications in material science, medicine, and bio-nanotechnology. For this system, we selected representative amino acids, a small polyamine,²⁹ and a drug, ibuprofen, that is often used in model studies.^{30–32}

As a second system, we chose zinc oxide which is widely used in the form of crystals and nanoparticles for applications

Received: October 3, 2019

Revised: October 14, 2019

Published: October 14, 2019